

Modeling and simulation of arterial walls with focus on damage and residual stresses

Von der Fakultät für Ingenieurwissenschaften,
Abteilung Bauwissenschaften
der Universität Duisburg-Essen
zur Erlangung des akademischen Grades

Doktor-Ingenieurin
genehmigte Dissertation

von

Dipl.-Ing. Sarah Brinkhues

aus Borken (Westf.)

Hauptreferent: Prof. Dr.-Ing. habil. Jörg Schröder

Korreferent: Prof. Dr. rer. nat. habil. Axel Klawonn

Tag der Einreichung: 12. Juli 2012

Tag der mündlichen Prüfung: 19. Oktober 2012

Fakultät für Ingenieurwissenschaften,
Abteilung Bauwissenschaften
der Universität Duisburg-Essen
Institut für Mechanik
Prof. Dr.-Ing. habil. J. Schröder

Herausgeber:

Prof. Dr.-Ing. habil. J. Schröder

Organisation und Verwaltung:

Prof. Dr.-Ing. habil. J. Schröder
Institut für Mechanik
Abteilung Bauwissenschaften
Fakultät für Ingenieurwissenschaften
Universität Duisburg-Essen
Universitätsstraße 15
45117 Essen
Tel.: 0201 / 183 - 2682
Fax: 0201 / 183 - 2680

© Sarah Brinkhues
Institut für Mechanik
Abteilung Bauwissenschaften
Fakultät für Ingenieurwissenschaften
Universität Duisburg-Essen
Universitätsstraße 15
45117 Essen

Alle Rechte, insbesondere das der Übersetzung in fremde Sprachen, vorbehalten. Ohne Genehmigung des Autors ist es nicht gestattet, dieses Heft ganz oder teilweise auf fotomechanischem Wege (Fotokopie, Mikrokopie), elektronischem oder sonstigem Wege zu vervielfältigen.

ISBN-10 3-9809679-6-4
ISBN-13 978-3-9809679-6-9
EAN 9783980967969

meinen Eltern

Preface

This work was developed during my time as research associate at the Institute of Mechanics at the University of Duisburg-Essen. Many people have accompanied and supported me on this way and I would like to thank some of them at this point.

First and foremost I thank my doctoral advisor Professor Jörg Schröder for the great opportunity to obtain my doctorate under his supervision. With his winning character and his extensive knowledge he captivates people and sparks their interest in mechanics. Jörg has always encouraged me to challenge myself and gave me the required support and the mechanical background to achieve my goals. Furthermore, I thank Professor Axel Klawonn for the intensive collaboration during the last years and for agreeing to act as second examiner of this thesis. In particular in the field of applied mathematical methods in continuum mechanics I could benefit a lot from his knowledge.

Furthermore, I thank Professor Gerhard A. Holzapfel for helpful scientific discussions and for the provision of experimental data for human arteries. My sincere thanks go to Oliver Rheinbach for many conversations we had about parallel computing and the corresponding simulation results. His continuous and immediate support regarding mathematical problems and the handling of the parallel computer system were very helpful for me.

Many thanks go to my colleagues for the comfortable working atmosphere, which played an important role for me: Moritz Bloßfeld, Dominik Brands, Bernhard Eidel, Veronika Jorisch, Matthias Labusch, Petra Lindner-Roullé, Vera Meyer, Tim Ricken, Lisa Scheunemann, Thomas Schmidt, Serdar Serdaş, Steffen Specht, Huy Ngoc Minh Thai, and Robin Wojnowski. Special thanks go also to my student assistants Simon Fausten and Anna-Katharina Tielke for the friendly cooperation and their helpful support.

In addition to that, I want to mention some colleagues which have played a crucial role during my graduation. First of all I thank Daniel Balzani who was the supervisor of my diploma thesis and who gave me the first insides into material modeling in biomechanics. I thank him for paving the way for my graduation and for the support he gave me during that time. My special thanks are due to Professor Joachim Bluhm for his joy of teaching, for lending an ear to everyone at any time, and for his commitment to the institute. Moreover, I thank Karl Steeger for being full of energy of life, for his sense of humor, and for his reliance. Special thanks go to a person, which I got to know at the very beginning of my studies. Alexander Schwarz accompanied me during my whole time at the university, became my colleague, and as a friend he was always ready to offer me help and advice.

My heartiest thanks go to my friends who gave me the right diversion from this work, different perspectives, and many reasons to smile. Especially I would like to thank Eva Albers, Bernhard Breil, Christina Delannay, Ina Graw, Thomas Hahn-Graw, Julia Heßbrüggen, Andrea Kampen, Sandra Risthaus, and Kai Timmermann.

I thank my whole family for their backing, in particular my brother Andreas Brinkhues and his wife Katja, my cousin Nicole Wesseling-Jätschmann, and certainly my parents Edith and Karl-Heinz Brinkhues. During my whole life my parents gave me the encouragement I needed and their trust in me makes my development easier. My deepest gratitude goes to my partner Marc-André Keip who has a clear mind and a warm heart. I thank him for his technical and above all for his emotional support in all situations of life.

Abstract

The present work deals with the continuum-mechanical modeling and analysis of arterial walls. One focus is on the construction of anisotropic damage models that are able to reflect damage effects in arterial tissues under therapeutic loading. Damage effects are assumed to be a main contributor to the success of a balloon angioplasty, which is a method of treatment of atherosclerotic arteries. Another main focus is on the elaboration of a numerical model for the incorporation of residual stresses in arterial walls. Residual stresses influence the circumferential stress distribution in such a way that they prevent large stress gradients in the arterial wall. Thus, a novel approach for the implementation of residual stresses is proposed. All models are adjusted to experimental data and applied to numerical simulations of patient-specific arterial walls. The quasi-incompressibility constraint is ensured by using the Penalty-Method and the Augmented-Lagrange-Method, which are analyzed with respect to their computational robustness.

Zusammenfassung

Die vorliegende Arbeit behandelt die kontinuumsmechanische Modellierung von Arterienwänden. Ein Schwerpunkt liegt in der Konstruktion von anisotropen Schädigungsmodellen zur Beschreibung von Schädigungseffekten in Arterienwänden, wie sie bei therapeutischen Maßnahmen auftreten. Solche Schädigungseffekte gelten als einer der wesentlichen Faktoren für eine erfolgreiche Behandlung von atherosklerotisch degenerierten Arterien mittels Ballonangioplastie. Ein weiterer Schwerpunkt liegt in der Erarbeitung eines numerischen Modells zur Berücksichtigung von Eigenspannungen in Arterienwänden. Eigenspannungen beeinflussen die Spannungsverteilung in Umfangsrichtung derart, dass sie zu einer Verringerung der Spannungsgradienten in der Arterienwand beitragen. Hierauf aufbauend wird ein neuer Ansatz zur Implementierung von Eigenspannungen vorgeschlagen. Alle Modelle werden an experimentelle Daten angepasst und auf die numerische Simulation von patientenspezifischen Arterienwänden angewendet. Die Quasi-Inkompressibilität des Materials wird zum einen durch die Verwendung einer Penalty-Methode und zum anderen über einen Augmented-Lagrange Ansatz erfüllt. Beide Methoden werden hinsichtlich ihres Einflusses auf die Robustheit numerischer Simulationen untersucht.

Contents

1	Introduction	1
2	Human arteries: composition and diseases	3
2.1	General composition of a healthy artery	4
2.2	Disease of arterial tissue and possible treatments	6
2.3	Mechanical behavior of arterial tissue	9
3	Fundamentals of the continuum mechanics of solids	11
3.1	Kinematical relations	11
3.2	Material time derivatives	15
3.3	The stress concept	16
3.4	Balance principles	18
3.4.1	Mass balance	18
3.4.2	Balance of linear momentum	19
3.4.3	Balance of angular momentum	19
3.4.4	Energy balance (1 st law of thermodynamics)	20
3.4.5	Entropy inequality (2 nd law of thermodynamics)	21
3.5	Basic principles in the framework of material modeling	23
3.5.1	Principle of material frame-indifference – Objectivity	24
3.5.2	Principle of material symmetry	25
3.6	Representation theorems of isotropic and anisotropic tensor functions	26
3.6.1	Representation theorems of isotropic tensor functions	26
3.6.2	Representation theorems of anisotropic tensor functions	28
4	Finite-Element-Method	31
4.1	Boundary value problem	31
4.2	Weak formulation of the field equations	31
4.3	Linearization of the weak forms	32
4.4	Finite element discretization	33
5	Material modeling of soft biological tissues	39
5.1	Polyconvex energy functions	39
5.1.1	Isotropic polyconvex energy functions	40
5.1.2	Transversely isotropic polyconvex energy functions	40
5.2	Incompressibility constraint	42

5.2.1	Kinematic split of the deformation gradient	42
5.2.2	Penalty-Method	44
5.2.3	Augmented-Lagrange-Method	45
6	Identification of material parameter	47
6.1	Adjustment to experimental data	47
6.2	Material parameters for the plaque components	50
6.2.1	Identification of plaque parameter	52
6.2.2	Influence of plaque behavior on arterial wall behavior	53
7	An anisotropic damage model for softening hysteresis in arterial walls	57
7.1	A short literature overview of damage in soft biological tissues	57
7.2	Damage variable, strain equivalence principle and anisotropic damage	59
7.3	Construction principle for damage models	62
7.3.1	Construction principle	62
7.3.2	Specification of the model for soft biological tissues	65
7.3.3	Algorithmic implementation	65
7.4	Specific constitutive models	69
7.5	Adjustment to experimental data	70
7.6	Numerical simulation of an arterial wall	73
8	Numerical analysis of the robustness of the Penalty-Method and the Augmented-Lagrange-Method	79
8.1	Constitutive model	79
8.2	Automatic time stepping	81
8.3	FEAP and FETI-DP Method	82
8.4	Simulation of an arterial segment with an axial length of 1 mm	84
8.5	Simulation of an arterial segment with an axial length of 10 mm	86
9	Incorporation of residual stresses in patient-specific arteries	93
9.1	State of the art in the modeling of residual stresses in arteries	93
9.2	Numerical simulation of an isotropic two-dimensional ideal tube	96
9.3	Derivation of suitable invariants for the definition of residual stresses in fiber-reinforced soft biological tissues	98
9.4	Incorporation of residual stresses	99
9.5	Numerical simulations	100
9.5.1	Anisotropic two-dimensional ideal tube	100

9.5.2	Two-dimensional realistic artery	103
9.5.3	Three-dimensional realistic artery	105
10	Summary and outlook	109
A	Notation and calculation rules	111
B	Voigt notation of the tangent modulus \mathbb{C}	114
C	Partial derivatives of the invariants with respect to C	115
	References	125

1 Introduction

In the last decades the field of biomechanics and related issues have emerged as a major area of research. It incorporates the study of the structure and the mechanical functionality of human, animal, and vegetal biomaterials. The goal of biomechanical research is to understand the biophysical phenomena arising in the field of biology and medicine, which affect normal and degenerative processes of the organism. The research is an iterative process, where hypotheses are formulated, proved by material models in computer simulations, reformulated, and verified by adjustment to experimental data.

As first biomechanists often Leonardo da Vinci (1452–1519; analysis of movement and anatomy of human joints, muscles, etc.) and Galileo Galilei (1564–1642; study of the strength of bones) are mentioned. Further pioneers in this field are René Descartes (1596–1650), Giovanni A. Borelli (1608–1679), Isaac Newton (1642–1727), Daniel Bernoulli (1700–1782), and Thomas Young (1773–1829), to mention a few. The biomechanical research made further progress in the 19th and 20th century, but received a new impetus with the development of digital computers and the invention of the Finite-Element-Method in the 1960s as well as the biological discoveries in the 1960s by Linus C. Pauling (1901–1994; structure of proteins), and Francis H. C. Crick (1916–2004; molecular structure of deoxyribonucleic, i.e. DNA, together with James D. Watson (born 1928)) among others. A exhaustive historical overview is e.g. given in Fung [1993] and Humphrey [1995, 2003].

This work deals with the continuum-mechanical analysis of soft biological tissues with a focus on the modeling of atherosclerotic arteries. Atherosclerosis is the result of biochemical and mechanical degenerative processes which lead to the formation of plaque deposits and therewith to narrowing of the lumen (the inside space of an artery). Considerable consequential diseases are among others heart attack or stroke, which are under the most common causes of death in the Western industrial nations. For example, the causes of death statistics of the federal statistical office of Germany states that in the year 2010 the most frequent cause of death in Germany are cardiovascular disease (352 689 of 858 768).

In order to provide a normal blood flow and to prevent the aggravation of the disease and the development of consequential diseases, the balloon angioplasty is an often used method of treatment. Here, the degenerated arterial wall is dilated by using a balloon catheter such that the lumen is increased. This pronounced therapeutic loading damages the artery in such a way that irreversible deformations remain, even after the balloon is deflated and removed from the artery. As a result, the *damage in the arterial wall* is a contributor to the success of this treatment. Therefore, the first main aim of this work is to model arterial tissues under therapeutic loading in order to gain more insight into the complex biomechanical processes arising in dilated, damaged arterial walls. This could also give information about the optimization of such therapeutic interventions. Another important phenomenon occurring in arteries is the presence of *residual stress*. Residual stresses are assumed to prevent large stress gradients in the arterial wall by homogenization of the circumferential stresses. The in-vivo stress distribution is strongly influenced by residual stresses. Thus, the second main goal of this work is to incorporate residual stresses into the continuum-mechanical model. In order to provide a realistic framework, the material models used in this work are *adjusted to experimental data* whenever suitable experiments are available. Otherwise, when such experimental data is not available (for example in the case of plaque deposits), reasonable parameters are chosen and their influence on

the overall mechanical behavior is tested. Additionally, realistic arterial cross-sections are taken into consideration, which have been obtained from patient-specific data. Since arterial walls consist of incompressible material, *robust computational schemes* for the incorporation of the incompressibility constraint are needed. For this purpose numerical methods based on the Penalty and the Augmented-Lagrange approach are employed.

This work is structured as follows. In **Chapter 2** biomechanical foundations of arterial walls are briefly discussed. Hereby, a deeper view is taken on the composition of arteries in order to explain their mechanical behavior. Additionally, typical vascular diseases and possible methods of treatment are mentioned.

The continuum-mechanical framework used in this work is explained in **Chapter 3**. A short review of some kinematical variables, measures of stress, the balance principles as well as of the representation theorems of isotropic and anisotropic tensor functions is given. The Finite-Element-Method is introduced in **Chapter 4**. First, the underlying nonlinear boundary value problem and the corresponding weak formulation are discussed. Then the needed linearized form is evaluated and the discretization of the domain with finite elements is explained. Furthermore, details of specific finite elements used in this work are provided.

For the material modeling of the soft biological tissues polyconvex energy functions will be used. The construction of such functions is discussed in **Chapter 5**. Furthermore, different methods for the consideration of the quasi-incompressibility of soft biological tissues as the Penalty-Method and the Augmented-Lagrange-Method are explained. In order to find adequate material parameters for the proposed strain-energy functions, a method for adjustment to experimental uniaxial extension tests is discussed in **Chapter 6**. If no experimental data is available, as for example in case of the plaque components, reasonable material parameters have to be chosen. The identification of different sets of parameters for the plaque and their influence is investigated.

A material model for the description of damage of soft biological tissues is proposed in **Chapter 7**. To provide an introduction into this subject a literature overview is given on material damage modeling and experimental findings in this field. Then some fundamentals in damage modeling are provided and the stress-strain hysteresis of over-expanded soft biological tissue is discussed in detail. Based on the principle for the construction of polyconvex energy functions, a construction principle for damage models as well as its algorithmic implementation is presented. Specific anisotropic constitutive models fulfilling the proposed construction principle are considered and adjusted to experimental data. In a numerical simulation of a two-dimensional realistic arterial cross-section the applicability of the anisotropic damage model as well as the working of the proposed algorithm in finite-element simulations are demonstrated.

In **Chapter 8** the Penalty-Method and the Augmented-Lagrange-Method are investigated with respect to their influence on the robustness of the numerical simulation. Here, special attention is paid to a boundary value problem with about a million degrees of freedom, which is solved using an iterative solution strategy.

A novel model for the incorporation of residual stresses in arterial walls is introduced in **Chapter 9**. This model is first tested in two-dimensional isotropic and anisotropic ideal tubes and later on applied to two- and three-dimensional patient-specific arterial walls. Additionally, the opening of unloaded arterial walls due to the presence of residual stresses is investigated.

Chapter 10 provides a summary of this work and some aspects for future developments.

2 Human arteries: composition and diseases

The word artery comes from the Greek and means “the one trailed on the pericardium (heart sac)”. Arteries carry blood away from the heart: the systemic arteries carry the oxygen-rich blood to the whole body, while the pulmonary arteries carry the blood with low oxygen content to the lungs. In general, there exist two distinct types of systemic arteries: elastic arteries and muscular arteries. Elastic arteries, for example the aorta and the common carotid and iliac arteries, are located close to the heart and have a larger diameter. They provide a pulsative, but continuous blood flow by passive contraction during the diastole¹ (windkessel effect). To the muscular type belong, amongst others, the femoral and renal arteries. They are smaller, peripheral vessels, which regulate the blood flow to the organs. Transitional arteries, which have both elastic and muscular properties are, for example, the internal carotids. For detailed information, the reader is referred to, for example, Humphrey [1995] and Junqueira and Carneiro [2005]. Fig. 2.1 shows a schematic of the human arterial tree.

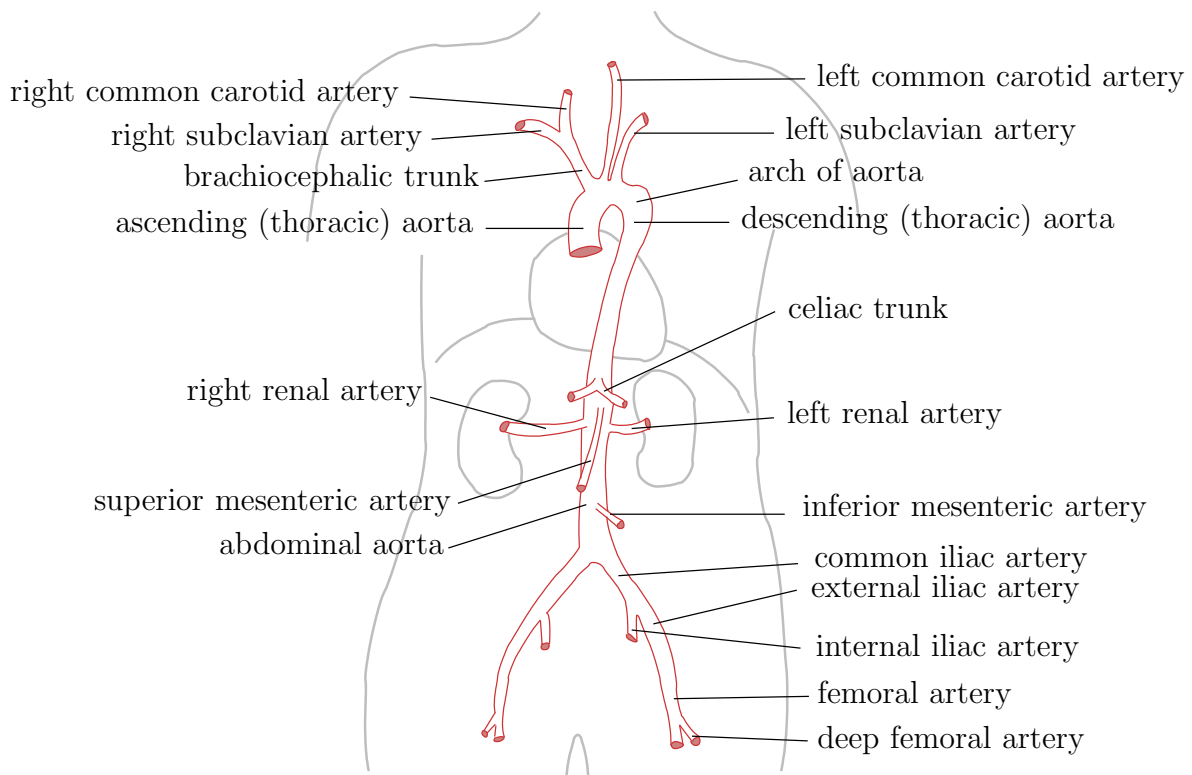


Figure 2.1: Selection of the most relevant systemic arteries in the human body.

In the following sections the general composition of a healthy artery, possible arterial diseases, and the mechanical behavior of arteries are discussed. The information on these topics are taken mainly from Rhodin [1980], Silver et al. [1989], Fung [1993], Humphrey [1995], Junqueira and Carneiro [2005], and Welsch [2006].

¹The diastole is the relaxing phase of the cardiac cycle. Opposed to that, the systole is the contraction phase.

2.1 General composition of a healthy artery

A healthy artery is mainly composed of three layers. From the lumen (the inner side of the artery) to the outer side we identify: (i) the intima, (ii) the media, and (iii) the adventitia, see the schematic illustration of a healthy elastic artery in Fig. 2.2.

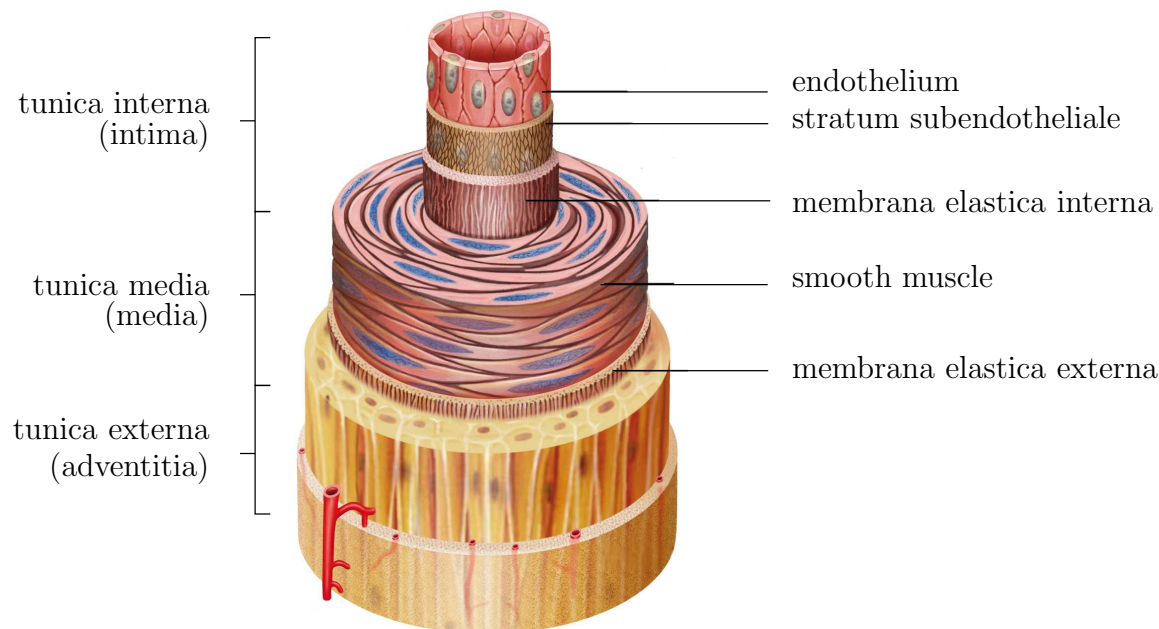


Figure 2.2: Composition of a healthy elastic artery, taken from the webpage www.e-visits.de.

Intima (tunica interna). The intima is the innermost layer, which consists mainly of endothelial cells and a subendothelial membrane (stratum subendotheliale). The flat, elongated endothelial cells are axially oriented and attached to a thin basal membrane. They build a monolayer, the endothelium, which prevents adhesion of blood to the luminal surface. The subendothelial membrane is composed of extracellular matrix, i.e. connective tissue² and an amorphous ground substance with proteoglycans³. The membrane, which separates the intima from the adjacent media is called membrana elastica interna. A difference between muscular and elastic arteries is, that the intima of muscular arteries is often thinner than the intima of the elastic type. This is due to the more pronounced subendothelial layer in elastic arteries. Furthermore, in elastic arteries it cannot easily be distinguished between the membrana elastica interna and the elastic membranes of the media, whereas in muscular arteries this membrane is relative thick and clearly defined.

Media (tunica media). The main constituents of the middle layer, the media, are circular smooth muscle cells⁴ and connective tissue fibers. It is the thickest of the three main layers. The boundary between the media and the adventitia is the membrana elastica externa. In the middle layer the main differences between muscular and elastic arteries become obvious. While in elastic arteries the media is formed by various concentric fenestrated elastin lamellae (30–70) and intermediate, axial smooth muscle cells, the media of the muscular type is composed of dense, circular smooth muscle layers (up to 40) con-

²Connective tissue is composed of collagen fibers, elastic fibers, and reticular collagen fibers.

³Proteoglycans: glycoproteins that have a core protein with covalently fixed glycosaminoglycan chains.

⁴Smooth muscle cells are contractile tissue constituents with a fusiform shape.

ected by gap junctions. The membrana elastica externa in elastic arteries cannot easily be distinguished from the other lamellae and in muscular arteries it can only be observed clearly in larger arteries. Following the arterial tree from the heart to peripheral muscular arteries, the amount of elastic fibers decreases and the amount of smooth muscle cells increases.

Adventitia (tunica externa). The outermost layer is the adventitia, which passes into the adjacent loose connective tissue. It is composed of axially oriented collagen fibrils with admixed elastic fibers (fibrils and elastin), and fibroblasts. In elastic arteries additionally nerves and the vasa vasorum exist. The vasa vasorum serves the outer parts of the vessel.

Very important constituents in arteries are the fiber proteins collagen and elastin.

Collagen. In collagenous structures, bundles of collagen fibers are present, see Fig. 2.3a. Each collagen fiber consists of collagen fibrils, which in turn are made up of micro-fibrils interconnected by proteoglycan filaments (PG), see Fig. 2.3b. A subunit of the micro-fibril is the tropocollagen, a collagen-molecule interconnect by cross-links (CL) on the molecular level. Each tropocollagen is composed of three polypeptide strands twisted together into a triple helix. Due to its structure, collagen has a high tensile strength and therefore it provides the arterial wall with rigidity. There exist various classifications of collagen types, which differ in their polymerized form (PF). In arteries mainly collagen of type I (PF: fibrils), type III (PF: fibrils), and type IV (PF: network; in basal membrane) exists.

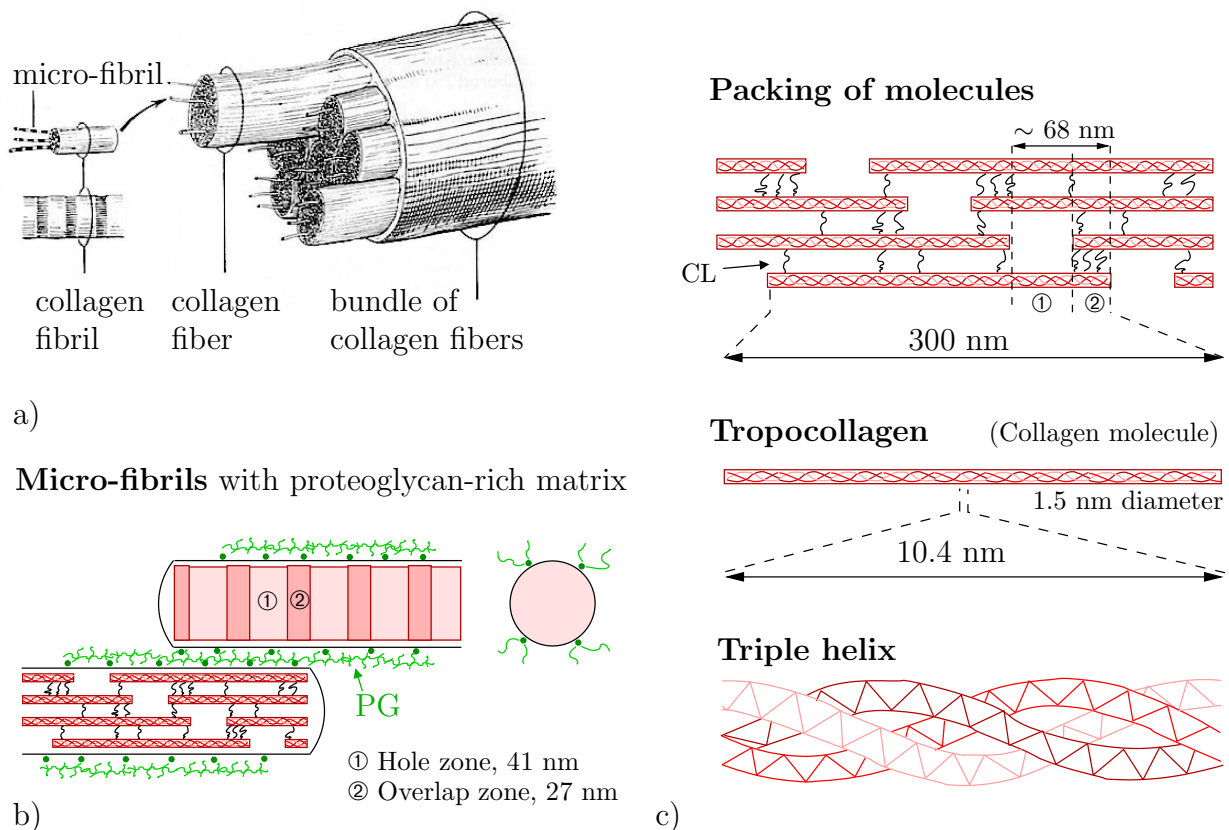


Figure 2.3: Composition of collagenous structures. a) Rough division of a collagen fiber bundle, taken from Junqueira and Carneiro [2005], page 61. b),c) Molecular structure of collagenous micro-fibrils connected by proteoglycan-rich matrix (PG), cf. Fratzl [2008], page 10 and Ross and Pawlina [2006], page 152. The main component is tropocollagen, which is in turn interconnected with cross-links (CL).

Elastin. Elastin is a structural protein consisting of elastic polypeptid chains, which are interconnected with cross-links. If the elastic fibers are stretched, the molecules are able to uncoil. By relaxation they recoil spontaneously, see Fig. 2.4. This provides the arterial structure with elasticity.

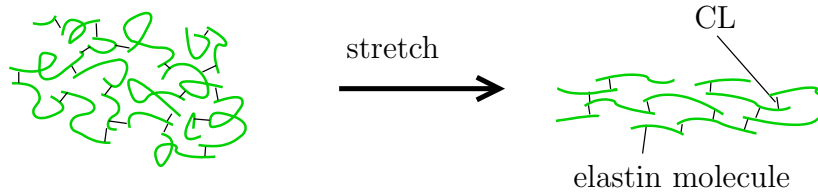


Figure 2.4: Schematic illustration of elastin molecules interconnected with cross-links (CL) in its relaxed and stretched configuration; cf. figure 4-28 in Alberts et al. [2004].

2.2 Disease of arterial tissue and possible treatments

Arteriosclerosis refers to a disease of arteries, in which the vessel wall becomes thicker and hardens. Three forms of appearance of these pathological changes can be differed: (i) atherosclerosis (see detailed explanation below), (ii) Mönckeberg's sclerosis (medial arteriosclerosis, calcium deposits in the media), and (iii) arteriolosclerosis (mostly small arteries and arterioles are affected). Here, the atherosclerosis has the highest clinical significance and is therefore treated in this work. For details see the textbooks Lenz [2007], Böcker et al. [2008], and Lüllmann-Rauch [2009], which served as the basis for this section.

Atherosclerosis. Atherosclerosis is a chronic and progressive disease primary of the intima, but also of the inner layers of the media. It appears mostly in elastic arteries and in larger arteries of the muscular type. Here, proliferation of connective tissue, accumulation of collagen fibers and proteoglycans, and deposit of fat (lipid), platelets (thrombocytes) and calcium lead to the formation of atheromatous plaques. As a result the lumen narrows (stenosis) and the blood flow is reduced, see the difference of normal and abnormal blood flow in Fig. 2.5a and b. By building of lesions in the plaque the blood clots so that a thrombus could evolve, which narrows the lumen additionally. The reduced or inhibited perfusion in turn causes an inadequate blood supply of the organs (ischemia) to the extent perhaps of a necrosis of the tissue, an infarct, or a stroke.

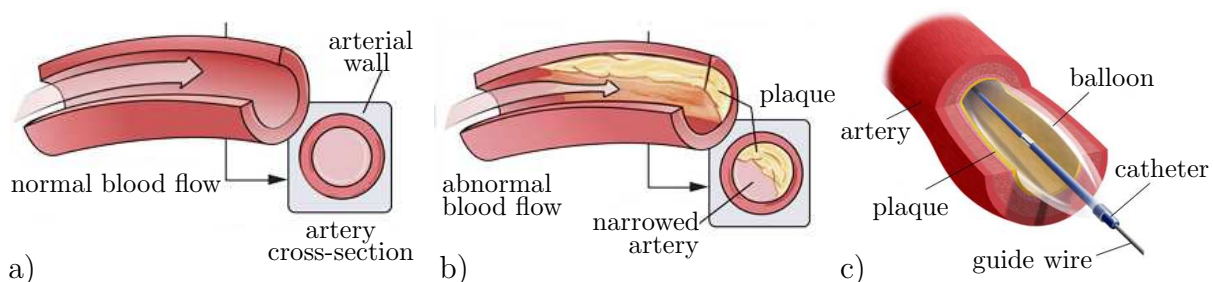


Figure 2.5: a) Artery with normal blood flow. b) Occluded artery with abnormal blood flow; a and b taken from the web page www.daviddarling.info/images. c) Inflation of a balloon inside an artery, taken from the web page www.csmc.edu.

The pathogenesis of the atherosclerosis is not yet fully understood due to the large amount of concerned factors and cellular interactions. Nevertheless, two central hypotheses exist:

- The *Response-to-injury* hypothesis was proposed in Ross and Glomset [1973, 1976], see also Ross [1982]. This hypothesis identified the injury of the endothelium by, for example, hypercholesterolemia, biochemical deterioration, or mechanical injuries (supported by hypertension), to be the cause for the disease. The lesion in the endothelium enables platelets and the monocytes (those become macrophages after migration into the tissue) to interact with the vessel wall and to release growth factors. As a result proliferation of smooth muscle cells takes place, which migrate from the media into the intima and produce extracellular matrix. Additionally, the macrophages accumulate LDL⁵ and become foam cells. In a histological preparations foam cells appear as “fatty streaks”.
- The *Lipoprotein-induced-atherosclerosis* hypothesis, see Brown and Goldstein [1983], states that the crucial catalyst of atherosclerosis is the oxidative modification of LDL to oxLDL (oxidized LDL). Due to oxLDL-receptors (scavenger receptor) macrophages absorb oxLDL faster and consequently the transformation to foam cells is faster.

The further pathogenesis of atherosclerosis is equal for both hypotheses. The foam cells become necrotic and their content leaks into the surrounding tissue, building a soft lipid-rich core, the so-called necrotic core. Additionally, a fibrous cap is formed and over time dense calcium inclusions appear. A thrombus (blood clot evolved from intravascular coagulation) formation evolves if the fibrous cap breaks open or if an endothelial erosion takes place. A detailed explanation of the atherogenesis and the complications of atherosclerosis is given in Libby and Ridker [2006].

Atherosclerotic plaques usually grow over a period of many years. Factors contributing to the spread of the atherosclerosis are arterial hypertension, nicotine abuse, diabetes mellitus, hypercholesterolemia, genetic (pre-) disposition, age, and male sex. Adiposity, lack of physical activity, psychosocial stress, and hormonal disorder can be seen as risk factors of second order. Several of these factors are not influenceable, the others can be reduced by adequate exercises, a dietary change, or lowering the blood pressure by means of a therapy. However, if the atherosclerosis is in an advanced stadium, invasive treatments are necessary in the majority of cases: a bypass surgery, an atherectomy (excision of the atheromatous plaque), or a balloon dilatation (sometimes with stent implantation).

Balloon dilatation/balloon angioplasty. A percutaneous transluminal angioplasty (PTA) is a method of treatment for the dilation of an narrowed vessel in order to re-establish the blood flow. If the dilation takes place through a balloon catheter⁶, it is called a balloon angioplasty. By this minimally invasive treatment the balloon catheter is introduced through the skin and guided to the narrowed vessel. If the narrowed lumen is reached, the balloon is shortly inflated with a pressure of 6 to 20 bar, see Fig. 2.5c.

⁵LDL: low density lipoprotein. LDL is a transportation protein, which transports cholesterol to the cells of the body. Here cholesterol is needed, for example, to repair the cell wall. In contrast, HDL (high density lipoprotein) carries excessive cholesterol to the liver, where it is broken down.

⁶A balloon catheter is a catheter composed of an empty and collapsed balloon, which is attached on a guide wire.

The inflation is repeated until the arterial lumen has been sufficiently opened. Then, the balloon is deflated and removed. During the procedure angiograms are made in order to ensure a successful treatment. Additionally, a stent can be inserted in order to support the vessel wall.

The vascular radiologist Charles Dotter discovered the transluminal angioplasty by chance in 1963 when he performed an abdominal aortogram and relieved an occlusive lesion in an iliac artery. Based on this finding he used the technique of multiple catheters with increasing diameter and treated atherosclerosis in femoral arteries, see Dotter and Judkins [1964]. The cardiologist Andreas Grüntzig developed a double-lumen, polyvinyl balloon catheter, see Grüntzig [1977], Grüntzig et al. [1978], and enabled a dilation of coronary arteries. He was the first who performed a balloon angioplasty and therefore he is a pioneer of a nowadays well-established and widely-used treatment. For a historical overview see Dotter [1980] and Landau et al. [1994].

Hypertension. Hypertension means high blood pressure. As a result of hypertension, the extracellular matrix and the smooth muscle cells in the media structurally change and therefore the media thickens. Hereby, hyperplasia is a higher replication of the cells and hypertrophy is the increase of the cell size, see section 8.1 in Humphrey [2002]. As mentioned before, hypertensive people have a higher risk to suffer from atherosclerosis. The JNC 7 (Seventh report of the Joint National Committee on prevention, detection, evaluation and treatment of high blood pressure; Chobanian et al. [2003]) classified the blood pressure into different levels. According to that, a systolic blood pressure up to 120 mmHg is normal, a systolic blood pressure of 120-139 mmHg is prehypertensive, and a systolic blood pressure over 140 mmHg is hypertensive, see Table 2.1. Thereby, prehypertensive persons are not yet diseased, but they have an increased chance to suffer from hypertension and should prevent the developing of the disease.

BP classification	systolic BP [mmHg]	diastolic BP [mmHg]
normal	<120	and <80
prehypertensive	120-139	or 80-89
stage 1 hypertension	140-159	or 90-99
stage 2 hypertension	≥ 160	or ≥ 100

Table 2.1: Classification of hypertension for different blood pressures (BP) of adults, taken from Chobanian et al. [2003]; 100 mmHg $\hat{=}$ 0.13332 bar $\hat{=}$ 13.332 kPa.

In this work we distinguish between two different loading types: the physiological and the supra-physiological loading domain.

Physiological loading domain. Arteries, which are under “normal” blood pressure up to approximately 120 mmHg (16 kPa) or up to 140 mmHg (18.7 kPa) and even higher in case of hypertension, are said to be in the physiological loading domain. In this work the upper limit of the physiological domain of 180 mmHg (24 kPa) is taken into account.

Supra-physiological loading domain. High inner pressure not naturally arising in arteries are referred to as supra-physiological or therapeutic, since such pressure arise, for example, due to a balloon dilation. In this loading domain the artery will be mechanically damaged, see Chapter 7.

2.3 Mechanical behavior of arterial tissue

From a mechanical perspective arteries are highly deformable structures composed of fibers embedded in a soft matrix material (extracellular matrix; ground substance). Additionally, arteries are assumed to be quasi-incompressible, see for example Carew et al. [1968], and Chuong and Fung [1984]. There are mainly two families of fibers reinforcing the artery, which are helically coiled around the artery. The ground substance, which has a much lower stiffness than the embedded fibers, is assumed to be isotropic and exhibits a nearly linear stress-strain response.

In Roach and Burton [1957] the tension-radius response of elastin-digested, collagen-digested and control samples of human iliac arteries was investigated. The experiments show, that the arterial response in the low loading domain is mainly carried by elastin and that the collagen is the load-carrying material at a higher loading range. At physiological pressure, both constituents are responsible for the stress-strain response, where the collagen is the dominant factor. In Fischer and Llaurodo [1966], Cox [1978], and Nichols and O'Rourke [1998] the correlation between the mechanical response of arterial tissue and the collagen and elastin content was investigated. It was shown, that the ratio of collagen to elastin effects the stiffness of the arterial wall such that a higher collagen content indicates a stiffer arterial wall behavior. Thus, the overall highly nonlinear stress-strain response with the typical (exponential) stiffening effect at higher pressures is a result of the straightening of the embedded wavy collagen fibers, see, for example, Gupta [2008]. Due to the arrangement of the elastin and collagen fibers, the arterial wall behaves anisotropic. One of the first works dealing with anisotropy in arterial walls is Patel and Fry [1969]. They stated, that arterial walls are cylindrically orthotropic.

As mentioned in Section 2.1, arteries are mainly composed of three layers. Due to their different composition, they have different mechanical properties and relevance. The intima is relatively thin in healthy young arteries and therefore their mechanical influence is rather insignificant. Arteriosclerotic degenerations lead to a thickening and stiffening of the intima with age, thus the influence may become more significant. Furthermore, pathological changes transform parts of the intima into plaque, leading to a total different mechanical behavior. Thus, in this work the intima is neglected in healthy parts of the artery and assumed to be a part of the plaque in degenerated arteries. The mechanically most important layers are the media and the adventitia, whereas the media is the load-bearing layer in the physiological loading range and the adventitia saves the arterial wall from rupture under higher loadings, see Holzapfel et al. [2000a]. Both layers are anisotropic as mentioned in, for example, von Maltzahn et al. [1984]. Here, bovine carotid arteries are investigated and it was stated that the media and the adventitia are stiffer in the axial direction than in the circumferential direction. Additionally, they observed higher stress values in the media compared with that in the adventitia under physiological conditions. At zero stress state Yu et al. [1993] measured the initial Young's modulus of inner layers (intima and media) and of the outer layer (adventitia) of pig aortas. A higher Young's modulus was observed in the inner layers. Xie et al. [1995] observed the same in rat aorta by application of a new experimental method. In Holzapfel et al. [2005] the mechanical behavior of the individual layers of human coronary arteries are discussed in the framework of finite strains. The authors found out that mechanical behavior of all tissues is different. However, it is nonlinear and anisotropic in all cases. The tissue samples of the adventitia are stiffer when tested in the axial direction than in circumferential direction. In contrast, the samples of the media show the exactly opposite behavior. Sommer et al.

[2010] analyzed the influence of axial pre-stretch on the circumferential and axial stress-strain behavior of human common and internal carotid arteries. High axial pre-stretches result in a stiffer response.

In the physiological range soft biological tissues as arteries behave (perfectly) elastic, see Holzapfel et al. [2000a]. The reviews in Fung [1993], Abé et al. [1996], Liu [1999], Humphrey [2002], and Holzapfel and Ogden [2006] give an overview on experimental findings on the material behavior of arteries within the physiological range of deformations. Under supra-physiological (therapeutic) loadings damage effects appear. These effects lead to a softening of the arterial wall and result in hysteresis in the stress-strain response under cyclic loading conditions. This topic is discussed in detail in Chapter 7. Another very important issue is the existence of residual stresses in arterial walls. Even in an unloaded state (when the artery is released from internal pressure), stresses are observed: these stresses are called residual stresses. This topic is treated in Chapter 9.

3 Fundamentals of the continuum mechanics of solids

The aim of this chapter is to briefly introduce the basic concepts of the continuum mechanics of solids used in the present work. In order to find more detailed information about continuum mechanics the reader is referred to, for example, Eringen [1980], Marsden and Hughes [1983], Stein and Barthold [1996], Chadwick [1999], Haupt [2000], Holzapfel [2000], Truesdell and Noll [2004], and Wriggers [2008].

3.1 Kinematical relations

In the field of continuum mechanics, the body of interest is modeled as a continuum, whereby the microscopic composition is not taken into account explicitly. We consider a material body \mathcal{B} as continuum in Euclidean space \mathbb{R}^3 , which consists of a continuous set of material points P . The boundary of the body is described as $\partial\mathcal{B}$. The undeformed state of the body is denoted as reference configuration \mathcal{B}_0 (material or Lagrangian configuration) and is defined by the position \mathbf{X} of the material points $P \in \mathcal{B}_0$ at time $t = t_0$

$$\mathbf{X} = \hat{\mathbf{X}}(\Theta^1, \Theta^2, \Theta^3) \quad \text{or} \quad \mathbf{X} = \hat{\mathbf{X}}(\Theta^i) \quad \text{with} \quad i = 1, 2, 3, \quad (3.1)$$

with the convective coordinates Θ^i . The convective coordinates can be imagined as lines carved on the body, i.e. when the body deforms the convective coordinates deform as well. The current configuration \mathcal{B} (spatial or Eulerian configuration) is the deformed state of the body. This state is defined by the position \mathbf{x} of the material points $P \in \mathcal{B}$ at time t

$$\mathbf{x} = \hat{\mathbf{x}}(\Theta^1, \Theta^2, \Theta^3, t) \quad \text{or} \quad \mathbf{x} = \hat{\mathbf{x}}(\Theta^i, t) \quad \text{with} \quad i = 1, 2, 3. \quad (3.2)$$

The cartesian coordinates can be written as functions of the convective coordinates: in the reference position $X^A = \hat{X}^A(\Theta^1, \Theta^2, \Theta^3)$ with $A = 1, 2, 3$ and in the current position $x^a = \hat{x}^a(\Theta^1, \Theta^2, \Theta^3)$ with $a = 1, 2, 3$. The position of the material points P in terms of the orthonormal (cartesian) basis \mathbf{E}_A and \mathbf{e}_a , respectively, yields

$$\mathbf{X} = X^A \mathbf{E}_A \quad \text{and} \quad \mathbf{x} = x^a \mathbf{e}_a. \quad (3.3)$$

The covariant basis vectors (*natural basis*) are the tangent vectors on the convective coordinates Θ^i and can be computed by the partial derivative of the position vectors \mathbf{X} and \mathbf{x} with respect to Θ^i . Therefore, the natural basis in the reference position \mathbf{G}_i and in the current position \mathbf{g}_i is given by

$$\mathbf{G}_i = \frac{\partial \mathbf{X}}{\partial \Theta^i} = \frac{\partial X^A}{\partial \Theta^i} \mathbf{E}_A = X^A_{,i} \mathbf{E}_A \quad \text{and} \quad \mathbf{g}_i = \frac{\partial \mathbf{x}}{\partial \Theta^i} = \frac{\partial x^a}{\partial \Theta^i} \mathbf{e}_a = x^a_{,i} \mathbf{e}_a. \quad (3.4)$$

The contravariant basis vectors (*dual basis*) follow from the conditions

$$\mathbf{G}_i \cdot \mathbf{G}^k = \delta_i^k \quad \text{and} \quad \mathbf{g}_i \cdot \mathbf{g}^k = \delta_i^k \quad \text{with} \quad \delta_i^k = \begin{cases} 1, & \text{if } i = k \\ 0, & \text{if } i \neq k \end{cases}. \quad (3.5)$$

Here, δ_i^k is the so-called Kronecker symbol. Therefore, the contravariant basis vectors in the reference position \mathbf{G}^i and in the current position \mathbf{g}^i can be computed by

$$\mathbf{G}^i = \frac{\partial \Theta^i}{\partial X^A} = \frac{\partial \Theta^i}{\partial X^A} \mathbf{E}^A \quad \text{and} \quad \mathbf{g}^i = \frac{\partial \Theta^i}{\partial x^a} = \frac{\partial \Theta^i}{\partial x^a} \mathbf{e}^a, \quad (3.6)$$

with $\mathbf{E}_A = \mathbf{E}^A$ and $\mathbf{e}_a = \mathbf{e}^a$. The convective coordinates and the resulting basis vectors are depicted in Fig. 3.1 for a simple two-dimensional problem.

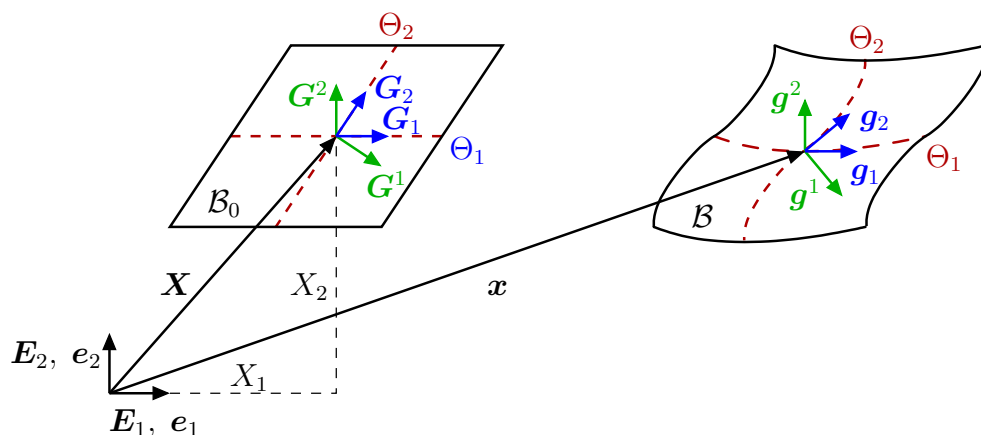


Figure 3.1: Schematic illustration of the reference configuration and the current configuration with convective coordinates and resulting basis vectors of the natural and dual basis.

Motion, deformation and strain. The deformation and motion of a body \mathcal{B} is given by the nonlinear deformation mapping $\varphi : \mathcal{B}_0 \mapsto \mathcal{B}$, which transfers the material points P from the reference configuration into the current configuration, see Fig. 3.2. At time $t \in \mathbb{R}^+$ the position of the points $\mathbf{X} \in \mathcal{B}_0$ is mapped onto the current position $\mathbf{x} \in \mathcal{B}$

$$\varphi(\mathbf{X}, t) : \mathbf{X} \mapsto \mathbf{x} = \varphi(\mathbf{X}, t) . \quad (3.7)$$

Due to the fact that the deformation mapping defines an injective function, deformation involving tearing and interpenetration of matter of the body is excluded and the inverse deformation mapping is well defined:

$$\varphi^{-1}(\mathbf{x}, t) : \mathbf{x} \mapsto \mathbf{X} = \varphi^{-1}(\mathbf{x}, t) . \quad (3.8)$$

The movement of a point P is described by the displacement vector $\mathbf{u}(\mathbf{X}, t)$ as the difference between the position vector of the current and the reference configuration

$$\mathbf{u}(\mathbf{X}, t) = \varphi(\mathbf{X}, t) - \mathbf{X} = \mathbf{x} - \mathbf{X} . \quad (3.9)$$

In order to describe the deformation process, the so-called *transport theorems* are used. They describe the mapping from the reference to current configuration of infinitesimal line, area, and volume elements, respectively. One of the most fundamental kinematic quantities is the deformation gradient \mathbf{F} , which is a primary measure of deformation defined by the partial derivative of the spatial position \mathbf{x} with respect to the material position \mathbf{X} ,

$$\mathbf{F}(\mathbf{X}, t) = \frac{\partial \mathbf{x}}{\partial \mathbf{X}} = \text{Grad} \mathbf{x} = \nabla \mathbf{x} . \quad (3.10)$$

Considering eq. (3.9) we get the alternative representation of the deformation gradient

$$\mathbf{F} = \text{Grad}[\mathbf{X} + \mathbf{u}(\mathbf{X}, t)] = \mathbf{1} + \text{Grad} \mathbf{u} = \mathbf{1} + \nabla \mathbf{u} , \quad (3.11)$$

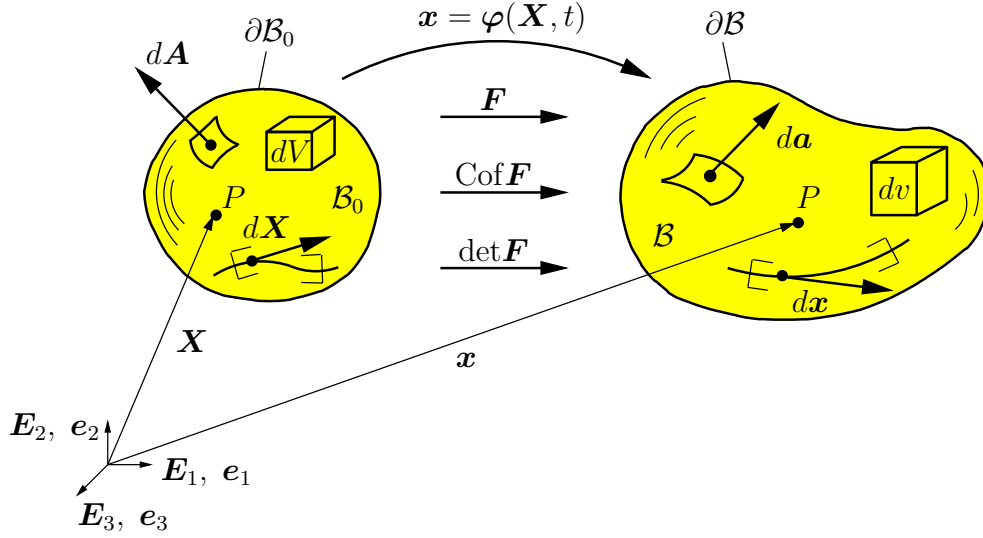


Figure 3.2: Schematic illustration of the reference configuration and the current configuration with the corresponding geometrical mappings (transport theorems).

with the second-order identity tensor $\mathbf{1}$. In convective and cartesian coordinates, respectively, the expression in eq. (3.10) yields

$$\mathbf{F} = \frac{\partial \mathbf{x}}{\partial \Theta^i} \otimes \frac{\partial \Theta^i}{\partial \mathbf{X}} = \mathbf{g}_i \otimes \mathbf{G}^i = \frac{\partial x^a}{\partial \Theta^i} \frac{\partial \Theta^i}{\partial X^A} \mathbf{e}_a \otimes \mathbf{E}^A = F^a_A \mathbf{e}_a \otimes \mathbf{E}^A, \quad (3.12)$$

and it can be seen that \mathbf{F} is a two-point tensor: one base vector is defined with respect to the Eulerian configuration and the other is defined with respect to the Lagrangian configuration. The deformation gradient is a linear operator and transforms an infinitesimal line element in the reference configuration $d\mathbf{X}$ into a current infinitesimal line element $d\mathbf{x}$ and the *mapping of an infinitesimal line element* reads

$$d\mathbf{x} = \mathbf{F} d\mathbf{X}. \quad (3.13)$$

From the condition that an inverse mapping exists follows that the deformation mapping is one-to-one. Thus, the deformation gradient \mathbf{F} cannot be singular and its inverse exists

$$\mathbf{F}^{-1} = \frac{\partial \mathbf{X}}{\partial \mathbf{x}} = \frac{\partial \mathbf{X}}{\partial \Theta^i} \otimes \frac{\partial \Theta^i}{\partial \mathbf{x}} = \mathbf{G}_i \otimes \mathbf{g}^i = \frac{\partial X^A}{\partial \Theta^i} \frac{\partial \Theta^i}{\partial x^a} \mathbf{E}_A \otimes \mathbf{e}^a = (F^{-1})^A_a \mathbf{E}_A \otimes \mathbf{e}^a. \quad (3.14)$$

From this follows that the determinant of the deformation gradient \mathbf{F} differs from zero,

$$\det \mathbf{F}(\mathbf{X}, t) \neq 0. \quad (3.15)$$

The *mapping of an infinitesimal volume element* can be computed by the scalar triple product which is defined as the dot product of one of the vectors with the cross product of the other two. Therefore, an infinitesimal referential volume element can be expressed by $dV = (d\mathbf{X}^1 \times d\mathbf{X}^2) \cdot d\mathbf{X}^3$ and the corresponding current volume by

$$dv = (d\mathbf{x}^1 \times d\mathbf{x}^2) \cdot d\mathbf{x}^3 = \det \begin{bmatrix} d\mathbf{x}^1 \\ d\mathbf{x}^2 \\ d\mathbf{x}^3 \end{bmatrix} = \det \begin{bmatrix} \mathbf{F} d\mathbf{X}^1 \\ \mathbf{F} d\mathbf{X}^2 \\ \mathbf{F} d\mathbf{X}^3 \end{bmatrix} = \det \mathbf{F} \det \begin{bmatrix} d\mathbf{X}^1 \\ d\mathbf{X}^2 \\ d\mathbf{X}^3 \end{bmatrix}, \quad (3.16)$$

where we have considered eq. (3.13). This leads to the mapping of an infinitesimal volume element

$$dv = \det \mathbf{F} dV = J dV \quad (3.17)$$

with the local volumetric deformation measure $J = \det \mathbf{F} = \frac{dv}{dV}$ called the *Jacobian determinant*. Since interpenetration of the body \mathcal{B} is excluded, eq. (3.15) must be further limited and the Jacobian determinant has to fulfill the condition

$$J = \det \mathbf{F}(\mathbf{X}, t) > 0. \quad (3.18)$$

The *mapping of an infinitesimal area element* is derived by eq. (3.17) considering eq. (3.13). Here, we compute first

$$\begin{aligned} dv &= d\mathbf{a} \cdot d\mathbf{x} = J d\mathbf{A} \cdot d\mathbf{X} = J dV \\ d\mathbf{a} \cdot \mathbf{F} d\mathbf{X} &= J d\mathbf{A} \cdot d\mathbf{X} \\ (\mathbf{F}^T d\mathbf{a} - J d\mathbf{A}) \cdot d\mathbf{X} &= 0. \end{aligned} \quad (3.19)$$

Since $d\mathbf{X}$ cannot be zero we obtain the so-called *Nanson's formula*

$$d\mathbf{a} = J \mathbf{F}^{-T} d\mathbf{A} = \text{Cof} \mathbf{F} d\mathbf{A}, \quad (3.20)$$

where an infinitesimal material area element $d\mathbf{A} = \mathbf{N} dA$, with the material unit outward normal vector \mathbf{N} , is mapped to an infinitesimal spatial area element $d\mathbf{a} = \mathbf{n} da$, with the spatial unit outward normal vector \mathbf{n} . A schematic representation of the transport theorems is given in Fig. 3.2 and the summarization of the transport theorems is

$$\boxed{\begin{aligned} d\mathbf{x} &= \mathbf{F} d\mathbf{X} \\ d\mathbf{a} &= J \mathbf{F}^{-T} d\mathbf{A} = \text{Cof} \mathbf{F} d\mathbf{A} \\ dv &= \det \mathbf{F} dV = J dV \end{aligned}}. \quad (3.21)$$

Decomposing the deformation into straining and rigid rotation at a material point, the deformation gradient can be written in its polar decomposition

$$\mathbf{F} = \mathbf{R} \mathbf{U} = \mathbf{V} \mathbf{R}, \quad (3.22)$$

with the *rotation tensor* \mathbf{R} and the *right and left stretch tensors* \mathbf{U} and \mathbf{V} , respectively. The rotation tensor is a proper orthogonal tensor, i.e. $\mathbf{R} \in \text{SO}(3)$ with $\mathbf{R}^{-1} = \mathbf{R}^T$. Although the deformation gradient incorporates all information of the deformation at a material point, it is not suitable for describing deformation in the sense of alteration of shape since it is affected by rigid body rotations. The *right Cauchy-Green deformation tensor* and the *left Cauchy-Green deformation tensor* (Finger tensor) are defined as

$$\begin{aligned} \mathbf{C} &= \mathbf{F}^T \mathbf{F} = (\mathbf{R} \mathbf{U})^T \mathbf{R} \mathbf{U} = \mathbf{U}^2 \quad \text{with} \quad C_{AB} = \delta_{ab} F^a{}_A F^b{}_B, \quad \text{and} \\ \mathbf{b} &= \mathbf{F} \mathbf{F}^T = (\mathbf{V} \mathbf{R})^T \mathbf{V} \mathbf{R} = \mathbf{V}^2 \quad \text{with} \quad b_{ab} = \delta^{AB} F^a{}_A F^b{}_B, \end{aligned} \quad (3.23)$$

which are free of rigid body rotations. Further deformation measures can be obtained by evaluating half the difference between the square of the norm of the line element in the current placement $ds = ||d\mathbf{x}||$ and the reference placement $dS = ||d\mathbf{X}||$, i.e.

$$\frac{1}{2}((ds)^2 - (dS)^2) = \frac{1}{2}(d\mathbf{x} \cdot d\mathbf{x} - d\mathbf{X} \cdot d\mathbf{X}). \quad (3.24)$$

Inserting eq. (3.13) and eq. (3.23) in eq. (3.24) yields the *Green-Lagrange strain tensor*

$$\mathbf{E} = \frac{1}{2}(\mathbf{C} - \mathbf{1}) \quad \text{with} \quad E_{AB} = \frac{1}{2}(C_{AB} - \delta_{AB}), \quad (3.25)$$

and usage of the inverse mapping $d\mathbf{X} = \mathbf{F}^{-1}d\mathbf{x}$ yields the *Euler-Almansi strain tensor*

$$\mathbf{e} = \frac{1}{2}(\mathbf{1} - \mathbf{b}^{-1}) \quad \text{with} \quad e_{ab} = \frac{1}{2}(\delta_{ab} - (b^{-1})_{ab}). \quad (3.26)$$

An alternative notation of the Green-Lagrange strain tensor in terms of the displacement vector \mathbf{u} is obtained by eq. (3.25) using eq. (3.11)

$$\mathbf{E} = \frac{1}{2}(\nabla\mathbf{u} + \nabla^T\mathbf{u} + \nabla^T\mathbf{u}\nabla\mathbf{u}). \quad (3.27)$$

In the so-called geometrically linear theory of solid mechanics the deformations of the body are assumed to be small. Therefore, geometric nonlinearities have not to be accounted for. By neglecting all nonlinear contributions in eq. (3.27) or by linearization of the equation, i.e.

$$\text{Lin}\mathbf{E} = \mathbf{E}|_{\mathbf{X}} + \Delta\mathbf{E} \quad \text{with} \quad \Delta\mathbf{E} = \left. \frac{d}{d\epsilon} [\mathbf{E}(\mathbf{X} + \epsilon\mathbf{u})] \right|_{\epsilon=0}, \quad (3.28)$$

with $\mathbf{E}|_{\mathbf{X}} = \mathbf{0}$ and the directional derivative, also called Gâteaux derivative, $\Delta\mathbf{E} = \left[\frac{1}{2}(\nabla\mathbf{u} + \nabla^T\mathbf{u} + \nabla^T\mathbf{u}\nabla(\epsilon\mathbf{u}) + \nabla^T(\epsilon\mathbf{u})\nabla\mathbf{u}) \right]_{\epsilon=0}$ we get the *linear strain tensor*

$$\boldsymbol{\varepsilon} = \frac{1}{2}(\nabla\mathbf{u} + \nabla^T\mathbf{u}) = \text{sym}[\nabla\mathbf{u}], \quad (3.29)$$

which is the symmetric part of the displacement gradient.

3.2 Material time derivatives

A material time derivative is the derivative with respect to time holding \mathbf{X} fixed, i.e. $\frac{D\xi}{Dt} = \left(\frac{\partial\xi}{\partial t} \right)|_{\mathbf{X}}$. For a material field $\Xi = \Xi(\mathbf{X}, t)$ and a spatial field $\xi = \xi(\mathbf{x}(\mathbf{X}, t), t)$ the material time derivative yields

$$\frac{D\Xi}{Dt} = \dot{\Xi} = \frac{\partial\Xi}{\partial t} \quad \text{and} \quad \frac{D\xi}{Dt} = \dot{\xi} = \frac{\partial\xi}{\partial t} + \frac{\partial\xi}{\partial\mathbf{x}} \cdot \frac{\partial\mathbf{x}}{\partial t} = \frac{\partial\xi}{\partial t} + \text{grad}\xi \cdot \dot{\mathbf{x}}. \quad (3.30)$$

Considering the velocity $\mathbf{v} = \dot{\boldsymbol{\varphi}}(\mathbf{X}, t)$ and the acceleration $\mathbf{a} = \dot{\mathbf{v}} = \ddot{\boldsymbol{\varphi}}(\mathbf{X}, t)$ as material time derivatives of material fields, we compute

$$\mathbf{v}(\mathbf{X}, t) = \frac{\partial\boldsymbol{\varphi}(\mathbf{X}, t)}{\partial t} \quad \text{and} \quad \mathbf{a}(\mathbf{X}, t) = \frac{\partial^2\boldsymbol{\varphi}(\mathbf{X}, t)}{\partial t^2}. \quad (3.31)$$

In contrast, if we consider material time derivatives of spatial fields, i.e. $\mathbf{V} = \dot{\boldsymbol{\varphi}}^{-1}(\mathbf{x}, t) = \mathbf{0}$ and $\mathbf{A} = \dot{\mathbf{V}} = \ddot{\boldsymbol{\varphi}}^{-1}(\mathbf{x}, t) = \mathbf{0}$, the velocity and the acceleration can be computed by

$$\mathbf{V} = \frac{\partial\boldsymbol{\varphi}^{-1}(\mathbf{x}, t)}{\partial t} + \frac{\partial\boldsymbol{\varphi}^{-1}(\mathbf{x}, t)}{\partial\mathbf{x}} \dot{\mathbf{x}} = \mathbf{0} \quad \rightarrow \quad \dot{\mathbf{x}} = \mathbf{v}(\mathbf{x}, t) \quad \text{and} \quad (3.32)$$

$$\mathbf{a} = \dot{\mathbf{v}}(\mathbf{x}, t) = \frac{\partial\mathbf{v}(\mathbf{x}, t)}{\partial t} + \frac{\partial\mathbf{v}(\mathbf{x}, t)}{\partial\mathbf{x}} \frac{\partial\mathbf{x}}{\partial t} = \frac{\partial\mathbf{v}}{\partial t} + \text{grad}\mathbf{v} \mathbf{v} = \frac{\partial\mathbf{v}}{\partial t} + \mathbf{l} \mathbf{v},$$

with the spatial velocity gradient \mathbf{l} . The material velocity gradient is given by

$$\dot{\mathbf{F}} = \frac{\partial \dot{\mathbf{x}}}{\partial \mathbf{X}} = \text{Grad} \dot{\mathbf{x}} \quad (3.33)$$

and the relation between the spatial and the material velocity gradient can be derived as

$$\mathbf{l} = \text{grad} \mathbf{v} = \frac{\partial \dot{\mathbf{x}}}{\partial \mathbf{x}} = \frac{\partial \dot{\mathbf{x}}}{\partial \mathbf{X}} \frac{\partial \mathbf{X}}{\partial \mathbf{x}} = \dot{\mathbf{F}} \mathbf{F}^{-1} . \quad (3.34)$$

An additive decomposition of \mathbf{l} into a symmetric part \mathbf{d} and a skew-symmetric part (spin) \mathbf{w} results in

$$\mathbf{l} = \mathbf{d} + \mathbf{w} \quad \text{with} \quad \mathbf{d} = \frac{1}{2}(\mathbf{l} + \mathbf{l}^T) = \text{sym}[\mathbf{l}] \quad \text{and} \quad \mathbf{w} = \frac{1}{2}(\mathbf{l} - \mathbf{l}^T) = \text{skew}[\mathbf{l}] . \quad (3.35)$$

The material time derivative of the Jacobian determinant is (using eq. (3.34))

$$\dot{J} = \frac{\partial J}{\partial \mathbf{F}} : \frac{\partial \mathbf{F}}{\partial t} = \frac{\partial \det \mathbf{F}}{\partial \mathbf{F}} : \dot{\mathbf{F}} = \det \mathbf{F} \mathbf{F}^{-T} : \dot{\mathbf{F}} = J \mathbf{F}^{-T} : \mathbf{l} \mathbf{F} = J \text{grad} \dot{\mathbf{x}} : \mathbf{1} = J \text{div} \dot{\mathbf{x}} . \quad (3.36)$$

3.3 The stress concept

In the following the concept of stresses in the framework of continuum mechanics is discussed. Considering a deformable continuum body on which external forces are applied, the field of internal forces acting on infinitesimal surfaces within the body as a reaction to the external forces is called stress.

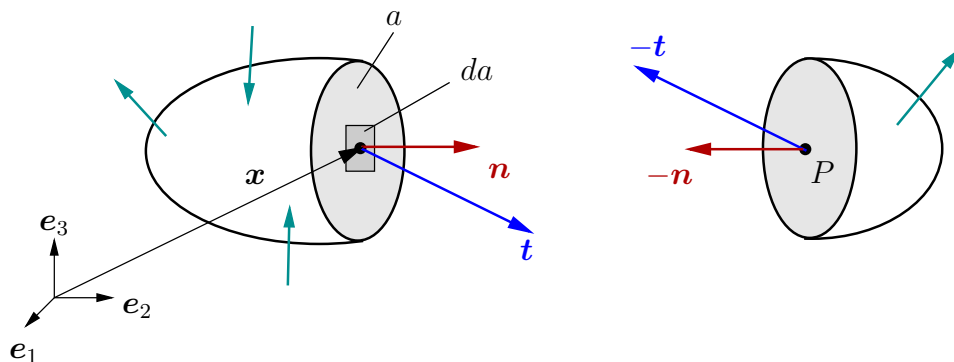


Figure 3.3: Body with cut free internal stress vector \mathbf{t} .

Let us consider a cutting surface a , which passes through a material point P , as depicted in Fig. 3.3. The continuum is subjected to external forces \mathbf{f} , consisting of external surface and body forces. As mechanical reaction to the external loadings, forces are transmitted from one segment to the other through the cutting surface, resulting in a force distribution on a small area Δa , with a normal unit vector \mathbf{n} . As Δa becomes infinitesimally small the ratio $\Delta \mathbf{f} / \Delta a$ becomes $d\mathbf{f} / da$. The resulting vector $d\mathbf{f} / da$ is defined as the traction vector given by

$$\mathbf{t}(\mathbf{x}, t) = \lim_{\Delta a \rightarrow 0} \frac{\Delta \mathbf{f}}{\Delta a} = \frac{d\mathbf{f}}{da} \quad (3.37)$$

at the point P associated with a plane with a normal vector \mathbf{n} . According to *Cauchy's postulate*, the traction vector \mathbf{t} persists for all surfaces passing through the point P and having the same normal vector \mathbf{n} at P . The state of stress at a point in the body is then defined by all stress vectors \mathbf{t} associated with all planes that pass through that point. In order to describe the stress state explicitly, *Cauchy's stress theorem* states that there exists a second-order tensor field $\boldsymbol{\sigma}(\mathbf{x}, t)$, independent of \mathbf{n} , such that \mathbf{t} is a linear function of \mathbf{n}

$$\mathbf{t}(\mathbf{x}, t, \mathbf{n}) = \boldsymbol{\sigma}(\mathbf{x}, t) \mathbf{n} \quad \text{with} \quad t^a = \sigma^{ab} n_b . \quad (3.38)$$

The *Cauchy stress tensor* $\boldsymbol{\sigma}$, also denoted as *true stress*, is a pure Eulerian stress tensor and relates the current force in the cutting plane to the current area element. Another stress tensor is obtained by multiplying the Cauchy stress tensor $\boldsymbol{\sigma}$ with the Jacobian determinant J . Therefore, the resulting *Kirchhoff stress tensor* $\boldsymbol{\tau}$ is also known as *weighted Cauchy stress tensor* and is given by

$$\boldsymbol{\tau} = J \boldsymbol{\sigma} \quad \text{with} \quad \tau^{ab} = J \sigma^{ab} . \quad (3.39)$$

The Lagrangian counterpart of the Eulerian Cauchy theorem can be formulated as

$$\mathbf{T}(\mathbf{X}, t, \mathbf{N}) = \mathbf{P}(\mathbf{X}, t) \mathbf{N} , \quad (3.40)$$

with the normal \mathbf{N} and the traction vector \mathbf{T} associated to the undeformed surface $\partial\mathcal{B}_0$, see Fig. 3.4.

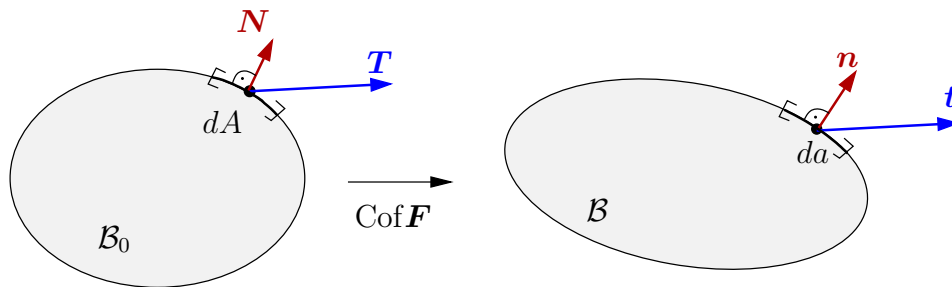


Figure 3.4: Traction vectors \mathbf{T} on $\partial\mathcal{B}_0$ and \mathbf{t} on $\partial\mathcal{B}$.

The referential traction vector \mathbf{T} points in the same direction as the traction vector \mathbf{t} and it follows for every surface element

$$\mathbf{T} dA = \mathbf{t} da . \quad (3.41)$$

The *first Piola-Kirchhoff stress tensor* \mathbf{P} is obtained from eq. (3.41) by considering eq. (3.20), eq. (3.38), and eq. (3.40), thus

$$\mathbf{P} = J \boldsymbol{\sigma} \mathbf{F}^{-T} \quad \text{with} \quad P^{aA} = J \sigma^{ab} (F^{-1})^A_b . \quad (3.42)$$

The stress tensor \mathbf{P} is a two-field tensor obtained by a Piola transformation of $\boldsymbol{\sigma}$ and relates the current force in the cutting plane to the referential area element and is also denoted as *nominal stress*. A pure Lagrangian stress tensor, the *second Piola-Kirchhoff stress tensor* \mathbf{S} , can be obtained by a pull-back operation of the Kirchhoff stress tensor

$$\mathbf{S} = \mathbf{F}^{-1} \boldsymbol{\tau} \mathbf{F}^{-T} \quad \text{with} \quad S^{AB} = (F^{-1})^A_a \tau^{ab} (F^{-1})^B_b . \quad (3.43)$$

A summary of the above mentioned stress tensors as well as the relations between the different stress measures is given in Table 3.1.

	$\boldsymbol{\sigma} = \sigma^{ab}$	$\boldsymbol{\tau} = \tau^{ab}$	$\boldsymbol{P} = P^{aA}$	$\boldsymbol{S} = S^{AB}$
$\boldsymbol{\sigma}$ Cauchy stress	$\boldsymbol{\sigma}$	$\frac{1}{J}\boldsymbol{\tau}$	$\frac{1}{J}\boldsymbol{P}\boldsymbol{F}^T$	$\frac{1}{J}\boldsymbol{F}\boldsymbol{S}\boldsymbol{F}^T$
$\boldsymbol{\tau}$ Kirchhoff stress	$J\boldsymbol{\sigma}$	$\boldsymbol{\tau}$	$\boldsymbol{P}\boldsymbol{F}^T$	$\boldsymbol{F}\boldsymbol{S}\boldsymbol{F}^T$
\boldsymbol{P} 1 st Piola-Kirchhoff stress	$J\boldsymbol{\sigma}\boldsymbol{F}^{-T}$	$\boldsymbol{\tau}\boldsymbol{F}^{-T}$	\boldsymbol{P}	$\boldsymbol{F}\boldsymbol{S}$
\boldsymbol{S} 2 nd Piola-Kirchhoff stress	$J\boldsymbol{F}^{-1}\boldsymbol{\sigma}\boldsymbol{F}^{-T}$	$\boldsymbol{F}^{-1}\boldsymbol{\tau}\boldsymbol{F}^{-T}$	$\boldsymbol{F}^{-1}\boldsymbol{P}$	\boldsymbol{S}

Table 3.1: Summary of the relations between different stress measures.

3.4 Balance principles

In this section some fundamental principles of continuum mechanics are provided. The fundamental balance principles discussed here are the *mass balance*, the *balance of linear momentum*, the *balance of angular momentum*, and the *energy balance* (also referred to as *1st law of thermodynamics*) as well as the *entropy inequality* (also referred to as *2nd law of thermodynamics*). They are valid for every continuum, since the balance principles are material-independent, and they have an axiomatic character. That means that they have universal validity, but, however, they can not be deduced from other natural laws. In the following the individual axioms, constituents and local forms are discussed briefly.

3.4.1 Mass balance

The conservation of mass is a conservation law, which means that during a motion the mass of a body does not change for all times. Therefore, the first global form of the mass balance is given by

$$m = \text{const.} \quad \rightarrow \quad \int_{\mathcal{B}_0} \rho_0 dV = \int_{\mathcal{B}} \rho dv \quad \text{and} \quad \dot{m} = \frac{d}{dt} \int_{\mathcal{B}} \rho dv = 0, \quad (3.44)$$

with the current density ρ and the referential density ρ_0 . From the second equation in eq. (3.44) with eq. (3.17) it follows that the Jacobian determinant is a volume ratio, i.e.

$$J = \frac{\rho_0}{\rho} \quad \forall \quad \boldsymbol{X} \in \mathcal{B}_0, \boldsymbol{x} \in \mathcal{B}, \quad (3.45)$$

which is the first local form of balance of mass. Evaluation of the third equation in eq. (3.44) under consideration of eq. (3.17) and eq. (3.36) leads to the second global form of balance of mass

$$\dot{m} = \frac{d}{dt} \int_{\mathcal{B}} \rho dv = \int_{\mathcal{B}_0} (\dot{\rho}J + \rho\dot{J}) dV = \int_{\mathcal{B}} (\dot{\rho} + \rho \operatorname{div} \dot{\boldsymbol{x}}) dv = 0 \quad (3.46)$$

and the corresponding second local form of balance of mass reads

$$\dot{\rho} + \rho \operatorname{div} \dot{\boldsymbol{x}} = 0 \quad \forall \quad \boldsymbol{x} \in \mathcal{B}. \quad (3.47)$$

It should be noted that a balance equation is not only valid for each local material point of the body and it is therefore reasonable to formulate a local form of the equation.

3.4.2 Balance of linear momentum

The balance of linear momentum states, that the temporal change of the linear momentum L , also called impulse, equals to the sum of forces K acting on the body \mathcal{B}

$$\dot{L} = K \quad \rightarrow \quad \frac{d}{dt} \int_{\mathcal{B}} \rho \dot{\mathbf{x}} dv = \int_{\mathcal{B}} \rho \mathbf{g} dv + \int_{\partial \mathcal{B}} \mathbf{t} da . \quad (3.48)$$

Herein, \mathbf{g} is the volume acceleration. Using eq. (3.17), eq. (3.36) and eq. (3.47) the material time derivative of L results in

$$\dot{L} = \frac{d}{dt} \int_{\mathcal{B}} \rho \dot{\mathbf{x}} dv = \int_{\mathcal{B}_0} [\dot{\mathbf{x}}(\dot{\rho} + \rho \operatorname{div} \dot{\mathbf{x}}) + \rho \ddot{\mathbf{x}}] J dV = \int_{\mathcal{B}} \rho \ddot{\mathbf{x}} dv , \quad (3.49)$$

and by usage of eq. (3.38) and eq. (A.16) the surface forces can be expressed by

$$\int_{\partial \mathcal{B}} \mathbf{t} da = \int_{\partial \mathcal{B}} \boldsymbol{\sigma} \mathbf{n} da = \int_{\mathcal{B}} \operatorname{div} \boldsymbol{\sigma} dv . \quad (3.50)$$

Therewith, the global form of balance of linear momentum results in

$$\int_{\mathcal{B}} \rho \ddot{\mathbf{x}} dv = \int_{\mathcal{B}} \rho \mathbf{g} dv + \int_{\mathcal{B}} \operatorname{div} \boldsymbol{\sigma} dv , \quad (3.51)$$

and the corresponding local form of balance of linear momentum reads

$$\operatorname{div} \boldsymbol{\sigma} + \rho(\mathbf{g} - \ddot{\mathbf{x}}) = \mathbf{0} \quad \forall \mathbf{x} \in \mathcal{B} . \quad (3.52)$$

3.4.3 Balance of angular momentum

The balance of angular momentum states, that the temporal change of the angular momentum $\mathbf{h}_{(0)}$, also referred to as moment of momentum, relative to a fixed point \mathbf{x}_0 equals to the sum of moments $\mathbf{m}_{(0)}$ acting on the body \mathcal{B} . With definition of the position vector $\mathbf{r} = \mathbf{x} - \mathbf{x}_0$ and the velocity at this point $\dot{\mathbf{r}} = \dot{\mathbf{x}} - \dot{\mathbf{x}}_0 = \dot{\mathbf{x}}$ the balance equation reads

$$\dot{\mathbf{h}}_{(0)} = \dot{\mathbf{m}}_{(0)} \quad \rightarrow \quad \frac{d}{dt} \int_{\mathcal{B}} \mathbf{r} \times \rho \dot{\mathbf{x}} dv = \int_{\mathcal{B}} \mathbf{r} \times \rho \mathbf{g} dv + \int_{\partial \mathcal{B}} \mathbf{r} \times \mathbf{t} da . \quad (3.53)$$

Using equation eq. (3.17), eq. (3.36) and eq. (3.47) and noting that $\dot{\mathbf{x}} \times \rho \dot{\mathbf{x}} = \mathbf{0}$ the material time derivative of $\mathbf{h}_{(0)}$ can be reformulated

$$\dot{\mathbf{h}}_{(0)} = \frac{d}{dt} \int_{\mathcal{B}} \mathbf{r} \times \rho \dot{\mathbf{x}} dv = \int_{\mathcal{B}_0} [\dot{\mathbf{x}} \times \rho \dot{\mathbf{x}} + \mathbf{r} \times \rho \ddot{\mathbf{x}} + \mathbf{r} \times \dot{\mathbf{x}}(\dot{\rho} + \rho \operatorname{div} \dot{\mathbf{x}})] J dV = \int_{\mathcal{B}} \mathbf{r} \times \rho \ddot{\mathbf{x}} dv . \quad (3.54)$$

The reformulation of the equation of the moment produced by the surface traction using Cauchy's theorem eq. (3.38) and the divergence theorem eq. (A.16) yields

$$\int_{\partial \mathcal{B}} \mathbf{r} \times \mathbf{t} da = \int_{\partial \mathcal{B}} \mathbf{r} \times \boldsymbol{\sigma} \mathbf{n} da = \int_{\mathcal{B}} [\mathbf{r} \times \operatorname{div} \boldsymbol{\sigma} + \boldsymbol{\epsilon} : \boldsymbol{\sigma}^T] dv , \quad (3.55)$$

with the permutation tensor $\boldsymbol{\epsilon}$, see eq. (A.15). The balance of angular momentum yields

$$\int_{\mathcal{B}} \mathbf{r} \times (\operatorname{div} \boldsymbol{\sigma} + \rho(\mathbf{g} - \ddot{\mathbf{x}})) dv + \int_{\mathcal{B}} \boldsymbol{\epsilon} : \boldsymbol{\sigma}^T dv = \mathbf{0} \quad \rightarrow \quad \int_{\mathcal{B}} \boldsymbol{\epsilon} : \boldsymbol{\sigma}^T dv = \mathbf{0}, \quad (3.56)$$

using eq. (3.52). This equation is only valid, if the Cauchy stresses $\boldsymbol{\sigma}$ are symmetric, i.e.

$$\boldsymbol{\sigma} = \boldsymbol{\sigma}^T \quad \forall \mathbf{x} \in \mathcal{B}, \quad (3.57)$$

known as *Cauchy's second equation of motion*.

3.4.4 Energy balance (1st law of thermodynamics)

The first fundamental theorem of thermodynamics is the balance of energy. The corresponding axiom says that the rate of total energy, which is the sum of internal energy \mathcal{E} and the kinetic energy \mathcal{K} , equals to the rate of mechanical work \mathcal{W} plus the rate of non-mechanical work. In case of thermo-mechanics with the thermal power \mathcal{Q} we obtain

$$\dot{\mathcal{E}} + \dot{\mathcal{K}} = \mathcal{W} + \mathcal{Q} \quad \rightarrow \quad \frac{d}{dt} \int_{\mathcal{B}} e \rho dv + \frac{d}{dt} \int_{\mathcal{B}} \frac{1}{2} \rho \dot{\mathbf{x}} \cdot \dot{\mathbf{x}} dv = \mathcal{W} + \mathcal{Q}, \quad (3.58)$$

with the specific energy density per unit mass e . Using the equations eq. (3.17), eq. (3.36) and eq. (3.47) the temporal change of the internal and the kinetic energy reads

$$\begin{aligned} \dot{\mathcal{E}} &= \frac{d}{dt} \int_{\mathcal{B}} e \rho dv = \int_{\mathcal{B}_0} (\dot{e} \rho + e[\dot{\rho} + \rho \operatorname{div} \dot{\mathbf{x}}]) J dV = \int_{\mathcal{B}} \dot{e} \rho dv, \quad \text{and} \\ \dot{\mathcal{K}} &= \frac{d}{dt} \int_{\mathcal{B}} \frac{1}{2} \rho \dot{\mathbf{x}} \cdot \dot{\mathbf{x}} dv = \frac{1}{2} \int_{\mathcal{B}_0} (\dot{\mathbf{x}} \cdot \dot{\mathbf{x}}[\dot{\rho} + \rho \operatorname{div} \dot{\mathbf{x}}] + 2\rho \dot{\mathbf{x}} \cdot \ddot{\mathbf{x}}) J dV = \int_{\mathcal{B}} \rho \dot{\mathbf{x}} \cdot \ddot{\mathbf{x}} dv, \end{aligned} \quad (3.59)$$

respectively. Mechanical work is caused by volume and surface forces acting on a body. Using Cauchy's theorem eq. (3.38), the divergence theorem eq. (A.16), and the equations eq. (3.57), eq. (3.34), eq. (3.35) and eq. (3.52) the rate of mechanical work yields

$$\mathcal{W} = \int_{\mathcal{B}} \dot{\mathbf{x}} \cdot \rho \mathbf{g} dv + \int_{\partial \mathcal{B}} \dot{\mathbf{x}} \cdot \mathbf{t} da = \int_{\mathcal{B}} (\dot{\mathbf{x}} \cdot \rho \ddot{\mathbf{x}} + \boldsymbol{\sigma} : \mathbf{d}) dv. \quad (3.60)$$

It should be noticed, that the rate of mechanical work consists of the rate of internal work $\mathcal{W}_{int} = \int_{\mathcal{B}} \boldsymbol{\sigma} : \mathbf{d} dv$ (internal stress power) and rate of kinetic work $\int_{\mathcal{B}} \dot{\mathbf{x}} \cdot \rho \ddot{\mathbf{x}} dv$. The thermal power is given by

$$\mathcal{Q} = \int_{\mathcal{B}} \rho r dv + \int_{\partial \mathcal{B}} q da = \int_{\mathcal{B}} (\rho r - \operatorname{div} \mathbf{q}) dv, \quad (3.61)$$

with the heat source per unit mass r supplying energy in form of heat and the heat flux $q(\mathbf{x}, t, \mathbf{n}) = -\mathbf{q}(\mathbf{x}, t) \cdot \mathbf{n}$ describing heat entering the body across the surface. Thus, the local form of the balance of energy reads

$$\rho \dot{e} = \boldsymbol{\sigma} : \mathbf{d} + \rho r - \operatorname{div} \mathbf{q} \quad \forall \mathbf{x} \in \mathcal{B}. \quad (3.62)$$

With eq. (3.17) and eq. (3.39) the the internal stress power \mathcal{W}_{int} is given by

$$\mathcal{W}_{int} = \int_{\mathcal{B}_0} \boldsymbol{\tau} : \mathbf{d} dV \quad (3.63)$$

and with eq. (3.34) and $\dot{\mathbf{E}} = \frac{1}{2}\dot{\mathbf{C}} = \mathbf{F}^T \mathbf{d}\mathbf{F}$ alternative forms of the stress power read

$$\begin{aligned} \mathcal{W}_{int} &= \int_{\mathcal{B}_0} \boldsymbol{\tau} : (\dot{\mathbf{F}}\mathbf{F}^{-1}) dV = \int_{\mathcal{B}_0} \boldsymbol{\tau}\mathbf{F}^{-T} : \dot{\mathbf{F}} dV = \int_{\mathcal{B}_0} \mathbf{P} : \dot{\mathbf{F}} dV \quad \text{and} \\ \mathcal{W}_{int} &= \int_{\mathcal{B}_0} \boldsymbol{\tau} : (\mathbf{F}^{-T}\dot{\mathbf{E}}\mathbf{F}^{-1}) dV = \int_{\mathcal{B}_0} \mathbf{F}^{-1}\boldsymbol{\tau}\mathbf{F}^{-T} : \dot{\mathbf{E}} dV = \int_{\mathcal{B}} \mathbf{S} : \dot{\mathbf{E}} dV . \end{aligned} \quad (3.64)$$

The stress power is the double contraction of a stress tensor and its associated rate of deformation. In this context, the quantities $(\boldsymbol{\tau}; \mathbf{d})$, $(\mathbf{P}; \dot{\mathbf{F}})$, and $(\mathbf{S}; \dot{\mathbf{E}})$ are so-called work conjugated pairs.

3.4.5 Entropy inequality (2nd law of thermodynamics)

The second fundamental theorem of thermodynamics is the entropy inequality, which gives information about the direction of an energy transfer within a thermomechanical process. The total rate of entropy production Γ equals to the difference between the rate of total entropy \dot{H} and the rate of entropy input \dot{Q} , i.e. $\Gamma = \dot{H} - \dot{Q}$. The axiom of entropy inequality states that the total rate of entropy production Γ is never negative, thus

$$\dot{H} \geq \int_{\mathcal{B}} \frac{1}{\vartheta} \rho r dv - \int_{\partial\mathcal{B}} \frac{1}{\vartheta} \mathbf{q} \cdot \mathbf{n} da \quad \rightarrow \quad \frac{d}{dt} \int_{\mathcal{B}} \rho \eta dv \geq \int_{\mathcal{B}} \frac{1}{\vartheta} \rho r dv - \int_{\partial\mathcal{B}} \frac{1}{\vartheta} \mathbf{q} \cdot \mathbf{n} da , \quad (3.65)$$

with the specific entropy $\eta = \eta(\mathbf{x}, t)$, the absolute temperature $\vartheta = \vartheta(\mathbf{x}, t)$ restricted to positive values, the flux of entropy \mathbf{q}/ϑ entering the body by conduction and the entropy source r/ϑ entering the body by radiation. With the temporal change of the total entropy

$$\dot{H} = \frac{d}{dt} \int_{\mathcal{B}} \rho \eta dv = \int_{\mathcal{B}_0} (\rho \dot{\eta} + \eta [\dot{\rho} + \rho \operatorname{div} \dot{\mathbf{x}}]) J dV = \int_{\mathcal{B}} \rho \dot{\eta} dv , \quad (3.66)$$

the global form of entropy inequality, also called Clausius-Duhem inequality, yields

$$\int_{\mathcal{B}} \rho \dot{\eta} dv \geq \int_{\mathcal{B}} \frac{1}{\vartheta} \rho r dv - \int_{\partial\mathcal{B}} \frac{1}{\vartheta} \mathbf{q} \cdot \mathbf{n} da , \quad (3.67)$$

and with the divergence theorem eq. (A.16) the local form can be derived as

$$\rho \dot{\eta} \geq \frac{1}{\vartheta} \rho r - \operatorname{div} \left(\frac{\mathbf{q}}{\vartheta} \right) . \quad (3.68)$$

Multiplying eq. (3.68) with the absolute temperature ϑ yields the spatial dissipation \mathcal{D} . By use of $\operatorname{div}(\mathbf{q}/\vartheta) = \operatorname{div} \mathbf{q}/\vartheta - \mathbf{q} \cdot \operatorname{grad} \vartheta/\vartheta^2$ and eq. (3.62) \mathcal{D} can be written as

$$\mathcal{D} := \rho (\vartheta \dot{\eta} - \dot{e}) + \boldsymbol{\sigma} : \mathbf{d} - \frac{1}{\vartheta} \mathbf{q} \cdot \operatorname{grad} \vartheta \geq 0. \quad (3.69)$$

An additive split of the dissipation into an internal part \mathcal{D}_{int} and a conductive part \mathcal{D}_{cond} , i.e. $\mathcal{D} = \mathcal{D}_{int} + \mathcal{D}_{cond}$, and postulation that both parts have to be positive or zero yields the Clausius-Planck inequality and the Fourier inequality

$$\mathcal{D}_{int} = \rho (\vartheta \dot{\eta} - \dot{e}) + \boldsymbol{\sigma} : \mathbf{d} \geq 0 \quad \text{and} \quad \mathcal{D}_{cond} = -\frac{1}{\vartheta} \mathbf{q} \cdot \text{grad} \vartheta \geq 0. \quad (3.70)$$

For thermal independent processes \mathcal{D}_{cond} vanishes. Let the Helmholtz free energy $\tilde{\psi} = e - \vartheta \eta$ be the thermodynamic potential, then after a Legendre transformation applied on eq. (3.70)₁ we get

$$\mathcal{D}_{int} = \boldsymbol{\sigma} : \mathbf{d} - \rho \left(\dot{\tilde{\psi}} + \dot{\vartheta} \eta \right) \geq 0. \quad (3.71)$$

Considering isothermal processes, i.e. for constant temperature ($\vartheta = \text{const.}$), the internal dissipation eq. (3.71) reduces to

$$\mathcal{D}_{int} = \boldsymbol{\sigma} : \mathbf{d} - \rho \dot{\tilde{\psi}} \geq 0. \quad (3.72)$$

Considering the work-conjugated pairs and using $\rho_0 \tilde{\psi} = \psi$ the material form of the internal dissipation reads

$$\mathcal{D}_{int} = \mathbf{S} : \dot{\mathbf{E}} - \dot{\psi} \geq 0. \quad (3.73)$$

If the Helmholtz free energy depends only on a strain tensor (e.g. \mathbf{E}), then it is referred to as stored energy and the material time derivative yields $\dot{\psi} = \partial_{\mathbf{E}} \psi : \dot{\mathbf{E}}$. Thus, we obtain

$$\mathcal{D}_{int} = \left(\mathbf{S} - \frac{\partial \psi}{\partial \mathbf{E}} \right) : \dot{\mathbf{E}} \geq 0. \quad (3.74)$$

In case of a perfectly elastic material, locally no entropy is produced, i.e. $\mathcal{D}_{int} = 0$, and therefore, all processes are reversible (no plastic deformation, no damage, etc.). In order to ensure $\mathcal{D}_{int} = 0$ for arbitrary $\dot{\mathbf{E}}$ due to the standard argument of rational continuum mechanics, we set the term in the parentheses in eq. (3.74) equal to zero and obtain the constitutive equation for the second Piola-Kirchhoff stresses as

$$\mathbf{S} = \frac{\partial \psi}{\partial \mathbf{E}} = 2 \frac{\partial \psi}{\partial \mathbf{C}}. \quad (3.75)$$

This relation characterizes a hyperelastic (or Green elastic) material, for which the stresses can be determined from a given stored-energy function, see Truesdell and Noll [2004], page 13. The corresponding standard elasticity tensor for hyperelasticity, see for example Holzapfel [2000], is given by

$$\mathbb{C} = \frac{\partial \mathbf{S}}{\partial \mathbf{E}} = 2 \frac{\partial \mathbf{S}}{\partial \mathbf{C}} = 4 \frac{\partial^2 \psi}{\partial \mathbf{C} \partial \mathbf{C}}, \quad (3.76)$$

which is a symmetric fourth order tensor.

A summary of the balance equations and the entropy inequality is given in Table 3.2.

Conservation of mass: $\dot{m} = 0$		
$m = \int_{\mathcal{B}} \rho \, dv$		$\rho_0 = J\rho$ and $\dot{\rho} + \rho \operatorname{div} \dot{\mathbf{x}} = 0$
Balance of linear momentum: $\dot{L} = K$		
$L = \int_{\mathcal{B}} \rho \dot{\mathbf{x}} \, dv$	$K = \int_{\mathcal{B}} \rho \mathbf{g} \, dv + \int_{\partial \mathcal{B}} \mathbf{t} \, da$	$\operatorname{div} \boldsymbol{\sigma} + \rho(\mathbf{g} - \ddot{\mathbf{x}}) = \mathbf{0}$
Balance of angular momentum: $\dot{\mathbf{h}}_{(0)} = \mathbf{m}_{(0)}$		
$\mathbf{h}_{(0)} = \int_{\mathcal{B}} \mathbf{x} \times \rho \dot{\mathbf{x}} \, dv$,	$\mathbf{m}_{(0)} = \int_{\mathcal{B}} \mathbf{x} \times \rho \mathbf{g} \, dv + \int_{\partial \mathcal{B}} \mathbf{x} \times \mathbf{t} \, da$	$\boldsymbol{\epsilon} : \boldsymbol{\sigma}^T = \mathbf{0} \quad \rightarrow \quad \boldsymbol{\sigma} = \boldsymbol{\sigma}^T$
Balance of energy: $\dot{\mathcal{E}} + \dot{\mathcal{K}} = \mathcal{W} + \mathcal{Q}$		
$\mathcal{E} = \int_{\mathcal{B}} e \rho \, dv$,	$\mathcal{W} = \int_{\mathcal{B}} \dot{\mathbf{x}} \cdot \rho \mathbf{g} \, dv + \int_{\partial \mathcal{B}} \dot{\mathbf{x}} \cdot \mathbf{t} \, da$	$\dot{e} \rho = \boldsymbol{\sigma} : \mathbf{d} + \rho r - \operatorname{div} \mathbf{q}$
$\mathcal{K} = \int_{\mathcal{B}} \frac{1}{2} \rho \dot{\mathbf{x}} \cdot \dot{\mathbf{x}} \, dv$,	$\mathcal{Q} = \int_{\mathcal{B}} \rho r \, dv - \int_{\partial \mathcal{B}} \mathbf{q} \cdot \mathbf{n} \, da$	
Entropy inequality: $\dot{H} \geq \int_{\mathcal{B}} \frac{r\rho}{\vartheta} \, dv - \int_{\partial \mathcal{B}} \frac{\mathbf{q}}{\vartheta} \cdot d\mathbf{a}$		
$H = \int_{\mathcal{B}} \rho \eta \, dv$		$\rho(\vartheta \dot{\eta} - \dot{e}) + \boldsymbol{\sigma} : \mathbf{d} - \mathbf{q} \cdot \frac{\operatorname{grad} \vartheta}{\vartheta} \geq 0$

Table 3.2: Balance equations and entropy inequality: axiom, constituents and local form.

3.5 Basic principles in the framework of material modeling

The description of material behavior is based on the derivation of mathematical models, the constitutive equations. In Section 3.4 eight field equations (1 from eq. (3.47), 3 from eq. (3.52), 3 from eq. (3.57), 1 from eq. (3.62)) were derived, which include 23 field quantities depending on the position and the time

$$\{\varphi_{|3}, \rho_{|1}, \boldsymbol{\sigma}_{|9}, \mathbf{g}_{|3}, \psi_{|1}, \eta_{|1}, \vartheta_{|1}, r_{|1}, \mathbf{q}_{|3}\} \quad \rightarrow \quad 23 \text{ field quantities.} \quad (3.77)$$

Since \mathbf{g} and r (four quantities) are given, the resulting quantities have to be computed by the eight field equations and additionally by 11 constitutive equations

$$f(\boldsymbol{\sigma}_{|6}, \psi_{|1}, \eta_{|1}, \mathbf{q}_{|3}) \quad \rightarrow \quad 11 \text{ constitutive equations.} \quad (3.78)$$

In order to construct physically reasonable constitutive equations several basic principles should be considered: *the principle of consistency*, *the principle of determinism*, *the principle of equipresence*, *the principle of fading memory*, *the principle of local agency*, *the principle of material frame indifference* (also referred to as *objectivity*), and *the principle of material symmetry*. A detailed overview concerning this subject is given in e.g. Truesdell [1969], Truesdell and Toupin [1960], Noll [1974], and Stein and Barthold [1996]. See

also Holzapfel [2000], in which special attention is paid to the principle of material frame indifference. In the present section the principle of material objectivity and the principle of material symmetry are discussed in more detail.

3.5.1 Principle of material frame-indifference – Objectivity

The principle of material frame-indifference or objectivity demands that

“Constitutive equations must be invariant under changes of frame of reference.”

And thus: *“The response of a material is the same for all observers.”*,

see e.g. Truesdell and Noll [2004]. Here, a frame of reference can be regarded as reference system. For a change of frame or change of observer from O to O^+ , the one-to-one mapping of an event in space described by the pair $\{\mathbf{x}, t\}$ to the corresponding pair $\{\mathbf{x}^+, t^+\}$ is given by the Euclidean transformation

$$\mathbf{x}^+ = \mathbf{c}(t) + \mathbf{Q}(t)\mathbf{x} \quad \forall \quad \mathbf{Q}(t) \in \text{SO}(3) \quad \text{and} \quad t^+ = t - \alpha, \quad (3.79)$$

where the vector $\mathbf{c}(t)$ depends on the choice of origin, $\alpha \in \mathbb{R}$ denotes the time shift and the proper orthogonal tensor $\mathbf{Q}(t)$ describes proper rotations, i.e. $\det \mathbf{Q} = 1$ and $\mathbf{Q}^T = \mathbf{Q}^{-1}$, see Fig. 3.5a. The proper orthogonal group $\text{SO}(3)$ is a subgroup of the orthogonal group $\text{O}(3)$, which contains only proper rotations. The orthogonal group contains also improper rotations (reflections and rotoinversions; $\det \mathbf{Q} = \pm 1$). Physical quantities are observer independent if they transform under an Euclidean transformation as given in Table 3.3.

quantity	basis in the		transformation
	current conf.	reference conf.	
Scalar field	–	–	$\gamma^+ = \gamma$
Eulerian vector field	one	–	$\boldsymbol{\gamma}^+ = \mathbf{Q}\boldsymbol{\gamma}$
Eulerian 2 nd order tensor	two	–	$\boldsymbol{\Gamma}^+ = \mathbf{Q}\boldsymbol{\Gamma}\mathbf{Q}^T$
Lagrangian quantity	–	two	$\mathbf{L}^+ = \mathbf{L}$
two-point tensor	one	one	$\mathbf{T}^+ = \mathbf{Q}\mathbf{T}$

Table 3.3: Objective Euclidean transformations of different arbitrary Eulerian and Lagrangian quantities as well as for a two-point tensor.

Nevertheless, not only the physical quantities but also the constitutive equations have to be objective. In case of the free energy the principle demands that

$$\psi(\mathbf{F}^+) = \psi(\mathbf{Q}\mathbf{F}) = \psi(\mathbf{F}) \quad \forall \quad \mathbf{Q} \in \text{SO}(3). \quad (3.80)$$

The right Cauchy-Green tensor is invariant against rigid body rotations $\mathbf{C} = \mathbf{U}^2$, see eq. (3.23), and considering the deformation gradient we notice that it is a priori objective

$$\mathbf{F}^+ = \frac{\partial \mathbf{x}^+}{\partial \mathbf{x}} \frac{\partial \mathbf{x}}{\partial \mathbf{X}} = \mathbf{Q}\mathbf{F} \quad \rightarrow \quad \mathbf{C}^+ = (\mathbf{F}^T)^+ \mathbf{F}^+ = (\mathbf{Q}\mathbf{F})^T \mathbf{Q}\mathbf{F} = \mathbf{F}^T \mathbf{Q}^T \mathbf{Q}\mathbf{F} = \mathbf{C}. \quad (3.81)$$

Therefore, it seems to be reasonable to formulate the constitutive equations in terms of the right Cauchy-Green tensor in the following. Now, the free energy in its reduced form

$$\psi(\mathbf{C}^+) = \psi(\mathbf{C}) \quad \forall \quad \mathbf{Q} \in \text{SO}(3) \quad (3.82)$$

satisfies the principle of material frame-indifference automatically.

3.5.2 Principle of material symmetry

The principle of material symmetry requires that

Constitutive equations have to be invariant with respect to all transformations of the material coordinates, which belong to the symmetry group \mathcal{G}_k of the underlying material.

Considering a material point $\mathbf{X} \in \mathcal{B}_0$ and transferring it to an alternative reference configuration \mathcal{B}_0^* by an arbitrary rigid body motion $\mathbf{Q} \in \mathcal{G}_k$ yields

$$\mathbf{X}^* = \mathbf{Q}^T \mathbf{X} \quad \forall \mathbf{Q} \in \mathcal{G}_k, \quad (3.83)$$

see Fig. 3.5b. Then the current position of each material point can be expressed by $\mathbf{x} = \mathbf{x}(\mathbf{X})$ or $\mathbf{x} = \mathbf{x}(\mathbf{X}^*)$ and the corresponding deformation gradient and the right Cauchy-Green tensor are given by

$$\mathbf{F}^* = \frac{\partial \mathbf{x}}{\partial \mathbf{X}} \frac{\partial \mathbf{X}}{\partial \mathbf{X}^*} = \mathbf{F} \mathbf{Q} \quad \text{and} \quad \mathbf{C}^* = (\mathbf{F}^*)^T \mathbf{F}^* = \mathbf{Q}^T \mathbf{C} \mathbf{Q}. \quad (3.84)$$

Concerning the second Piola-Kirchhoff stress tensor $\mathbf{S} = 2\partial_{\mathbf{C}}\psi(\mathbf{C})$ as constitutive equation, the principle of material symmetry requires that

$$\left. \begin{aligned} \psi(\mathbf{C}) &= \psi(\mathbf{Q}^T \mathbf{C} \mathbf{Q}) \\ \mathbf{Q}^T \mathbf{S}(\mathbf{C}) \mathbf{Q} &= \mathbf{S}(\mathbf{Q}^T \mathbf{C} \mathbf{Q}) \end{aligned} \right\} \quad \forall \mathbf{Q} \in \mathcal{G}_k. \quad (3.85)$$

A material is isotropic, if the symmetry group \mathcal{G}_k equals to the full orthogonal group $O(3)$, i.e. the material behavior is in all directions the same and thus a priori invariant with respect to arbitrary rotations onto the reference configuration.

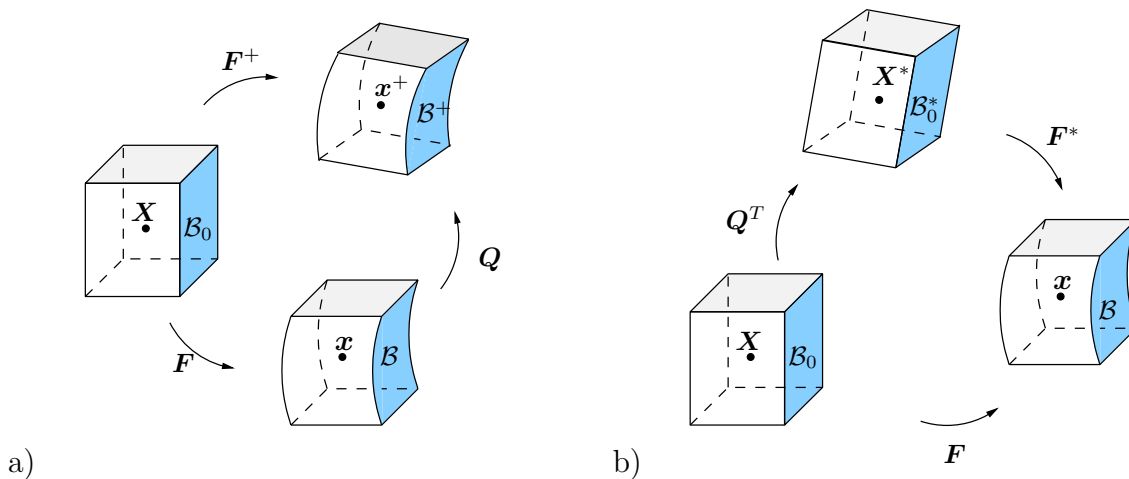


Figure 3.5: Rigid body motion applied to a) the current configuration, and b) the reference configuration.

Let us consider a scalar-valued function h , a vector-valued function \mathbf{h} , and a tensor-valued function of second order \mathbf{H} as functions of a finite set of vector-valued arguments \mathbf{v}_i and a finite set of tensor-valued arguments of second order \mathbf{V}_j (argument tensors of higher

order are not considered for simplicity). They are isotropic tensor functions, if they are invariant with respect to rotations of the orthogonal group $O(3)$, i.e.

$$\left. \begin{aligned} h(\mathbf{v}_i, \mathbf{V}_j) &= h(\mathbf{Q}^T \mathbf{v}_i, \mathbf{Q}^T \mathbf{V}_j \mathbf{Q}) \\ \mathbf{h}(\mathbf{v}_i, \mathbf{V}_j) &= \mathbf{h}(\mathbf{Q}^T \mathbf{v}_i, \mathbf{Q}^T \mathbf{V}_j \mathbf{Q}) \\ \mathbf{H}(\mathbf{v}_i, \mathbf{V}_j) &= \mathbf{H}(\mathbf{Q}^T \mathbf{v}_i, \mathbf{Q}^T \mathbf{V}_j \mathbf{Q}) \end{aligned} \right\} \quad \forall \mathbf{Q} \in O(3). \quad (3.86)$$

3.6 Representation theorems of isotropic and anisotropic tensor functions

The mathematical description of constitutive equations in continuum mechanics is mainly associated to scalar-, vector-, or tensor-valued tensor functions. Such constitutive tensor functions can be represented using coordinate-invariant scalar-valued quantities (invariants) together with corresponding tensor-valued quantities (tensor generators). Fundamental works in the framework of the invariant theory are given by e.g. Grace and Young [1903], Elliott [1913], Weyl [1946], Turnbull [1960], Gurevich [1964], and Schur [1968]. Representation theorems for isotropic tensor functions are proposed and discussed in Wang [1969a,b,c, 1970a,b, 1971], Smith [1970, 1971], and Boehler [1977]. These theorems are the basis for the description of anisotropic materials by use of structural tensors, i.e. by tensors reflecting the symmetry group of the considered material. Important works on the concept of structural tensors are, for example, Boehler [1979, 1987a]. In the context of representations of anisotropic tensor functions the reader is referred to, for example, Spencer [1971], Boehler [1987b], Zheng and Spencer [1993], and Betten [2001]. The invariant theory in the framework of continuum mechanics is also described in Rivlin and Ericksen [1955], Pipkin and Wineman [1963], Wineman and Pipkin [1964], Schröder [1996] and Truesdell and Noll [2004]. The content of this section is based on the works Schröder [1996] and Balzani [2006].

3.6.1 Representation theorems of isotropic tensor functions

In this section we focus on the representation theorems of isotropic tensor functions in the framework of the invariant theory. The aim of the invariant theory is to determine an invariant system of irreducible invariants. This set of irreducible invariants is the so-called integrity basis, see Schur [1968], from which all other invariants can be deduced. In this context, *Hilbert's theorem* postulates that for a finite number of vectors and tensors there exists a integrity basis consisting of a finite number of invariants, see the proof in Gurevich [1964]. The application of the representation theory, saying that each isotropic tensor function (cf. eq. (3.86)) can be expressed by a function of a finite set of scalar-valued invariants I_s and tensor generators $\mathbf{h}_k, \mathbf{H}_k$, provides

$$h(\mathbf{v}_i, \mathbf{V}_j) = h(I_s), \quad \mathbf{h}(\mathbf{v}_i, \mathbf{V}_j) = \sum_k \varphi_k(I_s) \mathbf{h}_k, \quad \text{and} \quad \mathbf{H}(\mathbf{v}_i, \mathbf{V}_j) = \sum_k \varphi_k(I_s) \mathbf{H}_k, \quad (3.87)$$

where $I_s = \{I_1, I_2, I_3, \dots, I_p\}$ is the integrity basis consisting of a set of p irreducible invariants and $\varphi_k(I_s)$ are scalar-valued functions of the irreducible invariants. For a more detailed derivation the reader is referred to Korsgaard [1990a,b].

The invariants of the right Cauchy-Green tensor \mathbf{C} are defined by the characteristic polynomial $\det[\lambda \mathbf{1} - \mathbf{C}] = \lambda^3 - I_1 \lambda^2 + I_2 \lambda - I_3 = 0$ with the eigenvalues λ of \mathbf{C} and the second

order identity tensor $\mathbf{1}$. The Cayley-Hamilton theorem states that every square matrix satisfies its own characteristic equation, thus

$$\mathbf{p}(\mathbf{C}) = \mathbf{C}^3 - I_1 \mathbf{C}^2 + I_2 \mathbf{C} - I_3 \mathbf{1} = \mathbf{0} , \quad (3.88)$$

with the set of isotropic principal invariants of the right Cauchy-Green tensor

$$I_1 = \text{tr} \mathbf{C}, \quad I_2 = \frac{1}{2}((\text{tr} \mathbf{C})^2 - \text{tr} \mathbf{C}^2) = \text{tr}[\text{cof} \mathbf{C}], \quad I_3 = \det \mathbf{C} . \quad (3.89)$$

The resulting isotropic polynomial basis (integrality basis of polynomial invariants) is

$$\mathcal{P}_{\text{iso}} = \{I_1, I_2, I_3\} . \quad (3.90)$$

Now we are able to express the free-energy function ψ as isotropic scalar-valued function in terms of the principal invariants of the right Cauchy-Green tensor

$$\psi(\mathbf{C}) = \psi(L_i | L_i \in \mathcal{P}_{\text{iso}}) . \quad (3.91)$$

Then, the second Piola-Kirchhoff stress tensor \mathbf{S} (see eq. (3.75)) as well as the tangent moduli \mathbb{C} (see eq. (3.76)) can be written as isotropic tensor functions

$$\mathbf{S} = 2 \partial_{\mathbf{C}} \psi = 2 \sum_i \frac{\partial \psi}{\partial L_i} \frac{\partial L_i}{\partial \mathbf{C}} , \quad (3.92)$$

and considering the symmetry conditions $\frac{\partial^2 \psi}{\partial L_i \partial L_j} = \frac{\partial^2 \psi}{\partial L_j \partial L_i}$

$$\mathbb{C} = 4 \sum_i \left[\sum_j \frac{\partial^2 \psi}{\partial L_i \partial L_j} \left\{ \frac{\partial L_i}{\partial \mathbf{C}} \otimes \frac{\partial L_j}{\partial \mathbf{C}} \right\} + \frac{\partial \psi}{\partial L_i} \frac{\partial^2 L_i}{\partial \mathbf{C} \partial \mathbf{C}} \right] , \quad (3.93)$$

with the invariants $L_i, L_j \in \mathcal{P}_{\text{iso}}$. Insertion of the partial derivatives of the invariants with respect to \mathbf{C} , see Appendix C, in eq. (3.92) yields the explicit expression for the isotropic second Piola-Kirchhoff stress tensor

$$\mathbf{S}^{\text{iso}} = 2 \left[\left(\frac{\partial \psi}{\partial I_1} + \frac{\partial \psi}{\partial I_2} I_1 \right) \mathbf{1} - \frac{\partial \psi}{\partial I_2} \mathbf{C} + \frac{\partial \psi}{\partial I_3} \text{Cof} \mathbf{C} \right] , \quad (3.94)$$

with the isotropic tensor generators $\mathbf{H}_{\text{iso}} = \{\mathbf{1}, \mathbf{C}, \text{Cof} \mathbf{C}\}$. Then, with further insertion into eq. (3.93) the isotropic tangent modulus is given by

$$\begin{aligned} \mathbb{C}^{\text{iso}} = 4 & \left[\frac{\partial^2 \psi}{\partial I_1 \partial I_1} \mathbf{1} \otimes \mathbf{1} + \frac{\partial^2 \psi}{\partial I_2 \partial I_2} \{I_1 \mathbf{1} - \mathbf{C}\} \otimes \{I_1 \mathbf{1} - \mathbf{C}\} \right. \\ & + \frac{\partial^2 \psi}{\partial I_3 \partial I_3} \text{Cof} \mathbf{C} \otimes \text{Cof} \mathbf{C} \\ & + \frac{\partial^2 \psi}{\partial I_2 \partial I_1} [\mathbf{1} \otimes \{I_1 \mathbf{1} - \mathbf{C}\} + \{I_1 \mathbf{1} - \mathbf{C}\} \otimes \mathbf{1}] \\ & + \frac{\partial^2 \psi}{\partial I_3 \partial I_1} [\mathbf{1} \otimes \text{Cof} \mathbf{C} + \text{Cof} \mathbf{C} \otimes \mathbf{1}] \\ & + \frac{\partial^2 \psi}{\partial I_3 \partial I_2} [\text{Cof} \mathbf{C} \otimes \{I_1 \mathbf{1} - \mathbf{C}\} + \{I_1 \mathbf{1} - \mathbf{C}\} \otimes \text{Cof} \mathbf{C}] \\ & \left. + \frac{\partial \psi}{\partial I_2} [\mathbf{1} \otimes \mathbf{1} - \mathbf{1} \boxtimes \mathbf{1}] + \frac{\partial \psi}{\partial I_3} I_3 [\mathbf{C}^{-1} \otimes \mathbf{C}^{-1} - \mathbf{C}^{-1} \boxtimes \mathbf{C}^{-1}] \right] , \quad (3.95) \end{aligned}$$

with $(\bullet) \boxtimes (\bullet)$ in index notation being $\{(\bullet)^{AB}\} \boxtimes \{(\bullet)^{CD}\} = (\bullet)^{AC} (\bullet)^{BD}$.

3.6.2 Representation theorems of anisotropic tensor functions

Anisotropic materials do not have the same material behavior in all directions. But, there may be special directions present, along which the physical properties are identical. For instance the material properties of a transversely isotropic material are the same in one preferred direction and perpendicular to that the properties are rotationally-symmetric. Thus, the underlying material symmetry group is given by

$$\mathcal{G}_{\text{ti}} = \{\pm \mathbf{1}, \mathbf{Q}(\alpha, \mathbf{A}) \text{ with } 0 < \alpha < 2\pi\}, \quad (3.96)$$

with α being the angle of rotation around the preferred direction \mathbf{A} in the reference configuration. For rotations belonging to this symmetry group the relations in eq. (3.85) hold. The direction-specific behavior can be described by the second-order structural tensor

$$\mathbf{M} = \mathbf{A} \otimes \mathbf{A} \quad \text{with} \quad \text{tr} \mathbf{M} = 1 \quad \text{and} \quad \|\mathbf{A}\| = 1, \quad (3.97)$$

which reflects the symmetry properties of the underlying transversely isotropic material,

$$\mathbf{M}^* = \mathbf{Q}^T \mathbf{M} \mathbf{Q} = \mathbf{M} \quad \forall \mathbf{Q} \in \mathcal{G}_{\text{ti}}. \quad (3.98)$$

Inserting the extended list of argument tensors into eq. (3.85) yields

$$\left. \begin{aligned} \psi(\mathbf{C}, \mathbf{M}) &= \psi(\mathbf{Q}^T \mathbf{C} \mathbf{Q}, \mathbf{M}) \\ \mathbf{Q}^T \mathbf{S}(\mathbf{C}, \mathbf{M}) \mathbf{Q} &= \mathbf{S}(\mathbf{Q}^T \mathbf{C} \mathbf{Q}, \mathbf{M}) \end{aligned} \right\} \quad \forall \mathbf{Q} \in \mathcal{G}_{\text{ti}}. \quad (3.99)$$

However, if we not only account for a rotation of the loading but also of the structural tensor we observe that the response functions remain unaltered, i.e.

$$\left. \begin{aligned} \psi(\mathbf{C}, \mathbf{M}) &= \psi(\mathbf{Q}^T \mathbf{C} \mathbf{Q}, \mathbf{Q}^T \mathbf{M} \mathbf{Q}) \\ \mathbf{Q}^T \mathbf{S}(\mathbf{C}, \mathbf{M}) \mathbf{Q} &= \mathbf{S}(\mathbf{Q}^T \mathbf{C} \mathbf{Q}, \mathbf{Q}^T \mathbf{M} \mathbf{Q}) \end{aligned} \right\} \quad \forall \mathbf{Q} \in \text{O}(3), \quad (3.100)$$

see also Fig. 3.6, which is the definition of isotropic tensor functions. Thus, we can derive a finite set of scalar-valued invariants and associated tensor generators, which represent the characteristics of the material. Consequently, the requirement of material symmetry is automatically fulfilled.

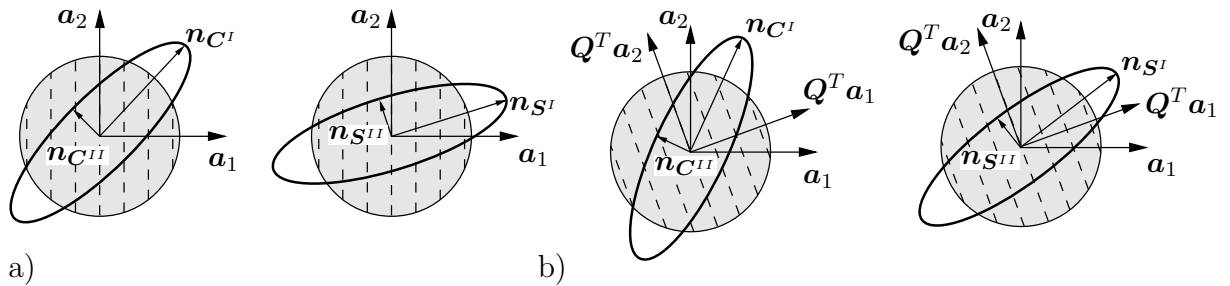


Figure 3.6: Eigenvectors $\mathbf{n}_{C^I}, \mathbf{n}_{C^{II}}$ of the deformation \mathbf{C} and eigenvectors $\mathbf{n}_{S^I}, \mathbf{n}_{S^{II}}$ of the stresses \mathbf{S} in a transversely isotropic body: a) due to initial loading, b) after rotation of both loading and structural properties. In the rotated system the principal strains and stresses remain unaltered.

Since the invariants of \mathbf{M} (e.g. $I_{M1} = \text{tr}\mathbf{M} = 1$) are no expedient invariants for the representation, we obtain the mixed invariants of the arguments \mathbf{C} and \mathbf{M}

$$J_4 = \text{tr}[\mathbf{C}\mathbf{M}], \quad J_5 = \text{tr}[\mathbf{C}^2\mathbf{M}], \quad J_6 = \det[\mathbf{C}\mathbf{M}^2], \quad J_7 = \text{tr}[\mathbf{C}^2\mathbf{M}^2], \quad (3.101)$$

see Boehler [1987b]. Note that $J_4 = J_6$ and $J_5 = J_7$, due to eq. (3.97)₃, then the polynomial basis will be extended for transversely isotropic materials to

$$\mathcal{P}_{\text{ti}}(\mathbf{C}, \mathbf{M}) = \{I_1, I_2, I_3, J_4, J_5\}, \quad (3.102)$$

and furthermore the free energy function ψ as will be written as

$$\psi(\mathbf{C}, \mathbf{M}) = \psi(L_i | L_i \in \mathcal{P}_{\text{ti}}(\mathbf{C}, \mathbf{M})). \quad (3.103)$$

Extending the second Piola-Kirchhoff stress tensor and the tangent moduli to transverse isotropy yields

$$\mathbf{S} = \mathbf{S}^{\text{iso}} + \mathbf{S}^{\text{ti}} \quad \text{and} \quad \mathbb{C} = \mathbb{C}^{\text{iso}} + \mathbb{C}^{\text{ti}}. \quad (3.104)$$

with the transversely isotropic second Piola-Kirchhoff stress tensor

$$\mathbf{S}^{\text{ti}} = 2 \left[\frac{\partial \psi}{\partial J_4} \mathbf{M} + \frac{\partial \psi}{\partial J_5} (\mathbf{C}\mathbf{M} + \mathbf{M}\mathbf{C}) \right]. \quad (3.105)$$

Let the new set of tensor generators be $\mathbf{H}_{\text{ti}} = \{\mathbf{1}, \mathbf{C}, \text{Cof}\mathbf{C}, \mathbf{M}, \{\mathbf{C}\mathbf{M} + \mathbf{M}\mathbf{C}\}\}$, then the transversely isotropic tangent modulus appears as

$$\begin{aligned} \mathbb{C}^{\text{ti}} = & 4 \left[\frac{\partial^2 \psi}{\partial J_4 \partial J_4} \mathbf{M} \otimes \mathbf{M} + \frac{\partial^2 \psi}{\partial J_5 \partial J_5} \{\mathbf{C}\mathbf{M} + \mathbf{M}\mathbf{C}\} \otimes \{\mathbf{C}\mathbf{M} + \mathbf{M}\mathbf{C}\} \right. \\ & + \frac{\partial^2 \psi}{\partial I_1 \partial J_4} [\mathbf{1} \otimes \mathbf{M} + \mathbf{M} \otimes \mathbf{1}] \\ & + \frac{\partial^2 \psi}{\partial I_1 \partial J_5} [\mathbf{1} \otimes \{\mathbf{C}\mathbf{M} + \mathbf{M}\mathbf{C}\} + \{\mathbf{C}\mathbf{M} + \mathbf{M}\mathbf{C}\} \otimes \mathbf{1}] \\ & + \frac{\partial^2 \psi}{\partial I_2 \partial I_4} [\{I_1 \mathbf{1} - \mathbf{C}\} \otimes \mathbf{M} + \mathbf{M} \otimes \{I_1 \mathbf{1} - \mathbf{C}\}] \\ & + \frac{\partial^2 \psi}{\partial I_2 \partial J_5} [\{I_1 \mathbf{1} - \mathbf{C}\} \otimes \{\mathbf{C}\mathbf{M} + \mathbf{M}\mathbf{C}\} + \{\mathbf{C}\mathbf{M} + \mathbf{M}\mathbf{C}\} \otimes \{I_1 \mathbf{1} - \mathbf{C}\}] \\ & + \frac{\partial^2 \psi}{\partial I_3 \partial J_4} [\text{Cof}\mathbf{C} \otimes \mathbf{M} + \mathbf{M} \otimes \text{Cof}\mathbf{C}] \\ & + \frac{\partial^2 \psi}{\partial I_3 \partial J_5} [\text{Cof}\mathbf{C} \otimes \{\mathbf{C}\mathbf{M} + \mathbf{M}\mathbf{C}\} + \{\mathbf{C}\mathbf{M} + \mathbf{M}\mathbf{C}\} \otimes \text{Cof}\mathbf{C}] \\ & + \frac{\partial^2 \psi}{\partial J_4 \partial J_5} [\{\mathbf{C}\mathbf{M} + \mathbf{M}\mathbf{C}\} \otimes \mathbf{M} + \mathbf{M} \otimes \{\mathbf{C}\mathbf{M} + \mathbf{M}\mathbf{C}\}] \\ & \left. + \frac{\partial \psi}{\partial J_5} [(\mathbf{1} \boxtimes \mathbf{M})^{\text{34}} + (\mathbf{M} \boxtimes \mathbf{1})^{\text{34}}] \right], \end{aligned} \quad (3.106)$$

with $(\bullet)^{\text{34}}$ in index notation being $\{(\bullet)^{ABCD}\}^{\text{34}} = (\bullet)^{ABDC}$.

4 Finite-Element-Method

In order to describe mathematically the physical phenomena occurring in materials, the balance equations are used. These balance equations are given as partial differential equations of field variables. For complex nonlinear problems an analytical (exact) solution of the problem can not be derived in general. Thus, an approximate solution of partial differential equations on arbitrary domains must be taken into account, for example the Finite-Element-Method (FEM). Here, firstly the continuous problem is transformed into a discrete counterpart, i.e. the domain is discretized by a number of finite elements, and then the discrete problem is solved using suitable numerical methods. Further information concerning this subject is given in the standard text books Zienkiewicz and Taylor [1989], Bathe [1996], Belytschko et al. [2000], Hughes [2000], Braess [2001], Zienkiewicz and Taylor [2005], Zienkiewicz et al. [2005], and Wriggers [2008].

4.1 Boundary value problem

In case of thermally independent, quasi-static conditions ($\ddot{\mathbf{x}} \approx \mathbf{0}$) the nonlinear boundary value problem is characterized by the local balance of linear momentum eq. (3.52) and boundary conditions. Then, the balance of linear momentum in the material setting can be derived from eq. (3.52) with using eq. (3.44). This gives us the partial differential equation

$$\text{Div} \mathbf{P} + \rho_0 \mathbf{g} = \mathbf{0}, \quad (4.1)$$

which is referred to as strong form of equilibrium. Since the boundary value problem is driven by the displacements \mathbf{u} as primary variable, the Dirichlet boundary conditions in terms of the displacements and the corresponding Neumann boundary conditions are

$$\mathbf{u} = \bar{\mathbf{u}} \quad \text{on} \quad \partial \mathcal{B}_{0u} \quad \text{and} \quad \mathbf{T} = \mathbf{P} \mathbf{N} = \bar{\mathbf{t}} \quad \text{on} \quad \partial \mathcal{B}_{0\sigma}. \quad (4.2)$$

Here, the surface of the body $\partial \mathcal{B}_0$ is divided into a part for prescribed deformations $\partial \mathcal{B}_{0u}$ and one part for prescribed stresses $\partial \mathcal{B}_{0\sigma}$ whereby the parts do not overlap

$$\partial \mathcal{B}_0 = \partial \mathcal{B}_{0u} \cup \partial \mathcal{B}_{0\sigma} \quad \text{with} \quad \partial \mathcal{B}_{0u} \cap \partial \mathcal{B}_{0\sigma} = \emptyset. \quad (4.3)$$

4.2 Weak formulation of the field equations

For complex boundary value problems it is in general impossible to derive an analytical solution. Therefore, the strong form of equilibrium is converted to a so-called weak form. We use the Galerkin method and multiply eq. (4.1) with an appropriate test function $\delta \mathbf{u}$, with $\delta \mathbf{u} = \mathbf{0}$ on $\partial \mathcal{B}_{0u}$, and integrate over the domain \mathcal{B}_0

$$G(\mathbf{u}, \delta \mathbf{u}) = - \int_{\mathcal{B}_0} (\text{Div} \mathbf{P} + \rho_0 \mathbf{g}) \cdot \delta \mathbf{u} \, dV = 0. \quad (4.4)$$

Application of the product rule $\text{Div} \mathbf{P} \cdot \delta \mathbf{u} = \text{Div}(\mathbf{P}^T \delta \mathbf{u}) - \mathbf{P} : \text{Grad} \delta \mathbf{u}$ yields the relation

$$G(\mathbf{u}, \delta \mathbf{u}) = \int_{\mathcal{B}_0} \mathbf{P} : \text{Grad} \delta \mathbf{u} \, dV - \int_{\mathcal{B}_0} \text{Div}(\delta \mathbf{u} \mathbf{P}) \, dV - \int_{\mathcal{B}_0} \rho_0 \mathbf{g} \cdot \delta \mathbf{u} \, dV = 0. \quad (4.5)$$

Using the Gauß divergence theorem (eq. (A.16)) and the relation $\text{Grad}\delta\mathbf{u} = \delta\mathbf{F}$ leads to the weak form of equilibrium

$$G(\mathbf{u}, \delta\mathbf{u}) = \underbrace{\int_{\mathcal{B}_0} \mathbf{P} : \delta\mathbf{F} dV}_{G^{int}} - \underbrace{\left\{ \int_{\partial\mathcal{B}_{0\sigma}} \bar{\mathbf{t}} \cdot \delta\mathbf{u} dA + \int_{\mathcal{B}_0} \rho_0 \mathbf{g} \cdot \delta\mathbf{u} dV \right\}}_{G^{ext}} = 0, \quad (4.6)$$

with the internal virtual work G^{int} and the external virtual work G^{ext} . With the relations

$$\begin{aligned} \mathbf{P} : \delta\mathbf{F} &= (\mathbf{F}\mathbf{S}) : \delta\mathbf{F} = \mathbf{S} : \text{sym}[\mathbf{F}^T \delta\mathbf{F}], \\ \delta\mathbf{C} &= (\delta\mathbf{F})^T \mathbf{F} + \mathbf{F}^T \delta\mathbf{F} = 2 \text{sym}[\mathbf{F}^T \delta\mathbf{F}], \end{aligned} \quad (4.7)$$

and $\delta\mathbf{E} = \frac{1}{2}\delta\mathbf{C}$ the alternative form of the internal part in terms of the symmetric second Piola-Kirchhoff stress tensor \mathbf{S} is given by

$$G^{int}(\mathbf{u}, \delta\mathbf{u}) = \int_{\mathcal{B}_0} \mathbf{S} : \delta\mathbf{E} dV = \int_{\mathcal{B}_0} \mathbf{S} : \frac{1}{2}\delta\mathbf{C} dV. \quad (4.8)$$

4.3 Linearization of the weak forms

In order to solve the weak form $G(\mathbf{u}, \delta\mathbf{u})$ the Newton-Raphson iteration method is used, since $G(\mathbf{u}, \delta\mathbf{u})$ is a nonlinear function in \mathbf{u} . Therefore, a linearization of the underlying equations is required. The linearization of the weak form of equilibrium at $\mathbf{u} = \bar{\mathbf{u}}$ is given by

$$\text{Lin}G(\bar{\mathbf{u}}, \delta\mathbf{u}, \Delta\mathbf{u}) = G(\bar{\mathbf{u}}, \delta\mathbf{u}) + \Delta G(\bar{\mathbf{u}}, \delta\mathbf{u}, \Delta\mathbf{u}), \quad (4.9)$$

with the linear increment $\Delta G(\bar{\mathbf{u}}, \delta\mathbf{u}, \Delta\mathbf{u})$. The increment is defined by the directional derivative of G at $\bar{\mathbf{u}}$ in the direction of an incremental deformation $\Delta\mathbf{u}$ as

$$\Delta G(\bar{\mathbf{u}}, \delta\mathbf{u}, \Delta\mathbf{u}) = DG(\bar{\mathbf{u}}, \delta\mathbf{u}) \cdot \Delta\mathbf{u} = \left. \frac{d}{d\epsilon} [G(\bar{\mathbf{u}} + \epsilon \Delta\mathbf{u}, \delta\mathbf{u})] \right|_{\epsilon=0}. \quad (4.10)$$

Under consideration of the incremental second Piola-Kirchhoff stress tensor $\Delta\mathbf{S}$, the incremental right Cauchy-Green tensor $\Delta\mathbf{C}$ and the increment of $\delta\mathbf{C}$ (see eq. (4.7)₂)

$$\begin{aligned} \Delta\mathbf{C} &= \Delta\mathbf{F}^T \mathbf{F} + \mathbf{F}^T \Delta\mathbf{F}, \\ \Delta\mathbf{S} &= \frac{\partial \mathbf{S}}{\partial \mathbf{C}} : \Delta\mathbf{C} = \frac{1}{2} \mathbb{C} : \Delta\mathbf{C} \quad \text{with} \quad \mathbb{C} = 2 \partial_{\mathbf{C}} \mathbf{S}, \\ \Delta\delta\mathbf{C} &= \delta\mathbf{F}^T \Delta\mathbf{F} + \Delta\mathbf{F}^T \delta\mathbf{F}, \end{aligned} \quad (4.11)$$

and in case of conservative loads (volume forces $\rho_0 \mathbf{g}$ and traction forces $\bar{\mathbf{t}}$ are independent of the displacements $\rightarrow \Delta G^{ext} = 0$) the directional derivative of eq. (4.10) is

$$\begin{aligned} \Delta G(\bar{\mathbf{u}}, \delta\mathbf{u}, \Delta\mathbf{u}) &= DG^{int}(\bar{\mathbf{u}}, \delta\mathbf{u}) \cdot \Delta\mathbf{u} = \int_{\mathcal{B}_0} \Delta\mathbf{S} : \frac{1}{2}\delta\mathbf{C} dV + \int_{\mathcal{B}_0} \mathbf{S} : \frac{1}{2}\Delta\delta\mathbf{C} dV \\ &= \underbrace{\int_{\mathcal{B}_0} \frac{1}{2}\delta\mathbf{C} : \mathbb{C} : \frac{1}{2}\Delta\mathbf{C} dV}_{\Delta G^{material}} + \underbrace{\int_{\mathcal{B}_0} \mathbf{S} : \frac{1}{2}\Delta\delta\mathbf{C} dV}_{\Delta G^{geometric}}. \end{aligned} \quad (4.12)$$

Here, the increment of G is divided into a material part $\Delta G^{material}$ and a geometric part $\Delta G^{geometric}$. Since G^{ext} is independent of \mathbf{u} the linearization of the weak form (eq. (4.9)) appears with eq. (4.8) and eq. (4.12) as

$$LinG(\bar{\mathbf{u}}, \delta \mathbf{u}, \Delta \mathbf{u}) = \int_{\mathcal{B}_0} \mathbf{S} : \frac{1}{2} \delta \mathbf{C} dV - G^{ext} + \Delta G^{material} + \Delta G^{geometric}. \quad (4.13)$$

4.4 Finite element discretization

In the framework of the Finite-Element-Method partial differential equations are solved on the discretized domain of a physical body. As shown in Fig. 4.1a for an arbitrary physical body, the domain in the reference configuration \mathcal{B}_0 is geometrically subdivided into a certain number of finite elements.

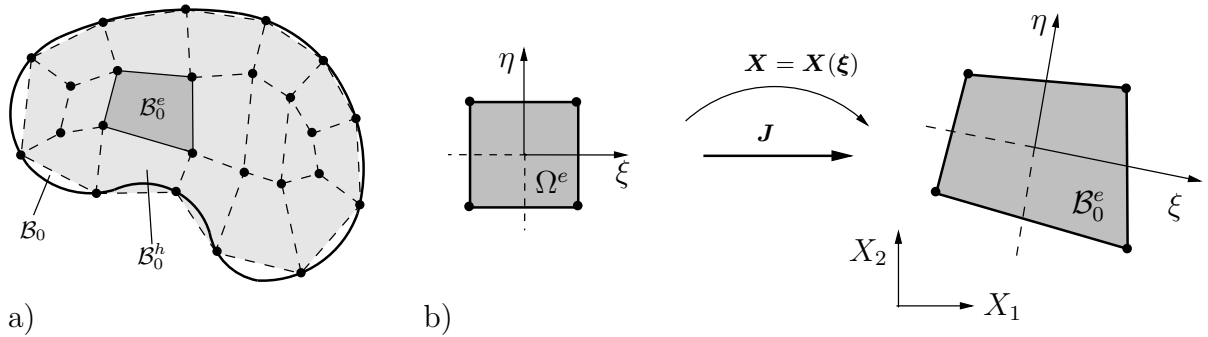


Figure 4.1: a) Discretization of the physical domain \mathcal{B}_0 resulting in an approximate domain \mathcal{B}_0^h . The approximate domain consists of individual finite elements \mathcal{B}_0^e . b) Four-noded quadrilateral element in the parameterized space Ω^e and the reference configuration \mathcal{B}_0^e .

Thus, the body \mathcal{B}_0 is approximated by a discrete counterpart \mathcal{B}_0^h consisting of n_{elem} finite elements \mathcal{B}_0^e , i.e.

$$\mathcal{B}_0 \approx \mathcal{B}_0^h = \bigcup_{e=1}^{n_{elem}} \mathcal{B}_0^e. \quad (4.14)$$

In order to derive a compact formulation a vector-matrix notation will be used for the following finite element formulation, i.e. some second-order tensor fields will be formulated in vector form and all present higher-order tensors as matrices signified with square brackets. For the symmetric second-order strain tensor \mathbf{C} and the second Piola-Kirchhoff stress tensor \mathbf{S} this convention results in the equivalent Voigt notation

$$[\mathbf{C}] := [C_{11}, C_{22}, C_{33}, 2C_{12}, 2C_{23}, 2C_{13}]^T \quad \text{and} \quad [\mathbf{S}] := [S_{11}, S_{22}, S_{33}, S_{12}, S_{23}, S_{13}]^T, \quad (4.15)$$

respectively. The matrix notation of the fourth-order mechanical moduli \mathbb{C} yields

$$[\mathbb{C}] := \begin{bmatrix} \mathbb{C}_{1111} & \mathbb{C}_{1122} & \mathbb{C}_{1133} & \mathbb{C}_{1112} & \mathbb{C}_{1123} & \mathbb{C}_{1113} \\ & \mathbb{C}_{2222} & \mathbb{C}_{2233} & \mathbb{C}_{2212} & \mathbb{C}_{2223} & \mathbb{C}_{2213} \\ & & \mathbb{C}_{3333} & \mathbb{C}_{3312} & \mathbb{C}_{3323} & \mathbb{C}_{3313} \\ & & & \mathbb{C}_{1212} & \mathbb{C}_{1223} & \mathbb{C}_{1213} \\ & sym. & & & \mathbb{C}_{2323} & \mathbb{C}_{2313} \\ & & & & & \mathbb{C}_{1313} \end{bmatrix} \quad (4.16)$$

with $[\mathbf{C}]_{ij} = [\mathbf{C}]_{ji}$. A more detailed derivation of the appearing matrix entries is given in Appendix B.

For the approximation of the unknown fields the isoparametric concept is taken into account. Here, the main idea is to use the same interpolation (shape) functions $N_I(\boldsymbol{\xi})$ for the approximation of the geometry

$$[\mathbf{X}] = [\mathbf{X}](\boldsymbol{\xi}) = \sum_{I=1}^{n_{node}} N_I(\boldsymbol{\xi}) [\mathbf{X}_I], \quad (4.17)$$

as well as for the unknown displacement fields and its virtual and incremental counterparts

$$[\mathbf{u}] = \sum_{I=1}^{n_{node}} N_I [\mathbf{d}_I], \quad [\delta \mathbf{u}] = \sum_{I=1}^{n_{node}} N_I [\delta \mathbf{d}_I], \quad \text{and} \quad [\Delta \mathbf{u}] = \sum_{I=1}^{n_{node}} N_I [\Delta \mathbf{d}_I]. \quad (4.18)$$

Here, $[\mathbf{d}_I]$, $[\delta \mathbf{d}_I]$, and $[\Delta \mathbf{d}_I]$ are the discrete nodal, virtual and incremental displacements at one of n_{node} discrete nodal points I of the element. The corresponding interpolation function N_I at each point I is a function of the natural coordinates $\boldsymbol{\xi} = [\xi, \eta, \zeta]^T$ on an isoparametric space Ω_e , which is mapped onto the reference configuration via the Jacobian

$$\mathbf{J} = \frac{\partial [\mathbf{X}]}{\partial \boldsymbol{\xi}} = \frac{\partial}{\partial \boldsymbol{\xi}} \sum_{I=1}^{n_{node}} N_I [\mathbf{X}_I] = \sum_{I=1}^{n_{node}} [\mathbf{X}_I] \otimes \nabla_{\boldsymbol{\xi}} N_I, \quad (4.19)$$

see Fig. 4.1b. The current position vector of an arbitrary point I is approximated by

$$[\mathbf{x}_I] = [\mathbf{X}_I] + [\mathbf{d}_I]. \quad (4.20)$$

The approximation of the virtual and incremental deformation gradient is given as

$$\begin{aligned} \delta \mathbf{F} &= \text{Grad}[\delta \mathbf{u}] = \sum_{I=1}^{n_{node}} [\delta \mathbf{d}_I] \otimes \text{Grad} N_I(\boldsymbol{\xi}), \quad \delta F^a{}_A = \sum_{I=1}^{n_{node}} N_{I,A} \delta d_I^a \quad \text{and} \\ \Delta \mathbf{F} &= \text{Grad}[\Delta \mathbf{u}] = \sum_{I=1}^{n_{node}} [\Delta \mathbf{d}_I] \otimes \text{Grad} N_I(\boldsymbol{\xi}), \quad \Delta F^a{}_A = \sum_{I=1}^{n_{node}} N_{I,A} \Delta d_I^a. \end{aligned} \quad (4.21)$$

Since the interpolation functions are functions of the natural coordinates $\boldsymbol{\xi}$, but the boundary value problem is defined in physical coordinates \mathbf{X} , we make use of the chain rule and derive for the derivative of the interpolation functions the relation

$$\text{Grad} N_I(\boldsymbol{\xi}) = \nabla_{\mathbf{X}} N_I = \frac{\partial N_I(\boldsymbol{\xi})}{\partial \mathbf{X}} = \frac{\partial N_I(\boldsymbol{\xi})}{\partial \boldsymbol{\xi}} \frac{\partial \boldsymbol{\xi}}{\partial \mathbf{X}} = \mathbf{J}^{-T} \frac{\partial N_I(\boldsymbol{\xi})}{\partial \boldsymbol{\xi}} = \mathbf{J}^{-T} \nabla_{\boldsymbol{\xi}} N_I. \quad (4.22)$$

The virtual and incremental right Cauchy-Green tensor (eq. (4.11) and eq. (4.7)) are approximated by

$$\frac{1}{2} [\delta \mathbf{C}] = \sum_{I=1}^{n_{node}} [\mathbf{B}_I] [\delta \mathbf{d}_I] \quad \text{and} \quad \frac{1}{2} [\Delta \mathbf{C}] = \sum_{I=1}^{n_{node}} [\mathbf{B}_I] [\Delta \mathbf{d}_I], \quad (4.23)$$

where the three-dimensional nodal B-matrices $[\mathbf{B}_I]$ are defined as

$$[\mathbf{B}_I] = \begin{bmatrix} F_{11}N_{I,1} & F_{21}N_{I,1} & F_{31}N_{I,1} \\ F_{12}N_{I,2} & F_{22}N_{I,2} & F_{32}N_{I,2} \\ F_{13}N_{I,3} & F_{23}N_{I,3} & F_{33}N_{I,3} \\ F_{11}N_{I,2} + F_{12}N_{I,1} & F_{21}N_{I,2} + F_{22}N_{I,1} & F_{31}N_{I,2} + F_{32}N_{I,1} \\ F_{12}N_{I,3} + F_{13}N_{I,2} & F_{22}N_{I,3} + F_{23}N_{I,2} & F_{32}N_{I,3} + F_{33}N_{I,2} \\ F_{11}N_{I,3} + F_{13}N_{I,1} & F_{21}N_{I,3} + F_{23}N_{I,1} & F_{31}N_{I,3} + F_{33}N_{I,1} \end{bmatrix}, \quad (4.24)$$

where $N_{I,i} = \partial N_I / \partial X_i$. Inserting the above derived relations into eq. (4.6) with G^{int} from eq. (4.8) the discretized weak form of equilibrium of an element in the reference configuration is

$$G^e = \sum_{I=1}^{n_{node}} [\delta \mathbf{d}_I]^T \left\{ \underbrace{\int_{\mathcal{B}_0^e} [\mathbf{B}_I]^T [\mathbf{S}] dV}_{[\mathbf{r}_I^{int}]} - \int_{\partial \mathcal{B}_{0\sigma}^e} N_I [\bar{\mathbf{t}}] dA - \int_{\mathcal{B}_0^e} N_I \rho_0 [\mathbf{g}] dV \right\} = 0. \quad (4.25)$$

Here, $[\mathbf{r}_I^{int}] + [\mathbf{r}_I^{ext}] := [\mathbf{r}_I]$ denote the residuals associated to node I , consisting of an internal and an external part. The discrete form of the material linear increment $\Delta G^{e,material}$ (cf. eq. (4.12)) is

$$\Delta G^{e,material} = \sum_{I=1}^{n_{node}} \sum_{J=1}^{n_{node}} [\delta \mathbf{d}_I]^T \underbrace{\int_{\mathcal{B}_0^e} [\mathbf{B}_I]^T [\mathbf{C}] [\mathbf{B}_J] dV}_{[\mathbf{k}_{IJ}^{material}]} [\Delta \mathbf{d}_J], \quad (4.26)$$

with the material nodal stiffness matrices $[\mathbf{k}_{IJ}^{material}]$. And by using the relation

$$\begin{aligned} \frac{1}{2} \Delta \delta C_{AB} &= \frac{1}{2} (\delta_{ab} \delta F^a_A \Delta F^b_B + \delta_{ab} \Delta F^a_A \delta F^b_B) \\ &= \frac{1}{2} \left(\sum_{I=1}^{n_{node}} N_{I,A} \delta d_I^a \delta_{ab} \sum_{J=1}^{n_{node}} N_{J,B} \Delta d_J^b + \sum_{I=1}^{n_{node}} N_{I,A} \Delta d_I^a \delta_{ab} \sum_{J=1}^{n_{node}} N_{J,B} \delta d_J^b \right) \\ &= \sum_{I=1}^{n_{node}} \sum_{J=1}^{n_{node}} N_{I,A} \delta d_I^a \delta_{ab} N_{J,B} \Delta d_J^b \end{aligned} \quad (4.27)$$

we obtain the approximation of the geometric linear increment

$$\Delta G^{e,geometric} = \sum_{I=1}^{n_{node}} \sum_{J=1}^{n_{node}} \delta d_I^a \delta_{ab} \underbrace{\int_{\mathcal{B}_0^e} N_{I,A} N_{J,B} S^{AB} dV}_{[\mathbf{k}_{IJ}^{geometric}]} \Delta d_J^b \quad (4.28)$$

with the geometric nodal stiffness matrices $[\mathbf{k}_{IJ}^{geometric}]$. Combining eq. (4.25), eq. (4.26), and eq. (4.28) we obtain the discrete form of the linearized weak form

$$LinG^e = \sum_{I=1}^{n_{node}} [\delta \mathbf{d}_I]^T [\mathbf{r}_I] + \sum_{I=1}^{n_{node}} \sum_{J=1}^{n_{node}} [\delta \mathbf{d}_I]^T [\mathbf{k}_{IJ}] [\Delta \mathbf{d}_J] = 0, \quad (4.29)$$

with the complete nodal stiffness matrices $[\mathbf{k}_{IJ}] = [\mathbf{k}_{IJ}^{material}] + [\mathbf{k}_{IJ}^{geometric}]$. The element vector of the virtual and incremental nodal displacements as well as the residual element vector are given by

$$\begin{aligned} [\delta \mathbf{d}^e] &= [[\delta \mathbf{d}_1]^T, [\delta \mathbf{d}_2]^T, [\delta \mathbf{d}_3]^T, \dots, [\delta \mathbf{d}_{n_{node}}]^T]^T, \\ [\Delta \mathbf{d}^e] &= [[\Delta \mathbf{d}_1]^T, [\Delta \mathbf{d}_2]^T, [\Delta \mathbf{d}_3]^T, \dots, [\Delta \mathbf{d}_{n_{node}}]^T]^T, \quad \text{and} \\ [\mathbf{r}^e] &= [[\mathbf{r}_1]^T, [\mathbf{r}_2]^T, [\mathbf{r}_3]^T, \dots, [\mathbf{r}_{n_{node}}]^T]^T. \end{aligned} \quad (4.30)$$

Analogously, the element stiffness matrix is defined as

$$[\mathbf{k}^e] = \begin{bmatrix} [\mathbf{k}_{11}] & [\mathbf{k}_{12}] & [\mathbf{k}_{13}] & \dots & [\mathbf{k}_{1n}] \\ [\mathbf{k}_{21}] & [\mathbf{k}_{22}] & [\mathbf{k}_{23}] & \dots & [\mathbf{k}_{2n}] \\ [\mathbf{k}_{31}] & [\mathbf{k}_{32}] & [\mathbf{k}_{33}] & \dots & [\mathbf{k}_{3n}] \\ \vdots & \vdots & \vdots & \ddots & \vdots \\ [\mathbf{k}_{n1}] & [\mathbf{k}_{n2}] & [\mathbf{k}_{n3}] & \dots & [\mathbf{k}_{nn}] \end{bmatrix} \quad \text{with } n = n_{node}. \quad (4.31)$$

The global element stiffness matrix $[\mathbf{K}]$, the global virtual and incremental displacements ($[\delta \mathbf{D}]$ and $[\Delta \mathbf{D}]$) as well as the global residual vector $[\mathbf{R}]$ can be obtained by an assembling procedure over all n_{elem} finite elements of the domain

$$[\mathbf{K}] = \mathbf{A}_{e=1}^{n_{elem}} [\mathbf{k}^e], \quad [\delta \mathbf{D}] = \mathbf{A}_{e=1}^{n_{elem}} [\delta \mathbf{d}^e], \quad [\Delta \mathbf{D}] = \mathbf{A}_{e=1}^{n_{elem}} [\Delta \mathbf{d}^e], \quad [\mathbf{R}] = \mathbf{A}_{e=1}^{n_{elem}} [\mathbf{r}^e]. \quad (4.32)$$

The overall discrete form of 4.29 leads to the system of equations

$$[\delta \mathbf{D}]^T \{[\mathbf{K}][\Delta \mathbf{D}] + [\mathbf{R}]\} = 0 \quad \Rightarrow \quad [\Delta \mathbf{D}] = -[\mathbf{K}]^{-1}[\mathbf{R}], \quad (4.33)$$

solved by the Newton-Raphson iteration method as mentioned before. Therefore, the global nodal displacement vector is updated by $\mathbf{D} \leftarrow \mathbf{D} + \Delta \mathbf{D}$ after each iteration until the norm of the residual vector $\|\mathbf{R}\|$ is lower than a given tolerance value.

In order to compute the integrals appearing in eq. (4.33) we make use of the Gauss quadrature and compute the volume integrals of a function $f(\mathbf{x})$ by

$$\int_{\mathcal{B}_e^e} f(\mathbf{X}) dV = \int_{\Omega^e} f(\boldsymbol{\xi}) \det \mathbf{J} d\Omega \approx \sum_{gp=1}^{n_{gp}} f(\boldsymbol{\xi}_{gp}) \det \mathbf{J} \omega_{gp} \quad (4.34)$$

considering a number of n_{gp} Gauß points per element, which are characterized by their location $\boldsymbol{\xi}_{gp}$ and their weighting factor ω_{gp} .

For specific finite elements used in the following the parameterized space Ω_e , the interpolation functions N_I and the Gauß points with corresponding weights are listed in Table 4.1.

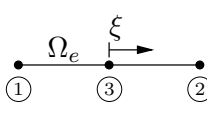
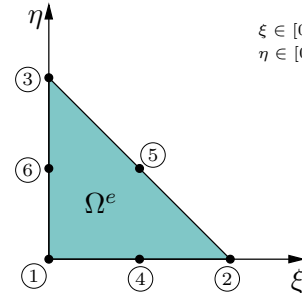
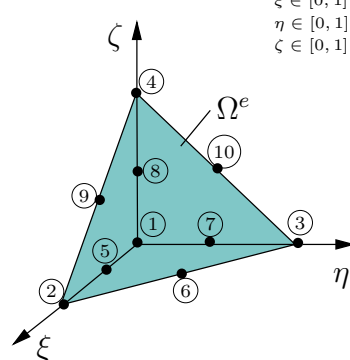
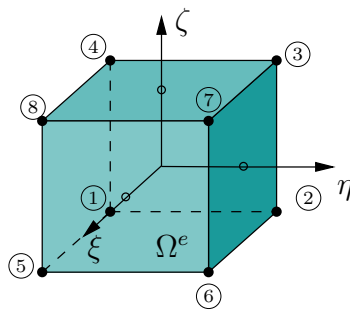
Parameterized space Ω_e	Interpolation functions	Gauß points and weights
 <p>$\xi \in [-1, 1]$</p>	$N^1 = \frac{1}{2}\xi(\xi - 1)$ $N^2 = \frac{1}{2}\xi(\xi + 1)$ $N^3 = 1 - \xi^2$	$\xi_{gp}^1 = -\sqrt{\frac{3}{5}}, \quad \omega_{gp}^1 = \frac{5}{9}$ $\xi_{gp}^2 = 0, \quad \omega_{gp}^2 = \frac{8}{9}$ $\xi_{gp}^3 = \sqrt{\frac{3}{5}}, \quad \omega_{gp}^3 = \frac{5}{9}$
 <p>$\xi \in [0, 1]$ $\eta \in [0, 1]$</p>	$N^1 = \lambda(2\lambda - 1)$ $N^2 = \xi(2\xi - 1)$ $N^3 = \eta(2\eta - 1)$ $N^4 = 4\xi\lambda$ $N^5 = 4\xi\eta$ $N^6 = 4\eta\lambda \quad (\lambda = 1 - \xi - \eta)$	$\xi_{gp}^1 = \left(\frac{1}{6}, \frac{1}{6}\right), \quad \omega_{gp}^1 = \frac{1}{6}$ $\xi_{gp}^2 = \left(\frac{2}{3}, \frac{1}{6}\right), \quad \omega_{gp}^2 = \frac{1}{6}$ $\xi_{gp}^3 = \left(\frac{1}{6}, \frac{2}{3}\right), \quad \omega_{gp}^3 = \frac{1}{6}$
 <p>$\xi \in [0, 1]$ $\eta \in [0, 1]$ $\zeta \in [0, 1]$</p>	$N^1 = \lambda(2\lambda - 1)$ $N^2 = \xi(2\xi - 1)$ $N^3 = \eta(2\eta - 1)$ $N^4 = \zeta(2\zeta - 1)$ $N^5 = 4\xi\lambda, \quad N^6 = 4\xi\eta$ $N^7 = 4\eta\lambda, \quad N^8 = 4\zeta\lambda$ $N^9 = 4\xi\zeta, \quad N^{10} = 4\eta\zeta$ $(\lambda = 1 - \xi - \eta - \zeta)$	$\xi_{gp}^1 = (\alpha, \alpha, \alpha), \quad \omega_{gp}^1 = \frac{1}{24}$ $\xi_{gp}^2 = (\beta, \alpha, \alpha), \quad \omega_{gp}^2 = \frac{1}{24}$ $\xi_{gp}^3 = (\alpha, \beta, \alpha), \quad \omega_{gp}^3 = \frac{1}{24}$ $\xi_{gp}^4 = (\alpha, \alpha, \beta), \quad \omega_{gp}^4 = \frac{1}{24}$ <p>$(\alpha = (5 + 3\sqrt{5})/20 = 0.5854,$ $\beta = (5 - \sqrt{5})/20 = 0.1382)$</p>
 <p>$\xi \in [-1, 1]$ $\eta \in [-1, 1]$ $\zeta \in [-1, 1]$</p>	$N^1 = \frac{1}{8}(1 - \xi)(1 - \eta)(1 - \zeta)$ $N^2 = \frac{1}{8}(1 + \xi)(1 - \eta)(1 - \zeta)$ $N^3 = \frac{1}{8}(1 + \xi)(1 + \eta)(1 - \zeta)$ $N^4 = \frac{1}{8}(1 - \xi)(1 + \eta)(1 - \zeta)$ $N^5 = \frac{1}{8}(1 - \xi)(1 - \eta)(1 + \zeta)$ $N^6 = \frac{1}{8}(1 + \xi)(1 - \eta)(1 + \zeta)$ $N^7 = \frac{1}{8}(1 + \xi)(1 + \eta)(1 + \zeta)$ $N^8 = \frac{1}{8}(1 - \xi)(1 + \eta)(1 + \zeta)$	$\xi_{gp}^1 = \left(\frac{-1}{\sqrt{3}}, \frac{-1}{\sqrt{3}}, \frac{-1}{\sqrt{3}}\right), \quad \omega_{gp}^1 = 1$ $\xi_{gp}^2 = \left(\frac{-1}{\sqrt{3}}, \frac{1}{\sqrt{3}}, \frac{-1}{\sqrt{3}}\right), \quad \omega_{gp}^2 = 1$ $\xi_{gp}^3 = \left(\frac{-1}{\sqrt{3}}, \frac{1}{\sqrt{3}}, \frac{1}{\sqrt{3}}\right), \quad \omega_{gp}^3 = 1$ $\xi_{gp}^4 = \left(\frac{-1}{\sqrt{3}}, \frac{-1}{\sqrt{3}}, \frac{1}{\sqrt{3}}\right), \quad \omega_{gp}^4 = 1$ $\xi_{gp}^5 = \left(\frac{1}{\sqrt{3}}, \frac{-1}{\sqrt{3}}, \frac{-1}{\sqrt{3}}\right), \quad \omega_{gp}^5 = 1$ $\xi_{gp}^6 = \left(\frac{1}{\sqrt{3}}, \frac{1}{\sqrt{3}}, \frac{-1}{\sqrt{3}}\right), \quad \omega_{gp}^6 = 1$ $\xi_{gp}^7 = \left(\frac{1}{\sqrt{3}}, \frac{1}{\sqrt{3}}, \frac{1}{\sqrt{3}}\right), \quad \omega_{gp}^7 = 1$ $\xi_{gp}^8 = \left(\frac{1}{\sqrt{3}}, \frac{-1}{\sqrt{3}}, \frac{1}{\sqrt{3}}\right), \quad \omega_{gp}^8 = 1$

Table 4.1: Finite element subspaces, interpolation functions, and Gauß integration.

In order to apply a load in form of a hydrostatic pressure p on the surface of a two-dimensional or three-dimensional element, respectively, a corresponding one-dimensional or two-dimensional element (see the first two rows in Table 4.1) is needed. Thus, the first part of the external virtual work eq. (4.6) changes by replacing $\bar{\mathbf{t}} = p\mathbf{n}$

$$G_{pressure}^{ext} = \int_{\partial\mathcal{B}_{0\sigma}} \bar{\mathbf{t}} \cdot \delta\mathbf{u} \, dA = \int_{\partial\mathcal{B}_{0\sigma}} p\mathbf{n} \cdot \delta\mathbf{u} \, dA \quad (4.35)$$

and we obtain the discretized form with

$$G_{pressure}^{e,ext} = \sum_{I=1}^{n_{node}} [\delta\mathbf{d}_I]^T \int_{\partial\mathcal{B}_{0\sigma}} N_I p [\mathbf{n}] \, dA . \quad (4.36)$$

Since the direction of hydrostatic pressure p changes with time, it is not a conservative load, thus $\Delta G^{ext} \neq 0$. For a detailed description of the linearization the reader is referred to Zienkiewicz and Taylor [1989] and Bathe [1996].

5 Material modeling of soft biological tissues

Arteries mainly consist of matrix a material (the ground substance) that is reinforced by two families of collagen fibers. Furthermore, they are composed of (thick-walled) layers: the intima, the media and the adventitia, see Section 2.1. As mentioned in Section 2.3 the intima is often neglected in continuum mechanical analyses due to its little mechanical influence. The distinct layers, media and adventitia, have a qualitatively similar mechanical response and therefore they are modeled with the same type of strain-energy function

$$\psi(\mathbf{C}, \mathbf{M}_{(1)}, \mathbf{M}_{(2)}) = \psi^{\text{vol}}(\det \mathbf{C}) + \psi^{\text{iso}}(\mathbf{C}) + \sum_{a=1}^2 \psi_{(a)}^{\text{ti}}(\mathbf{C}, \mathbf{M}_{(a)}) . \quad (5.1)$$

The isotropic part ψ^{iso} describes the matrix-material and the superimposed transversely isotropic energies $\psi_{(1)}^{\text{ti}}$ and $\psi_{(2)}^{\text{ti}}$ represent one fiber family in the fiber directions $\mathbf{A}_{(1)}$ and $\mathbf{A}_{(2)}$, respectively. Following eq. (3.92) with $\partial_{\mathbf{C}} \psi^{\text{vol}} = \partial_{I_3} \psi^{\text{vol}} \text{Cof} \mathbf{C}$ the general constitutive equation for the second Piola-Kirchhoff stress tensor is given by

$$\mathbf{S} = \mathbf{S}^{\text{vol}} + \mathbf{S}^{\text{iso}} + \sum_{a=1}^2 \mathbf{S}_{(a)}^{\text{ti}} \quad \text{with} \quad \mathbf{S}^{\text{vol}} = 2 \frac{\partial \psi^{\text{vol}}}{\partial I_3} \text{Cof} \mathbf{C} , \quad (5.2)$$

with \mathbf{S}^{iso} from eq. (3.94) and \mathbf{S}^{ti} from eq. (3.105). The function ψ^{vol} is a penalty function controlling the volumetric behavior and should become large for violations of the incompressibility constraint $J = 1$. The notion of incompressibility and the corresponding treatment within the continuum mechanical framework will be discussed in detail in Section 5.2. For the description of the strain energies in eq. (5.1) polyconvex functions are used and discussed in the next section.

5.1 Polyconvex energy functions

In the last decades, the material behavior of collagenous soft tissues has been described by use of numerous different material models. In this context, two-dimensional models have been proposed by Vaishnav et al. [1973] and Fung et al. [1979]. An extension to a three-dimensional model is given in Chuong and Fung [1983]. Weiss et al. [1996] were among the first who applied the use of a structural tensor and the representation theorems for anisotropic tensor functions to models for collagenous soft. Throughout this work we use polyconvex energy functions in order to describe the material behavior of soft biological tissues. Such kind of energy functions satisfy the Legendre-Hadamard condition, which is a physically reasonable requirement since the condition ensures real wave speeds and material stability. A proof can be done by investigation of the acoustic tensor, which has to be positive definite (i.e. all main minors have to be greater than zero). For more details about polyconvexity the reader is referred to Ball [1976, 1977], Marsden and Hughes [1983], and Ciarlet [1988]. Further information, especially with respect to the proof of polyconvexity of special energy functions and the derivation of polyconvex energy functions for transverse isotropy and orthotropy see e.g. Hartmann and Neff [2003], Schröder and Neff [2003], Schröder et al. [2005b], and Balzani [2006]. A first polyconvex model for the description of the exponential stiffening behavior of soft biological tissues has been proposed by Holzapfel et al. [2000a]. Further polyconvex models, which are able

to describe collagenous soft tissues, are for example proposed in Itskov and Aksel [2004], Balzani [2006], and Ehret and Itskov [2007].

5.1.1 Isotropic polyconvex energy functions

There exist a variety of well-known isotropic polyconvex functions, see e.g. Steigmann [2003], Hartmann and Neff [2003], Schröder and Neff [2003], and Mielke [2005]. In this section only those functions, which are considered in this work, are listed.

The compressible Mooney-Rivlin model, which is polyconvex and coercive, is given by

$$\psi_{\text{MR}}^{\text{iso}} = \eta_1 I_1 + \eta_2 I_2 + \eta_3 I_3 - \delta \ln \sqrt{I_3}, \quad \forall \quad \eta_1, \eta_2, \eta_3, \delta \geq 0. \quad (5.3)$$

Evaluation of the condition of a stress-free reference configuration yields a condition for the parameter δ , i.e.

$$\mathbf{S}(\mathbf{C} = \mathbf{1}) = 2 \left[(\eta_1 + 3\eta_2 - \eta_2 + \eta_3 - \frac{1}{2}\delta) \mathbf{1} \right] = \mathbf{0} \quad \rightarrow \quad \delta = 2\eta_1 + 4\eta_2 + 2\eta_3. \quad (5.4)$$

The isochoric neo-Hookean material model has the form

$$\psi_{\text{NH}}^{\text{iso}} = c_1 \left(\frac{I_1}{I_3^{1/3}} - 3 \right), \quad \forall \quad c_1 > 0. \quad (5.5)$$

Here, c_1 is a stress-like material parameter. This function has often been used for the description of the matrix material in soft biological tissues, for example, in Holzapfel et al. [2000a, 2004a]. In Gundiah et al. [2007] suitable strain energies are investigated for the description of arterial elastin, which is the main constituent of the ground-matrix, and they found out that the (classical) neo-Hookean model is a satisfactory descriptor. Further information about the modeling of the mechanical response of elastin for arterial tissue is given in Watton et al. [2009].

A penalty term $\psi_{\text{P}}^{\text{vol}}$ can be used in order to satisfy the incompressibility constraint,

$$\psi_{\text{P}}^{\text{vol}} = \varepsilon_1 (I_3^{\varepsilon_2} + I_3^{-\varepsilon_2} - 2), \quad \forall \quad \varepsilon_1 > 0, \varepsilon_2 \geq 1, \quad (5.6)$$

see Schröder and Neff [2003] and Hartmann and Neff [2003] for the proof of polyconvexity.

It should be noticed, that eq. (5.5) and eq. (5.6) fulfill a priori the requirement of a stress-free reference configuration.

5.1.2 Transversely isotropic polyconvex energy functions

For the description of transversely isotropic materials the possible polynomial basis $\mathcal{P}_{ti} := \{I_1, I_2, I_3, J_4^{(a)}, J_5^{(a)}\}$, was derived in Section 3.6.2, cf. eq. (3.102). Nevertheless, Merodio and Neff [2006] showed that the fifth invariant $J_5^{(a)}$ is not polyconvex. In Schröder and Neff [2003] an alternative polyconvex invariant function is given by

$$K_1^{(a)} := \text{tr}[\text{Cof} \mathbf{C} \mathbf{M}_{(a)}] = J_5^{(a)} - I_1 J_4^{(a)} + I_2, \quad (5.7)$$

which is geometrically motivated. Introducing an alternative structural tensor

$$\mathbf{D} = \mathbf{1} - \mathbf{M}_{(a)}, \quad \text{with} \quad \text{tr} \mathbf{D} = 2 \quad (5.8)$$

yields further alternative polyconvex invariant functions

$$K_2^{(a)} = \text{tr}[\mathbf{C} \mathbf{D}] = I_1 - J_4^{(a)} \quad \text{and} \quad K_3^{(a)} = \text{tr}[\text{Cof} \mathbf{C} \mathbf{D}] = I_1 J_4^{(a)} - J_5^{(a)}. \quad (5.9)$$

Now, the alternative polynomial basis used in this work is given by

$$\mathcal{P}_{\text{ti}} := \{I_1, I_2, I_3, J_4^{(a)}, K_i^{(a)}\} \quad \text{with} \quad i = 1, 2, 3. \quad (5.10)$$

In order to describe the material behavior of soft biological tissues in the physiological loading domain, principles for the construction of anisotropic polyconvex energies, which automatically fulfill the condition of a stress-free reference configuration, are derived in Balzani et al. [2006a] and Balzani [2006]. They are briefly repeated in the following. The first construction principle is given by:

Construction Principle 1: *Find a polyconvex function $P(X)$ which is zero in the reference configuration and include this function into any arbitrary convex and monotonically increasing function m , whose first derivative with respect to P vanishes in the origin; then the polyconvex function satisfying the stress-free reference configuration is given by $\psi = m(P(X))$,*

cf. Schröder and Neff [2003], Lemma B.9. As an example, such convex and monotonically increasing functions m are given by

$$m_1 := P^k \quad \text{and} \quad m_2 := \cosh(P) - 1, \quad \forall P > 0 \quad \text{and} \quad k > 1. \quad (5.11)$$

This leads to the following case distinction for the polyconvex energy function

$$\psi = \begin{cases} m_i & \text{for } P > 0 \\ 0 & \text{for } P \leq 0 \end{cases} \quad \text{with } i = 1, 2. \quad (5.12)$$

Additionally, if k is chosen to be greater than 2, the tangent modulus is continuous, see Balzani [2006]. The (internal) polyconvex functions P have to be zero in the reference configuration (i.e. $P(\mathbf{C} = \mathbf{1}) = 0$) and are given by, e.g.

$$P_1 := J_4^{(a)} - 1, \quad P_2 := K_1^{(a)} - 1, \quad P_3 := K_2^{(a)} - 1, \quad P_4 := K_3^{(a)} - 2. \quad (5.13)$$

It should be noticed, that these functions satisfy the energy-free reference configuration due to the fact that $\psi = m_i(P = 0) = 0$ in the natural state.

Additional polyconvex functions, which fulfill the natural-state condition, are given following the second construction principle:

Construction Principle 2: *Include any function $m(P(X))$, obtained by applying Construction Principle 1, into the exponential function $g(m) = \exp(m)$,*

cf. Balzani et al. [2006a]. With P defined above we find a number of further functions

$$\psi = \begin{cases} \exp(m_i(P)) & \text{for } P > 0 \\ 0 & \text{for } P \leq 0 \end{cases} \quad \text{with } i = 1, 2. \quad (5.14)$$

In this work we make use of functions which fit into these principles.

In Holzapfel et al. [2000a] a material model was provided that is able to reflect the strong stiffening effect of soft biological tissues at higher loadings due to its exponential character

$$\psi_{(a)}^{\text{ti,HGO}_1} = \frac{k_1}{2k_2} \left\{ \exp \left(k_2 \left\langle J_4^{(a)} - 1 \right\rangle^2 \right) - 1 \right\}, \quad \forall \quad k_1 > 0, k_2 > 0. \quad (5.15)$$

The parentheses $\langle(\bullet)\rangle$ denote the Macaulay brackets⁷ filtering out positive values. This seems to be reasonable since shortening of the fibers is assumed to generate no stress. The reason for that is the wavy structure of the collagen fibers, which buckle under compressive load and thus are not able to support any compression. Therefore, the anisotropic term is only activated in case of fiber-extension. The assumption that the collagen fibers are almost entirely responsible for the resistance to stretch in the high loading domain, see Roach and Burton [1957], can be obtained by a convenient choice of the parameter k_1 (dimension of stress) and the dimensionless parameter k_2 . The proof of convexity of eq. (5.15) is given in Schröder et al. [2005b].

Introducing the isochoric part of $J_4^{(a)}$ into eq. (5.15) yields a further polyconvex function

$$\psi_{(a)}^{\text{ti,HGO}_2} = \frac{k_1}{2k_2} \left\{ \exp \left(k_2 \left\langle J_4^{(a)} I_3^{-1/3} - 1 \right\rangle^2 \right) - 1 \right\}, \quad \forall \quad k_1 > 0, k_2 > 0. \quad (5.16)$$

5.2 Incompressibility constraint

In soft biological tissues often incompressible or nearly incompressible material behavior can be observed. In material modeling the incompressibility constraint can be enforced by different methods. Among others, there are two methods to be mentioned: the Penalty-Method, which is discussed in Section 5.2.2, and the Augmented-Lagrange-Method described in Section 5.2.3. These methods are often based on a multiplicative split of the deformation gradient in a volumetric and a unimodular part, see Section 5.2.1. In this work both methods are considered. For a numerical comparison of the two see Chapter 8.

5.2.1 Kinematic split of the deformation gradient

According to Flory [1961] the multiplicative split of the deformation gradient \mathbf{F} into a purely deviatoric part $\tilde{\mathbf{F}}$ and a volumetric part \mathbf{F}^{vol} , can be formulated as

$$\mathbf{F} = \mathbf{F}^{\text{vol}} \tilde{\mathbf{F}} = \tilde{\mathbf{F}} \mathbf{F}^{\text{vol}} \quad \text{with} \quad \mathbf{F}^{\text{vol}} = J^{1/3} \mathbf{1} \quad \text{and} \quad \tilde{\mathbf{F}} = J^{-1/3} \mathbf{F}, \quad (5.17)$$

and the Jacobian determinant, see eq. (3.18). From eq. (5.17) it follows that the Jacobian determinant J is the determinant of the volumetric deformation gradient and the determinant of the deviatoric term is equal to 1, i.e.

$$\det \mathbf{F}^{\text{vol}} = (J^{1/3})^3 = J \quad \text{and} \quad \det \tilde{\mathbf{F}} = (J^{-1/3})^3 \det \mathbf{F} = 1. \quad (5.18)$$

This approach has the disadvantage of the incompressibility-locking phenomenon. The reason for that is, that the deformation gradient is a function of the position and thus the condition for incompressibility $J = \det \mathbf{F} = 1$ must be fulfilled in each point, see Simo [1998], section 45.

⁷The Macaulay brackets are defined by $\langle(\bullet)\rangle = (|(\bullet)| + (\bullet))/2$, with $(\bullet) \in \mathbf{R}$. The result differs from zero only for positive values (\bullet) .

Modified deformation gradient $\bar{\mathbf{F}}$. In order to avoid incompressibility-locking the deformation gradient \mathbf{F} is replaced by a modified deformation gradient $\bar{\mathbf{F}}$, according to the approach of Simo et al. [1985], see also Simo and Taylor [1991], Weiss et al. [1996] and section 45 in Simo [1998]. Therefore, the determinant of the deformation gradient $\det \mathbf{F} = J$ is replaced by a volume dilation Θ , which is constant over the element. Thus, the modified deformation gradient arises as

$$\bar{\mathbf{F}} = \Theta^{1/3} \tilde{\mathbf{F}} \quad \text{with} \quad \det \bar{\mathbf{F}} = \Theta \quad \rightarrow \quad \bar{\mathbf{F}} = \left(\frac{\Theta}{J} \right)^{1/3} \mathbf{F} \quad (5.19)$$

i.e. the dilational part Θ is an independent field. Then, the associated modified right Cauchy-Green tensor is

$$\bar{\mathbf{C}} = \bar{\mathbf{F}}^T \bar{\mathbf{F}} = \Theta^{2/3} \tilde{\mathbf{C}} = \left(\frac{\Theta}{J} \right)^{2/3} \mathbf{C} \quad (5.20)$$

and the stored-energy function is now splitted into one part depending on $\bar{I}_1 = \text{tr} \bar{\mathbf{C}}$, one part depending on $\bar{I}_2 = \text{tr}[\text{Cof} \bar{\mathbf{C}}]$ and one part depending on $\bar{I}_3 = \det \bar{\mathbf{C}}$, i.e.

$$\begin{aligned} \bar{I}_1 &= \text{tr} \bar{\mathbf{C}} = \Theta^{2/3} \text{tr} \tilde{\mathbf{C}} = \left(\frac{\Theta}{J} \right)^{2/3} \text{tr} \mathbf{C} = \Theta^{2/3} \frac{I_1}{I_3^{1/3}}, \\ \bar{I}_2 &= \text{tr}[\text{Cof} \bar{\mathbf{C}}] = \Theta^{4/3} \frac{1}{2} \left[(\text{tr} \tilde{\mathbf{C}})^2 - \text{tr} \tilde{\mathbf{C}}^2 \right] = \left(\frac{\Theta}{J} \right)^{4/3} \text{tr}[\text{Cof} \mathbf{C}] = \Theta^{4/3} \frac{I_2}{I_3^{2/3}}, \\ \bar{I}_3 &= \det \bar{\mathbf{C}} = \Theta^2 \det \tilde{\mathbf{C}} = \left(\frac{\Theta}{J} \right)^2 \det \mathbf{C} = \Theta^2. \end{aligned} \quad (5.21)$$

The stored-energy function can also be decoupled into a deviatoric and a volumetric part

$$\bar{\psi}(\bar{\mathbf{C}}) = \psi_1(\text{tr} \bar{\mathbf{C}}) + \psi_2(\text{tr}[\text{Cof} \bar{\mathbf{C}}]) + \psi_3(\det \bar{\mathbf{C}}) = \psi^{\text{dev}}(\tilde{\mathbf{C}}) + \psi^{\text{vol}}(\Theta). \quad (5.22)$$

Three-field functional. Since the dilation Θ is an independent field and since the condition $J = \Theta$ will be enforced by a Lagrange multiplier p , the underlying three-field Hu-Washizu functional Π can be given as

$$\Pi(\boldsymbol{\varphi}, \Theta, p) = \int_{\mathcal{B}_0} \left(\psi^{\text{dev}}(\tilde{\mathbf{C}}(\boldsymbol{\varphi})) + \psi^{\text{vol}}(\Theta) + p(J(\boldsymbol{\varphi}) - \Theta) \right) dV + \Pi_{\text{ext}}(\boldsymbol{\varphi}), \quad (5.23)$$

with the potential energy of the external loading $\Pi^{\text{ext}} = G^{\text{ext}}$, see eq. (4.6). The variation of eq. (5.23) with respect to the independent field variables $\boldsymbol{\varphi}, p$ and Θ yields the three Euler-Lagrange equations

$$\begin{aligned} \partial_{\boldsymbol{\varphi}} \Pi \cdot \delta \boldsymbol{\varphi} &= \int_{\mathcal{B}_0} \frac{1}{2} \delta \mathbf{C} : \left[2 \frac{\partial \psi^{\text{dev}}}{\partial \tilde{\mathbf{C}}} : \frac{\partial \tilde{\mathbf{C}}}{\partial \mathbf{C}} + p J \mathbf{C}^{-1} \right] dV = 0, \\ \partial_p \Pi \delta p &= \int_{\mathcal{B}_0} \delta p (J - \Theta) dV = 0, \\ \partial_{\Theta} \Pi \delta \Theta &= \int_{\mathcal{B}_0} \delta \Theta \left[\frac{\partial \psi^{\text{vol}}}{\partial \Theta} - p \right] dV = 0. \end{aligned} \quad (5.24)$$

The variation with respect to p yields the condition $J = \Theta$, the variation with respect to Θ yields the constitutive equation for the pressure p , i.e. $p = \partial_{\Theta}\psi^{\text{vol}}$, and the variation with respect to $\boldsymbol{\varphi}$ yields the balance equation. By association the second Piola-Kirchhoff stresses \boldsymbol{S} , decoupled into a purely pressure-related and a purely deviatoric part, are

$$\boldsymbol{S} = p J \boldsymbol{C}^{-1} + 2 \frac{\partial \psi^{\text{dev}}}{\partial \tilde{\boldsymbol{C}}} : \frac{\partial \tilde{\boldsymbol{C}}}{\partial \boldsymbol{C}} \quad \text{with} \quad 2 \partial_{\boldsymbol{C}} \psi^{\text{dev}} = 2 J^{-2/3} \text{DEV} \left[\partial_{\tilde{\boldsymbol{C}}} \psi^{\text{dev}}(\tilde{\boldsymbol{C}}) \right], \quad (5.25)$$

with the definition $\text{DEV}[\bullet] = [\bullet] - \frac{1}{3}([\bullet] : \boldsymbol{C}) \boldsymbol{C}^{-1}$. Now the displacement field is assumed to be continuous over the discretized domain, whereas Θ and p are only continuous in each element. The independent variables Θ and p can be condensed on element level and we get a hybrid formulation, see Simo and Taylor [1991]. Furthermore, if the dilation Θ and the pressure p are assumed to be constant over the element we obtain a P0-formulation. The dilation can then be computed as volume average by

$$\Theta = \bar{\Theta} = \frac{1}{V} \int_V J dV = \frac{V}{V_0} \quad \text{and} \quad p = \bar{p} = \frac{1}{V} \int_V \partial_{\Theta} \psi^{\text{vol}} dV = \partial_{\Theta} \psi^{\text{vol}}(\bar{\Theta}). \quad (5.26)$$

Note, that the above P0-formulation gives the same response as the $\bar{\boldsymbol{F}}$ -approach of Nagtegaal et al. [1974]. For an extended approach using a five-field formulation see the recently published work Schröder et al. [2011]. A well written overview on the above mentioned methods is given, for example, in Freischläger [2000].

5.2.2 Penalty-Method

In order to enforce the incompressibility constraint often the Penalty-Method is taken into account, see e.g. Simo and Taylor [1982]. Incorporation of a penalty function $\psi^{\text{vol}}(\Theta) = \kappa_{\epsilon} \Gamma(\Theta)$ in the functional eq. (5.23) yields

$$\Pi(\boldsymbol{\varphi}, \Theta, p) = \int_{\mathcal{B}_0} [\psi^{\text{dev}} + \kappa_{\epsilon} \Gamma(\Theta) + p(J - \Theta)] dV + \Pi^{\text{ext}}(\boldsymbol{\varphi}). \quad (5.27)$$

The function $\Gamma(\Theta)$ obeys the following conditions:

$$\begin{cases} \Gamma : \mathbb{R}_+ \rightarrow \mathbb{R} \text{ convex} , \\ \Gamma(\Theta) \geq 0 \quad \forall \Theta \in \mathbb{R}_+ , \\ \Gamma(\Theta) = 0 \quad \text{iff } \Theta = 1 . \end{cases} \quad (5.28)$$

Following eq. (5.24)₃ the Lagrange multiplier p appear as

$$p := \kappa_{\epsilon} \Gamma'(\Theta), \quad (5.29)$$

and by association, if there exist another volumetric term ψ^* in addition to the penalty term such that $\psi^{\text{vol}}(\Theta) = \psi^*(\Theta) + \kappa_{\epsilon} \Gamma(\Theta)$, the Lagrange multiplier appears as

$$p := \kappa_{\epsilon} \Gamma'(\Theta) + \partial_{\Theta} \psi^*. \quad (5.30)$$

The penalty parameter κ_{ϵ} , which has to be greater than 0, has no physical relevance. It should be noticed, that the incompressibility constraint will be fulfilled exactly, i.e. Θ converges to one, only if κ_{ϵ} converges to infinity. Using high penalty parameters may lead to an ill-conditioning of the global stiffness matrix.

5.2.3 Augmented-Lagrange-Method

Using the penalty approach mentioned in the previous section the penalty parameter may become relatively large to enforce incompressibility. Therefore, the functional in eq. (5.27) is augmented by an additional term, which furthermore enforces incompressibility, in order to prevent ill-conditioning of the global stiffness matrix. In the context of the augmented Lagrangian solution strategy we refer to Hestenes [1969], Powell [1969], Fortin and Fortin [1985], Glowinski and Le Tallec [1984, 1988, 1989], and Simo and Taylor [1991]. The augmentation is performed only on the dilational part Θ and thus the augmented Lagrangian functional with the Lagrange multiplier λ follows as

$$\mathcal{L}(\boldsymbol{\varphi}, \Theta, p, \lambda) := \Pi(\boldsymbol{\varphi}, \Theta, p) + \int_{\mathcal{B}_0} \lambda h(\Theta) dV . \quad (5.31)$$

Now the pressure p can be computed by $p := \kappa_\epsilon \Gamma'(\Theta) + \lambda h'(\Theta)$. The function $h(\Theta)$ has to be a continuously differentiable function with the conditions

$$\begin{cases} h : \mathbb{R}_+ \rightarrow \mathbb{R} , \\ h(\Theta) = 0 \quad \text{iff } \Theta = 1 . \end{cases} \quad (5.32)$$

In this work, the function $h(\Theta) = \Theta - 1$ is used. For the update of the Lagrange multiplier

$$\lambda_{n+1} = \lambda_n + \kappa_{\text{al}} h(\Theta_n), \quad (5.33)$$

two different algorithms are used, which are both presented in Simo and Taylor [1991]: i) the Uzawa algorithm, for which the algorithm is given in Table 5.1, and ii) a simultaneous algorithm., see the algorithm in Table 5.2. Here, κ_{al} is a parameter associated to the Augmented-Lagrange-Method, which has to be chosen in a reasonable manner, and TOL is a tolerance value, which quantifies the maximum deviation of Θ from unity.

<p>Given $\boldsymbol{\varphi}$ and λ from last time step</p> <p>LOOP n, while $h(\Theta_n) > \text{TOL}$</p> <p style="padding-left: 20px;">LOOP i, while $\delta\Pi(\boldsymbol{\varphi}_n^i, \Theta_n^i, p_n^i, \lambda_n) \neq 0$</p> <p style="padding-left: 40px;">Compute Θ_n^i</p> <p style="padding-left: 40px;">Compute $p_n^i = \lambda_n h'(\Theta_n^i) + \kappa_\epsilon \Gamma'(\Theta_n^i)$</p> <p style="padding-left: 20px;">END LOOP</p> <p style="padding-left: 20px;">Compute $\lambda_{n+1} = \lambda_n + \kappa_{\text{al}} h(\Theta_n)$</p> <p>END LOOP</p>

Table 5.1: Algorithmic implementation of the nested iteration (Uzawa algorithm) for a typical time step with $\Delta t = {}^{k+1}t - {}^k t$, cf. Simo and Taylor [1991]. At the beginning of the simulation λ is initialized to zero.

In the Uzawa algorithm the iteration of λ is nested within the Newton iteration. Here, for each value of λ , a nonlinear system is solved using Newton's method.

```

Given  $\varphi$  and  $\lambda$  from last time step
LOOP  $i$ , while  $|h(\Theta^i)| > \text{TOL}$  and  $\delta\Pi(\varphi^i, \Theta^i, p^i, \lambda^i) \neq 0$ 
  Compute  $\Theta^i$ 
  Compute  $\lambda^i = \lambda^{i-1} + \kappa_{\text{al}} h(\Theta^i)$ 
  Compute  $p^i = \lambda^i h'(\Theta^i) + \kappa_{\epsilon} \Gamma'(\Theta^i)$ 
END LOOP

```

Table 5.2: Algorithmic implementation of the simultaneous iteration for a typical time step with $\Delta t = {}^{k+1}t - {}^k t$, cf. Simo and Taylor [1991]. At the beginning of the simulation λ is initialized to zero.

In the simultaneous Augmented-Lagrange-Method the iteration for the Lagrange multiplier λ is performed simultaneously with the Newton iteration. This can be seen as an inexact Newton method, such that quadratic convergence cannot be expected. In Fig. 5.1 such iteration is shown for a typical time step of the numerical example presented in Section 8.4. As can be seen, the convergence is linear as long as the Lagrange multiplier is iterated simultaneously. Once all elements fulfill the condition $\|h(\Theta^k)\| < \text{TOL}$, quadratic convergence is obtained.

```

Computing solution at time 1.00000000: Total proportional load 24.000000
Residual norm = 0.714490620000    1.000000000000
  number of elements with dabs(h(theta)) .gt. 1.d-3:    322
Residual norm =12.698878000000    17.773331000000
  number of elements with dabs(h(theta)) .gt. 1.d-3:    51
Residual norm = 4.407793800000    6.169141600000
  number of elements with dabs(h(theta)) .gt. 1.d-3:     8
Residual norm = 1.757445700000    2.459718300000
  number of elements with dabs(h(theta)) .gt. 1.d-3:     3
Residual norm = 0.929985650000    1.301606500000
Residual norm = 0.022476203000    0.031457660000
Residual norm = 0.000053131242    0.000074362407
Residual norm = 0.000000025876    0.000000036216

```

Figure 5.1: Simultaneous Augmented-Lagrange iteration for a typical time step of the numerical example presented in Section 8.4.

6 Identification of material parameter

In order to identify suitable material parameters for a numerical simulation of soft biological tissues the constitutive model is adjusted to experimental data. The general approach of the adjustment done in this work is explained in Section 6.1. If no sufficient experimental data is available, for example in case of the plaque components, the material parameters have to be chosen in a suitable way. In Section 6.2 the identification of five different parameter sets for the plaque is shown. In order to analyze the influence of the choice of parameters a subsequent investigation of the influence of the plaque behavior on the overall arterial wall behavior is conducted.

6.1 Adjustment to experimental data

The experimental data used in this work was obtained from uniaxial extension tests of human blood vessels. Here, the test strips were separated in circumferential or axial direction, see the schematic illustration in Fig. 6.1a,b. A detailed description of the dissection into circumferential and axial strips from human iliac arteries and the mechanical testing is given in Holzapfel et al. [2004b].

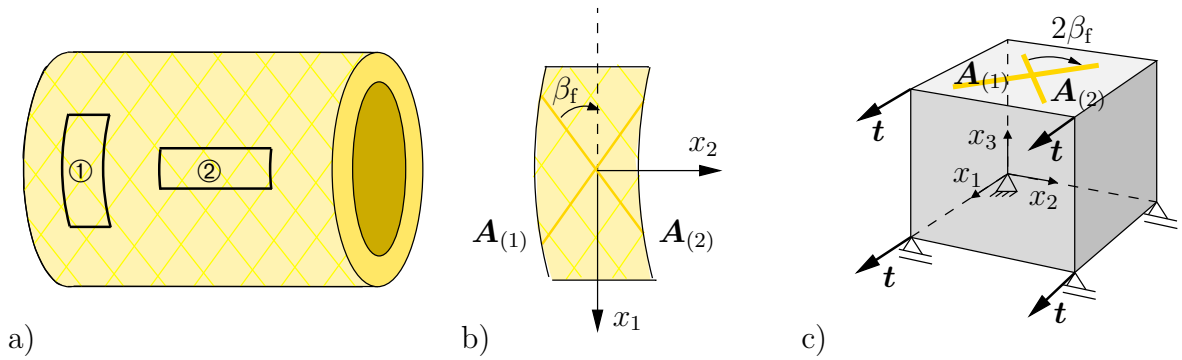


Figure 6.1: Schematic illustration a) of a segment of a human blood vessel with strips in circumferential (①) and axial (②) direction; b) of a strip in circumferential direction with the preferred directions $[\mathbf{A}_{(1)}] = [\cos\beta_f, -\sin\beta_f, 0]^T$ and $[\mathbf{A}_{(2)}] = [\cos\beta_f, \sin\beta_f, 0]^T$ (the fiber angle β_f is defined as the angle between the circumferential and the fiber direction); c) of a uniaxial extension in circumferential direction of the specimen.

The preferred directions indicated in Fig. 6.1b are given as

$$[\mathbf{A}_{(1)}] = [\cos\beta_f, -\sin\beta_f, 0]^T \quad \text{and} \quad [\mathbf{A}_{(2)}] = [\cos\beta_f, \sin\beta_f, 0]^T, \quad (6.1)$$

where the fiber angle β_f is the angle between the circumferential and the fiber direction, which is taken as a phenomenological (fitting) parameter. Let λ_1 be the stretch in the direction of the extension (x_1) and λ_2 the transverse stretch. Then the associated structural tensors appears as

$$[\mathbf{M}_{(1)}] = \begin{bmatrix} c^2 & -cs & 0 \\ -cs & s^2 & 0 \\ 0 & 0 & 0 \end{bmatrix} \quad \text{and} \quad [\mathbf{M}_{(2)}] = \begin{bmatrix} c^2 & cs & 0 \\ cs & s^2 & 0 \\ 0 & 0 & 0 \end{bmatrix}, \quad (6.2)$$

with the abbreviations $c := \cos\beta_f$ and $s := \sin\beta_f$. Since incompressible material is assumed, the deformation gradient \mathbf{F} and the right Cauchy-Green tensor \mathbf{C} are of the form

$$[\mathbf{F}] = \begin{bmatrix} \lambda_1 & 0 & 0 \\ 0 & \lambda_2 & 0 \\ 0 & 0 & \lambda_1^{-1}\lambda_2^{-1} \end{bmatrix} \quad \text{and} \quad [\mathbf{C}] = \begin{bmatrix} \lambda_1^2 & 0 & 0 \\ 0 & \lambda_2^2 & 0 \\ 0 & 0 & \lambda_1^{-2}\lambda_2^{-2} \end{bmatrix}. \quad (6.3)$$

In order to account for incompressibility, the volumetric part in eq. (5.1) is set to $\psi^{\text{vol}} = p(I_3 - 1)$ and thus the corresponding term in eq. (5.2) yields $\mathbf{S}^{\text{vol}} = 2p \text{Cof} \mathbf{C}$, with the pressure-like Lagrange multiplier p . Note, that the considered problem is symmetric and therefore $\psi^{\text{ti}} := \psi_{(1)}^{\text{ti}} = \psi_{(2)}^{\text{ti}}$. Then, evaluation of eq. (5.2) with eq. (3.94), eq. (3.105) and eq. (6.3) yields the S_{22} component of the second Piola-Kirchhoff stress tensor

$$\begin{aligned} S_{22} = & 2 \left\{ \frac{\partial \psi^{\text{iso}}}{\partial I_1} + \frac{\partial \psi^{\text{iso}}}{\partial I_2} (\lambda_1^2 + \lambda_1^{-2}\lambda_2^{-2}) + \left(p + \frac{\partial \psi^{\text{iso}}}{\partial I_3} \right) \lambda_2^{-2} \right. \\ & + 2 \left[\frac{\partial \psi^{\text{ti}}}{\partial I_1} + \frac{\partial \psi^{\text{ti}}}{\partial I_2} (\lambda_1^2 + \lambda_1^{-2}\lambda_2^{-2}) \right. \\ & \left. \left. + \frac{\partial \psi^{\text{ti}}}{\partial I_3} \lambda_2^{-2} + \frac{\partial \psi^{\text{ti}}}{\partial J_4^{(a)}} \sin^2\beta_f + \frac{\partial \psi^{\text{ti}}}{\partial J_5^{(a)}} 2 \lambda_2^2 \sin^2\beta_f \right] \right\}. \end{aligned} \quad (6.4)$$

The requirement $S_{22} = 0$ yields the Lagrange multiplier p and insertion of p into $S_{33} = 0$,

$$\begin{aligned} S_{33} = & 2 \left(\frac{\partial \psi^{\text{iso}}}{\partial I_1} (1 - \lambda_1^2\lambda_2^4) + \frac{\partial \psi^{\text{iso}}}{\partial I_2} (\lambda_1^2 - \lambda_1^4\lambda_2^4) \right. \\ & + 2 \left[\frac{\partial \psi^{\text{ti}}}{\partial I_1} (1 - \lambda_1^2\lambda_2^4) + \frac{\partial \psi^{\text{ti}}}{\partial I_2} (\lambda_1^2 - \lambda_1^4\lambda_2^4) \right. \\ & \left. \left. - \frac{\partial \psi^{\text{ti}}}{\partial J_4^{(a)}} \lambda_1^2\lambda_2^4 \sin^2\beta_f - 2 \frac{\partial \psi^{\text{ti}}}{\partial J_5^{(a)}} \lambda_1^2\lambda_2^6 \sin^2\beta_f \right] \right) = 0, \end{aligned} \quad (6.5)$$

yields a relation between the stretch quantities λ_1 and λ_2 . In general, the analytical solution of eq. (6.5) can not be evaluated and therefore a Newton-scheme is used. Let values with the index $^{j-1}(\bullet)$ be values at the last iteration step and values with the index $^j(\bullet)$ be values at the current iteration step, then the linearization of eq. (6.5) is given by

$$\text{Lin}S_{33} = {}^{j-1}S_{33} + \left. \frac{\partial S_{33}}{\partial \lambda_2} \right|_{j-1\lambda_2} {}^j\Delta\lambda_2 = 0. \quad (6.6)$$

Within each Newton step the increment ${}^j\Delta\lambda_2$ is computed and updated for a series of n_{mp} experimentally measured stretches $\lambda_{1,i}^{\text{exp}}$ with $i = 1, \dots, n_{\text{mp}}$, i.e.

$${}^j\lambda_{2,i} \Leftarrow {}^{j-1}\lambda_{2,i} + {}^j\Delta\lambda_{2,i} \quad \text{until} \quad \| S_{33}|_{j\lambda_2} \| < \epsilon, \quad (6.7)$$

with the tolerance parameter ϵ , which is close to computer accuracy. In each iteration procedure the value of the stretch λ_1 is given by the experimental stretch value, i.e. $\lambda_{1,1} = \lambda_{1,i}^{\text{exp}}$, and the starting value for the stretch λ_2 is defined as

$${}^0\lambda_{2,i} := \sqrt{C_{33}^{-1} \lambda_{1,i}^{-2}}, \quad (6.8)$$

wherein the incompressibility constraint $\det \mathbf{C} = 1$ is taken into account in order to improve the efficiency of the iteration. By dint of the achieved second Piola-Kirchhoff stress S_{11} in the x_1 -direction, the Cauchy stresses are calculated by $\sigma^{\text{comp}} = \lambda_1^2 S_{11}$, which can be compared with experimental data. Therewith, a relative error results in

$$r(\lambda_{1,i}, \boldsymbol{\alpha}) := \frac{|\sigma^{\text{exp}}(\lambda_{1,i}) - \sigma^{\text{comp}}(\lambda_{1,i}, \boldsymbol{\alpha})|}{\max(\sigma^{\text{exp}})}, \quad (6.9)$$

with the maximum value of experimental stresses in the considered extension cycle $\max(\sigma^{\text{exp}}) \neq 0$, which is used as a normalization factor, and a vector $\boldsymbol{\alpha}$, which contains all material parameters involved in the strain-energy function ψ . In Table 6.1 an algorithmic box for the computation of the relative error r is given.

<p>Do for $i = 1, \dots, n_{\text{mp}}$</p> <p>(I) Set $\lambda_{1,i} = \lambda_{1,i}^{\text{exp}}$, initialize $\mathbf{C} = \mathbf{1}$ and set $C_{11} = \lambda_{1,i}^2$ if $i > 1$ then $C_{22} = \tilde{C}_{22}/(\lambda_{1,i}/\lambda_{1,i-1})$ and $C_{33} = \tilde{C}_{33}/(\lambda_{1,i}/\lambda_{1,i-1})$</p> <p>(II) Compute initial value ${}^0\lambda_{2,i} = \sqrt{C_{33}^{-1} \lambda_{1,i}^{-2}}$</p> <p>(III) Do Newton iteration with index j</p> <p style="padding-left: 20px;">(i) Compute ${}^j S_{11} = S_{11} _{j\lambda_{2,i}}$, ${}^j S_{22} = S_{22} _{j\lambda_{2,i}}$, ${}^j S_{33} = S_{33} _{j\lambda_{2,i}}$</p> <p style="padding-left: 20px;">(ii) if $\ {}^j S_{33}\ < \epsilon$, with ϵ close to computer accuracy then $\tilde{\lambda}_{2,i} = {}^j \lambda_{2,i}$ and $\tilde{C}_{22} = \tilde{\lambda}_{2,i}^2$ and $\tilde{C}_{33} = \lambda_{1,i}^{-2} \tilde{\lambda}_{2,i}^{-2}$ and $S_{11} = {}^j S_{11}$ break</p> <p style="padding-left: 20px;">else update ${}^j \lambda_{2,i} \leftarrow {}^{j-1} \lambda_{2,i} + {}^j \Delta \lambda_{2,i}$ and go to (i)</p> <p>(IV) Compute Cauchy stresses $\sigma^{\text{comp}}(\lambda_{1,i}, \boldsymbol{\alpha}) = \lambda_{1,i}^2 S_{11}$</p> <p>(V) Compute relative error $r(\lambda_{1,i}, \boldsymbol{\alpha}) := \frac{ \sigma^{\text{exp}}(\lambda_{1,i}) - \sigma^{\text{comp}}(\lambda_{1,i}, \boldsymbol{\alpha}) }{\max(\sigma^{\text{exp}})}$</p>
--

Table 6.1: Algorithmic box for the computation of the relative error r as a function of the stretch $\lambda_{1,i}$ at each measuring point $i = 1, \dots, n_{\text{mp}}$ and a vector $\boldsymbol{\alpha}$, which contains all material parameters involved in the strain-energy function ψ .

The objective function of the optimization is given by the resulting total error

$$\bar{r}(\boldsymbol{\alpha}) = \sum_{e=1}^{n_e} \sqrt{\frac{1}{n_{\text{mp}}} \sum_{i=1}^{n_{\text{mp}}} \left(\frac{\sigma^{\text{exp}}(\lambda_{1,i}) - \sigma^{\text{comp}}(\lambda_{1,i}, \boldsymbol{\alpha})}{\max(\sigma^{\text{exp}})} \right)^2}, \quad (6.10)$$

for a number of $n_e = 2$ experiments, i.e. extension in circumferential and axial direction. In this work an SQP⁸ algorithm is used for the minimization of eq. (6.10).

⁸**SQP: sequential quadratic programming.** The SQP method is a gradient based method. The three key steps are (i) the update of the Hessian matrix using the BFGS (Broyden-Fletcher-Goldfarb-Shanno) method at each major iteration, (ii) a QP-subproblem is solved using an active-set strategy at each major point, (iii) a line-search algorithm with a merit function is used, where a small function denotes a good agreement of data and the model to be fitted. For a general overview of the SQP method see, for example, Gill et al. [1981], Powell [1983], and Fletcher [1987].

6.2 Material parameters for the plaque components

Arterial plaque appears as soft lipid pools covered by a fibrous cap, see e.g. Davies [1996]. There exist various patient-specific differences in the morphology and the composition of the plaque, as can be exemplarily seen in Fig. 6.2a in the different plaque constitution of eight human stenotic iliac arteries. The four major plaque components of the coronary plaque are fibrous tissue, fibrofatty tissue, necrotic-core tissue and dense calcified tissue. The fibrous tissue mainly consists of bundles of collagen fibers with little or no lipid deposits, while the fibrofatty tissue consists of loosely packed collagen fibers with lipid accumulation. The necrotic-core tissue exhibits a high level of lipid and many necrotic cells, remnants of dead lymphocytes and foam cells. The dense calcium is composed of compact calcium crystals. For the in-vivo examination of the arterial structure VH IVUS (virtual histology intravascular ultrasound) techniques can be used. Many publications deal with the application of this method, see e.g. Nair et al. [2002], König and Klauss [2007], Granada et al. [2007], Nasu et al. [2008], and Garcia-Garcia et al. [2010].

Virtual histology (VH) intravascular ultrasound (IVUS). The IVUS imaging is catheter based and provides a series of gray-scale cross-sectional images, see Fig. 6.2b. Using this method the degree of diseases in vessels can be identified so that decisions on the need of medical treatment are facilitated, see for example Böse et al. [2007]. On the basis of these gray-scale images the lumen-media interface and the media-adventitia interface can be determined. A spectrum analysis of IVUS radiofrequency data using VH IVUS⁹ results in a detailed analysis of the four major plaque constituents, such that a color-coded cross-sectional image can be derived, see Fig. 6.2c. For the following analyzes IVUS gray-scale images and the corresponding color-coded VH IVUS images were provided by Prof. Erbel and Dr. Böse from the West German Heart Center in Essen. One example of the provided IVUS gray-scale images and corresponding color-coded VH IVUS images is given in Fig. 6.2b,c. Note that in Fig. 6.2c large necrotic-core tissue was identified without evidence of a fibrous cap. On the basis of the VH IVUS images numerical models were generated, see for example Balzani et al. [2011] for details.

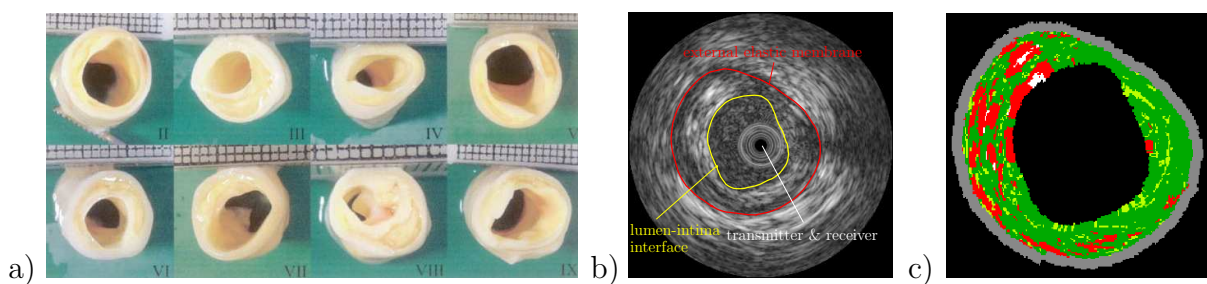


Figure 6.2: a) Macroscopic view of eight human stenotic iliac arteries (one side of a square is 1 mm), taken from Holzzapfel et al. [2004b]. b) IVUS (intravascular ultrasound) gray-scale image and c) corresponding color-coded VH (Virtual Histology) IVUS image, from Prof. Erbel and Dr. Böse (West German Heart Center, Essen).

Literature overview. In the last decades many scientific works investigated the plaque and plaque-cap properties and especially their influence on plaque rupture. In Richardson et al. [1989] plaques from patients who died from coronary thrombosis were investigated.

⁹VH IVUS technology is the proprietary of the Volcano Corporation, California, USA.

The plaque rupture occurred in three out of five cases at the junction of the cap. In the other cases the rupture evolves through the cap center. As one critical factor of plaque rupture the stress distribution in the plaque was mentioned. Lee et al. [1991, 1992] studied the mechanical behavior of three different types of fibrous caps (cellular, hypocellular and calcified) from atherosclerotic plaques of the human abdominal aorta under dynamic and static imposed uniaxial compression. They stated that the dynamic stiffness of the hypocellular fibrous caps were 1-2 times stiffer than the cellular caps, while the calcified caps were 4-5 times stiffer. Additionally, an increase in stiffness with increasing frequencies of stress was observed. In a further work in Loree et al. [1994] tensile tests were performed and they found out that the static tensile stiffness is less dependent on the cap-type. This was explained by the existence of fibrous collagen, which is present in each type of cap and dominates the mechanical behavior in case of tension. Ruptured and intact caps of human aortas were mechanically tested in Lendon et al. [1991, 1993]. In plaques with presence of a tear in the cap, the macrophage density was higher, the maximal stress at fracture was significantly lower, and the extension was significantly larger than in intact plaque caps. Experimental tests on human abdominal and iliac arteries were done by Topoleski and Salunke [2000] and Salunke et al. [2001] in order to study the mechanical behavior of different plaque types (calcified, fibrous, atheromatous) compared to healthy vessels. They concluded that the behavior of calcified plaques is different from the other plaque types and healthy arteries. Furthermore, they suggested that dividing the plaque into only three categories is not sufficient since in each category different responses are observed. Finite-Element simulations of atherosclerotic lesions were performed in Huang et al. [2001]. Here, it was shown that the increased biomechanical stresses in the fibrous cap of atherosclerotic plaque leading to plaque rupture is due to the presence of lipid pools, while the impact of calcification is rather low. In contrast to the above mentioned works Holzapfel et al. [2000b, 2004b] investigated not primarily the mechanical properties of the plaque cap but those of the individual tissue components in the atherosclerotic plaques. Here, the geometry of human iliac arteries with its different components was monitored by use of hrMRI (high resolution magnetic resonance imaging). By histological analysis eight different tissue types were identified, i.e. the adventitia, the non-diseased media, the non-diseased intima, the diseased fibrotic media and the atherosclerotic plaque (collagenous cap, fluid-like lipid pool, a fibrous part at the medial border, and calcification). With exception of calcifications and lipid pools all tissue types were mechanically tested by uniaxial extension tests in axial and circumferential direction. The results of Holzapfel et al. [2004b] were used in this work in Chapter 7. Baldewsing et al. [2004] measured IVUS elastograms, i.e. radial strain images, and used Finite-Element simulations in order to investigate the influence of plaque material properties, plaque geometry, and catheter position upon the peak radial strains. A clinical study was made in Rodriguez-Granillo et al. [2006] in order to clarify the role of the plaque composition, which was identified by spectral analysis of IVUS radiofrequency data, in the mechanisms of coronary-artery remodelling.

Nevertheless, there exists only few experimental data with respect to the mechanical behavior of the plaque. Due to that and because of the patient-specific differences, it is difficult to identify material parameters for the plaque components. In the next section the plaque is assumed to be a homogeneous and isotropic material. Physically reasonable material parameters are assumed and applied in a numerical simulation in order to analyze their influence of different material parameters.

6.2.1 Identification of plaque parameter

In the following the plaque is assumed to be homogeneous and isotropic. Therefore, the compressible Mooney-Rivlin model $\psi_{\text{MR}}^{\text{iso}}$, see eq. (5.3), is used to describe the plaque behavior. Following eq. (3.95) the isotropic elasticity tensor in the reference placement can be obtained by

$$\mathbb{C}^{\text{iso}}(\mathbf{C} = \mathbf{1}) = (4\eta_2 + 4\eta_3)\mathbf{1} \otimes \mathbf{1} + (2\delta - 4\eta_2 - 4\eta_3)\mathbf{1} \boxtimes \mathbf{1}. \quad (6.11)$$

The classical isotropic elastic constitutive tensor in matrix notation is given by

$$[\mathbb{C}] := \begin{bmatrix} \mathbb{C}_{1111} & \mathbb{C}_{1122} & \mathbb{C}_{1122} & 0 & 0 & 0 \\ & \mathbb{C}_{1111} & \mathbb{C}_{1122} & 0 & 0 & 0 \\ & & \mathbb{C}_{1111} & 0 & 0 & 0 \\ & & & \frac{1}{2}(\mathbb{C}_{1111} - \mathbb{C}_{1122}) & 0 & 0 \\ \text{sym.} & & & & \frac{1}{2}(\mathbb{C}_{1111} - \mathbb{C}_{1122}) & 0 \\ & & & & & \frac{1}{2}(\mathbb{C}_{1111} - \mathbb{C}_{1122}) \end{bmatrix}. \quad (6.12)$$

The relations between the Ogden-parameters and the isotropic elasticity tensor appear as

$$4\eta_2 + 4\eta_3 = \mathbb{C}_{1122} \quad \text{and} \quad 2\delta = \mathbb{C}_{1111}. \quad (6.13)$$

Furthermore, the expressions of the isotropic moduli in terms of the Lamé constants λ and μ are given by

$$\mathbb{C}_{1111} = \lambda + 2\mu \quad \text{and} \quad \mathbb{C}_{1122} = \lambda. \quad (6.14)$$

The solution of the equations in eq. (6.13) and eq. (5.4) for the material parameters $(\eta_1, \eta_2, \eta_3, \delta) \in \mathbb{R}^+$ under consideration of eq. (6.14) is given by

$$\left. \begin{aligned} \eta_3 &= \frac{1}{4} \xi \mathbb{C}_{1122} &= \frac{1}{4} \xi \lambda \\ \delta &= \frac{1}{2} \mathbb{C}_{1111} &= \frac{1}{2} (\lambda + \mu) \\ \eta_2 &= \frac{1}{4} \mathbb{C}_{1122}(1 - \xi) &= \frac{1}{4} (\lambda + 2\mu - (\xi - 2) \lambda) \\ \eta_1 &= \frac{1}{4} (\mathbb{C}_{1111} + (\xi - 2) \mathbb{C}_{1122}) &= \frac{1}{2} \mu - \frac{1}{4} \lambda + \frac{1}{4} \xi \lambda \end{aligned} \right\} \xi \in [0, 1]. \quad (6.15)$$

Thus, it is always possible to select a set of positive parameters λ and μ that satisfy eq. (6.15) with $(\eta_1, \eta_2, \eta_3, \delta) \in \mathbb{R}^+$, see Ciarlet [1988] and Schröder and Neff [2003].

In Table 6.2 the identified material parameters (parameter set I-V) for different configurations of the constants $\lambda = 2\mu\nu/(1 - 2\nu)$ and μ are listed.

	I	II	III	IV	V
λ [kPa]	13036	11950	6518	3259	1086
μ [kPa]	600	550	300	150	50
η_1 [kPa]	141	88	20	60	4
η_2 [kPa]	160	188	130	15	22
η_3 [kPa]	3100	2800	1500	800	250

Table 6.2: Five different sets (I-V) of material parameters for the plaque with $\nu = 0.478$.

The constants are chosen in such a way that the plaque behaves quasi-incompressible, i.e. the Poisson's ratio ν is nearly 0.5. In this section, a Poisson's ratio of $\nu = 0.478$ is assumed. In order to get a first impression of the material behavior of the plaque under consideration of the different parameter sets, a uniaxial tension and a compression test was performed, see Fig. 6.3. It is obvious that the stiffness continuously decreases from parameter set I to set V.

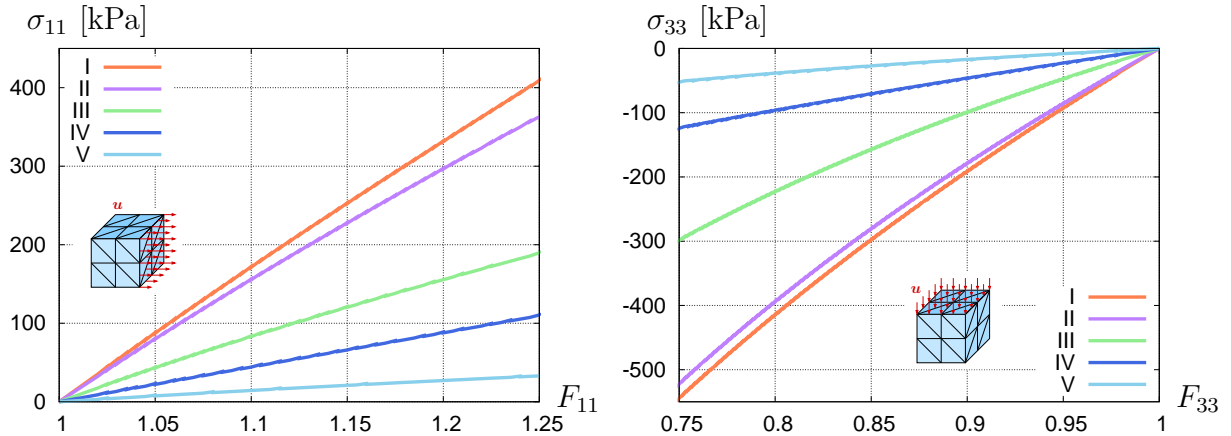


Figure 6.3: Stress-stretch relation of the plaque for the five different sets (I-V) of material parameters as a result of a) a tension test and b) a compression test.

6.2.2 Influence of plaque behavior on arterial wall behavior

In order to investigate the influence of the plaque behavior under consideration of the five different parameter sets with respect to the overall arterial wall behavior, a simulation of a two-dimensional arterial cross-section was performed, cf. also the diploma thesis Tielke [2009]. The patient-specific cross-section (Fig. 6.4b) was identified by an VH IVUS image (Fig. 6.4a) as described in the introduction of this section, and discretized with 6 015 quadratic triangular finite elements, see Fig. 6.4c.

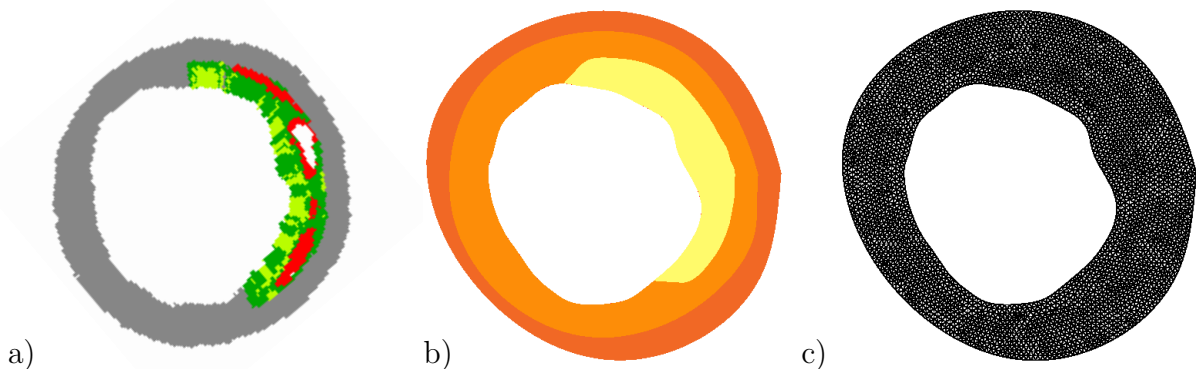


Figure 6.4: a) Patient specific VH IVUS image and b) corresponding two-dimensional numerical model of an arterial wall composed of adventitia, media and plaque and c) discretization of the cross-section with 6 015 quadratic triangular finite elements.

Since an artery has a very large dimension in x_3 -direction (axial) in comparison with the dimensions in x_1 - and x_2 -direction the simulations are conducted under plane strain conditions. As additional Dirichlet boundary conditions three outer boundary nodes are

fixed, such that the cross-section is not allowed to move radially and the system is statically determined. The material behavior of the media and the adventitia is modeled with the material model

$$\psi = \psi_{\text{MR}}^{\text{iso}} + \sum_{a=1}^2 \psi_{(a)}^{\text{ti,HGO1}}, \quad (6.16)$$

see eq. (5.3) and eq. (5.15) and the material parameters were fitted to experimental data¹⁰ according to Section 6.1. The resulting parameters are listed in Table 6.3. The stress-stretch results of the adjusted material model and the experimental data are shown in Fig. 6.5.

	c_1 [kPa]	c_2 [kPa]	c_3 [kPa]	k_1 [kPa]	k_2 [-]	β_f [°]
media	14.64	0.15	60.81	6.85	754.01	43.47
adventitia	2.33	6.17	60.64	3.13e-8	147.17	52.29

Table 6.3: Material parameters of the media and the adventitia.

In the simulations the quasi-incompressibility is enforced by using the Augmented-Lagrange-Method, see Section 5.2.3. Here, the nested iteration algorithm was used with $\kappa_{\text{al}} = 99.0$ for media and adventitia and $\kappa_{\text{al}} = 999.0$ in case of the plaque.

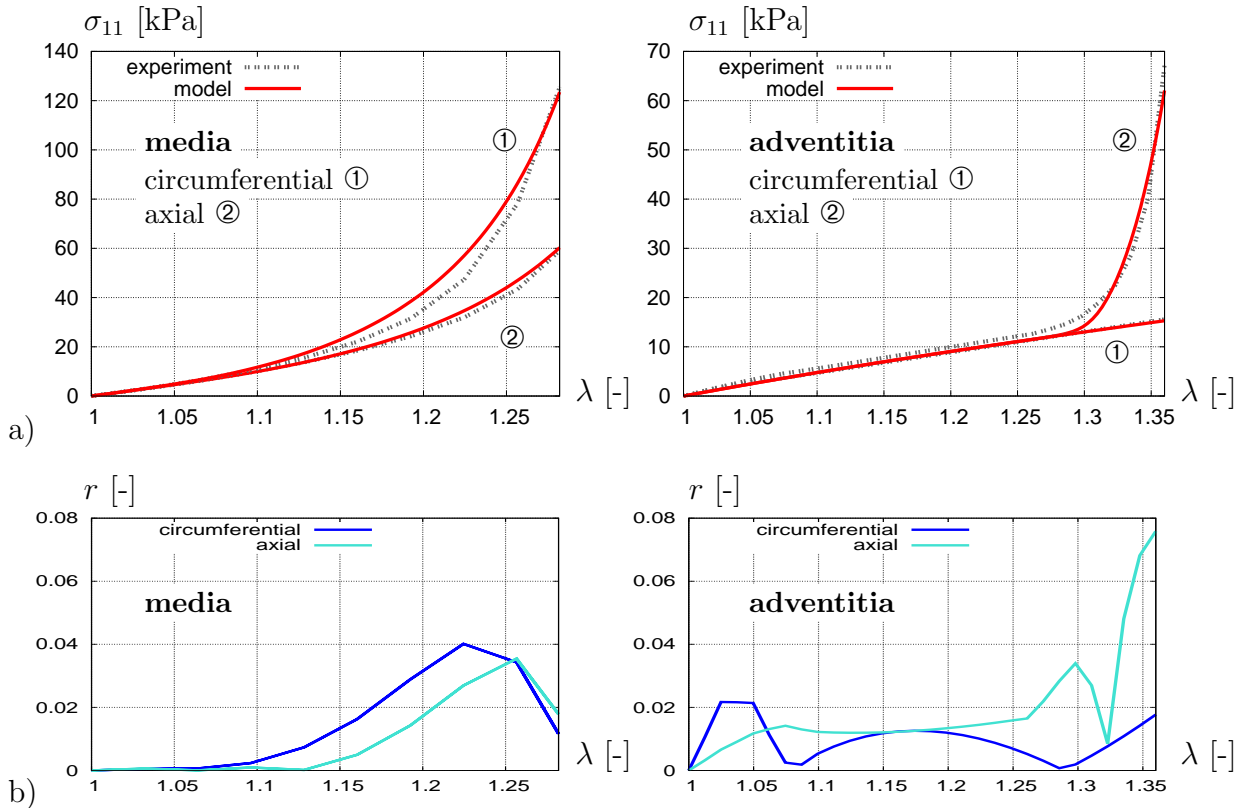


Figure 6.5: Uniaxial extension test: a) stress-stretch response (σ_{11} [kPa] vs. λ [-]) of the experiments and the material model for media and adventitia; b) relative error r [-].

¹⁰Uniaxial extension tests performed on test strips the media and adventitia of a human abdominal aorta (male, 40 years, primary disease: congestive cardiomyopathy); courtesy of Prof. Holzappel, TU Graz.

A good agreement between the experimental stress-stretch relation and the behavior of the material model can be observed. For the media as well as for the adventitia the relative error r is always smaller than 0.08 in axial direction and always smaller than 0.04 in circumferential direction, respectively.

In the numerical simulation of the arterial wall an internal hydrostatic pressure follower load of $p_i = 24$ kPa (180 mmHg) is applied stepwise by surface elements in order to represent the blood pressure. The appearing stress distribution of the Cauchy stresses in x_1 -direction, i.e. σ_{11} , is depicted in Fig. 6.6 exemplarily for parameter set I and V. Additionally, the distribution of stress in a vertical section through the artery is shown (in the direction of x_2 with $x_1 = 0$), which correspond to the circumferential stresses.

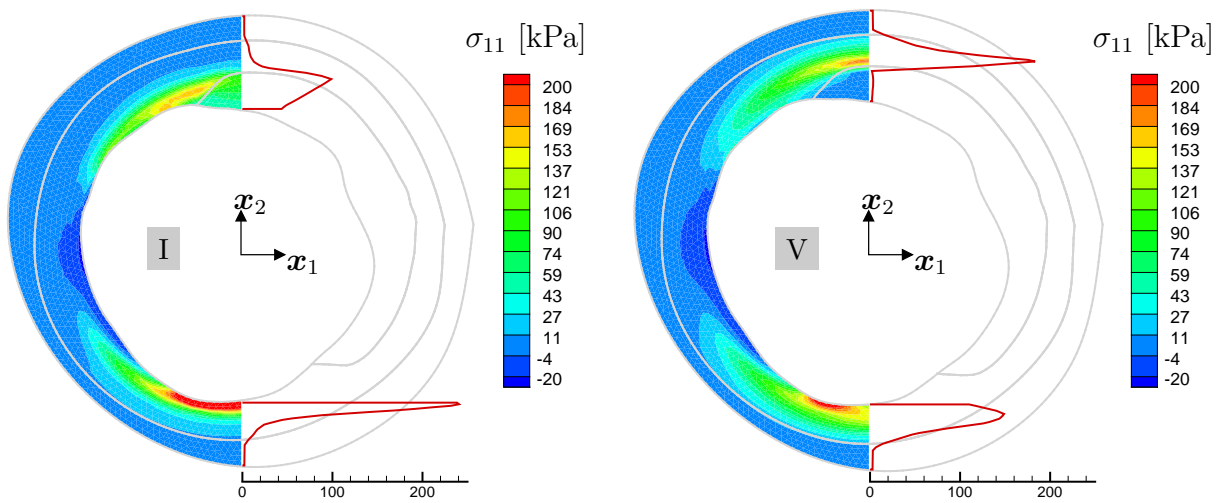


Figure 6.6: Distribution of the Cauchy stresses in x_1 -direction (σ_{11}) for two parameter sets, i.e. set I and V.

The diagram in Fig. 6.7a shows the σ_{11} -distribution for all parameter sets on the right hand side of the artery where the plaque is present.

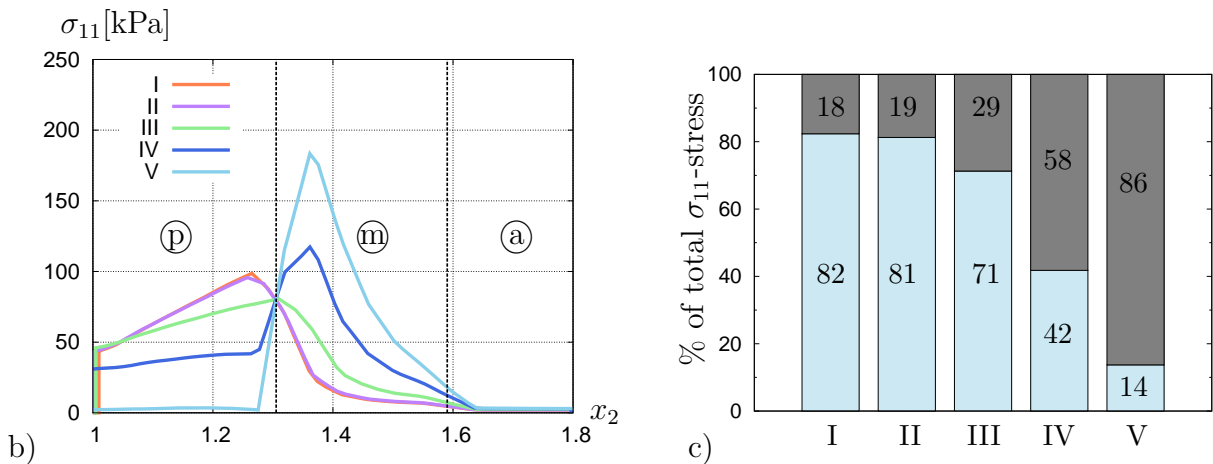


Figure 6.7: σ_{11} stress distribution in a slice through one side of the artery, where plaque (p), media (m) and adventitia (a) are present; c) Fraction of the σ_{11} -stress, which are captured by the plaque (light blue) and by the media/adventitia (gray).

A comparison of the particular sets makes obvious, that, if the plaque is relatively stiff (parameter set I), it carries the total load, whereas the adventitia and the media are almost stress-free. The softer the plaque is, the less stress it bears and the more the stresses are transferred to the media. Since the adventitia is the load carrying layer at higher load levels, see Section 2.3, it is always almost stress-free. In set V the plaque has the softest material behavior and is nearly stress-free. In Fig. 6.7b the diagram shows the fraction of the stresses, which is carried by the the plaque and the media/adventitia, respectively. It should be noticed, that although the material behavior of media and adventitia are adjusted to experiments, the stress distribution in the arterial cross-section is totally different, depending on whether the plaque is a rather stiff or a rather soft material.

7 An anisotropic damage model for softening hysteresis in arterial walls

This chapter deals with the modeling of damage in soft biological tissues. A literature survey of this topic with regard to the experimental observations and the mechanical modeling is given in Section 7.1. In Section 7.2 a brief overview of the characteristics of damage and of general assumptions concerning the modeling of damage is presented. In order to get a more general overview the reader is referred to Lemaitre and Chaboche [1990], Lemaitre [1996], Krajcinovic [1996], de Souza Neto et al. [1998], Skrzypek and Ganczarski [1999], and Lemaitre and Desmorat [2005]. In Section 7.3 a novel principle for the construction of damage models which is able to describe stress-softening hysteresis and remnant strains in the collagen fibers after unloading is proposed. This principle is applied to specific constitutive models in Section 7.4. The models are then adjusted to experimental data of cyclic uniaxial extension tests of the media and the adventitia of a human carotid artery in Section 7.5. In Section 7.6 a circumferential overstretch of a simplified atherosclerotic artery is simulated to demonstrate that the proposed damage model is working in finite element calculations. A part of the following results is published in the joint works Balzani et al. [2009b, 2012].

7.1 A short literature overview of damage in soft biological tissues

In arterial walls microscopic tissue damage takes place in a supra-physiological loading situation, i.e. by an inner pressure much higher than that occurring under normal (physiological) conditions. As a result of such micro-damage the arterial tissues undergo significant deterioration.

Experimental data. In Castaneda-Zuniga et al. [1980] it is shown that remnant deformations occur if a certain load level is exceeded during the overexpansion of the arterial lumen in the consequence of balloon angioplasty. Oktay et al. [1991] and Holzapfel et al. [2000b] observed analogous findings in experimental studies on carotid arteries of dogs and human iliac arteries. In Zollikofer et al. [1984] electron- and light microscopies were investigated in order to study the influence of an overexpansion on the intima, the myocytes and the collagen fibers of canine arteries over a period of six month. They discover a repairing of the dilated segments due to proliferation of myocytes and collagen, and intimal hyperplasia. In the study of Castaneda-Zuniga [1985] the main damage resulting from percutaneous arterial angioplasty was observed in the media. As mentioned in Schulze-Bauer et al. [2002b] the influence of dilation on damage in the adventitia is low, i.e. the adventitia behaves nearly elastically during an overexpansion. The same was observed in Sommer et al. [2010], in which furthermore biaxial extension tests of intact and layer-dissected human carotid arteries at physiological and supra-physiological loadings were performed and analyzed. Experiments in the form of cyclic extension tests in the supra-physiological loading range is less explored in the literature. One of the few works performing cyclic uniaxial extension tests is Horný et al. [2010]. Here, samples of human thoracic aorta were investigated. In Weisbecker et al. [2012] additionally layer-specific test were performed on human thoracic and abdominal aortic samples.

Constitutive modeling. A three-dimensional isotropic damage formulation at finite strains was proposed in Simo [1987], see also Simo and Ju [1987]. Here, a scalar valued internal variable (see Section 7.2) was used in order to reflect the discontinuous softening behavior of polymers, i.e. the Mullins effect (Mullins [1948]). This technique has also been applied in Govindjee and Simo [1991] and de Souza Neto et al. [1994]. An extension to the modeling of continuous damage was given by Miehe [1995] by using a distinct internal variable. Another phenomenological model for the description of damage was proposed in Miehe and Keck [2000]. Here, the saturation behavior of filled rubber is investigated in cyclic deformation processes. In Marckmann et al. [2002] micro-mechanical interpretations of the evolving damage as breakage of links in the material were adopted by a chain model in combination with network alteration theory. Here, the alteration of the mean chain length depends on the previous maximum chain stretch ratio. The idea of such network alteration was adapted by Horgan et al. [2004] in combination with the Gent model of rubber elasticity (Gent [1996]), and by Diani et al. [2006], which induced anisotropy by modeling the damage as a function of the maximum stretch in the material directions. Damage induced stress-softening effects combined with remanent deformations were modeled in Besdo and Ihlemann [2003] based on the idea of limiting stresses. A pseudo-elastic model was investigated previously by Ogden and Roxburgh [1999a,b] to model the Mullins effect. In the theory of pseudo-elasticity the loading and unloading/reloading paths are characterized by different strain-energy functions. In Dorfmann and Ogden [2003] the model is adopted in order to account for a hysteretic response due to loading, partial and complete unloading, and reloading cycles. By introduction of an additional internal variable Dorfmann and Ogden [2004] enabled the accumulation of remanent strains. A comparison of a continuum damage mechanics model used in, for example, Simo [1987], Miehe [1995], and the pseudo-elastic model combined with Gao's elastic law (Gao [1997]) was done in Guo and Sluys [2006]. For the description of anisotropic damage, internal variables as tensors of second order are introduced, for example, in Simo and Ju [1987], Zhu and Cescetto [1995], Hokanson and Yazdani [1997], and Menzel and Steinmann [2001]; in the framework of micro-macro approaches see, for example, Steinmann and Carol [1998] and Göktepe and Miehe [2005]. In Schröder et al. [2005a] and Balzani et al. [2007] the damage is assumed to take effect only in fiber direction, so that a scalar-valued damage variable could be used to describe the damage. Consequently, damage tensors could be avoided, which yields a more practical approach. Scalar-valued damage variables are also used in earlier works for isotropic damage, see, for example, Simo [1987] or Miehe and Keck [2000]. In Rodríguez et al. [2006] a scalar-valued damage variable is used in order to describe damage in the matrix. Fiber failure is modeled using a worm-like chain model, see also Rodríguez et al. [2008]. An individual damage formulation for the matrix and the fibers has also been proposed in, for example, Natali et al. [2003, 2005], Calvo et al. [2007], Alastrué et al. [2007b], Peña et al. [2009], and Peña [2011]. In Gasser and Holzapfel [2007] it is accounted for remanent strains after overstretch by using a finite-plasticity model. The model by Ehret and Itskov [2009] is able to reflect the preconditioning of fibrous soft biological tissues. Furthermore, the Mullins effect was investigated. The recently published approach by Weisbecker et al. [2012] uses a pseudo-elastic damage model in order to describe discontinuous softening in aortic arterial tissues, where damage in the fibers and in the matrix material can be accounted for individually. Furthermore, they fitted the model to experimental data.

7.2 Damage variable, strain equivalence principle and anisotropic damage

In solid mechanics damage can be considered as the result of the evolution of micro-cavities or micro-cracks resulting in discontinuities. Since we are interested in continuous media, we consider a representative volume element (RVE), which accounts for such damage discontinuities by using a homogenized (continuous) variable.

Scalar damage variable. A scalar variable for the description of micro-cavities or micro-cracks at small strains was proposed by Kachanov [1958]. Here, a cutting plane of an RVE at a material point M of a damaged body is considered, see Fig. 7.1a.

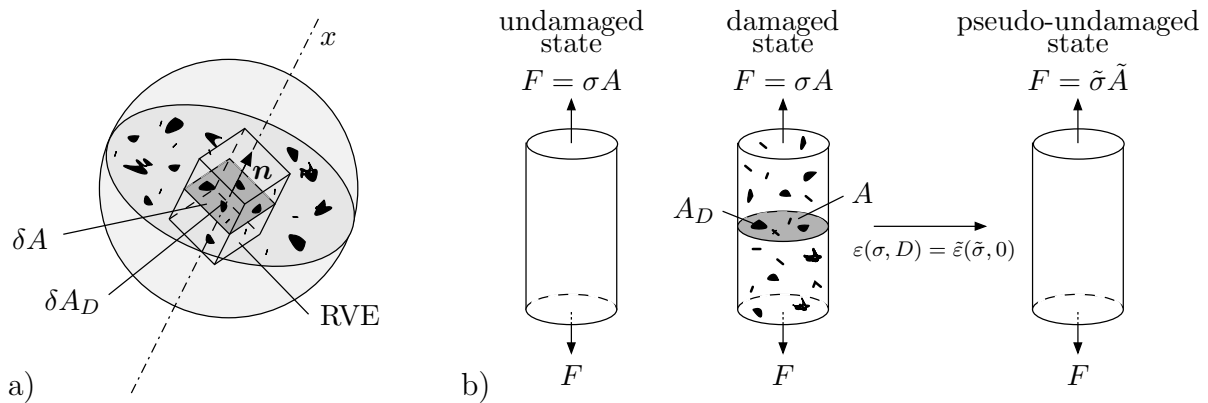


Figure 7.1: a) RVE of a damaged body at a material point M , cf. Lemaitre [1996], page 11; b) One-dimensional effective stress concept as a result of strain equivalence, cf. Skrzypek and Ganczarski [1999], page 10.

The cutting plane is defined by its area δA containing the area of all micro-cavities or micro-cracks $\delta A_D|_x$, by its normal \mathbf{n} and its position along the abscissa x , which is parallel to \mathbf{n} . Since we are interested in a representative continuous damage variable of the RVE, all damage variables $D(M, \mathbf{n}, x)$ of each cutting plane are considered and then the maximum is taken into account, i.e.

$$D(M, \mathbf{n}) = \sup_x [D(M, \mathbf{n}, x)] \quad \text{with} \quad D(M, \mathbf{n}, x) = \frac{\delta A_D|_x}{\delta A}. \quad (7.1)$$

This results in a damage variable, which is independent of the position x , i.e. $D(M, \mathbf{n}) = \frac{\delta A_D}{\delta A}$. Two extreme cases are possible: an undamaged material with $D = 0$ and a completely damaged material with $D = 1$, i.e. the damage variable varies between zero and one ($D \in [0, 1]$). The remaining (effective, undamaged) area is given by $\delta \tilde{A} = \delta A - \delta A_D$. If the damage parameter does not change with the normal vector orientation, the material can be regarded as isotropically damaged. In that case the problem under consideration reduces to the one-dimensional case and the damage variable is given by the surface density of micro-defects

$$D = \frac{A_D}{A} \quad \text{with} \quad D \in [0, 1]. \quad (7.2)$$

Strain equivalence principle and effective stress concept. The damage variable can be computed by the effective area using mathematical homogenization techniques, see Voyiadjis and Kattan [2006]. In that case, the shape and size of defects have to be

detected. In order to circumvent a difficult detection procedure, Rabotnov [1968] proposed the effective stress concept, see also the hypothesis of strain equivalence in Lemaitre [1971]. As shown in Fig. 7.1b, a one-dimensional volume element is accounted for with cross-section A , which is loaded by a uniaxial stress σ . In the undamaged state, the damage variable is zero. Then micro-defects arise and D becomes a value greater than zero, the material is damaged. It is assumed that this physical state can be transformed to a pseudo-undamaged state without changing the material response, i.e. the strain remains the same ($\tilde{\varepsilon} = \varepsilon$). Here, the stress σ is replaced by the effective stress $\tilde{\sigma}$, which can be regarded as fictitious undamaged stress acting on the reduced area \tilde{A}

$$\tilde{\sigma} = \frac{F}{\tilde{A}} = \frac{F}{A - A_D} = \frac{\sigma}{(1 - D)} \quad \rightarrow \quad \sigma = (1 - D)\tilde{\sigma}. \quad (7.3)$$

For a detailed description of this subject see Lemaitre [1996] (pp. 11), Skrzypek and Ganczarski [1999] (pp. 10), and Lemaitre and Desmorat [2005] (pp. 3).

Anisotropic damage in soft biological tissues. Soft biological tissues are fiber-reinforced and therefore not isotropic. To account for anisotropic damage, in several works internal variables are used as tensors of second or fourth order (see Section 7.1). Even though these anisotropic models are able to reflect the material response, the definition of damage tensors often complicates the material modeling. Therefore, in the present work a scalar-valued isotropic damage variable D is used in order to reflect the three-dimensional anisotropy of damage occurring in soft biological tissues by application of the $(1 - D)$ -approach directly to the energy function, which is associated to the fibers. The consideration of damage only in the fibers seems to be reasonable since the fiber reinforcements are the main load bearing elements. Incorporation of the $(1 - D)$ -approach directly to the energy function has been proposed in several works, see Section 7.1.

Damage and saturation effects in arterial walls. As mentioned in Section 2.3 healthy elastic arteries exhibit a highly non-linear and anisotropic stress-strain response. In Fig. 7.2a the typical stress-strain response of an arterial strip loaded within a cyclic uniaxial tension test is shown schematically. The cyclic application of the load, i.e. the three loading cycles up to three different load levels (I, II, III) and the corresponding unloading cycles shows Fig. 7.2b.

The first three cycles (load level I) are called the pre-conditioning. The material softens until the path ending in point ① is reached. Then, after the pre-conditioning the material behaves nearly perfectly elastic as expected due to in-vivo conditions and a physiological blood pressure. Loading beyond the elastic domain up to load level II (point ②), for example due to a transluminal angioplasty (see Section 2.2), results in stiffness reduction due to damage and plastic deformations, which remain after unloading. Thus, we follow a lower path (A) while unloading, which could be due to deflation of a balloon catheter. In the physiological stress range remanent strains $\varepsilon_{r,phys} = \Delta l_{r,phys}/l_0$ are observed, which are responsible for a dilation of the arterial lumen. The remanent strains are a result of the damage (i) directly, since the damage reduces the material stiffness and increases the strains in the physiological stress range, and (ii) indirectly, since the damage induces plastic strains $\varepsilon_{r,plas} = \Delta l_{r,plas}/l_0$. Application of further loading and unloading cycles by a fixed maximum load level (load level II) yields a diminishing softening until the stress hysteresis converges to a ‘saturated’ response curve (point ③). Only when a higher load level is reached (here the load level III), further softening effects occur (see path until point ④) and the saturation begins again.

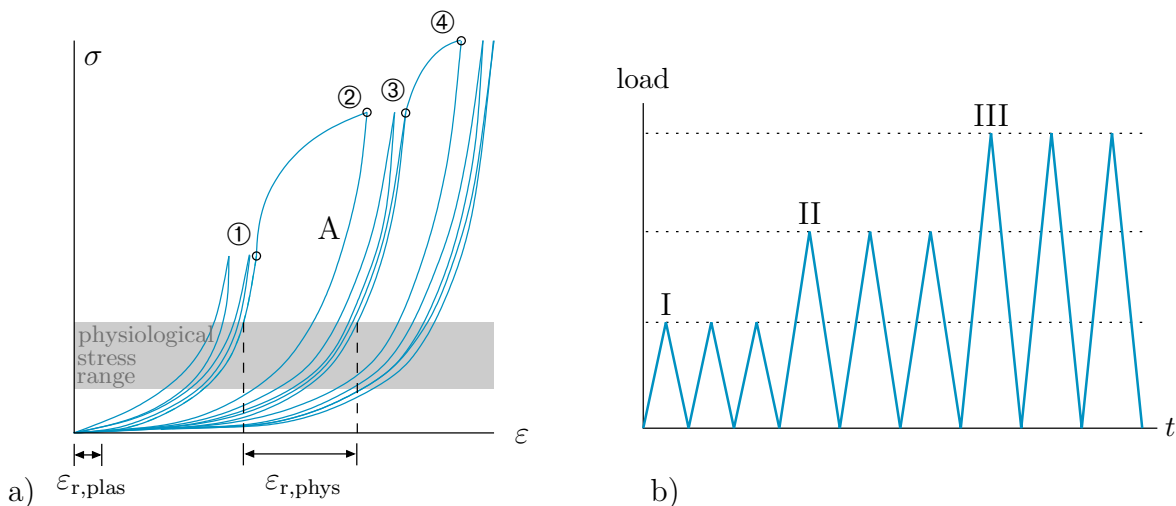


Figure 7.2: Schematic diagram showing a) a cyclic uniaxial stress-strain response (σ , $\varepsilon = \Delta l/l_0$) of an arterial strip, cf. Holzapfel et al. [2000a]. After pre-conditioning (point ①) the material behaves (perfectly) elastic. Loading beyond the elastic domain up to point ② results in softening due to damage effects. Further loading and unloading cycles softens the material until it is ‘saturated’ (point ③). Application of higher load levels (point ④) causes further damage and softening effects. The remanent strains due to elasto-plastic material behavior $\varepsilon_{r,plas} = \Delta l_{r,plas}/l_0$ and remanent strains after two over-expansions at the edge of the physiological stress range $\varepsilon_{r,phys} = \Delta l_{r,phys}/l_0$ are shown. b) Corresponding cyclic application of load (loading and unloading cycles) up to three different load levels (I, II, III).

In order to uncover the reason for the damage effects we have to take a closer look at the main components of an arterial wall, i.e. elastin and collagen. Elastin is the main constituent of the ground substance (the matrix material) and in combination with proteoglycans it provides the matrix with resilience, see Montes [1996]. As mentioned in Section 2.3 collagen rather than elastin is the load-bearing component at high strains where damage appears. Additionally, comparing the behavior of elastin and collagen fibers, significantly higher elastic strains are needed to cause a dissipative behavior in elastin, see, for example, Roach and Burton [1957]. In this work we do not account for damage in the matrix since it is assumed to be of secondary importance, see the experimental study of Weisbecker et al. [2012].

The embedded collagen fibers are the main load-carrying elements in arterial walls. On the molecular level the main component of the fibers is tropocollagen interconnected by cross-links, see Section 2.1. If the fibers are elongated in fiber direction the cross-links are straightened, and by exceeding a certain level (in the supra-physiological domain) the cross-links break, see Fig. 2.3b. A complete failure of the micro-fibril takes place if a certain number of cross-links have collapsed. Thus, the more load is applied, the less fibrils are intact to resist the load and the more the stiffness of the material is reduced. Oriented discontinuous damage takes place in fiber direction, if it is assumed that the cross-links and therefore the micro-fibrils break due to overstretch and cannot heal themselves. The reason for continuous damage effects may be a rearrangement of the cross-links, such that further damage appears during a re-loading cycle within the same loading range as the previous loading cycle. The saturation effect may be a result of the gradual breaking of all cross-links, which cannot resist the applied maximum load level. If all such cross-links have failed then the ‘saturated’ response curve is achieved. Furthermore, if a higher load level is applied, there exist again some cross-links not able to resist the higher stretch.

7.3 Construction principle for damage models

According to the construction principles for polyconvex energy functions for the hyperelastic regime derived in Balzani et al. [2006a], see also the short replication in Section 5.1.2, a principle for the construction of damage models, which are able to describe stress-softening hysteresis and remnant strains in the collagen fibers after unloading, is given in this section.

7.3.1 Construction principle

As mentioned before, the breaking of micro-fibrils results in remnant strains in soft biological tissues. The material model should be able to reflect such remnant strains, such that the following construction principle has to be taken into account

Consider the modified (internal) energy function $P := (1 - D)\bar{P} - c$ with the damage variable $D \in [0, 1[$ and polyconvex function \bar{P} . Then include P into any arbitrary (external) convex and monotonically increasing function $m(P(X))$, whose first derivative is zero in the origin,

see Balzani et al. [2012]. Here, the basic idea is to incorporate the $(1 - D)$ -term directly into the inner function P instead of prefixing it. This approach poses the important effect that by evolution of the damage function D the stress-free configuration is shifted resulting in remanent strains after unloading. In a similar manner this idea was investigated by Govindjee and Simo [1991] and Ogden and Roxburgh [1999b]. A number of seven possible functions \bar{P} and the corresponding values of the functions in the natural (undamaged) state c , i.e.

$$c = \bar{P}_i(\mathbf{C} = \mathbf{1}) \quad \text{for } i = 1, \dots, 7, \quad (7.4)$$

are given in Table 7.1. The value c is subtracted in order to satisfy the condition of a energy-free reference configuration for the undamaged case.

	$\bar{P}_1 := J_4^{(a)}$	$\bar{P}_2 := K_1^{(a)}$	$\bar{P}_3 := K_2^{(a)}$	$\bar{P}_4 := K_3^{(a)}$	$(\bar{P}_5 := I_1)$	$\bar{P}_6 := I_2)$	$\bar{P}_7 := I_3)$
c	1	1	1	2	3	3	1

Table 7.1: Possible functions \bar{P} and value of the function \bar{P} in the natural state c .

Considering the above mentioned construction principle for the investigation of damaged soft biological tissues the energy functions are of the type

$$\psi(\mathbf{C}, D) := m(P(\mathbf{C}, D)) \quad \text{with } P := (1 - D)\psi^0 - c, \quad (7.5)$$

where the fictitiously undamaged effective energy is defined as $\psi^0 := \bar{P}$.

With $\mathcal{D} = \mathcal{D}_{int}$ and isothermal processes we start from the dissipation inequality, see eq. (3.73), with $\dot{\mathbf{E}} = \frac{1}{2}\dot{\mathbf{C}}$ and obtain with the abbreviation $m' := \partial_P m$

$$\mathcal{D} = \frac{1}{2}\mathbf{S} : \dot{\mathbf{C}} - \dot{\psi} \geq 0 \quad \text{with } \dot{\psi} = \frac{\partial \psi}{\partial \mathbf{C}} : \dot{\mathbf{C}} + \frac{\partial \psi}{\partial D} \dot{D} = \frac{\partial \psi}{\partial \mathbf{C}} : \dot{\mathbf{C}} - m' \psi^0 \dot{D}. \quad (7.6)$$

Insertion of the time derivative of the strain-energy function into the dissipation inequality yields

$$\mathcal{D} = \left(\frac{1}{2} \mathbf{S} - \frac{\partial \psi}{\partial \mathbf{C}} \right) : \dot{\mathbf{C}} + m' \psi^0 \dot{D} \geq 0. \quad (7.7)$$

By application of the standard argument of rational continuum mechanics, cf. Section 3.4.5, the second Piola-Kirchhoff stress tensor is given by

$$\mathbf{S} = 2 \frac{\partial \psi}{\partial \mathbf{C}} = m'(1 - D) \mathbf{S}^0 \quad \text{with} \quad \mathbf{S}^0 := 2 \frac{\partial \psi^0}{\partial \mathbf{C}}, \quad (7.8)$$

cf. eq. (3.75). The reduced dissipation \mathcal{D}_{red} may be represented by the inequality

$$\mathcal{D}_{\text{red}} := m' \psi^0 \dot{D} \geq 0 \quad \Rightarrow \quad \dot{D} \geq 0. \quad (7.9)$$

Note, that from eq. (7.9)₁ follows that \dot{D} has to be greater or equal zero in order to ensure thermodynamic consistency, because the function m is assumed to be monotonically increasing and the energy functions are zero in the reference configuration.

In this work a damage function D is considered, which is assumed to depend on the fictitiously undamaged (effective) energy $\psi^0 = \bar{P}$, i.e.

$$D(\beta(\psi^0)) = D_s \left[1 - \exp \left(- \frac{\ln(1 - r_s)}{\beta_s} \beta(\psi^0) \right) \right], \quad (7.10)$$

with $D_s \in [0, 1[$, $r_s \in [0, 1[$, $\beta_s > 0$ is used, cf. Miehe [1995]. The only material parameter in eq. (7.10) is β_s , which represents the value of the internal variable $\beta(\psi^0)$ reached at a certain fraction r_s of the maximum damage value D_s for a fixed maximum load level, see Fig. 7.3a. In this work a fraction of $r_s = 0.99$ is taken into account. Therefore, β_s is the value of the internal variable β at a saturated damage value $D = 0.99 D_s$. In Fig. 7.3b it becomes visible that the smaller β_s is, the faster the maximum damage value D_s is reached.

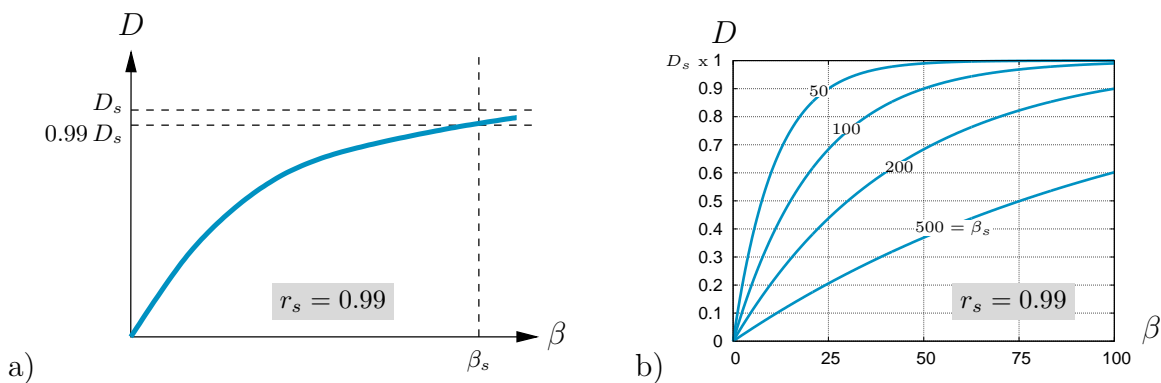


Figure 7.3: Relation between the damage variable D , its maximum value D_s and the internal variable β for a certain value $r_s = 0.99$: a) in general and b) for different values of the material parameter β_s .

The assumption that evolution of damage is activated in the loading and the reloading processes is taken into account by choosing the internal variable β as follows

$$\beta(\psi^0) := \left\langle \tilde{\beta} - \tilde{\beta}^{\text{ini}} \right\rangle \quad \text{with} \quad \tilde{\beta} = \int_0^t \left\langle \dot{\psi}^0(s) \right\rangle ds. \quad (7.11)$$

The variable $\tilde{\beta}^{\text{ini}}$ is the internal variable at an initial damage state, which ensures that the damage evolution starts at the beginning of the supra-physiological domain and not in the physiological range of deformations. The time $s \in \mathbb{R}^+$ reflects the loading history, while $t \in \mathbb{R}^+$ indicates the current loading situation. The Macaulay brackets^{7 (page 42)} ensure that no damage evolution takes place while unloading.

The evolution of the internal variable β drives the saturation of the damage function in eq. (7.10), which converges to a maximum value of damage D_s . This maximum value is not a fixed or predefined value, but rather a function of the same type as eq. (7.10), i.e.

$$D_s(\gamma(\psi^0)) = D_\infty \left[1 - \exp \left(\frac{\ln(1 - r_\infty)}{\gamma_\infty} \gamma(\psi^0) \right) \right], \quad (7.12)$$

with $D_\infty \in [0, 1]$, $r_\infty \in [0, 1[$ and $\gamma_\infty > 0$. Analogously, γ_∞ represents the value of the internal variable γ reached at the fraction r_∞ of D_∞ (in the following we use $r_\infty = 0.99$). The parameter D_∞ is fixed and predefined and represents the converging limit for the overall damage value. Not prefixing the maximal value D_s delivers the advantage to be able to account for (i) increased maximally reachable damage value for increased load levels and (ii) an unaltered maximum damage value under fixed maximum load levels for cyclic processes. Such behavior is enabled by defining the internal variable as the maximum value of the effective energy reached up to the current state

$$\gamma(\psi^0) = \sup_{s \in [0, t]} \langle \psi^0(s) - \psi_{\text{ini}}^0 \rangle. \quad (7.13)$$

The parameter ψ_{ini}^0 is the effective strain energy at the limit of the physiological domain, i.e. at the initial damage state. In order to enable the evolution of eq. (7.13) the following saturation criterion is defined inducing no evolution for $\phi \leq 0$, i.e.

$$\phi(\psi^0) := \langle \psi^0 - \psi_{\text{ini}}^0 \rangle - \gamma(\psi^0) \leq 0. \quad (7.14)$$

The proposed damage model is mainly driven by two material parameters (i) the parameter β_s describing the damage behavior in the individual cycles and (ii) the parameter γ_∞ describing the saturation behavior. These two parameters have to be fitted to experimental data. The third parameter D_∞ is the maximally reachable damage value, ideally equal to 1. Due to numerical reasons the adjustment results in values rather close to 1, see Section 7.5.

In order to ensure thermodynamical consistency, the evolution of the proposed damage variable has to be greater or equal to zero, see eq. (7.9). The evolution of the saturation variable D_s is obtained by the derivative of eq. (7.12), i.e.

$$\dot{D}_s = -\frac{D_\infty}{\gamma_\infty} \ln(1 - r_\infty) \exp \left(\frac{\ln(1 - r_\infty)}{\gamma_\infty} \gamma \right) \dot{\gamma} \geq 0. \quad (7.15)$$

The evolution of the damage variable (eq. (7.10)) is given by

$$\dot{D} = \dot{D}_s \left[1 - \exp \left(\frac{\ln(1 - r_s)}{\beta_s} \beta \right) \right] - \frac{D_s}{\beta_s} \ln(1 - r_s) \exp \left(\frac{\ln(1 - r_s)}{\beta_s} \beta \right) \dot{\beta} \geq 0. \quad (7.16)$$

Since eq. (7.15) and eq. (7.16) are greater or equal to zero the thermodynamical consistency of the damage model derived in consideration of the proposed construction principle is ensured.

7.3.2 Specification of the model for soft biological tissues

As mentioned in Section 7.2 micro-damage and the resulting remanent strains are assumed to evolve particularly in the fibers. Therefore, following the construction principle¹¹ described in the previous section we formulate the transversely isotropic part as

$$\psi_{(a)}^{\text{ti}} := m(P_{(a)}(\mathbf{C}, D_{(a)})) \quad \text{with} \quad P_{(a)} = (1 - D_{(a)}) \psi_{(a)}^{\text{ti},0} - c, \quad (7.17)$$

with the effective transversely isotropic strain-energy function $\psi_{(a)}^{\text{ti},0} = \bar{P}_{(a)}$. The first part of the inner function P , i.e. $(1 - D_{(a)})\bar{P}_{(a)}$, can be taken as the energy stored in the micro-fibrils, which is softened by the damage variable $D_{(a)}$ in the case of over-expansion. Accordingly, the (external) function m reflects the structural response and the interaction of the micro-fibrils. The second Piola-Kirchhoff stress tensor is computed by eq. (5.2), where the latter part is now given by

$$\mathbf{S}_{(a)}^{\text{ti}} = m'(1 - D_{(a)})\mathbf{S}_{(a)}^{\text{ti},0}, \quad \text{with} \quad \mathbf{S}_{(a)}^{\text{ti},0} = 2 \frac{\partial \psi_{(a)}^{\text{ti},0}}{\partial \mathbf{C}}. \quad (7.18)$$

In the following, we add a superscript (a) to the quantities whenever it appears reasonable in order to express that they have to be evaluated for each fiber direction $\mathbf{a}_{(a)}$.

7.3.3 Algorithmic implementation

In order to implement the proposed model in a finite-element framework the linearization of the second Piola-Kirchhoff stress tensor

$$\Delta \mathbf{S}(\mathbf{C}, D_{(a)}) = \frac{\partial \mathbf{S}^{\text{vol}}}{\partial \mathbf{C}} : \Delta \mathbf{C} + \frac{\partial \mathbf{S}^{\text{iso}}}{\partial \mathbf{C}} : \Delta \mathbf{C} + \sum_{a=1}^2 \left(\frac{\partial \mathbf{S}_{(a)}^{\text{ti}}}{\partial \mathbf{C}} : \Delta \mathbf{C} + \frac{\partial \mathbf{S}_{(a)}^{\text{ti}}}{\partial D_{(a)}} \Delta D_{(a)} \right) \quad (7.19)$$

is required. Here, the specific derivatives are given by

$$\frac{\partial \mathbf{S}_{(a)}^{\text{ti}}}{\partial D_{(a)}} = - [m' + m''(1 - D)\psi^{\text{ti},0}] \mathbf{S}_{(a)}^{\text{ti},0} \quad \text{and} \quad \Delta D_{(a)} = \frac{\partial D_{(a)}}{\partial \beta_{(a)}} \Delta \beta_{(a)} + \frac{\partial D_{(a)}}{\partial D_{s,(a)}} \frac{\partial D_{s,(a)}}{\partial \gamma_{(a)}} \Delta \gamma_{(a)}, \quad (7.20)$$

where we used eq. (7.18)₁, eq. (7.10) and eq. (7.12). The insertion of the linearizations of $\beta_{(a)}$ and $\gamma_{(a)}$ into eq. (7.20)₂ yields

$$\Delta D_{(a)} = \left(\frac{\partial D_{(a)}}{\partial \beta_{(a)}} \frac{\partial \beta_{(a)}}{\partial \psi_{(a)}^{\text{ti},0}} + \frac{\partial D_{(a)}}{\partial D_{s,(a)}} \frac{\partial D_{s,(a)}}{\partial \gamma_{(a)}} \frac{\partial \gamma_{(a)}}{\partial \psi_{(a)}^{\text{ti},0}} \right) \frac{\partial \psi_{(a)}^{\text{ti},0}}{\partial \mathbf{C}} : \Delta \mathbf{C}. \quad (7.21)$$

The compact notation of the incremental stress $\Delta \mathbf{S}$ follows, if we use the properties eq. (7.18)₂ and $\Delta \mathbf{C} = 2\Delta \mathbf{E}$, i.e. $\Delta \mathbf{S} = \mathbb{C} : \Delta \mathbf{E}$. Here, the elasticity tensor \mathbb{C} in the material description can be additively decoupled into an elastic part \mathbb{C}^{elas} and an transversely isotropic part $\mathbb{C}_{(a)}^{\text{ti}}$, which is in turn decoupled into three parts, i.e.

$$\mathbb{C} = \mathbb{C}^{\text{elas}} + \sum_{a=1}^2 \mathbb{C}_{(a)}^{\text{ti}} \quad \text{with} \quad \mathbb{C}_{(a)}^{\text{ti}} = \mathbb{C}_{(a)}^{\text{eD}} + \mathbb{C}_{(a)}^{\text{D}} + \mathbb{C}_{(a)}^{\text{Ds}}. \quad (7.22)$$

¹¹It should be noticed, that the construction principle for softening models can be applied to the isotropic part as well.

The elastic part \mathbb{C}^{elas} is given as the isotropic standard elasticity tensor for hyperelasticity

$$\mathbb{C}^{\text{elas}} = \mathbb{C}^{\text{vol}} + \mathbb{C}^{\text{iso}} = 4 \frac{\partial^2 \psi^{\text{vol}}}{\partial \mathbf{C} \partial \mathbf{C}} + 4 \frac{\partial^2 \psi^{\text{iso}}}{\partial \mathbf{C} \partial \mathbf{C}}, \quad (7.23)$$

cf. eq. (3.76). The first part of $\mathbb{C}_{(a)}^{\text{ti}}$, i.e. the part $\mathbb{C}_{(a)}^{\text{eD}}$, is the (standard) damaged transversely isotropic elasticity tensor and can be computed by

$$\mathbb{C}_{(a)}^{\text{eD}} = m'(1 - D_{(a)})\mathbb{C}_{(a)}^{\text{ti},0} + m''(1 - D_{(a)})^2 \mathbf{S}_{(a)}^{\text{ti},0} \otimes \mathbf{S}_{(a)}^{\text{ti},0}, \quad (7.24)$$

with $m'' := \partial_{PP}^2 m$ and the effective transversely isotropic elasticity tensor given by

$$\mathbb{C}_{(a)}^{\text{ti},0} = 4 \frac{\partial^2 \psi_{(a)}^{\text{ti},0}}{\partial \mathbf{C} \partial \mathbf{C}}. \quad (7.25)$$

The latter parts in eq. (7.22) are the damage-evolution part and the saturation-evolution part. In the case that $\psi_{(a)}^{\text{ti},0}$ is greater than zero, the damage-evolution part is

$$\mathbb{C}_{(a)}^{\text{D}} = - \left[m' + m''(1 - D_{(a)})\psi_{(a)}^{\text{ti},0} \right] \frac{\partial D_{(a)}}{\partial \beta_{(a)}} \frac{\partial \beta_{(a)}}{\partial \psi_{(a)}^{\text{ti},0}} \mathbf{S}_{(a)}^{\text{ti},0} \otimes \mathbf{S}_{(a)}^{\text{ti},0}, \quad (7.26)$$

and zero otherwise. The saturation-evolution part can be computed by

$$\mathbb{C}_{(a)}^{\text{Ds}} = - \left[m' + m''(1 - D_{(a)})\psi_{(a)}^{\text{ti},0} \right] \frac{\partial D_{(a)}}{\partial D_{s,(a)}} \frac{\partial D_{s,(a)}}{\partial \gamma_{(a)}} \frac{\partial \gamma_{(a)}}{\partial \psi_{(a)}^{\text{ti},0}} \mathbf{S}_{(a)}^{\text{ti},0} \otimes \mathbf{S}_{(a)}^{\text{ti},0} \quad (7.27)$$

whenever $\phi_{(a)}^{\text{trial}}$ is greater than zero, and it is zero otherwise. Here, $\phi_{(a)}^{\text{trial}}$ is the trial value of the saturation criterion in the current time step, i.e.

$$\phi_{(a)}^{\text{trial}} = \left\langle \psi_{(a)}^{\text{ti},0} - \psi_{\text{ini},(a)}^{\text{ti},0} \right\rangle - {}^k \gamma_{(a)}, \quad (7.28)$$

using eq. (7.13). This criterion evaluates whether an update of the saturation has to be performed. The discrete time steps with $t \in \{k+1t, {}^k t\}$ are considered for the numerical implementation. Here, values with the index ${}^{k+1}(\bullet)$ and ${}^k(\bullet)$ denote values at the current and the last time step, respectively. In order to obtain a clear notation, the index of the current time step is only assigned if necessary. If $\phi_{(a)}^{\text{trial}} > 0$ we have to fulfill $\phi_{(a)} = 0$ (eq. (7.14)) and the algorithmic current internal variable of the saturation term is computed by

$$\gamma_{(a)} = \left\langle \psi_{(a)}^{\text{ti},0} - \psi_{\text{ini},(a)}^{\text{ti},0} \right\rangle. \quad (7.29)$$

Otherwise, if $\phi_{(a)}^{\text{trial}} \leq 0$ it is set equal to the value of the last time step, i.e. $\gamma_{(a)} = {}^k \gamma_{(a)}$. Now, we define the algorithmic current internal variable of the damage term as

$$\beta_{(a)} = \left\langle \tilde{\beta}_{(a)} - \tilde{\beta}_{(a)}^{\text{ini}} \right\rangle \quad \text{with} \quad \tilde{\beta}_{(a)} = {}^k \tilde{\beta}_{(a)} + \left\langle \psi_{(a)}^{\text{ti},0} - {}^k \psi_{(a)}^{\text{ti},0} \right\rangle. \quad (7.30)$$

Following eq. (7.10) and eq. (7.30) and considering the derivative of the Macaulay brackets $\partial_X \langle X \rangle = \partial_X [\frac{1}{2}(|X| + X)] = \frac{1}{2}(\text{sign}[X] + 1)$, with the sign function $\text{sign}[X]$, we obtain

$$\begin{aligned} \frac{\partial D_{(a)}}{\partial \beta_{(a)}} &= -D_{s,(a)} \frac{\ln(1 - r_s)}{\beta_s} \exp \left(\frac{\ln(1 - r_s)}{\beta_s} \beta_{(a)} \right), \\ \frac{\partial \beta_{(a)}}{\partial \psi_{(a)}^{\text{ti},0}} &= \frac{1}{4} \left[\text{sign} \left(\tilde{\beta}_{(a)} - \tilde{\beta}_{(a)}^{\text{ini}} \right) + 1 \right] \left[\text{sign} \left(\psi_{(a)}^{\text{ti},0} - {}^k \psi_{(a)}^{\text{ti},0} \right) + 1 \right], \end{aligned} \quad (7.31)$$

<p>(I) Compute \mathbf{S}^{vol}, \mathbf{S}^{iso}, \mathbb{C}^{vol} and \mathbb{C}^{iso}</p> <p>(II) Do for $a = 1, 2$</p> <div style="border: 1px solid black; padding: 10px; margin: 10px 0;"> <p>(i) Compute effective transversely isotropic strain-energy function $\psi_{(a)}^{\text{ti},0}$</p> <p>(ii) Check initial damage state if $t < (t_{\text{ini}} - \epsilon)$, then go to (vi) else a) Read history ${}^k\psi_{(a)}^{\text{ti},0}$, ${}^k\tilde{\beta}_{(a)}$, ${}^k\psi_{\text{ini},(a)}^{\text{ti},0}$, ${}^k\tilde{\beta}_{(a)}^{\text{ini}}$ b) Compute $\tilde{\beta}_{(a)} = {}^k\tilde{\beta}_{(a)} + \langle \psi_{(a)}^{\text{ti},0} - {}^k\psi_{(a)}^{\text{ti},0} \rangle$ c) if $(t_{\text{ini}} - \epsilon) < t < (t_{\text{ini}} + \epsilon)$, then set $\psi_{\text{ini},(a)}^{\text{ti},0} = \psi_{(a)}^{\text{ti},0}$, $\tilde{\beta}_{(a)}^{\text{ini}} = \tilde{\beta}_{(a)}$ else set from history $\psi_{\text{ini},(a)}^{\text{ti},0} = {}^k\psi_{\text{ini},(a)}^{\text{ti},0}$, $\tilde{\beta}_{(a)}^{\text{ini}} = {}^k\tilde{\beta}_{(a)}^{\text{ini}}$</p> <p>(iii) Read history ${}^k\gamma_{(a)}$ and compute maximum damage saturation value a) Trial criterion $\phi_{(a)}^{\text{trial}} = \langle \psi_{(a)}^{\text{ti},0} - \psi_{\text{ini},(a)}^{\text{ti},0} \rangle - {}^k\gamma_{(a)}$ b) Check algorithmic saturation criterion if $\phi_{(a)}^{\text{trial}} > \epsilon$, then set $\gamma_{(a)} = \langle \psi_{(a)}^{\text{ti},0} - \psi_{\text{ini},(a)}^{\text{ti},0} \rangle$ else set from history $\gamma_{(a)} = {}^k\gamma_{(a)}$ c) Compute damage saturation value $D_{s,(a)} = D_{\infty} \left[1 - \exp \left(\frac{\ln(1 - r_{\infty})}{\gamma_{\infty}} \gamma_{(a)} \right) \right]$</p> <p>(iv) Compute internal variable $\beta_{(a)} = \langle \tilde{\beta}_{(a)} - \tilde{\beta}_{(a)}^{\text{ini}} \rangle$</p> <p>(v) Compute damage function $D_{(a)} = D_{s,(a)} \left[1 - \exp \left(\frac{\ln(1 - r_s)}{\beta_s} \beta_{(a)} \right) \right]$</p> <p>(vi) Compute transversely isotropic stress tensor a) Compute effective stress tensor $\mathbf{S}_{(a)}^{\text{ti},0} = 2\partial_{\mathbf{C}}\psi_{(a)}^{\text{ti},0}$ b) if $t > t_{\text{ini}}$, then $\mathbf{S}_{(a)}^{\text{ti}} = m' (1 - D_{(a)}) \mathbf{S}_{(a)}^{\text{ti},0}$ else $\mathbf{S}_{(a)}^{\text{ti}} = m' \mathbf{S}_{(a)}^{\text{ti},0}$</p> <p>(vii) Compute transversely isotropic part of the elasticity tensor (see Table 7.3)</p> </div> <p>(III) Compute total stress and elasticity tensors</p> $\mathbf{S} = \mathbf{S}^{\text{vol}} + \mathbf{S}^{\text{iso}} + \sum_{a=1}^2 \mathbf{S}_{(a)}^{\text{ti}} \quad \text{and} \quad \mathbb{C} = \mathbb{C}^{\text{vol}} + \mathbb{C}^{\text{iso}} + \sum_{a=1}^2 \mathbb{C}_{(a)}^{\text{ti}}$
--

Table 7.2: Algorithmic box (taken from Balzani et al. [2012]) for the computation of the stress and elasticity tensors. The initial values of the history variables at $k = 0$ are ${}^0\psi_{(a)}^{\text{ti}} = {}^0\tilde{\beta}_{(a)} = {}^0\psi_{\text{ini},(a)}^{\text{ti},0} = {}^0\tilde{\beta}_{(a)}^{\text{ini}} = {}^0\gamma_{(a)} = 0$, and the tolerance ϵ should be close to computer accuracy.

respectively. For the complete computation of the total tangent moduli \mathbb{C} the derivatives incorporated in eq. (7.27) are needed, which are given by

$$\begin{aligned}\frac{\partial D_{(a)}}{\partial D_{s,(a)}} &= 1 - \exp\left(\frac{\ln(1-r_s)}{\beta_s}\beta_{(a)}\right), \\ \frac{\partial D_{s,(a)}}{\partial \gamma_{(a)}} &= -D_\infty \frac{\ln(1-r_\infty)}{\gamma_\infty} \exp\left(\frac{\ln(1-r_\infty)}{\gamma_\infty}\gamma_{(a)}\right), \\ \frac{\partial \gamma_{(a)}}{\partial \psi_{(a)}^{\text{ti},0}} &= \frac{1}{2} \left[\text{sign}\left(\psi_{(a)}^{\text{ti},0} - \psi_{\text{ini},(a)}^{\text{ti},0}\right) + 1 \right],\end{aligned}\tag{7.32}$$

where we used eq. (7.10), eq. (7.12) and eq. (7.29). In Table 7.2 and Table 7.3 an overview of the algorithm to determine the stress and elasticity tensors is given. Before entering the supra-physiological state, the damage variable $D_{(a)}$ is set equal to zero. Only if the upper limit of the physiological domain is reached this damage algorithm is considered.

- | |
|--|
| <p>(i) Compute effective elasticity tensor $\mathbb{C}_{(a)}^{\text{ti},0} = 4\partial_{\mathbb{C}\mathbb{C}}^2 \psi_{(a)}^{\text{ti},0}$</p> <p>(ii) if $t > t_{\text{ini}}$, then</p> <p style="margin-left: 20px;">a) Compute derivatives from (7.31), (7.32)</p> $D'_{(a)} = \partial_{\beta_{(a)}} D_{(a)}, \quad \beta'_{(a)} = \partial_{\psi_{(a)}^{\text{ti},0}} \beta_{(a)},$ $D'_{(a)}{}^{D_s} = \partial_{D_{s,(a)}} D_{(a)}$ $D'_{s,(a)} = \partial_{\gamma_{(a)}} D_{s,(a)}, \quad \gamma'_{(a)} = \partial_{\psi_{(a)}^{\text{ti},0}} \gamma_{(a)},$ <p style="margin-left: 20px;">b) Compute parts of the transversely isotropic elasticity tensor</p> <ul style="list-style-type: none"> • $\mathbb{C}_{(a)}^{\text{ti}} := \mathbb{C}_{(a)}^{\text{eD}} = m'(1 - D_{(a)}) \mathbb{C}_{(a)}^{\text{ti},0} + m''(1 - D_{(a)}) \mathbf{S}_{(a)}^{\text{ti},0} \otimes \mathbf{S}_{(a)}^{\text{ti},0}$ • if $\left(\psi_{(a)}^{\text{ti},0} - k\psi_{(a)}^{\text{ti},0}\right) > \epsilon$, then <ul style="list-style-type: none"> $\mathbb{C}_{(a)}^D = - \left[m' + m''(1 - D_{(a)})\psi_{(a)}^{\text{ti},0} \right] D'_{(a)}\beta'_{(a)} \mathbf{S}_{(a)}^{\text{ti},0} \otimes \mathbf{S}_{(a)}^{\text{ti},0}$ $\mathbb{C}_{(a)}^{\text{ti}} \leftarrow \mathbb{C}_{(a)}^{\text{ti}} + \mathbb{C}_{(a)}^D$ • if $\phi_{(a)}^{\text{trial}} > \epsilon$, then <ul style="list-style-type: none"> $\mathbb{C}_{(a)}^{D_s} = - \left[m' + m''(1 - D_{(a)})\psi_{(a)}^{\text{ti},0} \right] D'_{(a)}{}^{D_s} D'_{s,(a)} \gamma'_{(a)} \mathbf{S}_{(a)}^{\text{ti},0} \otimes \mathbf{S}_{(a)}^{\text{ti},0}$ $\mathbb{C}_{(a)}^{\text{ti}} \leftarrow \mathbb{C}_{(a)}^{\text{ti}} + \mathbb{C}_{(a)}^{D_s}$ <p>else $\mathbb{C}_{(a)}^{\text{ti}} = m' \mathbb{C}_{(a)}^{\text{ti},0} + m'' \mathbf{S}_{(a)}^{\text{ti},0} \otimes \mathbf{S}_{(a)}^{\text{ti},0}$</p> |
|--|

Table 7.3: Algorithmic box (from Balzani et al. [2012]) for the computation of the transversely isotropic elasticity tensor $\mathbb{C}_{(a)}^{\text{ti}}$. The tolerance ϵ should be close to computer accuracy.

7.4 Specific constitutive models

In this section two specific constitutive models are investigated, which meet the construction principle mentioned in Section 7.3. They are adjusted to experimental data in order to analyze their ability to capture the behavior of soft biological tissues, in particular of human carotid arteries, under cyclic uniaxial extensions. In general form, the strain-energy functions read

$$\psi_{(\text{HGO})} := \psi^{\text{vol}} + \psi^{\text{iso}} + \sum_{a=1}^2 \psi_{(a)}^{\text{ti,HGO}} \quad \text{and} \quad \psi_{(\text{BNSH})} := \psi^{\text{vol}} + \psi^{\text{iso}} + \sum_{a=1}^2 \psi_{(a)}^{\text{ti,BNSH}}. \quad (7.33)$$

For the isotropic response the neo-Hookean function $\psi_{\text{NH}}^{\text{iso}}$ (eq. (5.5)) is used, and in order to enforce the incompressibility constraint the function $\psi_{\text{P}}^{\text{vol}}$ is applied, see eq. (5.6).

The first transversely isotropic function is a combination of the function $\psi_{(a)}^{\text{ti,HGO}_1}$ (eq. (5.15)) and the fiber-dispersion approach presented in Gasser et al. [2006]. Here, an additional scalar parameter κ is introduced, which reflects the variation in dispersion of collagen-fiber orientations in soft biological tissues. Thus, the range of κ characterizes a state between isotropic distribution with equally distributed collagen fibers and ideal alignment of collagen fibers. The individual expressions in eq. (7.17) can be identified as

$$m(P_{(a)}) = \frac{k_1}{2k_2} \left\{ \exp(k_2 \langle P_{(a)} \rangle^2) - 1 \right\}, \quad \bar{P}_{(a)} = \psi_{(a)}^{\text{ti},0} = \kappa I_1 + (1 - 3\kappa) J_4^{(a)}, \quad c = 1, \quad (7.34)$$

with the restrictions $k_1 > 0$, $k_2 > 0$ and $\kappa \in [0, 1/3]$. Now, the first transversely isotropic strain-energy function is completely given by

$$\psi_{(a)}^{\text{ti,HGO}} = \frac{k_1}{2k_2} \left\{ \exp \left[k_2 \left\langle (1 - D_{(a)}) \left(\kappa I_1 + (1 - 3\kappa) J_4^{(a)} \right) - 1 \right\rangle^2 \right] - 1 \right\}. \quad (7.35)$$

As second function a power function proposed in Balzani et al. [2006a] is combined with the fiber-dispersion approach and we identify

$$m(P_{(a)}) = \alpha_1 \langle P_{(a)} \rangle^{\alpha_2}, \quad \bar{P}_{(a)} = \psi_{(a)}^{\text{ti},0} = \kappa I_1 + \left(1 - \frac{3}{2}\kappa \right) K_3^{(a)}, \quad c = 2. \quad (7.36)$$

Here, the restrictions $\alpha_1 > 0$, $\alpha_2 > 1$ (for smooth tangent moduli $\alpha_2 > 2$), and $\kappa \in [0, 2/3]$ has to be enforced. Now, the complete expression for the second transversely isotropic strain-energy function is

$$\psi_{(a)}^{\text{ti,BNSH}} = \alpha_1 \left\langle (1 - D_{(a)}) \left[\kappa I_1 + \left(1 - \frac{3}{2}\kappa \right) K_3^{(a)} \right] - 2 \right\rangle^{\alpha_2}. \quad (7.37)$$

As mentioned in Section 5.1.2 the anisotropic term of the models is only activated if the fibers are extended, that is when $(1 - D_{(a)})\psi_{(a)}^{\text{ti},0} > c$.

It should be noticed, that $m(P_{(a)})$ is convex and monotonically increasing and P is polyconvex and zero in the reference state for both models. Therefore, the two models satisfy the construction principles in the physiological domain before reaching the initial damage state, see Section 5.1.2, and remain polyconvex in the hyperelastic regime.

7.5 Adjustment to experimental data

In the following the models are adjusted to experimental data, which has been obtained from uniaxial extension tests with two strip specimens from the media of a human carotid artery (one in circumferential direction, and the other one in the axial direction, i.e. $n_e = 2$), see Balzani et al. [2012]. The specimens were excised during autopsy and then tested within 24 hours after death. In order to accomplish pre-conditioning, five loading and unloading cycles were performed prior to testing for each test to achieve repeatable stress-strain curves in the physiological loading domain. Then, uniaxial extension tests in 0.9% NaCl solution at 37°C were performed with continuous recording of the tensile force, the strip width and the gage length. Details on the customized tensile testing machine are given in Schulze-Bauer et al. [2002b].

Physiological loading domain. In order to adjust the model response in the purely physiological domain rather moderate loads were investigated in the first loading cycle. Here, a number of $n_{mp} = 49$ measuring points for the axial and $n_{mp} = 43$ measuring points for the circumferential tension test were created. Then the two models $\psi_{(HGO)}$ and $\psi_{(BNSH)}$ in eq. (7.33) were adjusted to the experimental data using the method mentioned in Section 6.1. The achieved material parameters are given Table 7.4.

	c_1	k_1	k_2	α_1	α_2	κ	β_f	\bar{r}
	[kPa]	[kPa]	[-]	[kPa]	[-]	[-]	[°]	[-]
$\psi_{(HGO)}$	6.56	1482.38	564.81	-	-	0.16	37.03	3.7×10^{-2}
$\psi_{(BNSH)}$	7.54	-	-	984.29	2.18	0.055	39.48	3.6×10^{-2}

Table 7.4: Material parameters and resulting total error \bar{r} (eq. (6.10)) of the two models (eq. (7.33)) for the media of a human carotid artery in the physiological loading domain.

The resulting stress-strain response of the two models in comparison to experimental data is shown in Fig. 7.4. Additionally, the relative error r is depicted in Fig. 7.5, in order to show the accurate match of the models with the experimental data. The relative error r (eq. (6.9)) as well as the total error \bar{r} (eq. (6.10)), given in Table 7.4, are relatively small.

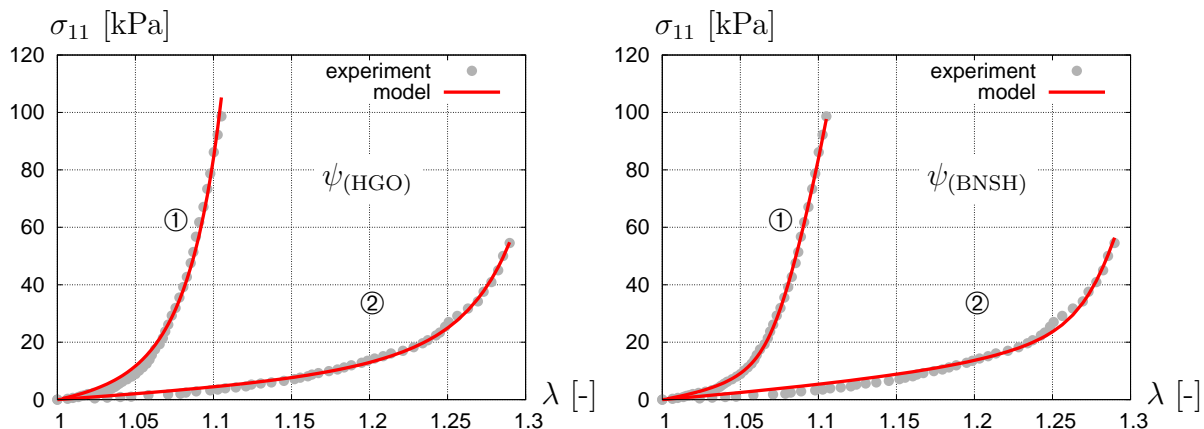


Figure 7.4: Comparison of the constitutive model response ($\psi_{(HGO)}$ and $\psi_{(BNSH)}$) with experimental data from uniaxial extension tests performed with strip specimens of the media of a human carotid artery in circumferential ① and axial ② directions.

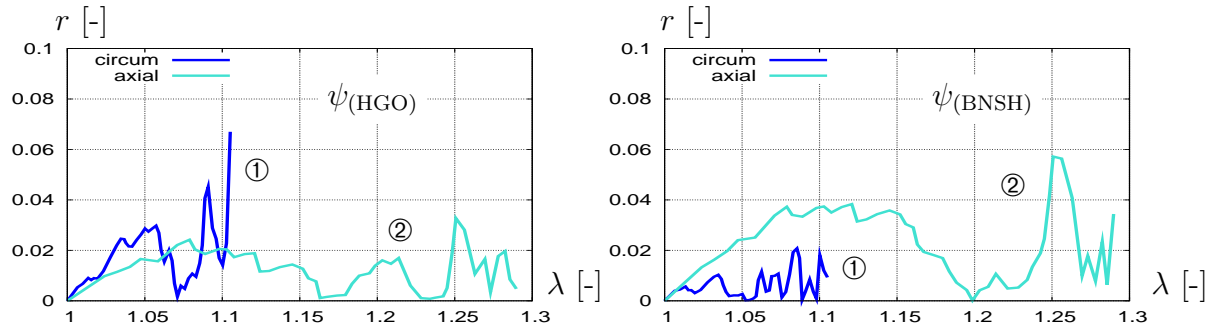


Figure 7.5: Relative error r corresponding to Table 7.4. For the model response the two strain-energy functions $\psi_{(\text{HGO})}$ and $\psi_{(\text{BNSH})}$ are used.

Supra-physiological loading domain. In the following the comparison of the model response to experimental data obtained from a significantly increased load corresponding to the supra-physiological loading domain is investigated. Cyclic uniaxial extension tests in the circumferential and in the axial direction were performed on the same specimens, see the stress-strain response in 7.6a, where a strong anisotropy as well as a pronounced softening hysteresis is visible.

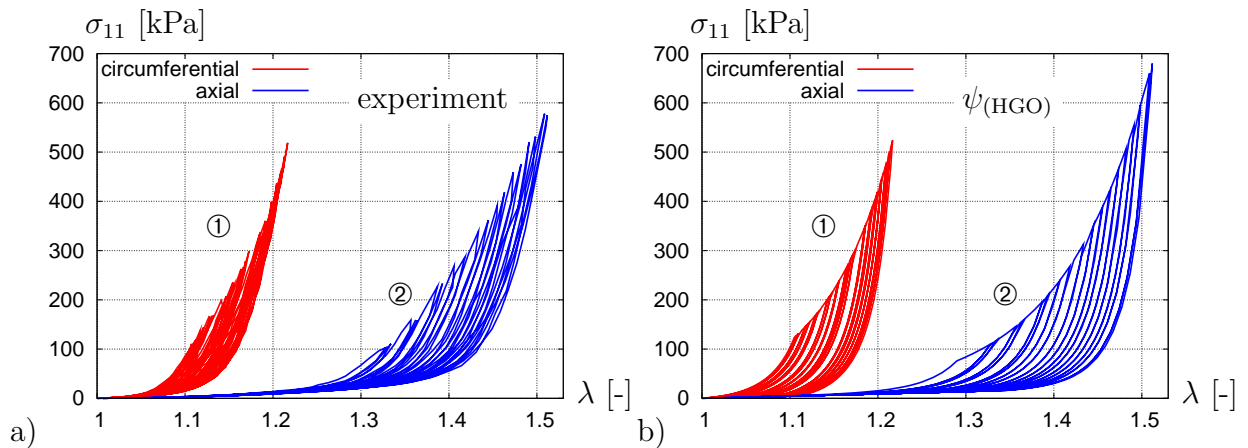


Figure 7.6: Cyclic uniaxial extension tests of the media of a human carotid artery in circumferential ① and axial ② directions: a) experimental data, and b) results of the constitutive model $\psi_{(\text{HGO})}$ using the material parameters given in Tables 7.4 and 7.5.

For the least-squares fit, two different procedures are taken into account:

i) The (hyperelastic) parameters (Table 7.4) of the constitutive model $\psi_{(\text{HGO})}$ are fixed, and only the damage parameters are adjusted. The resulting material parameters are listed in Table 7.5.

	D_∞	γ_∞	β_s	\bar{r}
	[kPa]	[kPa]	[-]	[-]
$\psi_{(\text{HGO})}$	0.99	6.52	0.37	0.11

Table 7.5: Damage parameters and error measure \bar{r} for the constitutive model $\psi_{(\text{HGO})}$ for the media of a human carotid artery in the supra-physiological loading domain. The adjustment was performed with fixed hyperelastic parameters.

The stress-strain response of the proposed model $\psi_{(\text{HGO})}$ is shown in Fig. 7.6b. Qualitatively and quantitatively the model correlates good with the experimental data and a relatively small error measure \bar{r} is obtained, see Table 7.5. Nevertheless, a slight overestimation of the exponential character is visible.

ii) Suitable bounds for the (hyperelastic) parameters on the basis of the fitted parameters given in Table 7.4 are prescribed. Then, the hyperelastic as well as the damage parameters are fitted to the experimental data, see Table 7.6.

	c_1	k_1	k_2	α_1	α_2	κ	β_f	D_∞	γ_∞	β_s	\bar{r}
	[kPa]	[kPa]	[-]	[kPa]	[-]	[-]	[°]	[kPa]	[kPa]	[-]	[-]
$\psi_{(\text{HGO})}$	7.50	1288.97	400.0	-	-	0.2	35.06	0.99	6.67	0.001	0.137
$\psi_{(\text{BNSH})}$	9.02	-	-	1400.0	2.20	1e-8	39.87	0.96	17.98	0.06	0.08

Table 7.6: Material parameters and error measure \bar{r} of the two models $\psi_{(\text{HGO})}$ and $\psi_{(\text{BNSH})}$ for the media of a human carotid artery in the supra-physiological loading domain. For the adjustment suitable bounds for the (hyperelastic) parameters, based on the results given in Table 7.4, have been considered.

As a result, the hyperelastic response is not as accurately mapped as above. Furthermore, a low sensitivity of the overall mechanical response with respect to changes in β_s in the range of values close to zero, i.e. for $\beta_s < 0.001$ was observed, leading to the additional constraint $\beta_s \geq 0.001$. The stress-strain response of the models $\psi_{(\text{HGO})}$ and $\psi_{(\text{BNSH})}$ is depicted in Fig. 7.7a and Fig. 7.7b, respectively. The correlation between the experiments and both models is qualitatively and quantitatively good. This impression is supported by a relatively small error measure \bar{r} , see Table 7.6. Nevertheless, the correlation is not perfect: using the model $\psi_{(\text{HGO})}$ the exponential character is slightly overestimated, as observed by the previous adjustment; using the model $\psi_{(\text{BNSH})}$ this characteristic is underestimated.

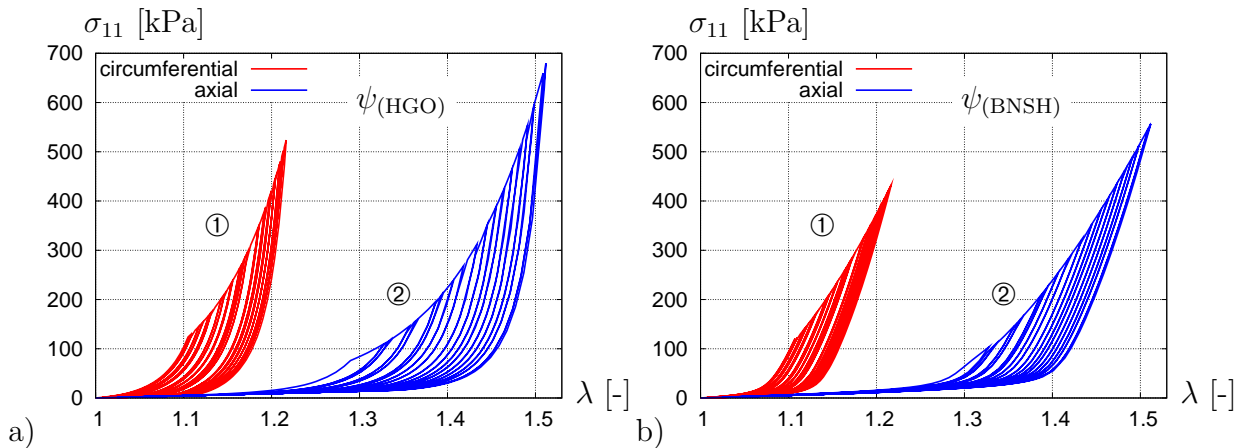


Figure 7.7: Cyclic uniaxial tension tests of the media of a human carotid artery in circumferential ① and axial ② directions: a) results of the constitutive model $\psi_{(\text{HGO})}$, and b) results of the constitutive model $\psi_{(\text{BNSH})}$. The material parameters are given in Table 7.6.

It should be noticed, that the remanent strain present in the fibers after unloading can not be observed in the Figs. 7.6 and 7.7. This is due to the superposition with the stresses in the matrix material, in which no remanent effects take place.

7.6 Numerical simulation of an arterial wall

In this section a numerical example of a two-dimensional cross-section of an artery with a pronounced atherosclerotic plaque is discussed, in order to show the applicability of the anisotropic damage model to finite-element simulations. The cross-section of the artery and its components are determined by high-resolution Magnetic Resonance Imaging (hrMRI) and histological analysis, see Fig. 7.8a. The identified components are non-diseased intima, fibrous cap, i.e. the fibrotic part at the luminal border, fibrotic intima at the medial border, calcification, lipid pool, non-diseased media, diseased fibrotic media, and adventitia. The cross-section of the arterial model was developed based on the hrMRI image and discretized with 6 048 quadratic triangular elements, see Fig. 7.8b. Here, the fibrotic intima at the medial border and the diseased fibrotic media are combined and treated as fibrotic media. Since the non-diseased intima has secondary importance with respect to the mechanical behavior we do not account for it in the numerical simulation.

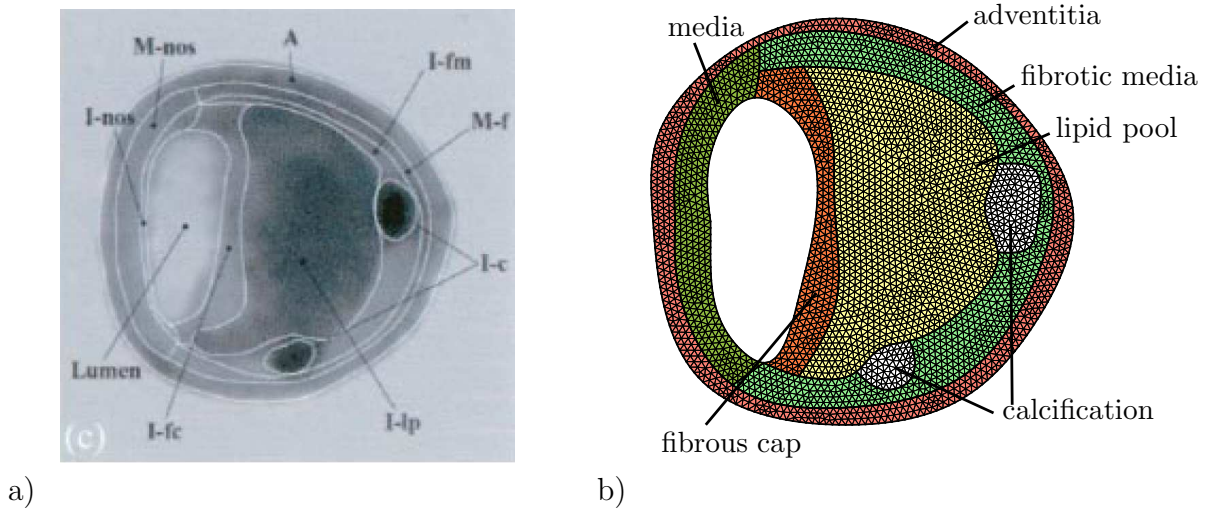


Figure 7.8: a) Human external iliac artery: high-resolution magnetic resonance image, filtered and (manually) segmented, taken from Holzapfel et al. [2004b], page 659. b) Cross-section of the arterial model discretized with 6 048 quadratic triangular finite elements; the considered components are adventitia, non-diseased media, fibrotic (diseased) media, fibrous cap, lipid pool, and calcification.

We use the constitutive model $\psi_{(\text{HGO})}$ and the adjusted parameters from Table 7.4 and Table 7.5 (Section 7.5) for the media. The set of material parameters used for the simulation of the adventitia and the plaque components are listed in Table 7.7.

	c_1 [kPa]	k_1 [kPa]	k_2 [-]	κ [-]	β_{f} [°]	D_{∞} [kPa]	γ_{∞} [kPa]	β_s [-]
adventitia	4.0	1640.23	115.63	0.097	45.60	0.99	10.84	7.36
fibrotic media	21.12	1951.48	925.37	0.095	25.55	0.99	6.52	0.37
fibrous cap	24.12	4778.44	1023.59	0.12	53.18	0.99	6.52	0.37
calcification	2250.0	—	—	—	—	—	—	—
lipid pool	2.5	—	—	—	—	—	—	—

Table 7.7: Hyperelastic and damage parameters of adventitia and plaque components.

For the simulation the parameters $r_s = r_\infty$ are set to 0.99. The parameters of the function ψ_P^{vol} (ε_1 and ε_2) are chosen such that $\det \mathbf{F} = 1 \pm 1\%$, see Table 7.8. The lower values for the calcification are due to the assumption that it is not incompressible.

	ε_1 [kPa]	ε_2 [-]
adventitia, non-diseased media, fibrotic media, fibrous cap	50.0	20.0
calcification	5.0	2.0
lipid pool	20.0	10.0

Table 7.8: Parameters of the penalty function ψ_P^{vol} for the different arterial constituents.

The material parameters of the adventitia are adjusted to experimental data of a human carotid artery. The stress-strain response of the model and the experimental data are depicted in Fig. 7.9. It can be observed that the model and experimental curves fit well.

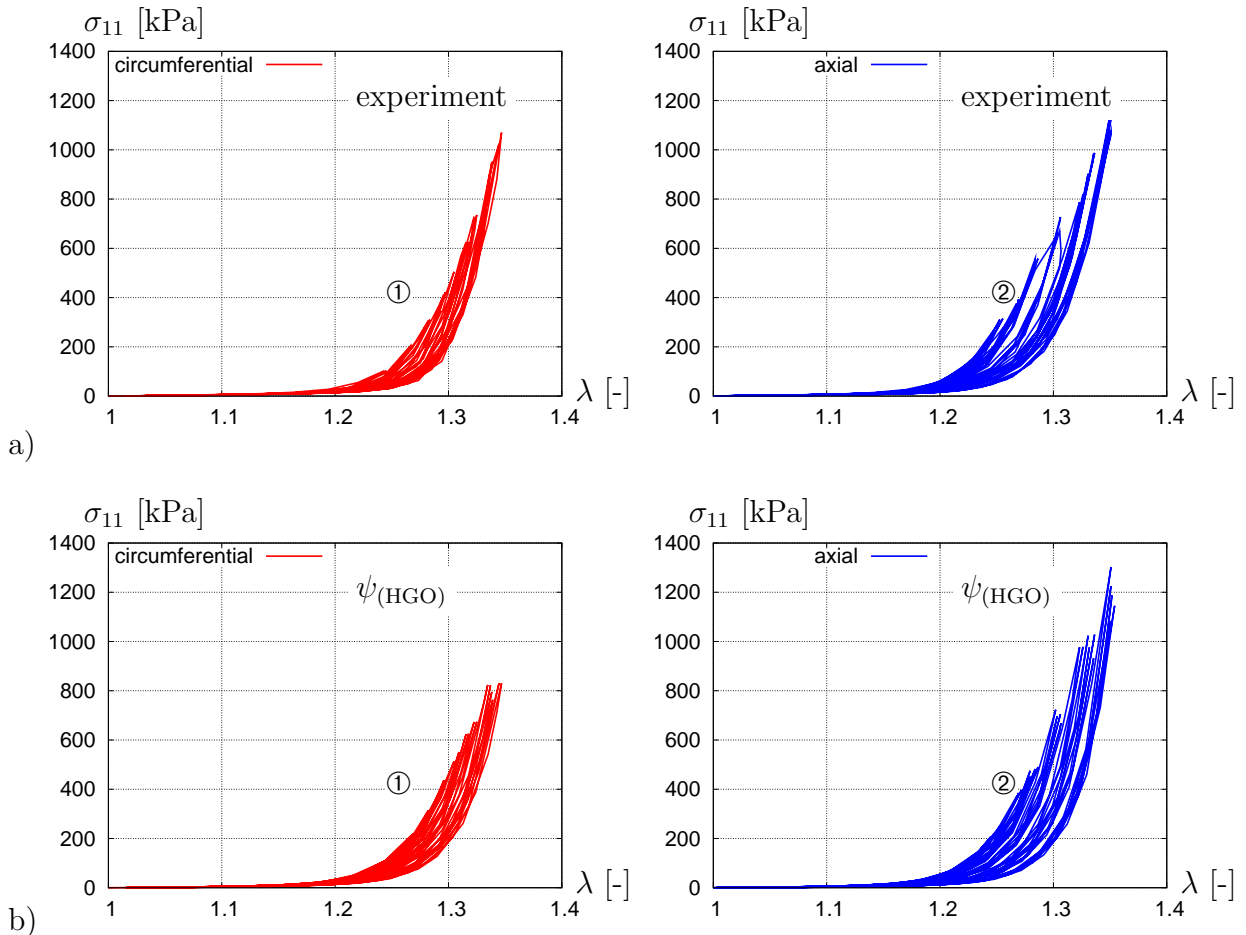


Figure 7.9: Cyclic uniaxial extension tests of the a) adventitia of a human carotid artery in circumferential ① and axial ② direction; b) associated response of the model $\psi_{(\text{HGO})}$.

For the fibrous cap and the fibrotic media cyclic extension tests are available only in the physiological loading range. Therefore, only the (hyperelastic) parameters are adjusted to experiments from Holzapfel et al. [2004b], see the stress-strain response of the model

and the experimental data in Fig. 7.10a. For the supra-physiological loading range the damage parameters are adopted from the adjustment of the media. The calcified regions and the lipid pool are modeled by the strain-energy function given in eq. (7.33)₁ with $\psi_{(a)}^{ti,HGO} = 0$, i.e. it is assumed that they are isotropic materials. The corresponding material parameters are chosen in accordance with the assumptions and investigations of Holzapfel et al. [2004b] (page 660 and 661, respectively). Thus, the mechanical response of the calcified regions close to the reference configuration exhibits an average Young's Modulus of 12 ± 4.7 MPa and the lipid pool is a butter-like, incompressible fluid that can be described with material parameters, which cause a significantly lower stiffness compared with the other components. Damage is neither considered in the lipid pool nor in the calcification due to the minor role of damage effects in these regions.

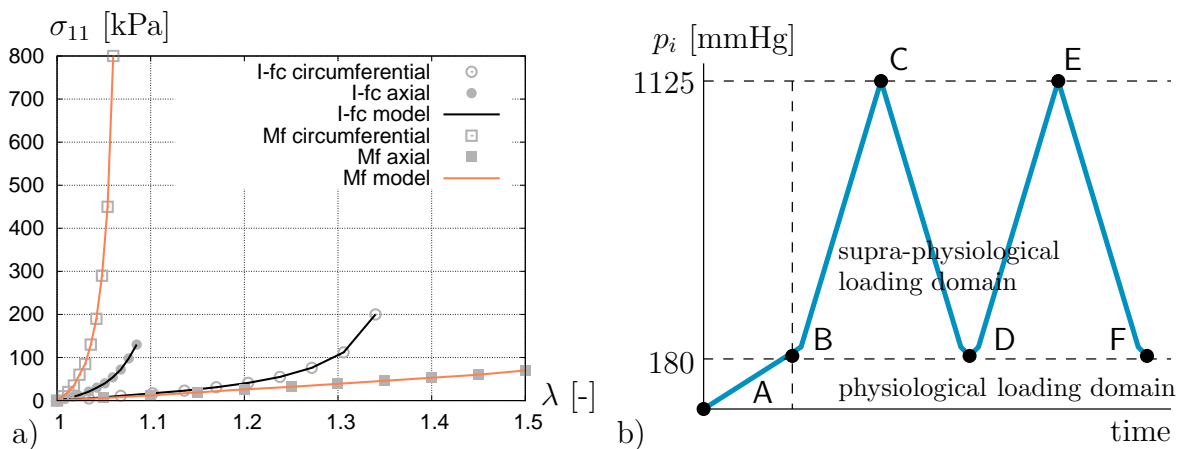


Figure 7.10: a) Uniaxial extension tests and constitutive model response of the fibrous cap (I-fc) and the fibrotic media (Mf). Symbols: experimental measuring points; Solid lines: constitutive model response. b) Variation of the applied internal pressure p_i [mmHg].

In Fig. 7.10b the applied loading path of the simulation is shown. Here, six markers (A-F) characterize important points in the loading path. In point A the artery is unloaded. Then an internal pressure of 24.0 kPa ($\hat{=}$ 180.0 mmHg) is applied, which characterizes the upper bound for the hypertensive pressure and furthermore the initial damage state (point B). Until point C the internal pressure increases to a value of 150.0 kPa ($\hat{=}$ 1125.0 mmHg). Up to this pressure level an over-expansion of the artery takes place. In the next step the internal pressure is decreased to the physiological state (24.0 kPa, point D). Path B to D can be interpreted as a balloon-angioplasty procedure. If the first overload is not sufficient for a successful balloon angioplasty treatment, the over-expansion procedure has to be repeated. This is simulated by considering of the loading path D to F. Until the final point of blood pressure in point F is reached, a total number of 140 load steps are applied. A time-stepping scheme is used in order to define the step size automatically ($\Delta t^{ini} = 0.0001$, $n_{it}^{max} = 6$, $n_{it}^{min} = 5$, $\Delta t^{max} = 0.2$), see Section 8.2 for further explanations.

The results of the numerical example are depicted in Fig. 7.11, Fig. 7.12, and Fig. 7.13. In Fig. 7.11 the distribution of the normalized damage variable $D_{(1)}/\max D_{(1)}$ under blood pressure is shown ($\max D_{(1)}$ is the maximum damage value reached in the simulation). Here, Fig. 7.11a represents the situation after a first over-expansion associated to point D and Fig. 7.11b represents the situation after the second over-expansion (point F). The first overstretch mainly induces damage in the media and the fibrous cap, which increases

during the second overstretch and reaches a higher maximum value. Furthermore, a pronounced concentration is observable at the interface of the media and the fibrous cap.

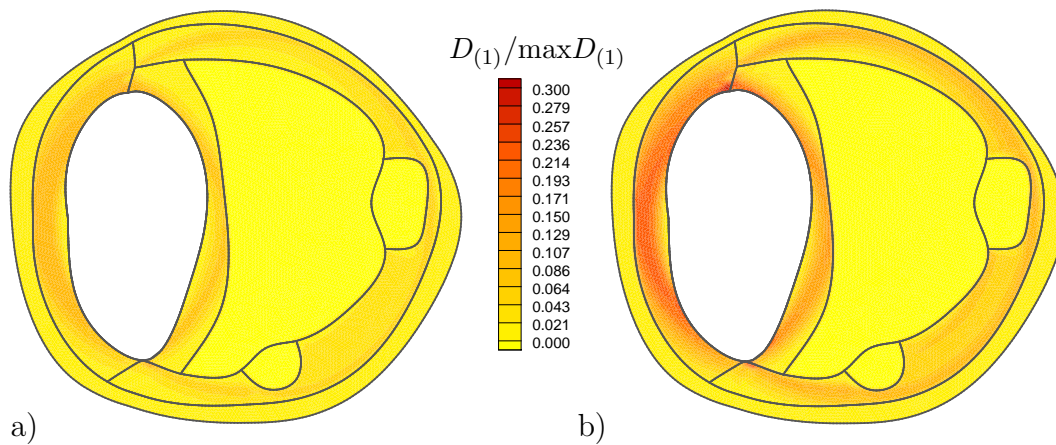


Figure 7.11: Distribution of the normalized damage variable $D_{(1)}/\max D_{(1)}$ in an arterial cross-section under blood pressure of 24 kPa after a) one over-expansion (point D in Fig. 7.10b), and b) after two over-expansions (point F in Fig. 7.10b).

In another numerical simulation axial residual strains of 5% were taken into account in order to analyze the assumption that they have a considerable influence on the damage evolution. It should be noticed, that circumferential residual strains were not considered in these simulations. This is a reasonable simplification, since the residual stresses are significantly lower compared with the stresses obtained during an arterial over-expansion. Firstly, the distribution of $(J_4^{(1)})^{1/2}$, which is associated to the stretch in the fiber direction, is taken under consideration in the physiological undamaged configuration at a blood pressure of 24 kPa (point B), see Fig. 7.12. Comparison of Fig. 7.12a (simulation without axial residual strains) and Fig. 7.12b (simulation with axial residual strains of 5%) makes visible, that the fiber stretch is higher if residual strains are taken into account. However, the difference is rather low.

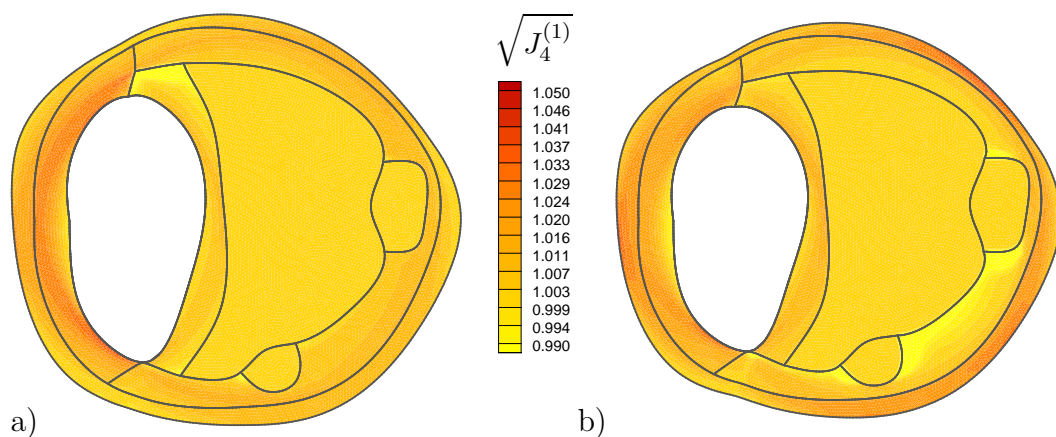


Figure 7.12: Distribution of the stretch $(J_4^{(1)})^{1/2}$ in the fiber direction of a loaded but undamaged artery at internal pressure of 24 kPa (point B in Fig. 7.10b): a) without axial residual strains and b) with axial residual strains of 5%.

Now we again take a look at the normalized damage variable $D_{(1)}/\max D_{(1)}$. In Fig. 7.13 the distribution associated to point E is shown, i.e. at the second over-expansion of the artery: again we compare the two cases in which no residual strains are taken into account (Fig. 7.13a) and residual strains of 5% are considered (Fig. 7.13b). Here, the difference between the two cases is much more pronounced as observed in Fig. 7.12: the normalized damage values are up to four times higher if we apply axial residual strains. Especially from a medical perspective, this is an interesting result since the rather high damage values at the fibrous-cap/media interface could increase the risk of plaque rupture.

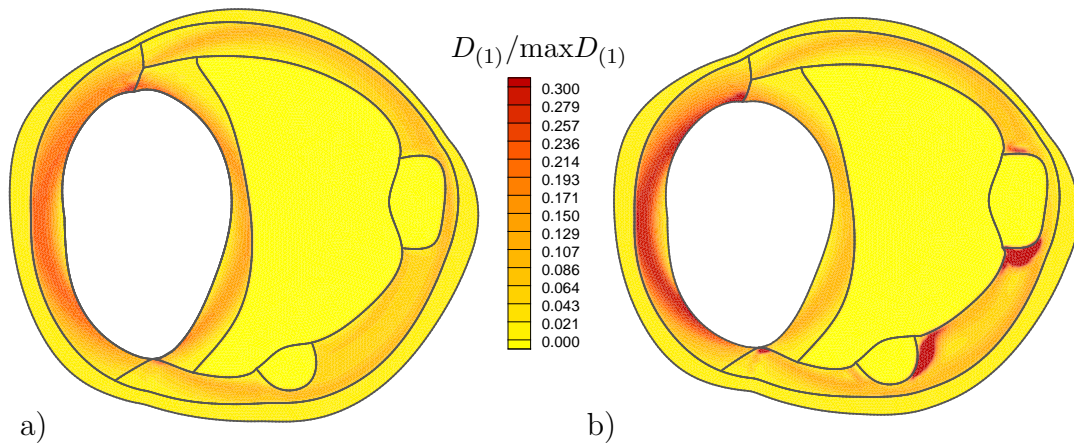


Figure 7.13: Distribution of the normalized damage variable $D_{(1)}/\max D_{(1)}$ in an arterial cross-section under blood pressure of 150 kPa (point E in Fig. 7.10b): a) without and b) with axial residual strains of 5%.

In order allow the comparison of Fig. 7.11 and Fig. 7.13 the same maximum damage value of $\max D_{(1)} = 0.0951$ has been used for the calculation of the normalized value.

8 Numerical analysis of the robustness of the Penalty-Method and the Augmented-Lagrange-Method

In this chapter the numerical robustness and the computational costs of three-dimensional simulations is investigated with regard to the use of a pure Penalty approach and with regard to the use of an Augmented-Lagrange approach with a nested or a simultaneous iteration of the Lagrange multiplier. The theory behind the different approaches was discussed in Section 5.2. For a proper comparison between the approaches we will make use of an automatic time step size control described in Section 8.2.

In Section 8.1 the constitutive model is described, which is used in the three-dimensional numerical simulations. The results of the simulations are discussed in Section 8.4 (1 mm long arterial segment) and in Section 8.5 (patient-specific 10 mm long arterial segment). Because of the high number of degrees of freedom (more than a million) in case of the simulation of the longer segment, the parallel implementation of FEAP¹² and the FETI-DP¹³ domain decomposition method is used, which is briefly discussed in Section 8.3. A part of the following results is published in Brinkhues et al. [2012].

8.1 Constitutive model

In the three-dimensional simulations that are considered in this section arterial walls are investigated, which are composed of media, adventitia and degenerated tissue. The degenerated tissue consists of plaque and in the numerical simulation in Section 8.4 additionally of calcified regions and extracellular lipid. The strain-energy function of the underlying media and adventitia material is

$$\psi = \psi_{\text{NH}}^{\text{iso}} + \psi_{\text{P}}^{\text{vol}} + \sum_{a=1}^2 \psi_{(a)}^{\text{ti,HGO}_2}, \quad (8.1)$$

see the individual energy functions in eq. (5.5), eq. (5.6), and eq. (5.16). For the identification of the parameters c_1 , k_1 , k_2 and β_f for the adventitia and the media the material model (eq. (8.1)) is adjusted to experimental data^{10 (page 54)} with the adjustment strategy proposed in Section 6.1. In Table 8.1 the resulting parameters are summarized.

	c_1	k_1	k_2	β_f	penalty		augmented	
	[kPa]	[kPa]	[-]	[°]	ε_1 [kPa]	ε_2 [-]	ε_1 [kPa]	ε_2 [-]
media	9.23	192.86	2626.84	43.9	360.0	9.0	10.0	4.0
adventitia	7.17	3.68e-3	51.15	54.7	70.0	8.5	10.0	4.0

Table 8.1: Material parameters for the media and the adventitia with penalty parameters ε_1 and ε_2 for the Penalty approach and the Augmented-Lagrange approach.

Since the adjustment is done under the assumption that the material is quasi-incompressible, the incompressibility constraint has to be enforced separately in the numerical simulation. Thus, the penalty parameters have to be chosen sufficiently large in case of the Penalty approach, such that $\det \mathbf{F} \approx 1$, see also Table 8.1. The volumetric

¹²Finite Element Analysis Program, R. L. Taylor, University of California.

¹³Finite Element Tearing and Interconnecting - Dual Primal.

change produced by the chosen penalty parameters is only known subsequently. Using an Augmented-Lagrange approach lower penalty parameters can be chosen, but an accurate stopping criterion has to be taken into account (i.e. a sufficiently small tolerance value TOL, see Fig. 5.1 and Fig. 5.2 must be used). Thus, the volumetric change is controlled during the iteration process by satisfying the element-wise condition $|\det \mathbf{F} - 1| \leq \text{TOL}$.

The stress-strain response of the material model in consideration of the adjusted parameters is shown in Fig. 8.1. Here, it is clearly visible that the experimental data and the material model fit very well for the media as well as for the adventitia in both directions, i.e. in axial and circumferential direction. Furthermore, the stress-strain response remains similar under consideration of a Penalty approach, displayed in Fig. 8.1a, compared to the use of an Augmented-Lagrange approach, see Fig. 8.1b.

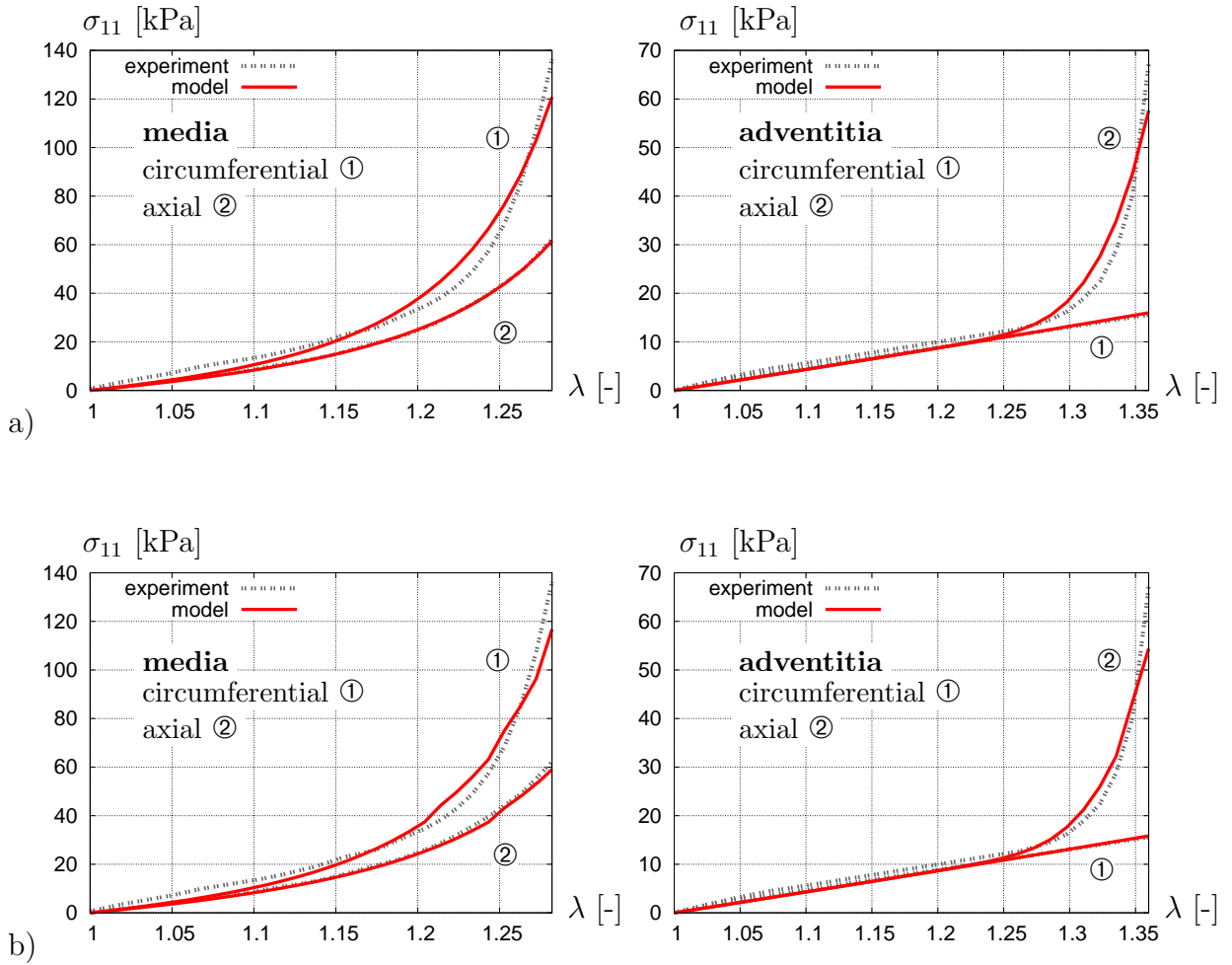


Figure 8.1: Comparison of the stretch-strain response of the experiments and the material model in a uniaxial extension test (media and adventitia) under consideration of a) a Penalty approach and b) an Augmented-Lagrange approach.

For the description of the plaque components the isotropic Mooney-Rivlin strain-energy function $\psi_{\text{MR}}^{\text{iso}}$ (eq. (5.3)) is used. For the extracellular lipid and the calcified regions the isotropic part of the energy function is taken into account. The parameters of the degenerated tissue are chosen as listed in Table 8.2.

	η_1	η_2	η_3	c_1	ε_1	ε_2
	[kPa]	[kPa]	[-]	[kPa]	[kPa]	[-]
plaque	80.0	250.0	2000.0	–	–	–
calcified regions	–	–	–	6800.0	50.0	10.0
extracellular lipid	–	–	–	700.0	5250.0	10.0

Table 8.2: Material parameters of the degenerated tissue.

Penalty term. The penalty term ψ_P^{vol} in eq. (8.1) models the incompressibility by penalizing deviations from the constraint $\det \mathbf{F} = 1$. The influence of the penalty parameter on the penalty function is shown in Fig. 8.2. Here, the curve of the penalty function used for the Penalty-Method is compared with the curve used in the Augmented-Lagrange-Method. It is clearly visible, that the curve belonging to the Penalty approach is very steep compared to the one belonging to the Augmented-Lagrange approach.

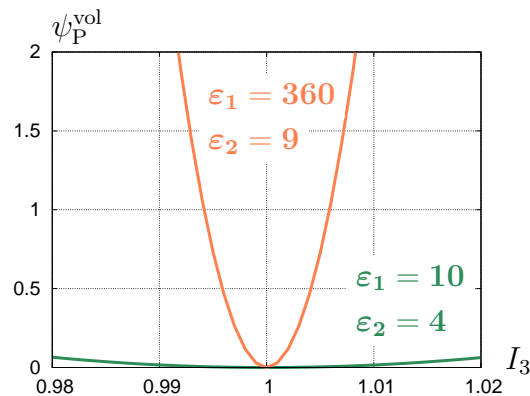


Figure 8.2: Comparison of the penalty function $\psi_P^{\text{vol}} = \varepsilon_1(I_3^{\varepsilon_2} + I_3^{-\varepsilon_2} - 2)$ for the two sets of parameters (Penalty approach and Augmented-Lagrange approach) for the media, see Table 8.1.

The second derivative of the penalty function is related to the material tangent. This derivative with respect to the invariant I_3 is given by

$$\frac{\partial^2 \psi}{\partial^2 I_3} = \varepsilon_1 \varepsilon_2 \left((\varepsilon_2 - 1) I_3^{\varepsilon_2 - 2} + \frac{\varepsilon_2 + 1}{I_3^{\varepsilon_2 + 2}} \right), \quad (8.2)$$

which grows linearly with ε_1 and exponentially with ε_2 . Thus, it may have a bad influence on the condition number of the stiffness matrix, i.e. the condition number may deteriorate.

8.2 Automatic time stepping

In order to ensure a proper comparison between the different approaches an automatic time stepping scheme is used, where the size of the incremental time steps is controlled. It should be noticed, that the notation “time” is used in the sense of a “pseudo” time. Here, the initial time step size Δt^{ini} is chosen. During the simulation the step size is reduced automatically by $\Delta t = \Delta t \cdot 10^{-1/5}$, if more than n_{it}^{max} Newton iterations are needed. On the other hand, if less than n_{it}^{min} Newton iterations are needed, the time step size is increased by $\Delta t = \Delta t \cdot 10^{1/5}$. The maximum time step size is bounded from above by Δt^{max} .

Regarding the nested Augmented-Lagrange approach only the number of Newton iterations in the first Newton step is considered. Generally, the later Newton steps converge faster than the first step. In the simultaneous Augmented-Lagrange approach (SAL) the iteration for the Lagrange multiplier is performed simultaneously with the Newton correction. As mentioned in Section 5.2.3 this can be seen as an inexact Newton method. Therefore, the bounds n_{it}^{\max} and n_{it}^{\min} are chosen higher.

8.3 FEAP and FETI-DP Method

The pre- and postprocessing of the computation is done by FEAP¹² (page 79), while the FETI-DP¹³ (page 79) method is used to subdivide the domain and to solve the solution vector with a parallel solution strategy. Within our parallel solver environment we use MPI¹⁴, PETSc¹⁵, UMFPACK¹⁶ and ACML¹⁷.

One global iteration can be divided into the following main steps:

- i) FEAP: Computation of element stiffnesses and element right-hand-sides and transferring the computed values by the use of an interface to the FETI-DP solver.
- ii) FETI-DP: Decomposition of the whole domain into subdomains, assembling of the systems of equations for all subdomains, and computation of the solution vector by the parallel solver.
- iii) Transferring the solution vector by the use of an interface to FEAP.
- iv) FEAP: Update of the displacement vector.

In this work the classical Newton-Krylov-FETI-DP approach is used. Here, firstly the linearization is done and thereafter the linearized systems are solved using the FETI-DP domain decomposition method.

FETI-DP domain decomposition method In Farhat and Roux [1991] FETI domain decomposition methods were first introduced. In the framework of domain decomposition methods an approximate inverse is built from solving small problems on subdomains and a small global problem. For an overview on domain decomposition methods see the textbooks Smith et al. [1996], Quarteroni and Valli [1999], and Toselli and Widlund [2005]. The more recent FETI-DP domain decomposition methods were proposed in Farhat et al. [2000a, 2001] and enhanced in, for example, Klawonn and Widlund [2001, 2002, 2005, 2006], Klawonn et al. [2002], Klawonn [2006], Klawonn and Rheinbach [2006, 2007a], Klawonn et al. [2011]. By using FETI methods, large structural-mechanics problems can be solved on massively parallel machines, see for example Farhat et al. [2000b], Bhardwaj et al. [2000], and Klawonn and Rheinbach [2010].

In the framework of FETI-DP methods the considered domain \mathcal{B}_0 is decomposed into a number of N nonoverlapping subdomains $\mathcal{B}_{0,i}$, $i = 1, \dots, N$, with diameter H and boundary $\partial\mathcal{B}_{0,i}$. A graph partitioner (Karypis et al. [2003]) is used in order to define the

¹⁴MPI: Message Passing Interface.

¹⁵PETSc: Portable, Extensible Toolkit for Scientific Computation; Balay et al. [2001, 2004, 1997].

¹⁶UMFPACK: Unsymmetric MultiFrontal PACKage; Davis [2004].

¹⁷ACML: AMD Core Math Library released by the american company AMD (Advanced Micro Devices).

decomposition into unions of finite elements with matching finite-element nodes on the boundaries of neighboring subdomains across the interface

$$\Gamma := \bigcup_{i \neq j} \partial \mathcal{B}_{0,i} \cap \partial \mathcal{B}_{0,j} \quad \text{and} \quad \Gamma = \bigcup_{i=1}^N \partial \mathcal{B}_{0,i} \setminus \partial \mathcal{B}_0, \quad (8.3)$$

with $\partial \mathcal{B}_{0,i} \cap \partial \mathcal{B}_{0,j}$. This process does not need access to geometric data since it is a completely algebraic process. After decomposition one or several subdomains can be allotted to each processor.

The linearized subdomain problems, cf. eq. (4.33), are identified for each subdomain $\mathcal{B}_{0,i}$ with the local stiffness matrices $\mathbf{K}^{(i)}$, the load vectors $\mathbf{f}^{(i)}$, and the local displacement increment $\Delta \mathbf{D}^{(i)}$, i.e.

$$\mathbf{K}^{(i)} \Delta \mathbf{D}^{(i)} = \mathbf{f}^{(i)} \quad \text{with} \quad i = 1, \dots, N. \quad (8.4)$$

We distinguish between nonprimal variables with index $(\bullet)_B$ and primal variables with index $(\bullet)_\Pi$. Furthermore, the nonprimal variables are subdivided into internal variables with index $(\bullet)_I$ and dual variables with index $(\bullet)_\Delta$. Thus, the local stiffness matrices are given by

$$\mathbf{K}^{(i)} = \begin{bmatrix} \mathbf{K}_{BB}^{(i)} & (\mathbf{K}_{\Pi B}^{(i)})^T \\ \mathbf{K}_{\Pi B}^{(i)} & \mathbf{K}_{\Pi \Pi}^{(i)} \end{bmatrix} \quad \text{with} \quad \mathbf{K}_{BB}^{(i)} = \begin{bmatrix} \mathbf{K}_{II}^{(i)} & (\mathbf{K}_{\Delta I}^{(i)})^T \\ \mathbf{K}_{\Delta I}^{(i)} & \mathbf{K}_{\Delta \Delta}^{(i)} \end{bmatrix}. \quad (8.5)$$

Generally, the N independent local problems in eq. (8.4) lead to discontinuous solutions across the subdomain interfaces Γ . In order to enforce continuity of the solution in the primal variables, a finite-element subassembly is performed

$$\begin{bmatrix} \mathbf{K}_{BB} & (\mathbf{K}_{\Pi B})^T \\ \mathbf{K}_{\Pi B} & \mathbf{K}_{\Pi \Pi} \end{bmatrix} = \begin{bmatrix} \mathbf{K}_{BB}^{(1)} & \cdots & 0 & (\mathbf{K}_{\Pi B}^{(1)})^T \\ \vdots & \ddots & \vdots & \vdots \\ 0 & \cdots & \mathbf{K}_{BB}^{(N)} & (\mathbf{K}_{\Pi B}^{(N)})^T \\ \mathbf{K}_{\Pi B}^{(1)} & \cdots & \mathbf{K}_{\Pi B}^{(N)} & \sum_{i=1}^N \mathbf{K}_{\Pi \Pi}^{(i)} \end{bmatrix}. \quad (8.6)$$

Using a global-to-local map \mathbf{R}_Π with entries from $\{0, 1\}$ and the identity \mathbf{I}_B applied on the nonprimal variables, we achieve the partially assembled, global stiffness matrix

$$\tilde{\mathbf{K}} = \begin{bmatrix} \mathbf{K}_{BB} & (\tilde{\mathbf{K}}_{\Pi B})^T \\ \tilde{\mathbf{K}}_{\Pi B} & \tilde{\mathbf{K}}_{\Pi \Pi} \end{bmatrix} = \begin{bmatrix} \mathbf{I}_B & \mathbf{0} \\ \mathbf{0} & (\mathbf{R}_\Pi)^T \end{bmatrix} \begin{bmatrix} \mathbf{K}_{BB} & (\mathbf{K}_{\Pi B})^T \\ \mathbf{K}_{\Pi B} & \mathbf{K}_{\Pi \Pi} \end{bmatrix} \begin{bmatrix} \mathbf{I}_B & \mathbf{0} \\ \mathbf{0} & \mathbf{R}_\Pi \end{bmatrix}, \quad (8.7)$$

which is coupled in the primal variables yielding a coarse problem for the method. An appropriate choice of the primal variables yields a positive definite matrix $\tilde{\mathbf{K}}$. The corresponding global load vector and global displacement increment appear as

$$\tilde{\mathbf{f}} = \begin{bmatrix} \mathbf{f}_B \\ \tilde{\mathbf{f}}_\Pi \end{bmatrix} = \begin{bmatrix} \mathbf{I}_B & \mathbf{0} \\ \mathbf{0} & (\mathbf{R}_\Pi)^T \end{bmatrix} \begin{bmatrix} \mathbf{f}_B \\ \sum_{i=1}^N \mathbf{f}_\Pi^{(i)} \end{bmatrix} = \begin{bmatrix} \mathbf{f}_B^{(1)} \\ \vdots \\ \mathbf{f}_B^{(N)} \\ \tilde{\mathbf{f}}_\Pi \end{bmatrix} \quad \text{and} \quad \Delta \tilde{\mathbf{D}} = \begin{bmatrix} \Delta \mathbf{D}_B \\ \Delta \tilde{\mathbf{D}}_\Pi \end{bmatrix}. \quad (8.8)$$

In order to enforce equality of the solution of the other subdomain interface variables $\Delta \mathbf{D}_\Delta$, the continuity constraint $\mathbf{B} \Delta \tilde{\mathbf{D}} = \mathbf{0}$, with $\mathbf{B} = [\mathbf{0}, \mathbf{B}_\Delta, \mathbf{0}]$, is introduced. The matrices $\mathbf{B} = [\mathbf{B}^{(1)}, \dots, \mathbf{B}^{(N)}]$ are denoted as jump operators and have entries from $\{-1, 0, 1\}$. We use Lagrange multipliers $\boldsymbol{\lambda}$ and obtain the minimization problem

$$\left. \begin{aligned} \tilde{\mathbf{K}} \Delta \tilde{\mathbf{D}} + \mathbf{B}^T \boldsymbol{\lambda} &= \tilde{\mathbf{f}} \\ \mathbf{B} \Delta \tilde{\mathbf{D}} &= \mathbf{0} \end{aligned} \right\}, \quad (8.9)$$

yielding the saddle point system

$$\begin{bmatrix} \tilde{\mathbf{K}} & \mathbf{B}^T \\ \mathbf{B} & \mathbf{0} \end{bmatrix} \begin{bmatrix} \Delta \tilde{\mathbf{D}} \\ \boldsymbol{\lambda} \end{bmatrix} = \begin{bmatrix} \tilde{\mathbf{f}} \\ \mathbf{0} \end{bmatrix}. \quad (8.10)$$

By eliminating the displacement variables $\Delta \tilde{\mathbf{D}}$ we obtain the Schur-complement system

$$\mathbf{F}_{\text{FETI}} \boldsymbol{\lambda} = \mathbf{d}, \quad \text{with} \quad \mathbf{F}_{\text{FETI}} = \mathbf{B} \tilde{\mathbf{K}}^{-1} \mathbf{B}^T \quad \text{and} \quad \mathbf{d} = \mathbf{B} \tilde{\mathbf{K}}^{-1} \tilde{\mathbf{f}}. \quad (8.11)$$

We solve eq. (8.11) iteratively with a preconditioned Krylov subspace method, the GMRES (generalized minimum residual) method. Hereby, the memory requirements are significantly reduced by performing the iteration only on the interface. As preconditioner we use the Dirichlet preconditioner $\mathbf{M}^{-1} := \mathbf{B}_D \mathbf{R}_\Gamma^T \mathbf{S} \mathbf{R}_\Gamma \mathbf{B}_D^T$, with the Schur complement \mathbf{S} , the restriction matrix \mathbf{R}_Γ with elements $\{0, 1\}$ (removes interior variables $\Delta \mathbf{D}_I$ from $\Delta \tilde{\mathbf{D}}$), and scaled variants of the jump operator \mathbf{B} , i.e. \mathbf{B}_D . For further information on the FETI-DP solver the reader is referred to Rheinbach [2006] and Klawonn and Rheinbach [2006, 2007b], it has been also used in Balzani et al. [2009a].

8.4 Simulation of an arterial segment with an axial length of 1 mm

The tree-dimensional arterial model investigated in this section was generated by an extrusion of an arterial cross-section, such that the model is 1 mm in depth, i.e. in axial direction. In Fig. 8.3 the model is shown, which is discretized with 8 812 quadratic tetrahedral elements with 14 594 nodes, which gives 43 782 degrees of freedom.

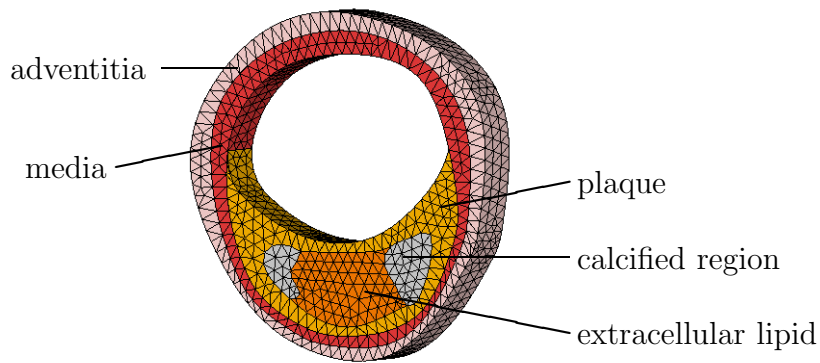


Figure 8.3: Model of the artery, which consists of adventitia, media and degenerated intima (plaque, extracellular lipid, calcified regions).

In the simulation all nodes of the cross-section in the front and the back of the arterial model are fixed in axial direction. Additionally, the displacements of two nodes are fixed

vertically and the displacements of one node is fixed horizontally. The constitutive model for the individual components is described in Section 8.1 and the material parameters are listed in Table 8.1 and Table 8.2.

For the enforcement of incompressibility the following methods are used and analyzed regarding the robustness of the simulation: i) the Penalty-Method, ii) the Augmented-Lagrange-Method with a nested iteration (NAL) and an adherence of the $(\det \mathbf{F} = 1)$ -condition with a tolerance of $\pm 1\%$ and $\kappa_{\text{al}} = 999.0$, and iii) the Augmented-Lagrange-Method with a simultaneous iteration (SAL) and an adherence of the $(\det \mathbf{F} = 1)$ -condition with a tolerance of $\pm 1\%$ and $\kappa_{\text{al}} = 999.0$.

For the automatic time stepping scheme the initial time step size value is $\Delta t^{\text{ini}} = 0.001$ and the maximum time step size is $\Delta t_{\text{max}} = 0.1$. For the simulations with the Penalty approach and the nested Augmented-Lagrange-Method the bounds are $n_{\text{it}}^{\text{max}} = 9$ and $n_{\text{it}}^{\text{min}} = 6$ and for the simulation with simultaneous Augmented-Lagrange-Method $n_{\text{it}}^{\text{max}} = 11$ and $n_{\text{it}}^{\text{min}} = 8$.

The distribution of $\det \mathbf{F}$ under an inner pressure $p_i = 24$ kPa is shown in Fig. 8.4. The quasi-incompressibility condition can be regarded as met in a sufficient manner: for the two simulations with the Augmented-Lagrange approach the tolerance value is maintained and also for the simulation with the Penalty approach $\det \mathbf{F} \approx 1 \pm 0.01$.

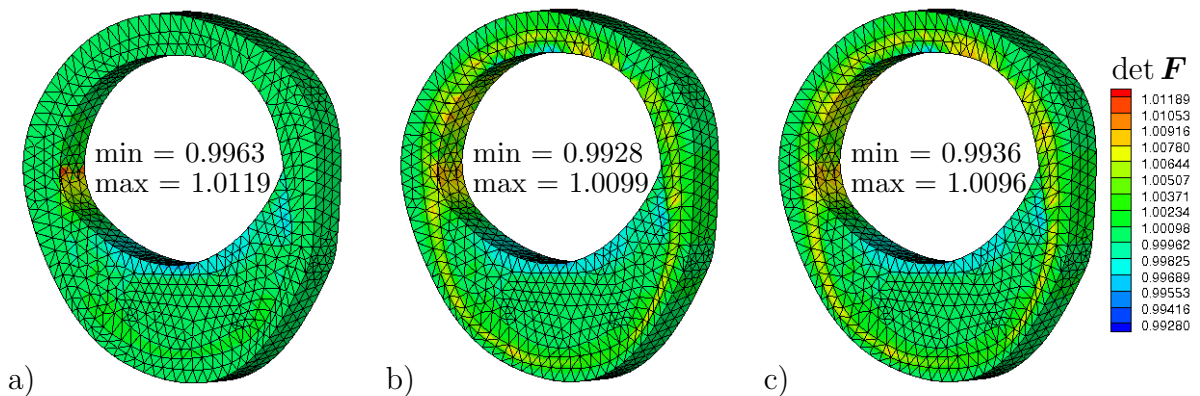


Figure 8.4: Distribution of the determinant of the deformation gradient $\det \mathbf{F}$ under an inner pressure $p_i = 24$ kPa using a) the Penalty-Method and using the Augmented-Lagrange-Method with b) a nested iteration and c) a simultaneous iteration.

An evaluation of the numerical simulation with regard to the robustness is given in Fig. 8.5. Here, the diagrams show the time increment, the last absolute residual norm and the number of Newton iterations over time. In the simulation with the Penalty-Method more time steps are needed. It can be stated that during the automatic time stepping scheme the maximum time increment Δt^{max} is reached faster when the Augmented-Lagrange-Method is used. Furthermore, in most cases the value of the last residual norm using an Augmented-Lagrange-Method is below the value using the Penalty-Method. Comparison of the two Augmented-Lagrange approaches shows, that more Newton iterations are needed using the nested iteration compared to the simultaneous iteration. In summary, the highest robustness of the simulation can be obtained by using the Augmented-Lagrange-Method with a simultaneous iteration.

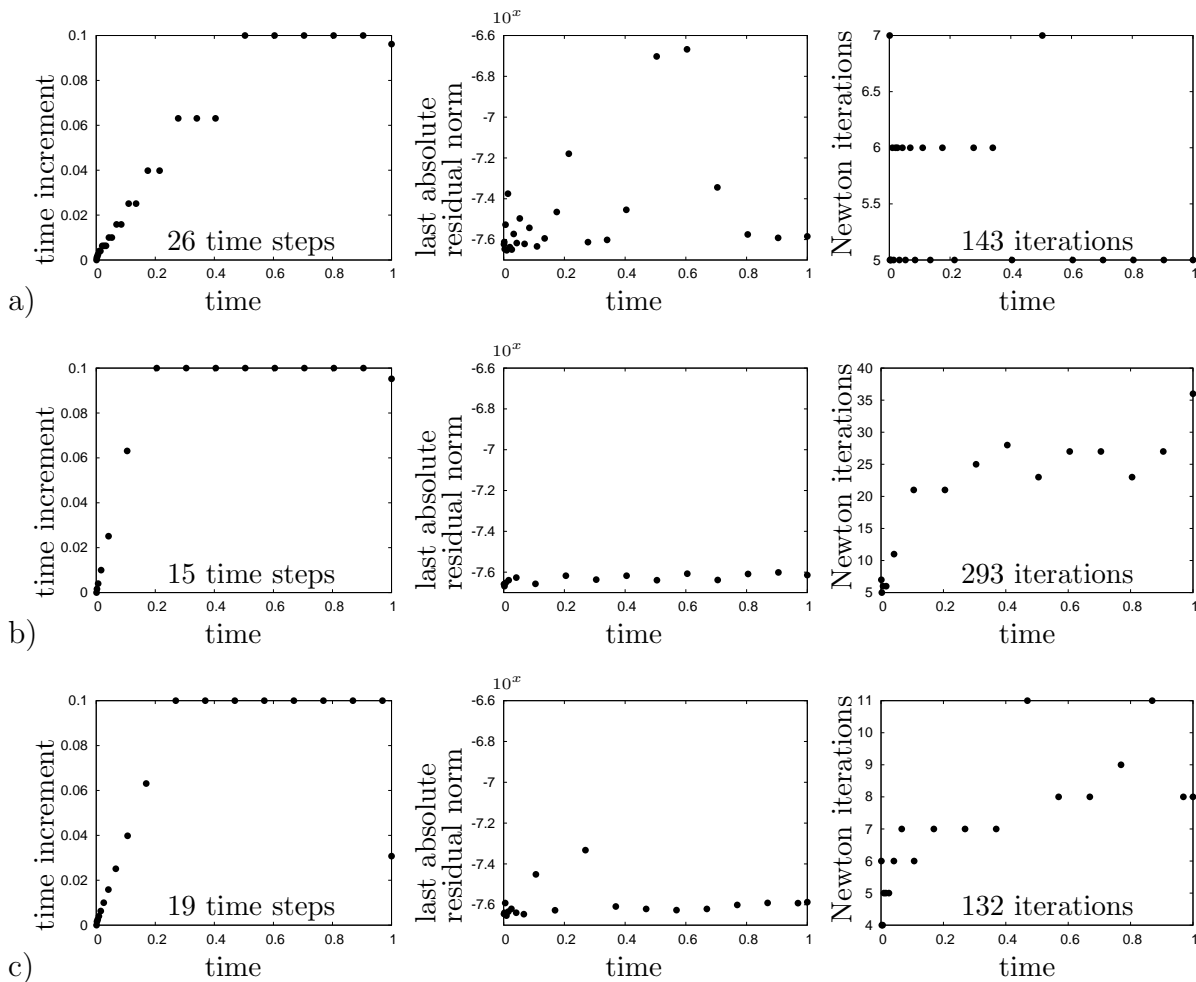


Figure 8.5: Time increment, last absolute residual norm of the time step and number of Newton iterations over time: a) Penalty-Method; Augmented-Lagrange-Method with b) nested iteration and with c) simultaneous iteration.

8.5 Simulation of an arterial segment with an axial length of 10 mm

The three-dimensional geometry of the artery analyzed in the following numerical simulation is based on histological pictures, cf. Brands et al. [2009], Balzani et al. [2011]. The artery is composed of media, adventitia and of a large inclusion of plaque, see Fig. 8.6.

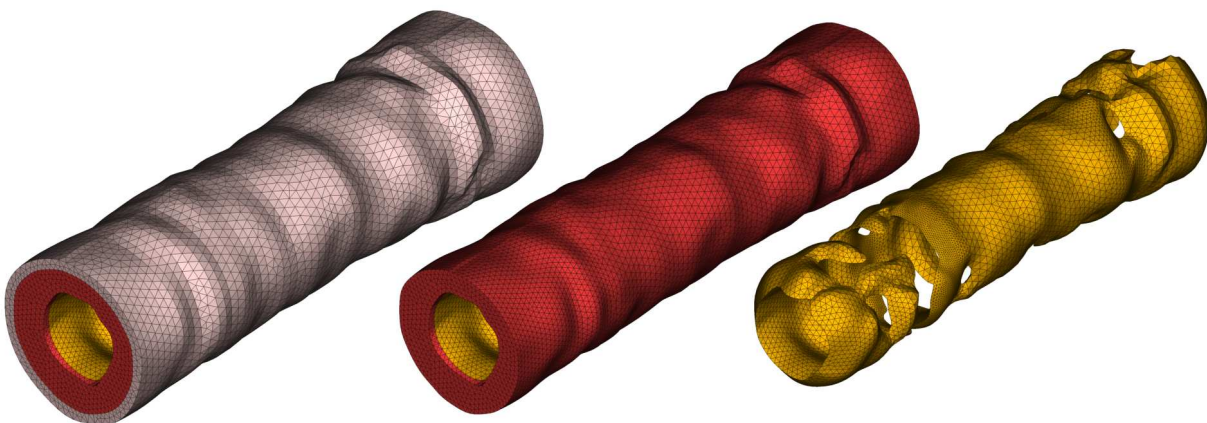


Figure 8.6: Layered finite element model of the arterial segment discretized using 10-noded tetrahedral elements: a) complete arterial model, b) blanked adventitia and c) plaque.

The model is discretized with 305 033 quadratic tetrahedral elements yielding 434 517 nodes and therefore 1 303 551 degrees of freedom. Due to such a large number of degrees of freedom, the FETI-DP domain decomposition method is used parallel to the Finite Element Program FEAP, see Section 8.3. The Newton method stops if a reduction of the absolute residual norm to a value less than 10^{-6} or a value less than 10^{-4} for three consecutive Newton steps is achieved. In the FETI-DP Krylov iteration the stopping criterion is an absolute residual less than $5 \cdot 10^{-9}$. The domain is decomposed into 224 subdomains, see Fig. 8.7.

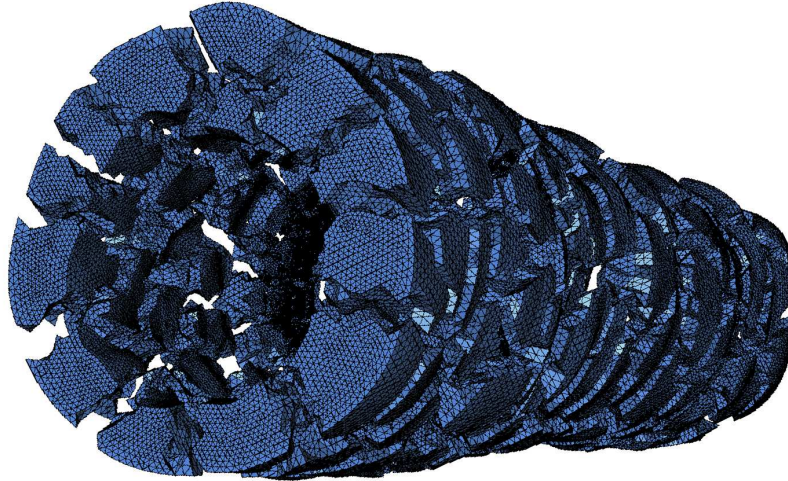


Figure 8.7: Domain decomposition of the arterial segment into 224 subdomains. For a better view of the nonoverlapping method the subdomains are dispersed.

The following different methods are used in order to enforce quasi-incompressibility:

- Penalty-Method
- Augmented-Lagrange-Method with the nested iteration and enforcement of the condition $|\det \mathbf{F} - 1| \leq 0.01$, i.e. TOL = 1%, and the parameter $\kappa_{al} = 499.0$
- Augmented-Lagrange-Method with the simultaneous iteration and enforcement of the condition $|\det \mathbf{F} - 1| \leq 0.01$, i.e. TOL = 1%, and the parameter $\kappa_{al} = 500.0$
- Augmented-Lagrange-Method with the simultaneous iteration and enforcement of the condition $|\det \mathbf{F} - 1| \leq 0.001$, i.e. TOL = 1‰, and the parameter $\kappa_{al} = 1\,000.0$

For the automatic time stepping scheme the initial time step size value is $\Delta t^{ini} = 0.001$ and the maximum time step size is $\Delta t_{max} = 0.4$. For the simulations with the Penalty approach and the nested Augmented-Lagrange-Method (NAL) the bounds are $n_{it}^{max} = 9$ and $n_{it}^{min} = 6$ and for the simulation with simultaneous Augmented-Lagrange-Method (SAL) $n_{it}^{max} = 36$ and $n_{it}^{min} = 18$.

The artery is loaded with an internal pressure of $p_i = 33.331$ kPa (≈ 250 mmHg). In Fig. 8.8a the range of the determinant of the deformation gradient $\det \mathbf{F}$ under full loading is shown for the different approaches. In the Augmented-Lagrange approaches the predefined conditions $|\det \mathbf{F} - 1| \leq 0.01$ and $|\det \mathbf{F} - 1| \leq 0.001$, respectively, are met. The solution using the Penalty approach only satisfies $|\det \mathbf{F} - 1| \leq 0.0209$. Additionally,

Fig. 8.8 shows the distribution of the determinant of the deformation gradient $\det \mathbf{F}$. The distribution is depicted for the Penalty approach, the NAL, and the SAL approach with a tolerance value of 10^{-2} . The overall distribution is very smooth in case of all three different simulations. Furthermore, due to the equal tolerance value, the two simulations, in which the Augmented-Lagrange-Method are used, exhibit an almost identical distribution. One reason for the difference to the simulation using the Penalty-Method is that it is not possible to explicitly define a tolerance value.

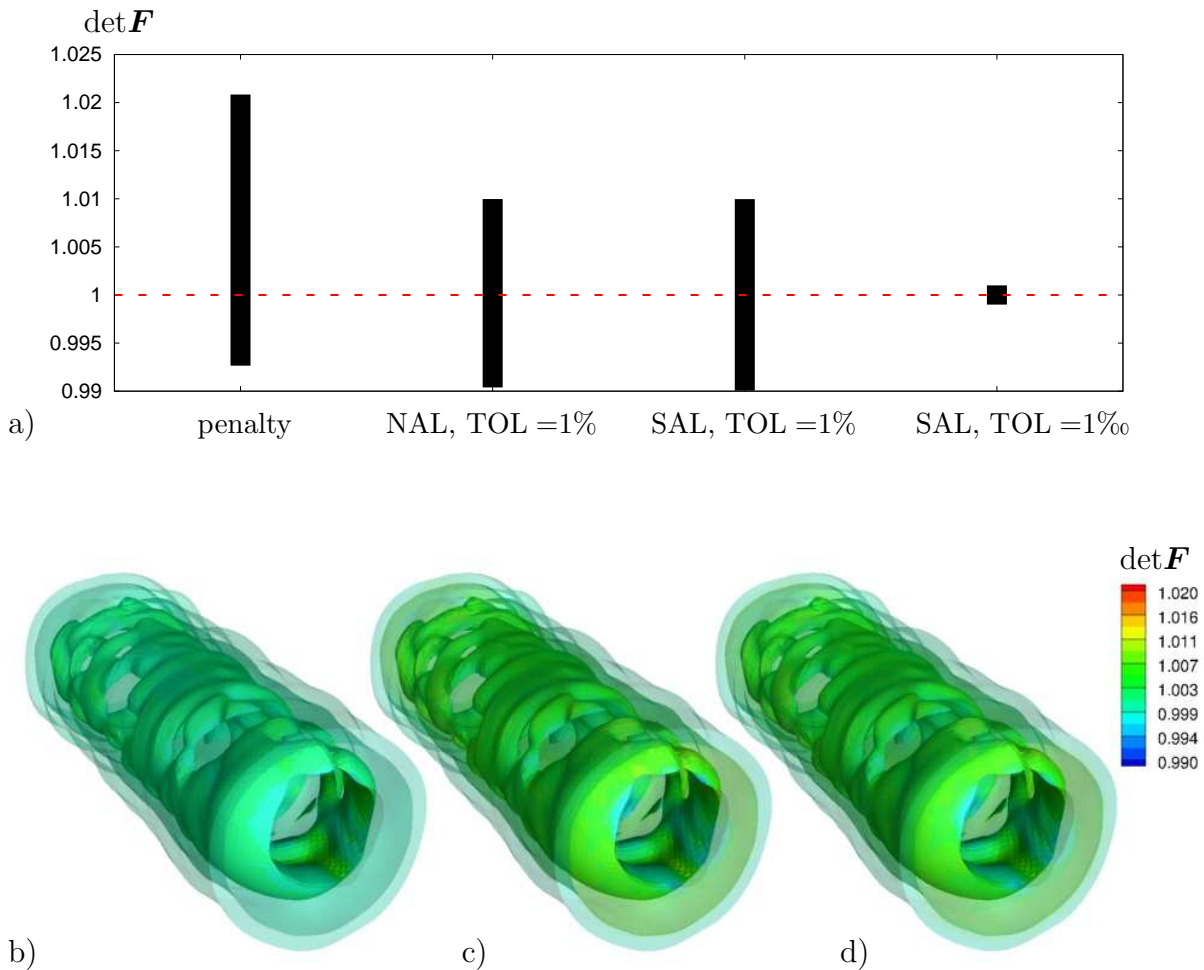


Figure 8.8: a) Diagram showing the range of the determinant of the deformation gradient for the different used approaches. The minimum and maximum values ($\det \mathbf{F}_{\min}/\det \mathbf{F}_{\max}$) are as follows: penalty (0.9926/1.0209), NAL with TOL = 0.01 (0.9901/1.0099), SAL with TOL = 0.01 (0.9902/1.01), SAL with TOL = 0.001 (0.9990/1.001); Distribution of the determinant of the deformation gradient $\det \mathbf{F}$: b) Penalty approach, c) NAL (TOL= 10^{-2}), and d) SAL with TOL= 10^{-2} .

In Fig. 8.9, Fig. 8.10, Fig. 8.11 and Fig. 8.12 the evaluations of the simulations are displayed. The diagrams show the time increment, the last absolute residual norm, the number of Newton iterations, and the number of FETI-DP iterations for each approach. Additionally, the main facts are summarized in compact form in Table 8.3. Here, also the total costs of the computations are listed, which can roughly be estimated by multiplying the number of global Newton steps (summary of all Newton steps needed within the simulation) with the corresponding average number of (inner) FETI-DP iterations.

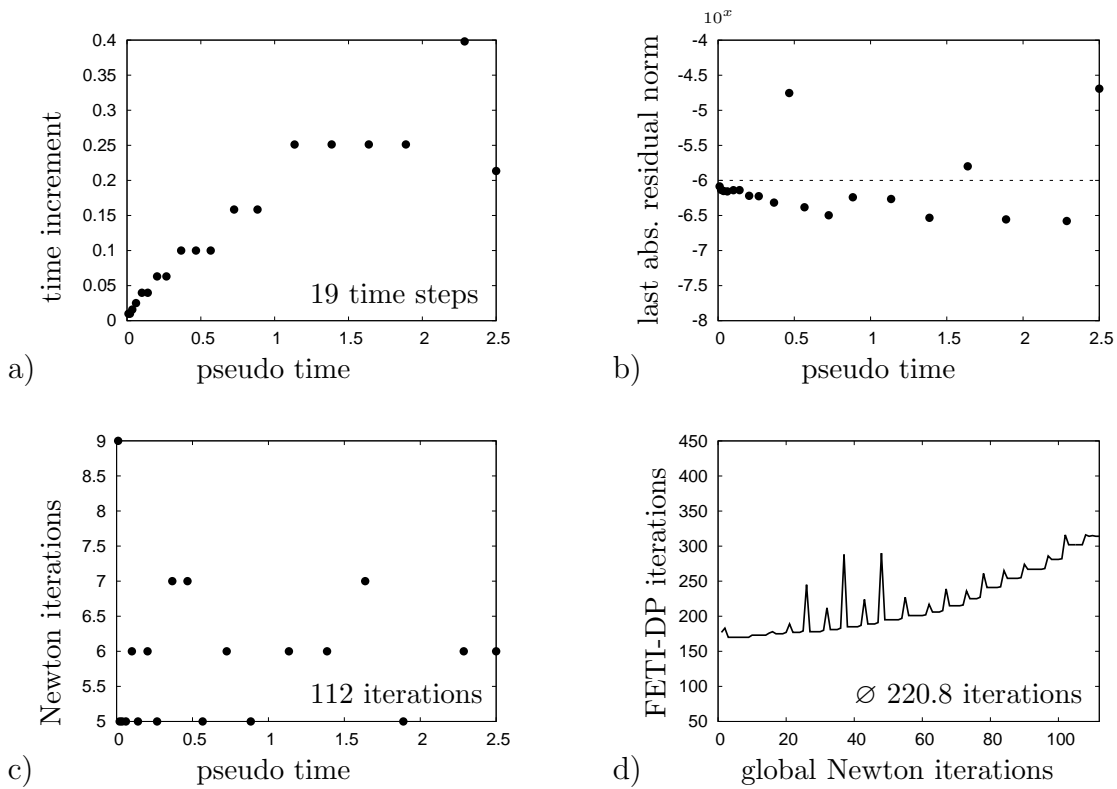


Figure 8.9: Penalty-Method: a) time increment, b) last absolute residual norm, c) number of Newton iterations, and d) FETI-DP iterations over time.

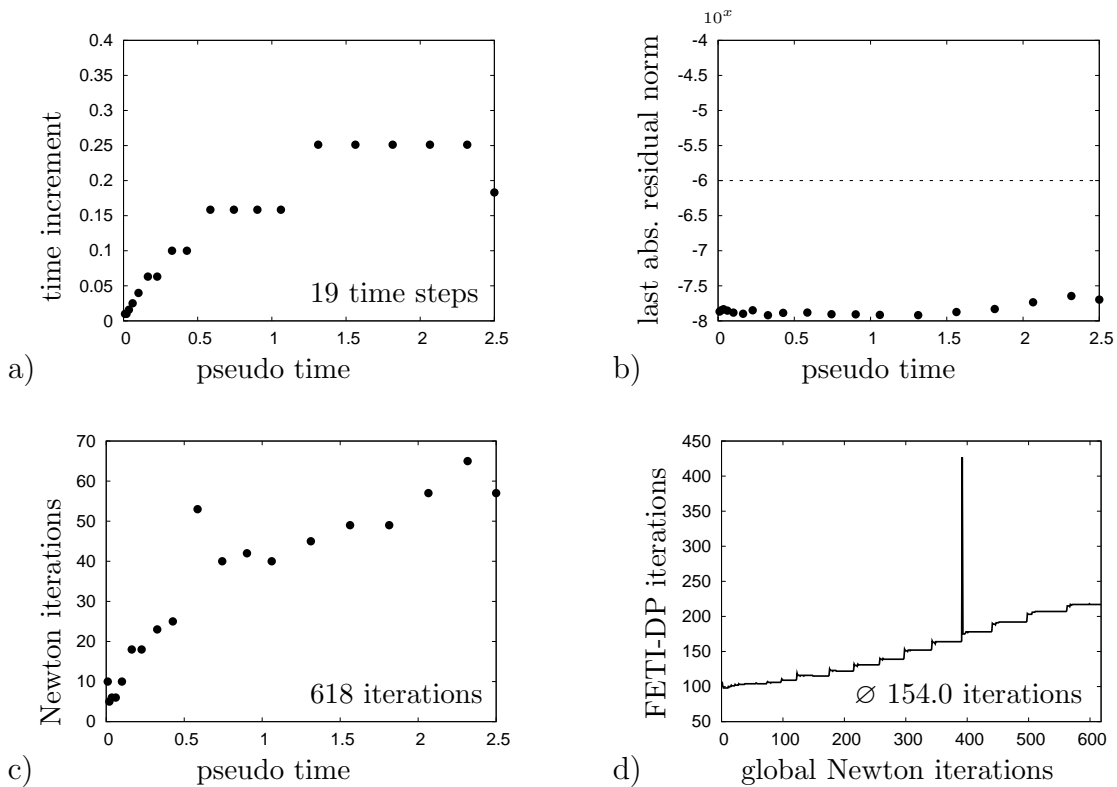


Figure 8.10: NAL method: a) time increment, b) last absolute residual norm, c) number of Newton iterations, and d) FETI-DP iterations over time.

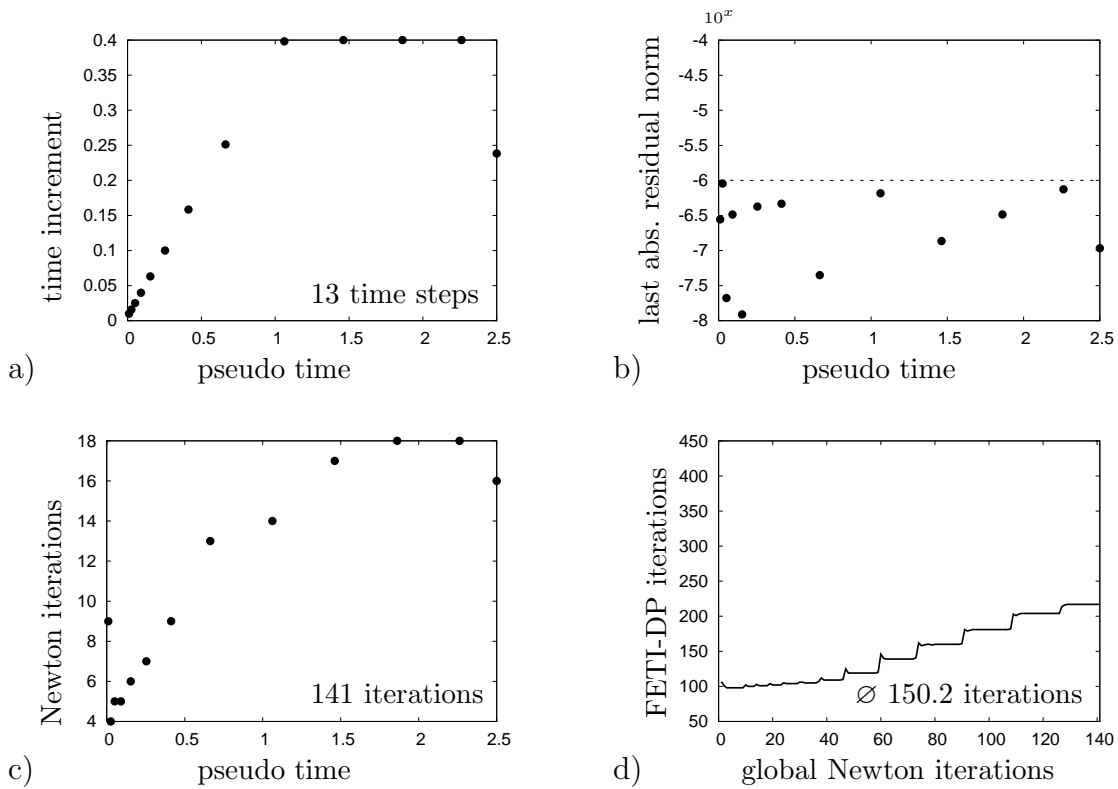


Figure 8.11: SAL method with $TOL = 0.01$: a) time increment, b) last absolute residual norm, c) number of Newton iterations, and d) number of FETI-DP iterations over time.

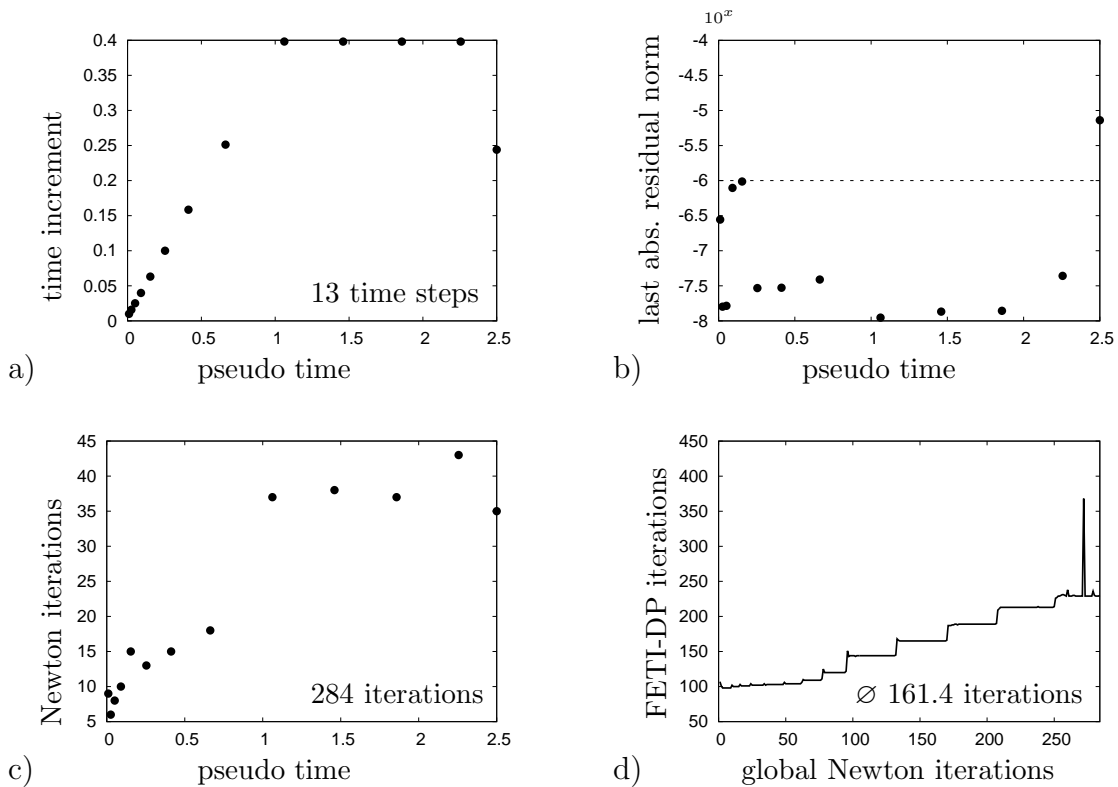


Figure 8.12: SAL method with $TOL = 0.001$: a) Time increment, b) last absolute residual norm, c) number of Newton iterations, and d) number of FETI-DP iterations over time.

If we compare the number of Newton iterations needed in the Penalty-Method in Fig. 8.9 with the number needed in the simultaneous Augmented-Lagrange-Method with $TOL = 0.01$ (see Fig. 8.11) more Newton iterations are needed in the SAL approach due to the additional Augmented-Lagrange iterations. Nevertheless, the convergence of the nonlinear scheme and the linear iterative solver is much faster in case of the SAL method, so that the total costs are less, see also Table 8.3. The total cost of the nested Augmented-Lagrange approach (Fig. 8.10) is distinctly higher due to the high amount of the Newton iterations.

In Fig. 8.10c, Fig. 8.11c and Fig. 8.12c it is visible that the number of Newton iterations becomes greater during the simulation. A reason for that may be, that only a very small number of finite elements violate the element-wise condition $|\det \mathbf{F} - 1| \leq TOL$ in the beginning of the simulation and this number increases in the course of the simulation.

We can also observe, that the number of FETI-DP iterations becomes greater during the simulations, see Fig. 8.9d, Fig. 8.10d, Fig. 8.11d and Fig. 8.12d. This may be a result of the increasing influence of the incompressibility constraint during the simulation. In Balzani et al. [2009a] it was found out that the convergence of the nonlinear iteration scheme as well as the convergence of the iterative linear solver is measurably influenced by the anisotropies resulting from the energy terms of the fibers. Thus, an alternative explanation is that the increase of iterations is due to exponential stiffening of the fibers.

Summarizing the above, it can be concluded that the use of the Augmented-Lagrange-Method can significantly improve the properties of the linearized systems appearing in the nonlinear solution scheme. Here, a lower number of iterations is needed for convergence of the FETI-DP iterative method. Furthermore, larger time steps Δt can be chosen, such that the convergence of the nonlinear scheme is also improved. Nevertheless, the Augmented-Lagrange approach needs an additional iteration process for the Lagrange multiplier.

	time steps	global Newton iterations	\varnothing FETI-DP iterations	total costs
penalty	19	112	220.8 (min = 170, max = 316)	24 729.6
SAL, TOL = 0.01	13	141	150.2 (min 98, max = 217)	21 178.2
NAL, TOL = 0.01	19	618	154.0 (min = 98, max = 427)	95 172.0
SAL, TOL = 0.001	13	248	161.4 (min = 98, max = 368)	40 027.2

Table 8.3: Comparison of the methods in the framework of the FETI-DP method. The Finite-Element model has approx. 1.3 million degrees of freedom, see Fig. 8.6. The total cost can be estimated roughly by multiplying the number of global Newton iterations by the average number of FETI-DP iterations. This table is taken from Brinkhues et al. [2012].

9 Incorporation of residual stresses in patient-specific arteries

In this chapter a method for the incorporation of residual stresses into a numerical model for the simulation of arterial walls is introduced. Section 9.1 gives an overview of the state of the art in this field of research. The proposed new method, see also Schröder and Brinkhues [2012], is based on the assumption that residual stresses reduce the gradient of the wall stresses in radial direction. An experimental motivation for such an approach is given in, for example, Takamizawa and Hayashi [1987] or Fung [1991]. The idea is to use the local difference of the circumferential stresses with respect to its volume average for the estimation of the residual stresses. In Section 9.2 a plausibility check of the new approach is done by a simple numerical simulation of an isotropic two-dimensional ideal tube. Here, the gradients of the circumferential stresses are reduced through the residual stresses. Since arterial walls are anisotropic and exhibit a distinct material behavior in fiber direction, suitable stress measures (the fiber stresses) are defined. The associated invariants, which are used for the definition of the residual stresses in soft biological tissues are derived in Section 9.3. Since an arterial geometry is not rotationally symmetric, the numerical realization of this method is based on a decomposition of the domain into different segments, see Section 9.4. Furthermore, each segment is subdivided into sectors depending on how many different fiber reinforced layers the segments consist of (e.g. adventitia and media). Such sectoral division seems to be evident, since the individual layers exhibit different opening angles and therefore a different residual stress distribution, see Holzapfel et al. [2007], especially figure 6 on page 537. In Section 9.5 numerical simulations are performed in order to show the suitability of the proposed approach.

9.1 State of the art in the modeling of residual stresses in arteries

Until the early 1980's a cylindrical arterial segment, which is not loaded with any external force, was assumed to be stress free. This assumption was disproved experimentally by Vaishnav and Vossoughi [1983]. They sliced circular rings of bovine and porcine abdominal aortas radially; for a schematic illustration see Fig. 9.1. After the radial sectioning the rings opened up into a horseshoe leading to the conclusion that the aorta is residually stressed in circumferential direction when it is intact but free from external forces. However, Bergel [1960] seems to be the first who observed this phenomenon.

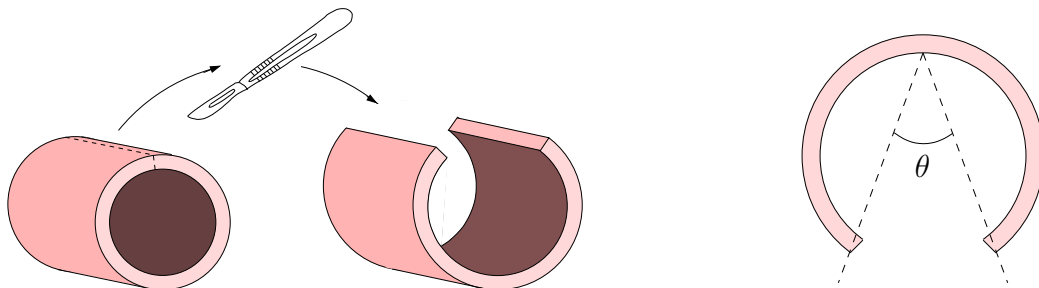


Figure 9.1: Schematic of longitudinal cut through an artery and resulting opening angle θ .

In Chuong and Fung [1986] it was stated that residual stresses reduce the magnitude of the stresses and the stress gradient of a pressurized artery significantly, see also Fung [1991]. Takamizawa and Hayashi [1987] suggested that the residual stresses cause an almost uniform circumferential strain distribution under physiological pressure; this is called the

uniform-strain hypothesis. In Nollert et al. [1992] it is stated that a reduction of the stress gradient at the inner side of the arterial wall may reduce the risk of atherogenesis. Further experimental observations on rat aortas showed that the level of the segmental opening differs depending on the position of the segment in the aortic tree, see Liu and Fung [1988]. Thus, the opening angle θ gradually varies from the ascending aorta to the lumbar region: it starts by 160° , follows a curve to 60° , tends toward zero before becoming slightly negative and increases again over 60° . Liu and Fung [1989] banded abdominal rat aortas near the celiac trunk in order to establish hypertension. Then they discussed the change of the opening angle as a result of hypertension and hypertrophy and found out that a change in blood pressure changes the residual strains and therefore the opening angle significantly. They stated that the residual-strain change is stress-modulated. A study on the circumferential residual stresses in the left ventricle and the trachea is given in Omens and Fung [1990] and Han and Fung [1991], respectively. The zero-stress state of small blood vessels, which consists of 79–57% smooth muscles, was investigated by Fung and Liu [1992]. Additionally, the effect of several drugs on the microvessels were presented. Experiments on bovine aortas done by Vossoughi et al. [1993] showed that even the cutted configuration is not fully stress-free. Additional circumferential cuts caused different opening angles for the individual arterial layers. Thus, the magnitude of opening of the inner layers increases while those of the outer layers reduces indicating that stresses still remain after the radial cut. Experiments on human aortas in Schulze-Bauer et al. [2002a] revealed also that residual stresses are not vanishing by a single cut, see also the study of Matsumoto et al. [2004] on porcine thoracic aortas. Greenwald et al. [1997] investigated aortas from rats and provided similar results concerning the different opening angles of the individual layers after mechanical removal of the other layers. Additionally, they showed that elastase treated (elimination of elastin) specimens offer smaller opening angles while collagenase treated (elimination of collagen) and frozen (destruction of smooth muscle cells) specimens behave like the untreated control specimens. First studies on human thoracic and abdominal aortas were done by Saini et al. [1995]. Here, the influence of age, sex, the position along the artery, and atherosclerosis on the opening of sliced arterial rings was discussed. It was stated that the value of the opening angle increases with increasing distance from the heart (female: 150° – 200° , male: 200° – 250°). They also observed larger opening angles in aged and atherosclerotic diseased vessels, and in those obtained from male samples. Three-dimensional residual deformations of intact human abdominal aortas were shown in Holzapfel et al. [2007]. In this study arterial rings were cut open and then separated into three layers. Furthermore, residual deformations on axial strips were investigated. It was stated that, due to the occurrence of the residual deformations in three dimensions, they cannot be described by a single parameter. A review of experimental methods for residual-strain measurement was given by Rachev and Greenwald [2003].

Chuong and Fung [1986] were probably the first to use a constitutive model to compute residual stresses. They discussed a procedure for the description of the geometry of an open artery, whose closed counterpart was regarded as thick-walled cylindrical tube with constant thickness. This method is known as *opening-angle method*. Therewith they computed the two-dimensional residual stresses in the unloaded closed artery and showed that the residual stresses enforce compression on the inner side of the vessel wall and tension on the outer side of the vessel wall. Many works are based on the opening-angle method to achieve an analytical solution for the residual strains of initially open ideal tubes, which were closed by an initial bending. Rachev [1997] derived a mathematical

model for the stress-dependent remodeling of a two-layer arterial tube. The assumption that the stress and strain values are equal under hypertensive and normotensive conditions was taken into account by means of remodeling of the zero-stress configuration by thickening of the layers. They also observed remaining residual stresses in the opened-up configuration of a hypertensive artery. Using a one-layer model Chaudhry et al. [1997] showed that circumferential stresses and gradients are reduced significantly at the inner wall. The opening-angle method was also used by Holzapfel for an analytical solution of the initial deformation tensor for multilayered arterial tubes. In Holzapfel et al. [2000a] the opening-angle method was applied to a two-layered tube and different material models were investigated. Another key objective was to analyze the effect of the residual stresses onto the overall stress distribution in the physiological regime. The high-pressure response is analyzed in Holzapfel and Gasser [2007]. Peña et al. [2006] applied the opening-angle method to more realistic arterial geometries and conducted corresponding finite-element simulations. To account for residual stresses, Alastrué et al. [2007a] used a special form of the multiplicative decomposition of the deformation gradient, in which one part corresponds to the opening angle experiment. This approach was also investigated by Alastrué et al. [2008], where growth was included, and implemented in a micro-sphere model in Alastrué et al. [2009]. A combination of the opening-angle method and a constrained mixture model of vascular growth and remodeling was suggested in Cardamone et al. [2009]. Here, the mixture components are the individual constituents of the artery, i.e. elastin, collagen and smooth muscle. One aim of the authors was find the origin of residual stress. For the modeling of growth and remodeling in the framework of constrained mixture models see also Alford et al. [2008] and Valentin and Humphrey [2009]. Holzapfel and Ogden [2010] accounted for the different behavior of the three main arterial layers and used different opening angles for the individual layers. Additionally, they extended the opening-angle method by accounting for bending and stretching in both circumferential and axial directions in order to reflect the three-dimensional residual stretch and stress state. A further extension of the model was done by Bustamante and Holzapfel [2010], which accounted for opening angles depending on axial and radial position, i.e. different opening angles along the tube. Furthermore, a different set of opening angles for intima, media and adventitia were considered. Ståhlhand et al. [2004] used experimental data in order to derive a residual-strain state. In order to do so, a minimization problem was derived for an approximate identification of material parameters including the residual strains. The parameters for the residual strains were presumed in the sense of the opening-angle method. This parameter identification algorithm is used in Olsson et al. [2006] to determine an initial local deformation tensor, which is able to describe the residual strain, see also Klarbring et al. [2007]. An extension of the model was given by Olsson and Klarbring [2008], which introduced the evolution of growth. In the recent paper of Chen and Eberth [2012] a uniform circumferential stress was obtained by introducing a special class of constitutive functions without considering a residually stressed state. This idea could be attractive for the design of engineered blood vessels.

In contrast to the above mentioned methods Balzani et al. [2006b, 2007] used a numerical method in order to establish a residual-strain state. Here, an initially open artery was numerically closed within a displacement-driven procedure. This model is appropriate, but nevertheless numerically extensive. In this work a novel model for the incorporation of residual stresses is proposed. An advantage of this model is that it is suitable for the incorporation of residual stresses in patient-specific three-dimensional arterial models.

9.2 Numerical simulation of an isotropic two-dimensional ideal tube

As a plausibility check of the new approach two-dimensional numerical simulations of an isotropic ideal tube are performed. The circular ring has an inner radius $r = 1$ mm and an outer radius of $r = 2$ mm and is discretized with 6 100 quadratic triangular elements, see Fig. 9.2a. The material behavior is reflected by the Mooney-Rivlin model $\psi = \psi_{\text{MR}}^{\text{iso}}$ introduced in eq. (5.3). The corresponding material parameters are randomly chosen and listed in Table 9.1. According to the procedure introduced in Section 6.2.1 the Lamé constants are $\mu = 30$ [kPa] and $\lambda = 345$ [kPa] and the Poisson's ratio is $\nu = 0.46$.

c_1	c_2	c_3
[kPa]	[kPa]	[kPa]
8.75	6.25	80.0

Table 9.1: Material parameters of the isotropic ideal tube.

Under an inner pressure of $p_i = 16$ kPa (120 mmHg) the distribution of the stresses in circumferential direction with the normal vector \mathbf{n}_φ

$$\sigma_\varphi = \boldsymbol{\sigma} : (\mathbf{n}_\varphi \otimes \mathbf{n}_\varphi) \quad (9.1)$$

arises as depicted in Fig. 9.2b (solid line). The maximum stresses are located at the inner surface ($r = 1$ mm) and decrease towards the outer surface ($r = 2$ mm), such that a stress gradient of the circumferential stresses in radial direction can be observed. According to the above mentioned approach this gradient should be reduced as a consequence of residual stresses in circumferential direction.

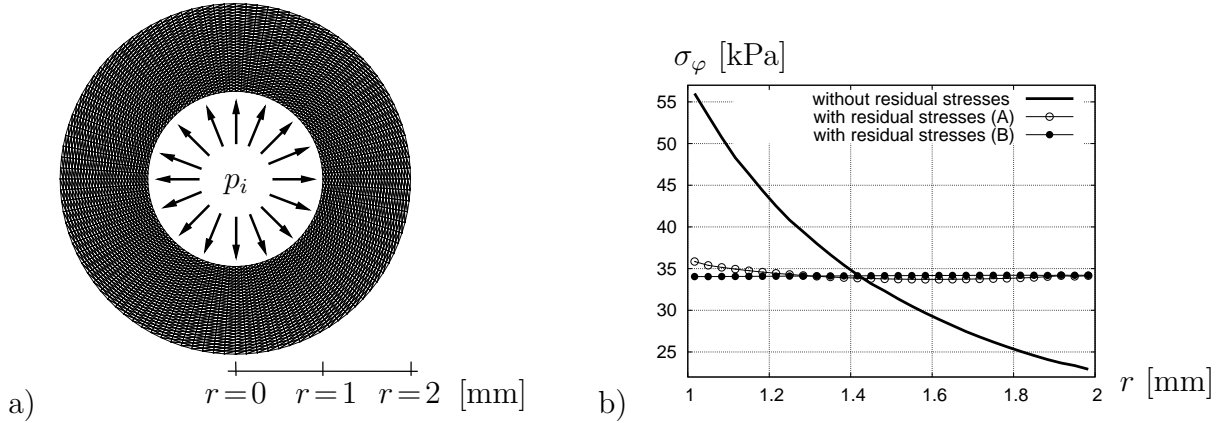


Figure 9.2: a) Ideal two-dimensional circular ring discretized with 6 100 quadratic triangular elements. b) Circumferential stresses σ_φ [kPa] plotted over the radius r [mm] without and with application of residual stresses at an inner pressure of $p_i = 16$ kPa \approx 120 mmHg; (A) after the first application of residual stresses and (B) after a further application.

Firstly the average value of the circumferential stresses in radial direction are computed. In this special case for a rotationally symmetric distribution of stress we get

$$\bar{\sigma}_\varphi = \frac{1}{V} \int_{\mathcal{B}} \sigma_\varphi(\mathbf{x}) dv . \quad (9.2)$$

It should be noted that eq. (9.2) only holds for this rotationally symmetric stress distribution. The difference between the circumferential stresses and the average value is used to compute the residual stress distribution

$$\boldsymbol{\sigma}^{\text{res}} = \Delta\sigma_\varphi \mathbf{n}_\varphi \otimes \mathbf{n}_\varphi \quad \text{with} \quad \Delta\sigma_\varphi = \sigma_\varphi - \bar{\sigma}_\varphi. \quad (9.3)$$

After the application of the residual stresses by a stress update $\boldsymbol{\sigma} \leftarrow \boldsymbol{\sigma} - \boldsymbol{\sigma}^{\text{res}}$ the circumferential stresses arise as depicted in Fig. 9.2b (line with circles). If this procedure¹⁸ is repeated another time a fully homogeneous stress distribution is obtained as indicated by line with solid circles in Fig. 9.2b. The stress distribution along the tube before and after the application of the smoothing-loop are shown in Fig. 9.3a and b.

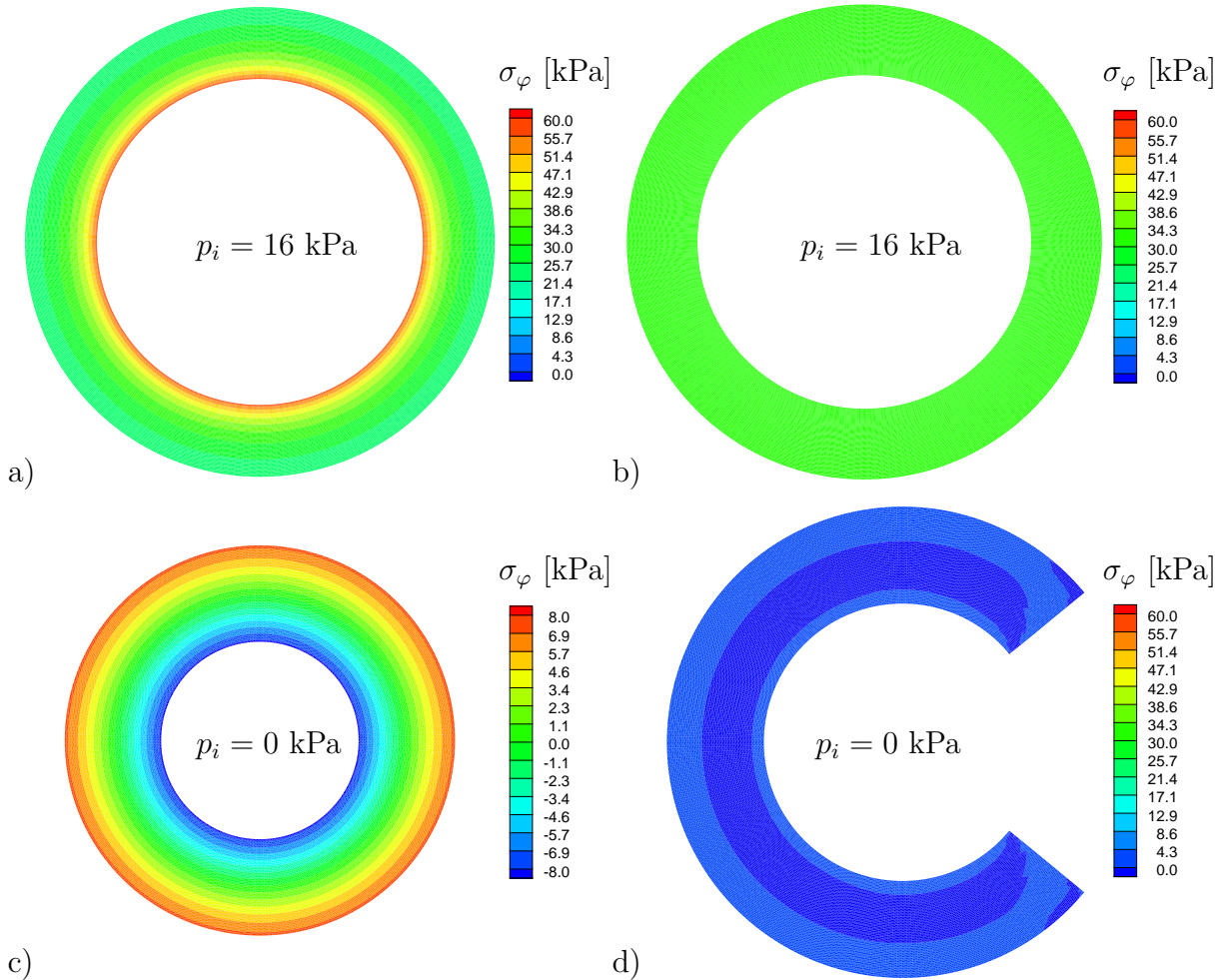


Figure 9.3: Stress distribution of circumferential stresses σ_φ in an isotropic two-dimensional circular ring under an inner pressure of $p_i = 16$ kPa: a) without considering residual stresses and b) after application of the residual stresses. c) Pure residual stress distribution in an unloaded circular ring ($p_i = 0$ kPa) and d) opening of the ring due to residual stresses.

If the circular ring is unloaded to zero internal pressure, i.e. $p_i = 0$ kPa, only the residual stresses remain as depicted in Fig. 9.3c. It is clearly visible that the residual stresses enforce pressure at the inner surface and tension at the outer surface as was expected. In a further step, the tube is sliced radially. As shown in Fig. 9.3d, the circular ring opens due to the residual stresses. An opening angle can be observed and the circumferential stresses are almost zero.

¹⁸Each of those applications of residual stresses we call a “smoothing-loop”.

9.3 Derivation of suitable invariants for the definition of residual stresses in fiber-reinforced soft biological tissues

In patient-specific arteries circumferential stress cannot uniquely be defined. Furthermore, due to the heterogeneous composition of arteries as well as from a biological and physical point of view, the usage of the circumferential stresses is not suitable for the purpose of defining residual stresses in fiber reinforced soft biological tissues. Therefore, the definition of physically and biologically motivated invariants is of crucial importance.

Soft biological tissues are assumed to be quasi-incompressible materials. Generally, in case of such kinematically constrained materials the true stresses $\boldsymbol{\sigma}$ are decomposed into deviatoric and hydrostatic parts. Furthermore, fiber-reinforced tissues like arterial walls exhibit a distinct behavior in the direction of the fibers. Therefore, the Cauchy stresses are additively decomposed into deviatoric ground stresses $\boldsymbol{\sigma}^*$, which depend on the deformation, and reaction stresses $\boldsymbol{\sigma}^r$

$$\boldsymbol{\sigma} = \boldsymbol{\sigma}^* + \boldsymbol{\sigma}^r . \quad (9.4)$$

The second part of the stresses, $\boldsymbol{\sigma}^r$, is a reaction to the constraints and cannot be computed from constitutive equations. For the definition of suitable invariants we assume (in addition to the incompressibility of the material) the (fictive) inextensibility of the fibers. Since the material is assumed to be incompressible and inextensible in the current fiber directions $\mathbf{a}_{(1)}$ and $\mathbf{a}_{(2)}$, the reaction is composed of a hydrostatic pressure p and tensions $T_{(1)}$ and $T_{(2)}$ in the direction of inextensibility $\mathbf{a}_{(1)}$ and $\mathbf{a}_{(2)}$, respectively. Thus, the reaction stress tensor $\boldsymbol{\sigma}^r$ results from the equilibrium conditions in consideration of the side conditions of the boundary value problem and arises as

$$\boldsymbol{\sigma}^r = -p \mathbf{1} + T_{(1)} \tilde{\mathbf{m}}_{(1)} + T_{(2)} \tilde{\mathbf{m}}_{(2)} . \quad (9.5)$$

Here, $\tilde{\mathbf{m}}_{(1)}$ and $\tilde{\mathbf{m}}_{(2)}$ are the structural tensors associated to the preferred directions $\tilde{\mathbf{a}}_{(1)}$ and $\tilde{\mathbf{a}}_{(2)}$ in the current placement, i.e.

$$\tilde{\mathbf{m}}_{(a)} = \tilde{\mathbf{a}}_{(a)} \otimes \tilde{\mathbf{a}}_{(a)} \quad \text{with} \quad \tilde{\mathbf{a}}_{(a)} = \frac{\mathbf{a}_{(a)}}{\|\mathbf{a}_{(a)}\|} \quad \text{and} \quad \mathbf{a}_{(a)} = \mathbf{F} \mathbf{A}_{(a)} \quad \text{for} \quad a = 1, 2 . \quad (9.6)$$

Following eq. (9.5) the expressions $\text{tr} \boldsymbol{\sigma}^*$, $\boldsymbol{\sigma}^* : \tilde{\mathbf{m}}_{(1)}$ and $\boldsymbol{\sigma}^* : \tilde{\mathbf{m}}_{(2)}$ are absorbed into the functions $p, T_{(1)}$ and $T_{(2)}$ leading to the side conditions on the ground stresses

$$\text{tr} \boldsymbol{\sigma}^* = 0 , \quad \boldsymbol{\sigma}^* : \tilde{\mathbf{m}}_{(1)} = 0 \quad \text{and} \quad \boldsymbol{\sigma}^* : \tilde{\mathbf{m}}_{(2)} = 0 . \quad (9.7)$$

The general idea of this approach is based on Spencer [1972] and Rogers [1987], see also Schröder [1996]. It should be noticed, that the assumption of inextensible fibers is intended for the motivation of suitable invariants only. This assumption is not taken into account in the constitutive modeling of the arterial behavior. In consideration of eq. (9.5) and eq. (9.7) the projection of the stresses onto the current preferred directions and the evaluation of the volumetric part of the stresses lead to the following three conditions

$$\begin{aligned} \boldsymbol{\sigma} : \tilde{\mathbf{m}}_{(1)} &= -p + T_{(1)} & + T_{(2)} \tilde{\mathbf{m}}_{(2)} : \tilde{\mathbf{m}}_{(1)} , \\ \boldsymbol{\sigma} : \tilde{\mathbf{m}}_{(2)} &= -p + T_{(1)} \tilde{\mathbf{m}}_{(1)} : \tilde{\mathbf{m}}_{(2)} + T_{(2)} , \\ \mathbf{1} : \boldsymbol{\sigma} &= -3p + T_{(1)} & + T_{(2)} , \end{aligned} \quad (9.8)$$

from which the hydrostatic pressure p and the fiber stresses $T_{(1)}$ and $T_{(2)}$ can be obtained

$$\begin{aligned}
 p &= [-(\xi + 1) \mathbf{1} : \boldsymbol{\sigma} + \boldsymbol{\sigma} : \tilde{\mathbf{m}}_{(1)} + \boldsymbol{\sigma} : \tilde{\mathbf{m}}_{(2)}] / [3\xi + 1], \\
 T_{(1)} &= [(1 - \xi) \mathbf{1} : \boldsymbol{\sigma} - 2 \boldsymbol{\sigma} : \tilde{\mathbf{m}}_{(1)} + (3\xi - 1) \boldsymbol{\sigma} : \tilde{\mathbf{m}}_{(2)}] / \Xi, \\
 T_{(2)} &= [(1 - \xi) \mathbf{1} : \boldsymbol{\sigma} + (3\xi - 1) \boldsymbol{\sigma} : \tilde{\mathbf{m}}_{(1)} - 2 \boldsymbol{\sigma} : \tilde{\mathbf{m}}_{(2)}] / \Xi.
 \end{aligned} \tag{9.9}$$

Here, the abbreviations $\xi = \tilde{\mathbf{m}}_{(1)} : \tilde{\mathbf{m}}_{(2)} = \cos^2 \phi$ and $\Xi = 3\xi^2 - 2\xi - 1$ are introduced, where ϕ denotes the inclination angle between the two current preferred directions.

9.4 Incorporation of residual stresses

The incorporation of residual stresses is based on a decomposition of the domain, which is carried out in two consecutive steps. First, the arterial cross-section, which consists of n_{MAT} layers or materials, respectively, is initially decomposed into n_{SG} segments. Then, each segment is further subdivided into n_{MAT} sectors, depending on the number of materials the segments consists of. Considering a two-dimensional arterial cross-section, the number of sectors can be specified as

$$n_{\text{SC}}^{2\text{D}} = n_{\text{SG}} \cdot n_{\text{MAT}}. \tag{9.10}$$

In Fig. 9.4a the decomposition of a two-dimensional arterial cross-section consisting of two layers is depicted schematically.

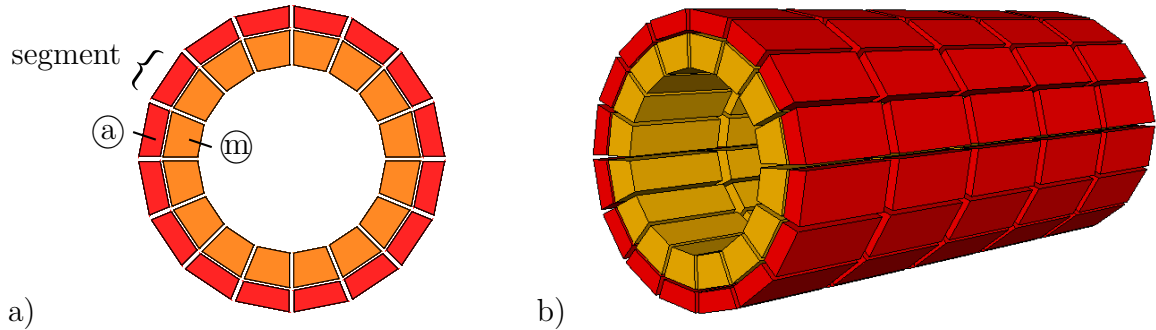


Figure 9.4: Schematic illustration of the decomposition of an arterial cross-section, which consists of two materials (media \textcircled{m} and adventitia \textcircled{a}), i.e. $n_{\text{MAT}} = 2$, $n_{\text{SG}} = 16$; a) two-dimensional cross-section decomposed into $n_{\text{SC}}^{2\text{D}} = 32$ sectors and b) additional longitudinal decomposition in $n_{\text{L}} = 5$ parts yielding $n_{\text{SC}} = 32 \cdot 5 = 160$ sectors.

The consideration of three-dimensional numerical simulations requires an additional decomposition in longitudinal direction. Thus, a decomposition in n_{L} longitudinal section increases the number of sectors to $n_{\text{SC}} = n_{\text{SC}}^{2\text{D}} \cdot n_{\text{L}}$, see Fig. 9.4b.

When the artery is loaded with a physiological internal pressure, the local volume average values of the fiber stresses are computed for each sector¹⁹ with the subvolumes V_i , i.e.

$$\bar{T}_{(1)}^i = \frac{1}{V_i} \int_{\mathcal{B}_i} T_{(1)}(\mathbf{x}) \, dv \quad \text{and} \quad \bar{T}_{(2)}^i = \frac{1}{V_i} \int_{\mathcal{B}_i} T_{(2)}(\mathbf{x}) \, dv, \tag{9.11}$$

¹⁹These average values provide well-defined values only for (nearly) coaxial preferred directions in each sector. Thus, the increase of the amount of segments provides more and more suitable values.

with $i = 1, \dots, n_{\text{SC}}$ and $\mathbf{x} \in \mathcal{B}_i$. The difference between this mean value and the fiber stresses yields the stresses

$$\Delta T_{(1)} = T_{(1)} - \bar{T}_{(1)}^i \quad \text{and} \quad \Delta T_{(2)} = T_{(2)} - \bar{T}_{(2)}^i \quad \text{in } \mathcal{B}_i . \quad (9.12)$$

These stresses in turn are used for an estimation of the residual stresses

$$\boldsymbol{\sigma}^{\text{res}} = -\Delta p \mathbf{1} + \Delta T_{(1)} \tilde{\mathbf{m}}_{(1)} + \Delta T_{(2)} \tilde{\mathbf{m}}_{(2)} . \quad (9.13)$$

Since the residual stresses should not cause changes in volume, Δp can be computed from the condition $\text{tr} \boldsymbol{\sigma}^{\text{res}} = 0$ and yields

$$\Delta p = \frac{1}{3} (\Delta T_{(1)} + \Delta T_{(2)}) . \quad (9.14)$$

The estimation of the residual stresses is accomplished within an iterative process, as mentioned in the isotropic example in Section 9.2. Here, the so-called smoothing-loops (SL) are applied with a certain amount of the computed residual stresses in eq. (9.13) in a stepwise manner. After that the residual stresses are stored and considered in the following simulations in form of the second Piola-Kirchhoff stress tensor

$$\mathbf{S}^{\text{res}} = J \mathbf{F}^{-1} \boldsymbol{\sigma}^{\text{res}} \mathbf{F}^{-T} . \quad (9.15)$$

9.5 Numerical simulations

In this section some numerical simulations are investigated in order to show the suitability of the proposed approach. In Section 9.5.1 an anisotropic two-dimensional ideal tube is considered. Here, a pitch circle, which consists of only one material, is investigated as well as a whole circular ring consisting of two materials (media and adventitia). A two-dimensional realistic artery is investigated in Section 9.5.2. The cross-section originates from patient-specific VH IVUS data, see Section 6.2. Finally, three-dimensional parts of a patient-specific arterial wall are simulated in Section 9.5.3. For the media and adventitia we use the strain-energy function

$$\psi = \psi_{\text{MR}}^{\text{iso}} + \sum_{a=1}^2 \psi_{(a)}^{\text{ti,HGO}_1} , \quad (9.16)$$

see eq. (5.3) and eq. (5.15) and the material parameters from Section 6.2.2, Table 6.3. The plaque is modeled according to Section 6.2.1 where the parameter set IV is used, see Table 6.2. The condition of quasi-incompressibility is enforced by an augmented Lagrangian solution strategy, see Section 5.2.3.

9.5.1 Anisotropic two-dimensional ideal tube

This section is subdivided into two parts. In the first part a pitch circle of -5° to 5° is considered, which consists purely of media material. Here, the smoothing effect on the gradients of some stress measures as a result of the incorporation of the residual stresses is investigated. In the second part of this section a complete circular ring is considered, which consists of media and adventitia. In this simulation the focus will be on the opening of the circular ring due to residual stresses.

Analysis of a pitch circle consisting of media material. The pitch circle, which consists only of media material, is discretized with 10 015 triangular elements, see Fig. 9.5. The cross-section is subdivided into $n_{\text{SC}}^{2\text{D}} = 2 \cdot 1$ sectors²⁰ since $n_{\text{MAT}} = 1$. The pitch circle is loaded with an internal pressure of $p_i = 16.0$ kPa and a number of 10 smoothing-loops (SL) is applied with 100%.

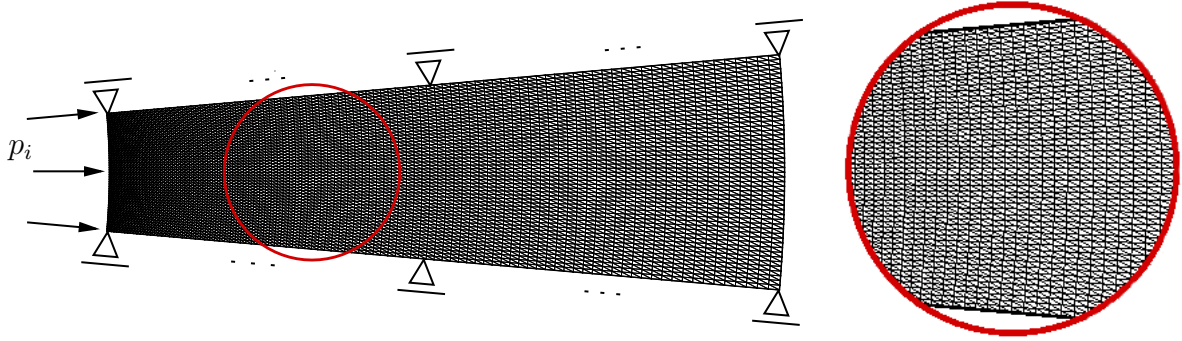


Figure 9.5: Pitch circle with boundary conditions, which is discretized with 10 015 quadratic triangular elements. On the right hand side a detail of the mesh is depicted.

In Fig. 9.6a the fiber stress $T_{(1)}$ in the fiber direction $\mathbf{a}_{(1)}$ over the radius r is depicted. The different curves show the fiber stress distribution without considering residual stresses (normal) and after application of residual stresses using 2, 5 or 10 SLs. A strong gradient is visible if no residual stresses are considered. The gradient decreases as a consequence of the application of residual stresses. After 10 SL the distribution is almost linear.

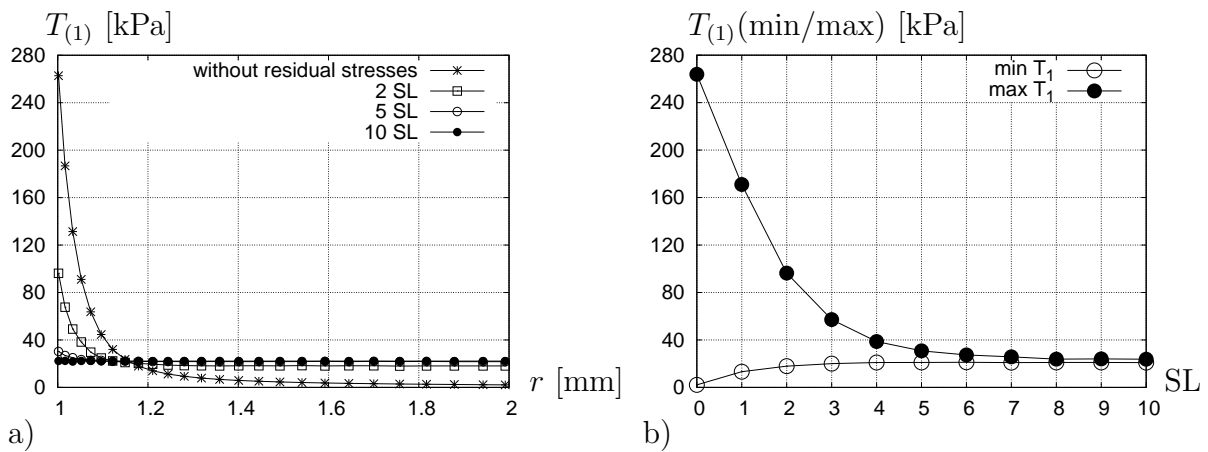


Figure 9.6: a) Fiber stress $T_{(1)}$ in the direction $\mathbf{a}_{(1)}$ over the radius r [mm] in a radial cut without and with residual stresses (2, 5, and 10 smoothing-loops (SL)). b) Maximum and minimum value of the fiber stress $T_{(1)}$ in one of the two sectors after each applied SL.

The diagram in Fig. 9.6b shows the minimum and maximum values of the fiber stress $T_{(1)}$ in one of the two sectors after each applied smoothing-loop. It is clearly visible that the difference of the minimum and maximum values decreases continuously. As a consequence the stress-gradient in the sector, in which the element is located, decreases.

The distributions of the fiber stresses of the overall pitch circle without considering residual stresses and after application of the residual stresses are depicted in Fig. 9.7. Additionally,

²⁰Note, that the use of only one sector would be sufficient due to the homogeneous material.

the distributions of some values in a horizontal slice through the pitch circle at $x_2 = 0$ mm are shown: the fiber stresses $T_{(1)}$, the pressure p , the Cauchy stress σ_{11} and σ_{22} as well as the gradient of the σ_{22} -stresses σ'_{22} . In this slice the stresses σ_{11} are equal to the radial stresses σ_r and the stresses σ_{22} are equal to the circumferential stresses σ_φ . In the simulation, in which no residual stresses are considered, the stresses $T_{(1)}$, σ_{11} , σ_{22} , and the pressure p exhibit a highly exponential character and therefore a strong gradient. The gradient of the σ_{22} -stresses (σ'_{22}) is very high at the inner side of the pitch circle. After the application of the residual stresses, the gradients are smoothed such that the stresses are nearly linear and the gradient σ'_{22} is almost zero.

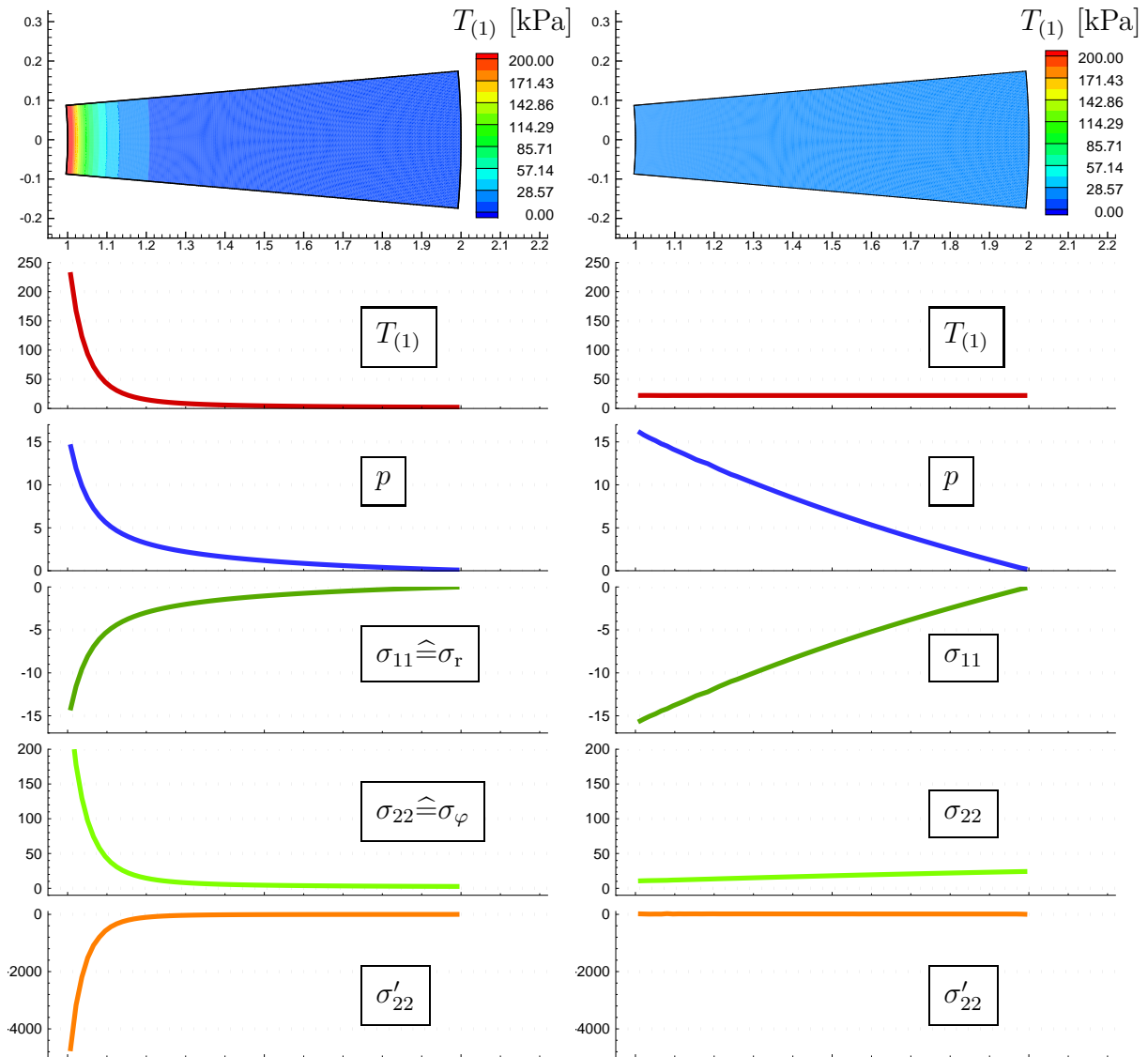


Figure 9.7: Distribution of the fiber stresses $T_{(1)}$ [kPa] of the overall pitch circle without considering residual stresses (left hand side) and after application of the residual stresses (right hand side) and distribution of some values in a horizontal slice through the pitch circle at $x_2 = 0$ mm: the fiber stresses $T_{(1)}$, the pressure p , the Cauchy stresses σ_{11} and σ_{22} (which are equal to the radial stress σ_r and the circumferential stress σ_φ , respectively) as well as the gradient of the σ_{22} -stresses σ'_{22} .

Analysis of a circular ring consisting of media and adventitia material. The cross-section of the circular ring is composed of two materials ($n_{\text{MAT}} = 2$: media and adventitia) and discretized with 6 100 quadratic triangular elements, see Fig. 9.8a. It is decomposed into $n_{\text{SC}}^{2\text{D}} = 36 \cdot 2$ sectors and loaded with an internal pressure of $p_i = 16.0$ kPa. The corresponding distribution of the fiber stresses $T_{(1)}$ over the radius is depicted in Fig. 9.8b and in Fig. 9.8c. After application of 2, 5, and 10 smoothing-loops with an amount of 100% the fiber-stress distribution arises as shown in Fig. 9.8b. Since the stresses are smoothed in an appropriate way after 2 smoothing-loops the further simulations are performed with the residual stresses obtained at this stage of the simulation, see Fig. 9.8d. Here, an almost homogeneous distribution can be observed in the media and in the adventitia, respectively. If the ring is unloaded and then sliced, it opens as a result of the residual stresses and an opening angle appears, see Fig. 9.8e.

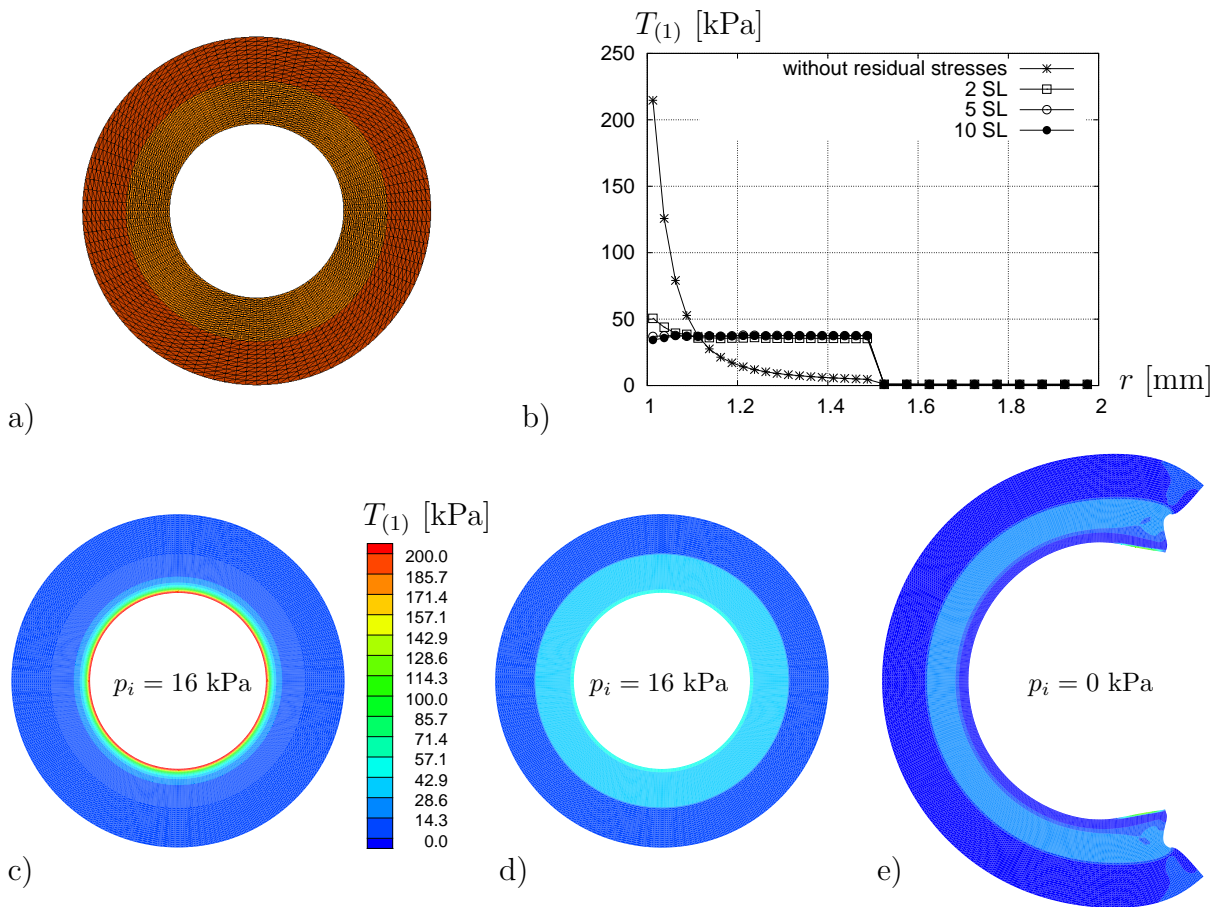


Figure 9.8: a) Two-dimensional circular ring discretized with 6 100 quadratic triangular elements, which consists of media and adventitia material. Fiber-stress $T_{(1)}$ under an inner pressure of $p_i = 16$ kPa: b) over radius r [mm] (without residual stresses and after application of 2, 5, and 10 smoothing-loops); c) distribution without residual stresses and d) after application of residual stresses. e) Opening due to residual stresses ($p_i = 0$ kPa).

9.5.2 Two-dimensional realistic artery

In this section the simulation of a two-dimensional patient-specific arterial cross-section in consideration of residual stresses is discussed. The arterial model is identical to that in Section 6.2.2, see Fig. 6.4. It is decomposed into $n_{\text{SC}}^{2\text{D}} = 36 \cdot 2$ sectors, even though

there exist three materials (adventitia, media, and plaque) $n_{\text{MAT}} = 2$. This is due to the reasonable assumption that the plaque exhibits no fibers ($T_{(1)} = T_{(2)} = 0$) and thus no residual stresses. At an internal pressure of $p_i = 16.0$ kPa a number of 13 smoothing-loops are applied with 10% of magnitude. The fiber stresses $T_{(1)}$ at $x_2 = 0$ mm before and after the application of the smoothing-loops arise as depicted in Fig. 9.9.

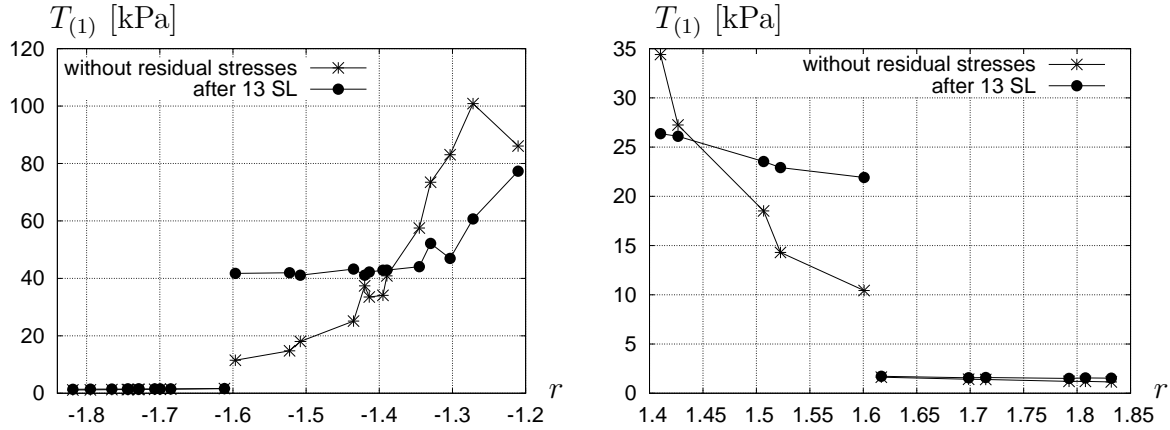


Figure 9.9: Fiber stresses $T_{(1)}$ without and with residual stresses (after application of 13 smoothing-loops (SL)) in the direction $\mathbf{a}_{(1)}$ in a diagram over the radius r [mm] ($x_2 = 0$ mm; left: left hand side of the domain, right: right hand side of the domain without plaque; the origin of the coordinate system is approximately in the center of the domain).

Throughout the whole procedure the adventitia is almost stress free. However, in the media the smoothing of the strong gradient as a result of the application of the residual stresses is visible. The smoothing of the stresses can also be seen in Fig. 9.10a. Here, the σ_{22} stress distribution is displayed.

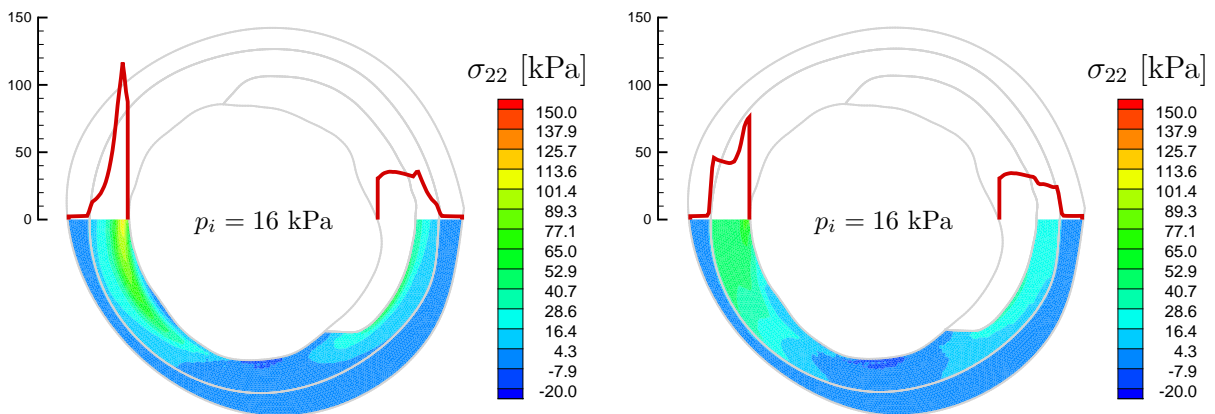


Figure 9.10: Stress distribution of the σ_{22} stresses without and with residual stresses (left hand side and right hand side, respectively).

In order to allow for a more quantitative statement about the smoothing of the stress distribution, we take a look at the stress gradient σ'_{22} . In Fig. 9.11 the gradients σ'_{22} corresponding to the σ_{22} stresses are depicted in the horizontal slice through the artery. It can be observed that the gradients in consideration of residual stresses are two times to four times lower compared to those without residual stresses.

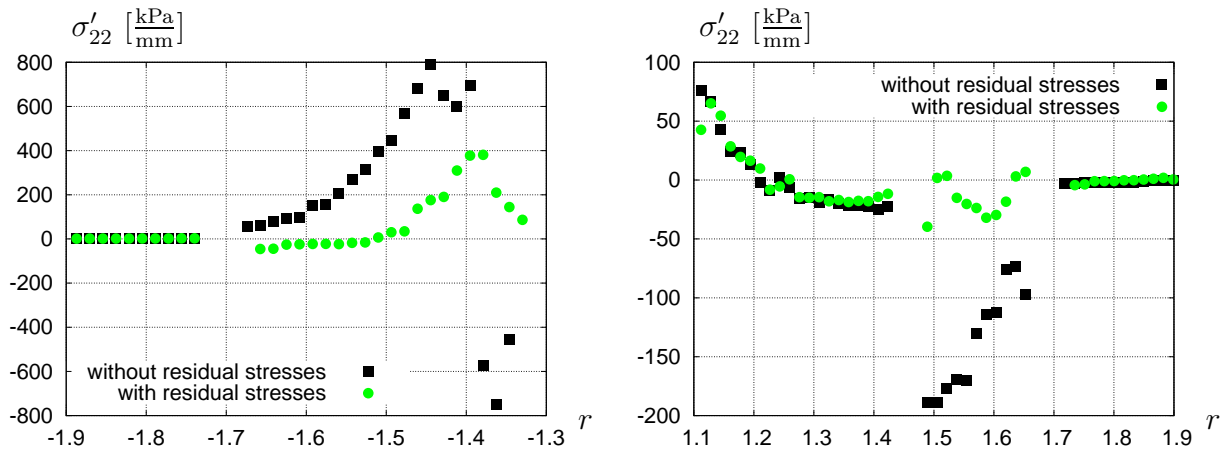


Figure 9.11: Diagram of the gradients σ'_{22} [$\frac{\text{kPa}}{\text{mm}}$], which correspond to the σ_{22} stress. The gradients are depicted over the current radius r [mm] in a horizontal slice through the artery.

Next, we analyze the behavior of the unloaded artery with residual stresses after a radial cut. In order to do so, a sliced, but geometrically closed cross-section is taken into account. The residual-stress distribution, which has been computed in the previous numerical simulation, is applied on the cross-section. In Fig. 9.12 the result of the simulation is shown. The artery opens due to the residual stresses and an opening angle of $\theta \approx 50^\circ$ arises.

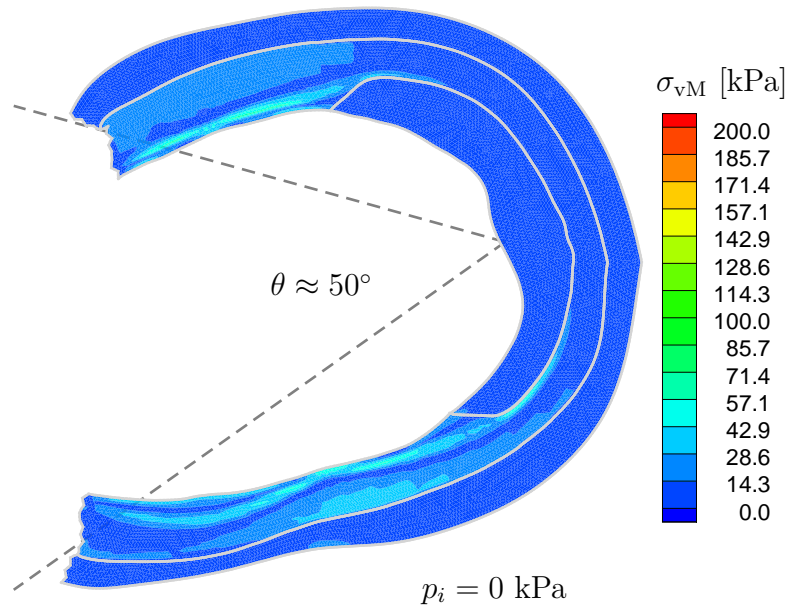


Figure 9.12: Distribution of the von Mises stress σ_{vM} [kPa] in an opened artery (opening angle $\theta \approx 50^\circ$). The opening is only due to residual stresses as the internal pressure is zero.

The von Mises stresses, defined by $\sigma_{vM} = \sqrt{\frac{3}{2}} \|\text{dev}\boldsymbol{\sigma}\|$ with $\text{dev}\boldsymbol{\sigma} = \boldsymbol{\sigma} - \frac{1}{3}\text{tr}\boldsymbol{\sigma}\mathbf{1}$, are close to zero in the opened state. However, the stresses are not exactly equal to zero, which is in agreement with the experimental findings of Vossoughi et al. [1993].

9.5.3 Three-dimensional realistic artery

In this section the proposed approach is applied to the incorporation of residual stresses in three-dimensional simulations of patient-specific arterial walls. We consider a construction of the arterial geometry based on two sequenced two-dimensional VH IVUS images, see

Section 6.2, with a distance of 0.5 mm to each other²¹. In the first example we consider the geometry depicted in Fig. 9.13. The model is discretized with 2 725 triangular elements with quadratic shape functions.

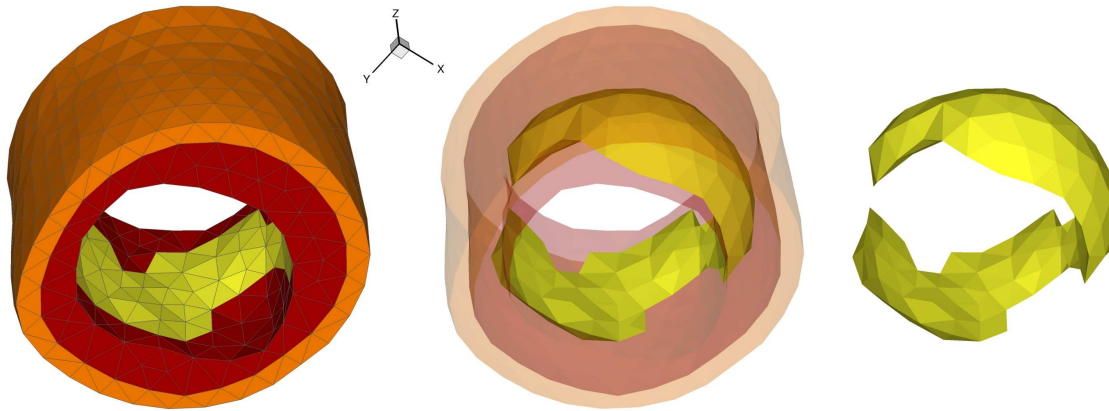


Figure 9.13: Three-dimensional patient-specific arterial model consisting of adventitia (orange), media (red), and plaque (yellow). Discretization was done with 2 725 elements.

The geometry is decomposed into $n_{SC} = 10 \cdot 2 \cdot 3 = 60$ sectors. Since we consider the adventitia and the media for the computation of the residual stresses we have $n_{MAT} = 2$, as explained in Section 9.5.2. As mentioned in Section 9.4 a segmentation in longitudinal direction is also needed. Therefore, $n_L = 3$ segments are investigated in this direction. In the simulation the arterial wall is loaded with an internal pressure of $p_i = 16.0$ kPa. Thereafter, a number of seven smoothing-loops is applied, each with an amount of 10%. In Fig. 9.14 the distribution of the σ_{22} stresses is depicted for the case that no residual stresses are considered and after the application of the smoothing-loops.

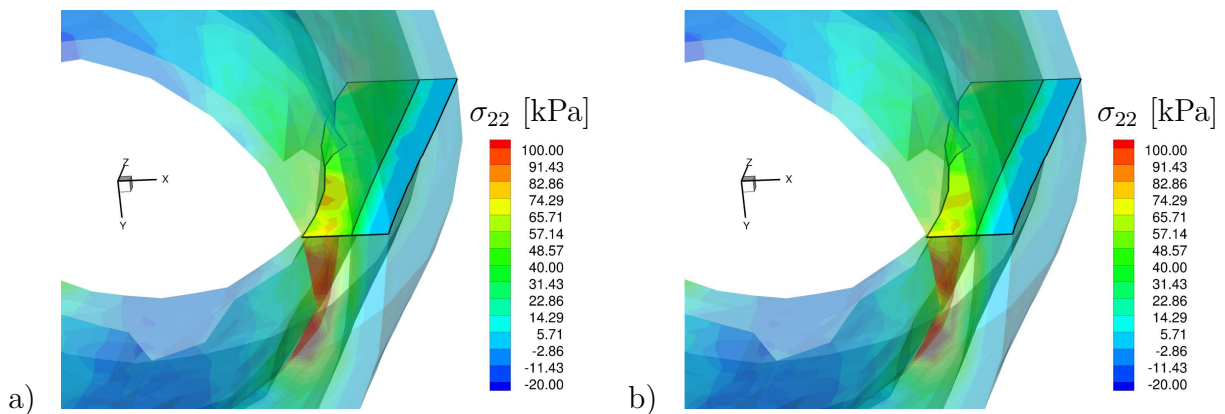


Figure 9.14: Distribution of the stresses σ_{22} [kPa]: a) without considering residual stresses and b) after the application of the smoothing-loops.

It is visible that the residual stresses influence the stress distribution in the physiological loading range such that the stresses are smoothed. Nevertheless, in this three-dimensional simulation the smoothing is not as pronounced as in the two-dimensional case. The opening of the artery as a result of the residual stresses is analyzed in an unloaded but sliced configuration, see Fig. 9.15. In the opened state the von Mises stresses are nearly zero and an opening angle of $\theta \approx 30^\circ$ arises.

²¹For a detailed discussion of the construction principle the reader is referred to Balzani et al. [2011].

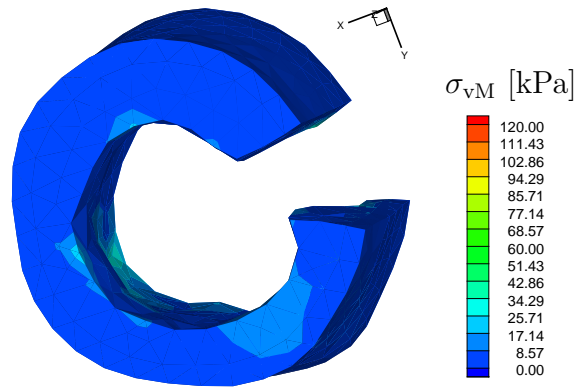


Figure 9.15: Distribution of the von Mises stresses σ_{vM} [kPa] in an open artery. The opening is due to residual stresses.

In two further simulations, the application of the residual stresses is applied on distinct three-dimensional arterial-wall geometries. The segmentation was again done with $n_{SC} = 60$ sectors. The first model is discretized with 5 620 triangular elements with quadratic shape functions, as shown in Fig. 9.16a.

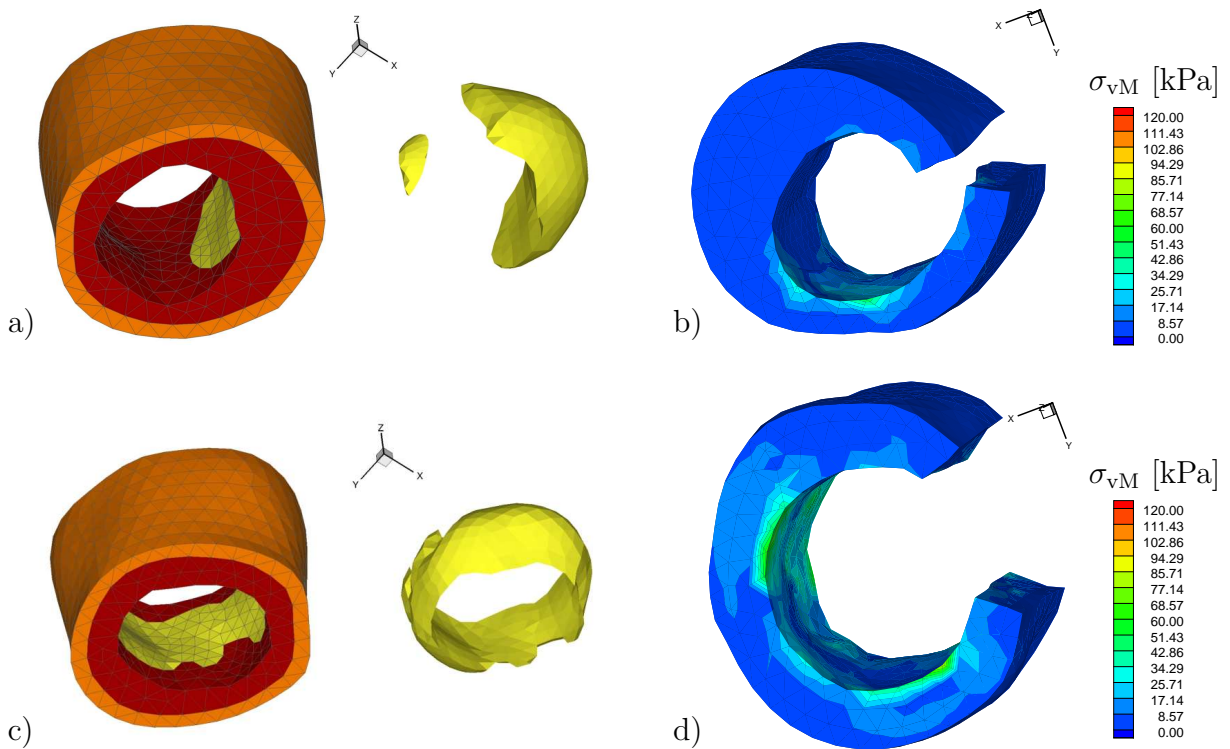


Figure 9.16: a/c) Three-dimensional patient-specific arterial models. b/d) Corresponding distribution of the von Mises stresses σ_{vM} [kPa] in the opened artery.

Here, six smoothing-loops are applied with an amount of 10%. Again, the residual stresses lead to an opening of the artery when it is sliced in radial direction, see Fig. 9.16b. In Fig. 9.16c the discretization of the second model is shown. Here, 5 452 triangular elements with quadratic shape functions are used. During this simulation 11 smoothing-loops are applied with an equal amount of 10%. In Fig. 9.16d the opening of the artery is shown. Comparison of the opening angles of the three simulations shows that the respective angles are different, which can be explained by the difference in the arterial-wall compositions.

10 Summary and outlook

This work dealt with the constitutive modeling of soft biological tissues with a focus on i) the *construction of suitable damage models* for the simulation of degenerated arteries and ii) the *development of a novel model for the incorporation of residual stresses* in arterial-wall simulations.

Summary. In order to motivate the work a general overview on the composition and the mechanics of arterial walls was provided with a special focus on diseases and possible treatments. It was discussed that atherosclerosis, as one of the most frequent degenerations of the human vessels, contributes immensely to serious diseases such as heart attack and stroke. The understanding of the mechanisms of the related treatments as for example the overexpansion of the vessel using a balloon angioplasty could help to improve and facilitate corresponding medical therapies. A key to understand the mechanical behavior of the human artery is given by continuum mechanics. Therefore, the fundamental continuum-mechanical relations were provided and discussed in detail. Since the typical deformations of the vessel during treatment are rather large, the theory is provided in the general, non-linear case and the field equations are formulated in terms of non-linear deformation and stress measures. Since analytical solutions of the occurring field equations on any domains under general boundary conditions do not exist, a numerical scheme given by the Finite-Element-Method was used in this work. Thus, some fundamental procedures of the non-linear Finite-Element-Method were introduced and discussed in detail. We started with the strong form of the balance of linear momentum and converted it into a weak formulation using Galerkin's method. Based on that, a discrete version was derived using discretization with finite elements. In order to provide a concise representation of the procedures, vector-matrix notation was used throughout the derivations.

Material models of soft biological tissues are based on suitable energy functions which describe the constitutive response of the underlying material. In this work, we focused on polyconvex free energies since they guarantee the existence of minimizers and material stability. The construction of such polyconvex functions was discussed and several energies were provided, which are suitable for the description of the physical behavior of arterial walls. Since the biological tissues which are analyzed in this work do not change their volume under applied loading we had to employ a suitable method for the consideration of this incompressibility constraint. The Penalty-Method as well as the Augmented-Lagrange-Method were explained in detail. Later on, the robustness of related numerical simulations with regard to the incorporation of these two different methods was investigated. Here, a special focus was on a boundary value problem with about a million degrees of freedom describing the structure of a patient-specific arterial segment with 10 mm in length. In order to solve the arising equations, an iterative solution strategy (FETI-DP) was used, which is based on domain decomposition. The FETI-DP domain decomposition method was explained briefly. It was found out, that the use of an augmented Lagrange algorithm provides advantages for the nonlinear and the iterative solution in terms of the number of iterations needed for obtaining convergence of the FETI-DP iterative method and the possibility to apply larger time steps. Adequate material parameters of the free energy were identified from experimental uniaxial extension tests by using a least-squares method. Whenever no experimental data was available reasonable parameters were chosen.

In order to get an insight into the field of damage mechanics, this work provided a literature overview as well as a detailed discussion of the hysteretic stress-strain behavior of soft biological tissues. For the construction of damage models a construction principle was proposed, which is based on the construction principle of polyconvex energy functions. This principle was applied to some specific constitutive models, which were then adjusted to experimental data. In a two-dimensional simulation of a realistic arterial cross-section the applicability of the anisotropic damage model was shown. As a further aspect axial strains were taken into consideration. The proposed algorithm worked in the framework of finite element simulations and the damage models were able to reflect the experimental stress-strain behavior accurately.

There exist a variety of publications in the scientific literature on the incorporation of residual stresses, which were outlined in this work. Many of these works are based on the so-called opening angle method, which is, however, restricted to ideal geometries. In this work, a novel model was proposed, which is concerned with the numerical implementation of residual stresses in patient-specific geometries. The basic idea of this approach is to reduce the stress gradients in circumferential direction. In an isotropic simulation this effect was incorporated by application of residual stresses, which were computed under physiological loadings. When the residually stressed body was sliced it opened as a result of the residual stresses. In order to apply the method to fiber-reinforced soft biological tissues, first suitable invariants were defined as function of the stresses in the direction of the embedded fibers. These fiber stresses were used to compute the residual stresses in particular segments of the arterial wall. The segmentation was done for two reasons: i) in order to account for the heterogeneous composition of the arterial wall and ii) in order to reflect the distinct residual stress behavior in the particular layers. In the performed numerical simulations of an anisotropic ideal tube and of two- and three-dimensional patient-specific arterial walls, the expected results were achieved. The stresses in circumferential direction exhibited a smoothed distribution under physiological loadings and an opening angle was observed after application of the residual stresses to the unloaded, but sliced arterial walls.

Outlook. Biomechanics is a scientific field, which will always bear new aspects and motivation for further research. Here, only a few aspects related to this work are mentioned:

- (i) In order to describe the material behavior of soft biological tissues as accurate as possible, a focus should be on the micro-mechanical response of the individual components of the tissue. For this reason material models could be developed, which reflect the macro-mechanical behavior based on micro-mechanical information. Especially for the modeling of the damage behavior this could give further insight into the complex structural interactions.
- (ii) In order to allow for more realistic simulations, the method for the incorporation of the residual stresses could be applied to larger arterial segments. For such large-scale simulations parallel solution strategy are necessary. Thus, the residual-stress approach could be implemented in the FETI-DP scheme. In this way the biomechanical analysis of patient-specific arteries could be improved.

A Notation and calculation rules

Tensor operations in tensor and index notation

$$\begin{aligned}
 \text{1}^{\text{st}}\text{-order contraction:} \quad c &= \mathbf{a} \cdot \mathbf{b} \quad \text{or} \quad c = a_i b_i \\
 &\mathbf{a} = \mathbf{A} \mathbf{b} \quad \text{or} \quad a_i = A_{ij} b_j \\
 &\mathbf{A} = \mathbf{B} \mathbf{C} \quad \text{or} \quad A_{ij} = B_{ik} C_{kj} \\
 \text{2}^{\text{nd}}\text{-order contraction:} \quad c &= \mathbf{A} : \mathbf{B} \quad \text{or} \quad c = A_{ij} B_{ij} \\
 &\mathbf{A} = \mathbb{A} : \mathbf{B} \quad \text{or} \quad A_{ij} = \mathbb{A}_{ijkl} B_{kl} \\
 \text{dyadic product:} \quad \mathbf{A} &= \mathbf{a} \otimes \mathbf{b} \quad \text{or} \quad A_{ij} = a_i b_j
 \end{aligned} \tag{A.1}$$

Arrangement of a matrix

$$\mathbf{A} = A_{ij} = \begin{pmatrix} A_{11} & A_{12} & \cdots & A_{1m} \\ A_{21} & A_{22} & \cdots & A_{2m} \\ \vdots & \vdots & \ddots & \vdots \\ A_{n1} & A_{n2} & \cdots & A_{nm} \end{pmatrix} \begin{array}{l} \leftarrow \text{1}^{\text{st}} \text{ row} \\ \leftarrow \text{2}^{\text{nd}} \text{ row} \\ \dots \\ \leftarrow \text{n}^{\text{th}} \text{ row} \end{array}$$

$$\begin{array}{cccc} \uparrow & \uparrow & & \uparrow \\ \text{1}^{\text{st}} & \text{2}^{\text{nd}} & \dots & \text{m}^{\text{th}} \text{ column} \end{array}$$

Transposed of a matrix

$$\mathbf{A}^T \quad \text{or} \quad (A_{ij})^T = A_{ji} \tag{A.2}$$

$$\text{with } (\mathbf{A}^T)^T = \mathbf{A}, \quad (\mathbf{A} + \mathbf{B})^T = \mathbf{A}^T + \mathbf{B}^T, \quad (\mathbf{A}\mathbf{B})^T = \mathbf{B}^T \mathbf{A}^T \tag{A.3}$$

Identity matrix (also 2nd-order identity tensor)

$$\mathbf{1} = \delta_{ij} = \begin{pmatrix} 1 & 0 & \cdots & 0 \\ 0 & 1 & \cdots & 0 \\ \vdots & \vdots & \ddots & \vdots \\ 0 & 0 & \cdots & 1 \end{pmatrix} \tag{A.4}$$

Trace of a matrix (also trace of a 2nd-order tensor)

$$\text{tr } \mathbf{A} = \mathbf{A} : \mathbf{1} = c \quad \text{or} \quad A_{11} + A_{22} + \dots + A_{nn} = \sum_{i=1}^n A_{ii} = c \tag{A.5}$$

A symmetric matrix is characterized by

$$\mathbf{A} = \mathbf{A}^T \tag{A.6}$$

A skew-symmetric matrix is characterized by

$$\mathbf{A} = -\mathbf{A}^T \quad \text{and} \quad \text{tr } \mathbf{A} = 0 \tag{A.7}$$

Matrix notations of some 4th-order unity tensors

$$\mathbb{I} = \mathbb{I}_{ijkl} = \frac{1}{2}(\delta_{ik}\delta_{jl} + \delta_{il}\delta_{jk}) = \begin{pmatrix} 1 & 0 & 0 & 0 & 0 & 0 \\ 0 & 1 & 0 & 0 & 0 & 0 \\ 0 & 0 & 1 & 0 & 0 & 0 \\ 0 & 0 & 0 & 1/2 & 0 & 0 \\ 0 & 0 & 0 & 0 & 1/2 & 0 \\ 0 & 0 & 0 & 0 & 0 & 1/2 \end{pmatrix} \quad (\text{A.8})$$

$$\bar{\mathbb{I}} = \bar{\mathbb{I}}_{ijkl} = \mathbf{1} \otimes \mathbf{1} = \delta_{ij}\delta_{kl} = \begin{pmatrix} 1 & 1 & 1 & 0 & 0 & 0 \\ 1 & 1 & 1 & 0 & 0 & 0 \\ 1 & 1 & 1 & 0 & 0 & 0 \\ 0 & 0 & 0 & 0 & 0 & 0 \\ 0 & 0 & 0 & 0 & 0 & 0 \\ 0 & 0 & 0 & 0 & 0 & 0 \end{pmatrix} \quad (\text{A.9})$$

$$\hat{\mathbb{I}} = \hat{\mathbb{I}}_{ijkl} = \delta_{ik}\delta_{jl} = \begin{pmatrix} 1 & 0 & 0 & 0 & 0 & 0 \\ 0 & 1 & 0 & 0 & 0 & 0 \\ 0 & 0 & 1 & 0 & 0 & 0 \\ 0 & 0 & 0 & 1 & 0 & 0 \\ 0 & 0 & 0 & 0 & 1 & 0 \\ 0 & 0 & 0 & 0 & 0 & 1 \end{pmatrix} \quad (\text{A.10})$$

Gradient of a scalar s , of a vector \mathbf{v} , and of a 2nd-order tensor \mathbf{T}

$$\text{grad} = \nabla = \begin{pmatrix} \frac{\partial}{\partial x} \\ \frac{\partial}{\partial y} \\ \frac{\partial}{\partial z} \end{pmatrix}, \quad \text{grad } s = \begin{pmatrix} \frac{\partial s}{\partial x} \\ \frac{\partial s}{\partial y} \\ \frac{\partial s}{\partial z} \end{pmatrix}, \quad \text{grad } \mathbf{v} = \begin{pmatrix} \frac{\partial v_x}{\partial x} & \frac{\partial v_x}{\partial y} & \frac{\partial v_x}{\partial z} \\ \frac{\partial v_y}{\partial x} & \frac{\partial v_y}{\partial y} & \frac{\partial v_y}{\partial z} \\ \frac{\partial v_z}{\partial x} & \frac{\partial v_z}{\partial y} & \frac{\partial v_z}{\partial z} \end{pmatrix}$$

$$\begin{aligned} \text{grad } s = \nabla s = \mathbf{v} & \quad \text{or } s_{,i} = v_i & \rightarrow \text{vector} \\ \text{grad } \mathbf{v} = \nabla \mathbf{v} = \mathbf{T} & \quad \text{or } v_{i,j} = T_{ij} & \rightarrow \text{2}^{\text{nd}}\text{-order tensor} \\ \text{grad } \mathbf{T} = \nabla \mathbf{T} = \bar{\mathbf{T}} & \quad \text{or } T_{ij,k} = \bar{T}_{ijk} & \rightarrow \text{3}^{\text{rd}}\text{-order tensor} \end{aligned} \quad (\text{A.11})$$

Divergence of a vector \mathbf{v} and a 2nd-order tensor \mathbf{T}

$$\text{div } \mathbf{v} = \frac{\partial v_x}{\partial x} + \frac{\partial v_y}{\partial y} + \frac{\partial v_z}{\partial z}, \quad \text{div } \mathbf{T} = \begin{pmatrix} \frac{\partial T_{xx}}{\partial x} + \frac{\partial T_{xy}}{\partial y} + \frac{\partial T_{xz}}{\partial z} \\ \frac{\partial T_{yx}}{\partial x} + \frac{\partial T_{yy}}{\partial y} + \frac{\partial T_{yz}}{\partial z} \\ \frac{\partial T_{zx}}{\partial x} + \frac{\partial T_{zy}}{\partial y} + \frac{\partial T_{zz}}{\partial z} \end{pmatrix}$$

$$\begin{aligned} \text{div } \mathbf{v} = \text{grad } \mathbf{v} : \mathbf{1} = \nabla \mathbf{v} : \mathbf{1} = s & \quad \text{or } v_{i,i} = s & \rightarrow \text{scalar} \\ \text{div } \mathbf{T} = \text{grad } \mathbf{T} : \mathbf{1} = \nabla \mathbf{T} : \mathbf{1} = \mathbf{v} & \quad \text{or } T_{ij,j} = v_i & \rightarrow \text{vector} \end{aligned} \quad (\text{A.12})$$

Some calculation rules

$$\begin{aligned}
 \operatorname{div}(s\mathbf{v}) &= \mathbf{v} \cdot \operatorname{grad} s + s \operatorname{div} \mathbf{v} \\
 \operatorname{div}(s\mathbf{T}) &= \mathbf{T} \cdot \operatorname{grad} s + s \operatorname{div} \mathbf{T} \\
 \operatorname{div}(\mathbf{T}\mathbf{v}) &= (\operatorname{div} \mathbf{T}^T) \cdot \mathbf{v} + \mathbf{T}^T : \operatorname{grad} \mathbf{v}
 \end{aligned}
 \tag{A.13}$$

Another tensor operation that is often used is the tensor product of a tensor with a vector. Let \mathbf{A} be a tensor and let \mathbf{v} be a vector. Then the tensor cross product gives a tensor \mathbf{C} defined by

$$\mathbf{C} = \mathbf{A} \times \mathbf{v} \implies C_{ij} = e_{klj} A_{ik} v_l, \tag{A.14}$$

or $\mathbf{T} = \mathbf{v} \times \mathbf{v}$ via $T_{ij} = \epsilon_{ijk} v_k$. The permutation symbol e_{ijk} is defined as

$$e_{ijk} = \begin{cases} 1 & \text{if } ijk = 123, 231, \text{ or } 312 \\ -1 & \text{if } ijk = 321, 132, \text{ or } 213 \\ 0 & \text{if any two indices are alike} \end{cases}
 \tag{A.15}$$

Divergence theorem (also referred to as Gauß's theorem)

$$\begin{aligned}
 \int_{\mathcal{B}} \operatorname{div}[v\mathbf{v}] dV &= \int_{\partial\mathcal{B}} v\mathbf{v} \cdot \mathbf{n} dA = \int_{\partial\mathcal{B}} v\mathbf{v} \cdot d\mathbf{A} \\
 \int_{\mathcal{B}} \operatorname{div}\mathbf{T} dV &= \int_{\partial\mathcal{B}} \mathbf{T} \cdot \mathbf{n} dA = \int_{\partial\mathcal{B}} \mathbf{T} \cdot d\mathbf{A}
 \end{aligned}
 \tag{A.16}$$

B Voigt notation of the tangent modulus \mathbb{C}

The arrangement of the 4th-order elasticity tensor \mathbb{C} in 9×9 matrix notation based on the vector notation of the stresses $[\hat{\boldsymbol{\sigma}}] = [\sigma_{11}, \sigma_{22}, \sigma_{33}, \sigma_{12}, \sigma_{23}, \sigma_{13}, \sigma_{21}, \sigma_{32}, \sigma_{31},]$ and the strains $[\hat{\boldsymbol{\varepsilon}}] = [\varepsilon_{11}, \varepsilon_{22}, \varepsilon_{33}, \varepsilon_{12}, \varepsilon_{23}, \varepsilon_{13}, \varepsilon_{21}, \varepsilon_{32}, \varepsilon_{31}]$ is given by

$$[\mathbb{C}^{9 \times 9}] = \begin{bmatrix} \mathbb{C}_{1111} & \mathbb{C}_{1122} & \mathbb{C}_{1133} & \mathbb{C}_{1112} & \mathbb{C}_{1123} & \mathbb{C}_{1113} & \mathbb{C}_{1121} & \mathbb{C}_{1132} & \mathbb{C}_{1131} \\ \mathbb{C}_{2211} & \mathbb{C}_{2222} & \mathbb{C}_{2233} & \mathbb{C}_{2212} & \mathbb{C}_{2223} & \mathbb{C}_{2213} & \mathbb{C}_{2221} & \mathbb{C}_{2232} & \mathbb{C}_{2231} \\ \mathbb{C}_{3311} & \mathbb{C}_{3322} & \mathbb{C}_{3333} & \mathbb{C}_{3312} & \mathbb{C}_{3323} & \mathbb{C}_{3313} & \mathbb{C}_{3321} & \mathbb{C}_{3332} & \mathbb{C}_{3331} \\ \mathbb{C}_{1211} & \mathbb{C}_{1222} & \mathbb{C}_{1233} & \mathbb{C}_{1212} & \mathbb{C}_{1223} & \mathbb{C}_{1213} & \mathbb{C}_{1221} & \mathbb{C}_{1232} & \mathbb{C}_{1231} \\ \mathbb{C}_{2311} & \mathbb{C}_{2322} & \mathbb{C}_{2333} & \mathbb{C}_{2312} & \mathbb{C}_{2323} & \mathbb{C}_{2313} & \mathbb{C}_{2321} & \mathbb{C}_{2332} & \mathbb{C}_{2331} \\ \mathbb{C}_{1311} & \mathbb{C}_{1322} & \mathbb{C}_{1333} & \mathbb{C}_{1312} & \mathbb{C}_{1323} & \mathbb{C}_{1313} & \mathbb{C}_{1321} & \mathbb{C}_{1332} & \mathbb{C}_{1331} \\ \mathbb{C}_{2111} & \mathbb{C}_{2122} & \mathbb{C}_{2133} & \mathbb{C}_{2112} & \mathbb{C}_{2123} & \mathbb{C}_{2113} & \mathbb{C}_{2121} & \mathbb{C}_{2132} & \mathbb{C}_{2131} \\ \mathbb{C}_{3211} & \mathbb{C}_{3222} & \mathbb{C}_{3233} & \mathbb{C}_{3212} & \mathbb{C}_{3223} & \mathbb{C}_{3213} & \mathbb{C}_{3221} & \mathbb{C}_{3232} & \mathbb{C}_{3231} \\ \mathbb{C}_{3111} & \mathbb{C}_{3122} & \mathbb{C}_{3133} & \mathbb{C}_{3112} & \mathbb{C}_{3123} & \mathbb{C}_{3113} & \mathbb{C}_{3121} & \mathbb{C}_{3132} & \mathbb{C}_{3131} \end{bmatrix}. \quad (\text{B.1})$$

Based on the Voigt notation of the stresses $[\boldsymbol{\sigma}] = [\sigma_{11}, \sigma_{22}, \sigma_{33}, \sigma_{12}, \sigma_{23}, \sigma_{13},]$ and the strains $[\boldsymbol{\varepsilon}] = [\varepsilon_{11}, \varepsilon_{22}, \varepsilon_{33}, 2\varepsilon_{12}, 2\varepsilon_{23}, 2\varepsilon_{13},]$ the 9×9 matrix can be transformed into the 6×6 matrix

$$[\mathbb{C}^{6 \times 6}] = \begin{bmatrix} \mathbb{C}_{1111} & \mathbb{C}_{1122} & \mathbb{C}_{1133} & \mathbb{C}_{11(12)} & \mathbb{C}_{11(23)} & \mathbb{C}_{11(13)} \\ \mathbb{C}_{2211} & \mathbb{C}_{2222} & \mathbb{C}_{2233} & \mathbb{C}_{22(12)} & \mathbb{C}_{22(23)} & \mathbb{C}_{22(13)} \\ \mathbb{C}_{3311} & \mathbb{C}_{3322} & \mathbb{C}_{3333} & \mathbb{C}_{33(12)} & \mathbb{C}_{33(23)} & \mathbb{C}_{33(13)} \\ \mathbb{C}_{(12)11} & \mathbb{C}_{(12)22} & \mathbb{C}_{(12)33} & \mathbb{C}_{(12)(12)} & \mathbb{C}_{(12)(23)} & \mathbb{C}_{(12)(13)} \\ \mathbb{C}_{(23)11} & \mathbb{C}_{(23)22} & \mathbb{C}_{(23)33} & \mathbb{C}_{(23)(12)} & \mathbb{C}_{(23)(23)} & \mathbb{C}_{(23)(13)} \\ \mathbb{C}_{(13)11} & \mathbb{C}_{(13)22} & \mathbb{C}_{(13)33} & \mathbb{C}_{(13)(12)} & \mathbb{C}_{(13)(23)} & \mathbb{C}_{(13)(13)} \end{bmatrix}. \quad (\text{B.2})$$

where $\mathbb{C}_{(ij)kl} = \frac{1}{2}(\mathbb{C}_{ijkl} + \mathbb{C}_{jikl})$, $\mathbb{C}_{ij(kl)} = \frac{1}{2}(\mathbb{C}_{ijkl} + \mathbb{C}_{ijlk})$, and $\mathbb{C}_{(ij)(kl)} = \frac{1}{2}(\mathbb{C}_{(ij)kl} + \mathbb{C}_{(ij)(kl)})$. With the symmetries $\mathbb{C}_{ijkl} = \mathbb{C}_{jikl} = \mathbb{C}_{ijlk} = \mathbb{C}_{klij}$ we get the final representation

$$[\mathbb{C}] = \begin{bmatrix} \mathbb{C}_{1111} & \mathbb{C}_{1122} & \mathbb{C}_{1133} & \mathbb{C}_{1112} & \mathbb{C}_{1123} & \mathbb{C}_{1113} \\ & \mathbb{C}_{2222} & \mathbb{C}_{2233} & \mathbb{C}_{2212} & \mathbb{C}_{2223} & \mathbb{C}_{2213} \\ & & \mathbb{C}_{3333} & \mathbb{C}_{3312} & \mathbb{C}_{3323} & \mathbb{C}_{3313} \\ & & & \mathbb{C}_{1212} & \mathbb{C}_{1223} & \mathbb{C}_{1213} \\ & \text{sym} & & & \mathbb{C}_{2323} & \mathbb{C}_{2313} \\ & & & & & \mathbb{C}_{1313} \end{bmatrix}. \quad (\text{B.3})$$

C Partial derivatives of the invariants with respect to \mathbf{C}

In this appendix some partial derivatives of the invariants with respect to the right Cauchy-Green tensor \mathbf{C} are provided. The first derivative of the principal invariants are given by

$$\begin{aligned}\frac{\partial I_1}{\partial \mathbf{C}} &= \frac{\partial \operatorname{tr} \mathbf{C}}{\partial \mathbf{C}} = \frac{\partial \mathbf{C} : \mathbf{1}}{\partial \mathbf{C}} = \mathbf{1}, \\ \frac{\partial I_3}{\partial \mathbf{C}} &= \frac{\partial \det \mathbf{C}}{\partial \mathbf{C}} = \det \mathbf{C} \mathbf{C}^{-1} = \operatorname{Cof} \mathbf{C}, \\ \frac{\partial I_2}{\partial \mathbf{C}} &= \frac{\partial \operatorname{tr}[\operatorname{Cof} \mathbf{C}]}{\partial \mathbf{C}} = \frac{\partial \{\det \mathbf{C} \mathbf{C}^{-1}\} : \mathbf{1}}{\partial \mathbf{C}} = \frac{\partial \det \mathbf{C} \{\mathbf{C}^{-1} : \mathbf{1}\}}{\partial \mathbf{C}} \\ &= \operatorname{Cof} \mathbf{C} \operatorname{tr}[\mathbf{C}^{-1}] - \det \mathbf{C} \mathbf{C}^{-2} = \operatorname{Cof} \mathbf{C} [\operatorname{tr}[\mathbf{C}^{-1}] - \mathbf{C}^{-1}].\end{aligned}\tag{C.1}$$

Using the Cayley-Hamilton theorem multiplied with \mathbf{C}^{-1} we obtain $\mathbf{C}^2 = I_1 \mathbf{C} - I_2 \mathbf{1} + I_3 \mathbf{C}^{-1}$, and with $\operatorname{tr}[\operatorname{Cof} \mathbf{C}] = \operatorname{tr}[\mathbf{C}^{-1}] \det \mathbf{C}$ we get $\operatorname{Cof} \mathbf{C} = \mathbf{C}^2 - I_1 \mathbf{C} + I_2 \mathbf{1}$. Thus we compute the first derivative of the second invariant alternatively as

$$\begin{aligned}\frac{\partial I_2}{\partial \mathbf{C}} &= \mathbf{C}^2 \operatorname{tr}[\mathbf{C}^{-1}] - I_1 \mathbf{C} \operatorname{tr}[\mathbf{C}^{-1}] + I_2 \mathbf{1} \operatorname{tr}[\mathbf{C}^{-1}] - \mathbf{C}^2 \mathbf{C}^{-1} + \operatorname{tr} \mathbf{C} \mathbf{C} \mathbf{C}^{-1} - I_2 \mathbf{1} \mathbf{C}^{-1} \\ &= \operatorname{tr}[\mathbf{C}^{-1}] [\mathbf{C}^2 - I_1 \mathbf{C} + I_2 \mathbf{1} - I_3 \mathbf{C}^{-1}] - \mathbf{C} + \operatorname{tr} \mathbf{C} \mathbf{1} = \operatorname{tr} \mathbf{C} \mathbf{1} - \mathbf{C}.\end{aligned}\tag{C.2}$$

The first derivatives of the mixed invariants are given by

$$\begin{aligned}\frac{\partial J_4}{\partial \mathbf{C}} &= \frac{\partial \operatorname{tr}[\mathbf{C} \mathbf{M}]}{\partial \mathbf{C}} = \frac{\partial \mathbf{C} \mathbf{M} : \mathbf{1}}{\partial \mathbf{C}} = \mathbf{M}, \\ \frac{\partial J_5}{\partial \mathbf{C}} &= \frac{\partial \operatorname{tr}[\mathbf{C}^2 \mathbf{M}]}{\partial \mathbf{C}} = \frac{\partial \mathbf{C}^2 \mathbf{M} : \mathbf{1}}{\partial \mathbf{C}} = \mathbf{C} \mathbf{M}^T + \mathbf{M}^T \mathbf{C} = \mathbf{C} \mathbf{M} + \mathbf{M} \mathbf{C},\end{aligned}\tag{C.3}$$

with the symmetric structural tensor $\mathbf{M}^T = \mathbf{M}$. The second derivative of the first invariant is zero, i.e. $\partial_{\mathbf{C} \mathbf{C}} \partial^2 I_1 = \partial_{\mathbf{C}} \mathbf{1} = \mathbf{0}$, and the second derivative of the second principal invariant is given by

$$\frac{\partial^2 I_2}{\partial \mathbf{C} \partial \mathbf{C}} = \frac{\partial \{\operatorname{tr} \mathbf{C} \mathbf{1} - \mathbf{C}\}}{\partial \mathbf{C}} = \mathbf{1} \otimes \mathbf{1} - \mathbf{1} \boxtimes \mathbf{1}.\tag{C.4}$$

with $(\bullet) \boxtimes (\bullet)$ in index notation is defined as $\{(\bullet)^{AB}\} \boxtimes \{(\bullet)^{CD}\} = (\bullet)^{AC} (\bullet)^{BD}$. The second derivative of the third principal invariant is given by

$$\frac{\partial^2 I_3}{\partial \mathbf{C} \partial \mathbf{C}} = \frac{\partial \operatorname{Cof} \mathbf{C}}{\partial \mathbf{C}} = \frac{\partial \det \mathbf{C} \mathbf{C}^{-1}}{\partial \mathbf{C}} = \det \mathbf{C} \mathbf{C}^{-1} \otimes \mathbf{C}^{-1} - \det \mathbf{C} \mathbf{C}^{-1} \boxtimes \mathbf{C}^{-1}.\tag{C.5}$$

The second derivative of the fourth invariant is zero, i.e. $\partial_{\mathbf{C} \mathbf{C}} \partial^2 J_4 = \partial_{\mathbf{C}} \mathbf{M} = \mathbf{0}$, and of the fifth invariant it is given by

$$\frac{\partial^2 J_5}{\partial \mathbf{C} \partial \mathbf{C}} = \frac{\partial \{\mathbf{C} \mathbf{M} + \mathbf{M} \mathbf{C}\}}{\partial \mathbf{C}} = (\mathbf{1} \boxtimes \mathbf{M})^{\boxtimes 34} + (\mathbf{M} \boxtimes \mathbf{1})^{\boxtimes 34},\tag{C.6}$$

with $(\bullet)^{\boxtimes 34}$ in index notation is defined as $\{(\bullet)^{ABCD}\}^{\boxtimes 34} = (\bullet)^{ABDC}$.

List of figures

2.1	Selection of the most relevant systemic arteries in the human body.	3
2.2	Composition of a healthy elastic artery, taken from the webpage <i>www.e-visits.de</i>	4
2.3	Composition of collagenous structures. a) Rough division of a collagen fiber bundle, taken from Junqueira and Carneiro [2005], page 61. b),c) Molecular structure of collagenous micro-fibrils connected by proteoglycan-rich matrix (PG), cf. Fratzl [2008], page 10 and Ross and Pawlina [2006], page 152. The main component is tropocollagen, which is in turn interconnected with cross-links (CL).	5
2.4	Schematic illustration of elastin molecules interconnected with cross-links (CL) in its relaxed and stretched configuration; cf. figure 4-28 in Alberts et al. [2004].	6
2.5	a) Artery with normal blood flow. b) Occluded artery with abnormal blood flow; a and b taken from the web page <i>www.daviddarling.info/images</i> . c) Inflation of a balloon inside an artery, taken from the web page <i>www.csmc.edu</i>	6
3.1	Schematic illustration of the reference configuration and the current configuration with convective coordinates and resulting basis vectors of the natural and dual basis.	12
3.2	Schematic illustration of the reference configuration and the current configuration with the corresponding geometrical mappings (transport theorems).	13
3.3	Body with cut free internal stress vector \mathbf{t}	16
3.4	Traction vectors \mathbf{T} on $\partial\mathcal{B}_0$ and \mathbf{t} on $\partial\mathcal{B}$	17
3.5	Rigid body motion applied to a) the current configuration, and b) the reference configuration.	25
3.6	Eigenvectors $\mathbf{n}_{CI}, \mathbf{n}_{CII}$ of the deformation \mathbf{C} and eigenvectors $\mathbf{n}_{SI}, \mathbf{n}_{SII}$ of the stresses \mathbf{S} in a transversely isotropic body: a) due to initial loading, b) after rotation of both loading and structural properties. In the rotated system the principal strains and stresses remain unaltered.	28
4.1	a) Discretization of the physical domain \mathcal{B}_0 resulting in an approximate domain \mathcal{B}_0^h . The approximate domain consists of individual finite elements \mathcal{B}_0^e . b) Four-noded quadrilateral element in the parameterized space Ω^e and the reference configuration \mathcal{B}_0^e	33
5.1	Simultaneous Augmented-Lagrange iteration for a typical time step of the numerical example presented in Section 8.4.	46
6.1	Schematic illustration a) of a segment of a human blood vessel with strips in circumferential (①) and axial (②) direction; b) of a strip in circumferential direction with the preferred directions $[\mathbf{A}_{(1)}] = [\cos\beta_f, -\sin\beta_f, 0]^T$ and $[\mathbf{A}_{(2)}] = [\cos\beta_f, \sin\beta_f, 0]^T$ (the fiber angle β_f is defined as the angle between the circumferential and the fiber direction); c) of a uniaxial extension in circumferential direction of the specimen.	47

6.2	a) Macroscopic view of eight human stenotic iliac arteries (one side of a square is 1 mm), taken from Holzapfel et al. [2004b]. b) IVUS (intravascular ultrasound) gray-scale image and c) corresponding color-coded VH (Virtual Histology) IVUS image, from Prof. Erbel and Dr. Böse (West German Heart Center, Essen).	50
6.3	Stress-stretch relation of the plaque for the five different sets (I-V) of material parameters as a result of a) a tension test and b) a compression test.	53
6.4	a) Patient specific VH IVUS image and b) corresponding two-dimensional numerical model of an arterial wall composed of adventitia, media and plaque and c) discretization of the cross-section with 6015 quadratic triangular finite elements.	53
6.5	Uniaxial extension test: a) stress-stretch response (σ_{11} [kPa] vs. λ [-]) of the experiments and the material model for media and adventitia; b) relative error r [-].	54
6.6	Distribution of the Cauchy stresses in x_1 -direction (σ_{11}) for two parameter sets, i.e. set I and V.	55
6.7	σ_{11} stress distribution in a slice through one side of the artery, where plaque (Ⓟ), media (Ⓜ) and adventitia (ⓐ) are present; c) Fraction of the σ_{11} -stress, which are captured by the plaque (light blue) and by the media/adventitia (gray).	55
7.1	a) RVE of a damaged body at a material point M , cf. Lemaitre [1996], page 11; b) One-dimensional effective stress concept as a result of strain equivalence, cf. Skrzypek and Ganczarski [1999], page 10.	59
7.2	Schematic diagram showing a) a cyclic uniaxial stress-strain response (σ , $\varepsilon = \Delta l/l_0$) of an arterial strip, cf. Holzapfel et al. [2000a]. After preconditioning (point ①) the material behaves (perfectly) elastic. Loading beyond the elastic domain up to point ② results in softening due to damage effects. Further loading and unloading cycles softens the material until it is ‘saturated’ (point ③). Application of higher load levels (point ④) causes further damage and softening effects. The remanent strains due to elasto-plastic material behavior $\varepsilon_{r,plas} = \Delta l_{r,plas}/l_0$ and remanent strains after two over-expansions at the edge of the physiological stress range $\varepsilon_{r,phys} = \Delta l_{r,phys}/l_0$ are shown. b) Corresponding cyclic application of load (loading and unloading cycles) up to three different load levels (I, II, III).	61
7.3	Relation between the damage variable D , its maximum value D_s and the internal variable β for a certain value $r_s = 0.99$: a) in general and b) for different values of the material parameter β_s	63
7.4	Comparison of the constitutive model response ($\psi_{(HGO)}$ and $\psi_{(BNSH)}$) with experimental data from uniaxial extension tests performed with strip specimens of the media of a human carotid artery in circumferential ① and axial ② directions.	70
7.5	Relative error r corresponding to Table 7.4. For the model response the two strain-energy functions $\psi_{(HGO)}$ and $\psi_{(BNSH)}$ are used.	71

7.6	Cyclic uniaxial extension tests of the media of a human carotid artery in circumferential ① and axial ② directions: a) experimental data, and b) results of the constitutive model $\psi_{(\text{HGO})}$ using the material parameters given in Tables 7.4 and 7.5.	71
7.7	Cyclic uniaxial tension tests of the media of a human carotid artery in circumferential ① and axial ② directions: a) results of the constitutive model $\psi_{(\text{HGO})}$, and b) results of the constitutive model $\psi_{(\text{BNSH})}$. The material parameters are given in Table 7.6.	72
7.8	a) Human external iliac artery: high-resolution magnetic resonance image, filtered and (manually) segmented, taken from Holzapfel et al. [2004b], page 659. b) Cross-section of the arterial model discretized with 6 048 quadratic triangular finite elements; the considered components are adventitia, non-diseased media, fibrotic (diseased) media, fibrous cap, lipid pool, and calcification.	73
7.9	Cyclic uniaxial extension tests of the a) adventitia of a human carotid artery in circumferential ① and axial ② direction; b) associated response of the model $\psi_{(\text{HGO})}$	74
7.10	a) Uniaxial extension tests and constitutive model response of the fibrous cap (I-fc) and the fibrotic media (Mf). Symbols: experimental measuring points; Solid lines: constitutive model response. b) Variation of the applied internal pressure p_i [mmHg].	75
7.11	Distribution of the normalized damage variable $D_{(1)}/\max D_{(1)}$ in an arterial cross-section under blood pressure of 24 kPa after a) one over-expansion (point D in Fig. 7.10b), and b) after two over-expansions (point F in Fig. 7.10b).	76
7.12	Distribution of the stretch $(J_4^{(1)})^{1/2}$ in the fiber direction of a loaded but undamaged artery at internal pressure of 24 kPa (point B in Fig. 7.10b): a) without axial residual strains and b) with axial residual strains of 5%.	76
7.13	Distribution of the normalized damage variable $D_{(1)}/\max D_{(1)}$ in an arterial cross-section under blood pressure of 150 kPa (point E in Fig. 7.10b): a) without and b) with axial residual strains of 5%.	77
8.1	Comparison of the stretch-strain response of the experiments and the material model in a uniaxial extension test (media and adventitia) under consideration of a) a Penalty approach and b) an Augmented-Lagrange approach.	80
8.2	Comparison of the penalty function $\psi_{\text{P}}^{\text{vol}} = \varepsilon_1(I_3^{\varepsilon_2} + I_3^{-\varepsilon_2} - 2)$ for the two sets of parameters (Penalty approach and Augmented-Lagrange approach) for the media, see Table 8.1.	81
8.3	Model of the artery, which consists of adventitia, media and degenerated intima (plaque, extracellular lipid, calcified regions).	84
8.4	Distribution of the determinant of the deformation gradient $\det \mathbf{F}$ under an inner pressure $p_i = 24$ kPa using a) the Penalty-Method and using the Augmented-Lagrange-Method with b) a nested iteration and c) a simultaneous iteration.	85

8.5	Time increment, last absolute residual norm of the time step and number of Newton iterations over time: a) Penalty-Method; Augmented-Lagrange-Method with b) nested iteration and with c) simultaneous iteration.	86
8.6	Layered finite element model of the arterial segment discretized using 10-noded tetrahedral elements: a) complete arterial model, b) blanked adventitia and c) plaque.	86
8.7	Domain decomposition of the arterial segment into 224 subdomains. For a better view of the nonoverlapping method the subdomains are dispersed.	87
8.8	a) Diagram showing the range of the determinant of the deformation gradient for the different used approaches. The minimum and maximum values ($\det \mathbf{F}_{\min}/\det \mathbf{F}_{\max}$) are as follows: penalty (0.9926/1.0209), NAL with TOL = 0.01 (0.9901/1.0099), SAL with TOL = 0.01 (0.9902/1.01), SAL with TOL = 0.001 (0.9990/1.001); Distribution of the determinant of the deformation gradient $\det \mathbf{F}$: b) Penalty approach, c) NAL (TOL= 10^{-2}), and d) SAL with TOL= 10^{-2}	88
8.9	Penalty-Method: a) time increment, b) last absolute residual norm, c) number of Newton iterations, and d) FETI-DP iterations over time.	89
8.10	NAL method: a) time increment, b) last absolute residual norm, c) number of Newton iterations, and d) FETI-DP iterations over time.	89
8.11	SAL method with TOL = 0.01: a) time increment, b) last absolute residual norm, c) number of Newton iterations, and d) number of FETI-DP iterations over time.	90
8.12	SAL method with TOL = 0.001: a) Time increment, b) last absolute residual norm, c) number of Newton iterations, and d) number of FETI-DP iterations over time.	90
9.1	Schematic of longitudinal cut through an artery and resulting opening angle θ	93
9.2	a) Ideal two-dimensional circular ring discretized with 6 100 quadratic triangular elements. b) Circumferential stresses σ_φ [kPa] plotted over the radius r [mm] without and with application of residual stresses at an inner pressure of $p_i = 16$ kPa ≈ 120 mmHg; (A) after the first application of residual stresses and (B) after a further application.	96
9.3	Stress distribution of circumferential stresses σ_φ in an isotropic two-dimensional circular ring under an inner pressure of $p_i = 16$ kPa: a) without considering residual stresses and b) after application of the residual stresses. c) Pure residual stress distribution in an unloaded circular ring ($p_i = 0$ kPa) and d) opening of the ring due to residual stresses.	97
9.4	Schematical illustration of the decomposition of an arterial cross-section, which consists of two materials (media \textcircled{m} and adventitia \textcircled{a}), i.e. $n_{\text{MAT}} = 2$, $n_{\text{SC}} = 16$; a) two-dimensional cross-section decomposed into $n_{\text{SC}}^{2D} = 32$ sectors and b) additional longitudinal decomposition in $n_L = 5$ parts yielding $n_{\text{SC}} = 32 \cdot 5 = 160$ sectors.	99

- 9.5 Pitch circle with boundary conditions, which is discretized with 10 015 quadratic triangular elements. On the right hand side a detail of the mesh is depicted. 101
- 9.6 a) Fiber stress $T_{(1)}$ in the direction $\mathbf{a}_{(1)}$ over the radius r [mm] in a radial cut without and with residual stresses (2, 5, and 10 smoothing-loops (SL)). b) Maximum and minimum value of the fiber stress $T_{(1)}$ in one of the two sectors after each applied SL. 101
- 9.7 Distribution of the fiber stresses $T_{(1)}$ [kPa] of the overall pitch circle without considering residual stresses (left hand side) and after application of the residual stresses (right hand side) and distribution of some values in a horizontal slice through the pitch circle at $x_2 = 0$ mm: the fiber stresses $T_{(1)}$, the pressure p , the Cauchy stresses σ_{11} and σ_{22} (which are equal to the radial stress σ_r and the circumferential stress σ_φ , respectively) as well as the gradient of the σ_{22} -stresses σ'_{22} 102
- 9.8 a) Two-dimensional circular ring discretized with 6 100 quadratic triangular elements, which consists of media and adventitia material. Fiber-stress $T_{(1)}$ under an inner pressure of $p_i = 16$ kPa: b) over radius r [mm] (without residual stresses and after application of 2, 5, and 10 smoothing-loops); c) distribution without residual stresses and d) after application of residual stresses. e) Opening due to residual stresses ($p_i = 0$ kPa). 103
- 9.9 Fiber stresses $T_{(1)}$ without and with residual stresses (after application of 13 smoothing-loops (SL)) in the direction $\mathbf{a}_{(1)}$ in a diagram over the radius r [mm] ($x_2 = 0$ mm; left: left hand side of the domain, right: right hand side of the domain without plaque; the origin of the coordinate system is approximately in the center of the domain). 104
- 9.10 Stress distribution of the σ_{22} stresses without and with residual stresses (left hand side and right hand side, respectively). 104
- 9.11 Diagram of the gradients σ'_{22} [$\frac{\text{kPa}}{\text{mm}}$], which correspond to the σ_{22} stress. The gradients are depicted over the current radius r [mm] in a horizontal slice through the artery. 105
- 9.12 Distribution of the von Mises stress σ_{vM} [kPa] in an opened artery (opening angle $\theta \approx 50^\circ$). The opening is only due to residual stresses as the internal pressure is zero. 105
- 9.13 Three-dimensional patient-specific arterial model consisting of adventitia (orange), media (red), and plaque (yellow). Discretization was done with 2 725 elements. 106
- 9.14 Distribution of the stresses σ_{22} [kPa]: a) without considering residual stresses and b) after the application of the smoothing-loops. 106
- 9.15 Distribution of the von Mises stresses σ_{vM} [kPa] in an open artery. The opening is due to residual stresses. 107
- 9.16 a/c) Three-dimensional patient-specific arterial models. b/d) Corresponding distribution of the von Mises stresses σ_{vM} [kPa] in the opened artery. . 107

List of Tables

2.1	Classification of hypertension for different blood pressures (BP) of adults, taken from Chobanian et al. [2003]; 100 mmHg $\hat{=}$ 0.13332 bar $\hat{=}$ 13.332 kPa.	8
3.1	Summary of the relations between different stress measures.	18
3.2	Balance equations and entropy inequality: axiom, constituents and local form.	23
3.3	Objective Euclidean transformations of different arbitrary Eulerian and Lagrangian quantities as well as for a two-point tensor.	24
4.1	Finite element subspaces, interpolation functions, and Gauß integration. . .	37
5.1	Algorithmic implementation of the nested iteration (Uzawa algorithm) for a typical time step with $\Delta t = {}^{k+1}t - {}^k t$, cf. Simo and Taylor [1991]. At the beginning of the simulation λ is initialized to zero.	45
5.2	Algorithmic implementation of the simultaneous iteration for a typical time step with $\Delta t = {}^{k+1}t - {}^k t$, cf. Simo and Taylor [1991]. At the beginning of the simulation λ is initialized to zero.	46
6.1	Algorithmic box for the computation of the relative error r as a function of the stretch $\lambda_{1,i}$ at each measuring point $i = 1, \dots, n_{mp}$ and a vector $\boldsymbol{\alpha}$, which contains all material parameters involved in the strain-energy function ψ	49
6.2	Five different sets (I-V) of material parameters for the plaque with $\nu = 0.478$.	52
6.3	Material parameters of the media and the adventitia.	54
7.1	Possible functions \bar{P} and value of the function \bar{P} in the natural state c . . .	62
7.2	Algorithmic box (taken from Balzani et al. [2012]) for the computation of the stress and elasticity tensors. The initial values of the history variables at $k = 0$ are ${}^0\psi_{(a)}^{\text{ti}} = {}^0\tilde{\beta}_{(a)} = {}^0\psi_{\text{ini},(a)}^{\text{ti},0} = {}^0\tilde{\beta}_{(a)}^{\text{ini}} = {}^0\gamma_{(a)} = 0$, and the tolerance ϵ should be close to computer accuracy.	67
7.3	Algorithmic box (from Balzani et al. [2012]) for the computation of the transversely isotropic elasticity tensor $\mathbb{C}_{(a)}^{\text{ti}}$. The tolerance ϵ should be close to computer accuracy.	68
7.4	Material parameters and resulting total error \bar{r} (eq. (6.10)) of the two models (eq. (7.33)) for the media of a human carotid artery in the physiological loading domain.	70
7.5	Damage parameters and error measure \bar{r} for the constitutive model $\psi_{(\text{HGO})}$ for the media of a human carotid artery in the supra-physiological loading domain. The adjustment was performed with fixed hyperelastic parameters.	71
7.6	Material parameters and error measure \bar{r} of the two models $\psi_{(\text{HGO})}$ and $\psi_{(\text{BNSH})}$ for the media of a human carotid artery in the supra-physiological loading domain. For the adjustment suitable bounds for the (hyperelastic) parameters, based on the results given in Table 7.4, have been considered. .	72
7.7	Hyperelastic and damage parameters of adventitia and plaque components.	73

7.8	Parameters of the penalty function ψ_p^{vol} for the different arterial constituents.	74
8.1	Material parameters for the media and the adventitia with penalty parameters ε_1 and ε_2 for the Penalty approach and the Augmented-Lagrange approach.	79
8.2	Material parameters of the degenerated tissue.	81
8.3	Comparison of the methods in the framework of the FETI-DP method. The Finite-Element model has approx. 1.3 million degrees of freedom, see Fig. 8.6. The total cost can be estimated roughly by multiplying the number of global Newton iterations by the average number of FETI-DP iterations. This table is taken from Brinkhues et al. [2012].	91
9.1	Material parameters of the isotropic ideal tube.	96

References

- H. Abé, K. Hayashi, and M. Sato, editors. *Data book on mechanical properties of living cells, tissues, and organs*. Springer Verlag, New York, 1996.
- V. Alastrué, E. Peña, M. Ángel, M.A. Martínez, and M. Doblaré. Assessing the use of the "opening angle method" to enforce residual stresses in patient-specific arteries. *Annals of Biomedical Engineering*, 35:1821–1837, 2007a.
- V. Alastrué, J.F. Rodríguez, B. Calvo, and M. Doblaré. Structural damage models for fibrous biological soft tissues. *International Journal of Solids and Structures*, 44(18-19): 5894–5911, 2007b.
- V. Alastrué, M.A. Martínez, and M. Doblaré. Modelling adaptive volumetric finite growth in patient-specific residually stressed arteries. *Journal of Biomechanics*, 41:1773–1781, 2008.
- V. Alastrué, M.A. Martínez, M. Doblaré, and A. Menzel. Anisotropic micro-sphere-based finite elasticity applied to blood vessel modelling. *Journal of the Mechanics and Physics of Solids*, 57:178–203, 2009.
- B. Alberts, D. Bray, K. Hopkin, A. Johnson, M. Raff, K. Roberts, and P. Walter. *Essential Cell Biology*. Garland Science, 2nd edition, 2004.
- P.W. Alford, J.D. Humphrey, and L.A. Taber. Growth and remodeling in a thick-walled artery model: effects of spatial variations in wall constituents. *Biomechanics and Modeling in Mechanobiology*, 7(4):245–262, 2008.
- S. Balay, V. Eijkhout, W.D. Gropp, L.C. McInnes, and B.F. Smith. Efficient management of parallelism in object oriented numerical software libraries. In E. Arge, A. M. Bruaset, and H. P. Langtangen, editors, *Modern Software Tools in Scientific Computing*, pages 163–202. Birkhäuser Press, 1997.
- S. Balay, K. Buschelman, W.D. Gropp, D. Kaushik, M. Knepley, L.C. McInnes, B.F. Smith, and H. Zhang. PETSc home page, 2001.
- S. Balay, K. Buschelman, V. Eijkhout, W.D. Gropp, D. Kaushik, M.G. Knepley, L.C. McInnes, B.F. Smith, and H. Zhang. PETSc users manual. Technical Report ANL-95/11 - Revision 2.1.5, Argonne National Laboratory, 2004.
- R.A. Baldewsing, C.L. de Korte, J.A. Schaar, F. Mastik, and A.F.W. van der Steen. Finite element modeling and intravascular ultrasound elastography of vulnerable plaques: parameter variation. *Ultrasonics*, 42:723–729, 2004.
- J.M. Ball. Convexity conditions and existence theorems in nonlinear elasticity. *Archive for Rational Mechanics and Analysis*, 63:337–403, 1976.
- J.M. Ball. Constitutive inequalities and existence theorems in nonlinear elastostatics. In R.J. Knops, editor, *Symposium on Non-Well Posed Problems and Logarithmic Convexity*, volume 316. Springer-Lecture Notes in Mathematics, 1977.

- D. Balzani. *Polyconvex anisotropic energies and modeling of damage applied to arterial walls*. Phd-thesis, University Duisburg-Essen, Verlag Glückauf Essen, 2006.
- D. Balzani, P. Neff, J. Schröder, and G.A. Holzapfel. A polyconvex framework for soft biological tissues. Adjustment to experimental data. *International Journal of Solids and Structures*, 43:6052–6070, 2006a.
- D. Balzani, J. Schröder, and D. Gross. Simulation of discontinuous damage incorporating residual stresses in circumferentially overstretched atherosclerotic arteries. *Acta Biomaterialia*, 2:609–618, 2006b.
- D. Balzani, J. Schröder, and D. Gross. Numerical simulation of residual stresses in arterial walls. *Computational Materials Science*, 39:117–123, 2007.
- D. Balzani, D. Brands, A. Klawonn, O. Rheinbach, and J. Schröder. On the mechanical modeling of anisotropic biological soft tissue and iterative parallel solution strategies. *Archive of Applied Mechanics*, 80:479–488, 2009a.
- D. Balzani, S. Brinkhues, and G.A. Holzapfel. Comparative study of polyconvex strain-energy functions used for the modeling of damage hysteresis in overstretched arterial walls. In *Proceedings of the 7th EUROMECH Solid Mechanics Conference*, 2009b.
- D. Balzani, D. Böse, D. Brands, R. Erbel, A. Klawonn, O. Rheinbach, and J. Schröder. Parallel simulation of patient-specific atherosclerotic arteries for the enhancement of intravascular ultrasound diagnostics. *Engineering Computations*, 2011. In press.
- D. Balzani, S. Brinkhues, and G.A. Holzapfel. Constitutive framework for the modeling of damage in soft biological tissues. *Computer Methods in Applied Mechanics and Engineering*, 213–216:139–151, 2012.
- K.J. Bathe. *Finite element procedures*. Prentice Hall, New Jersey, 1996.
- T. Belytschko, W. K. Liu, and B. Moran. *Nonlinear Finite Elements for Continua and Structures*. John Wiley and Sons, 2000.
- D.H. Bergel. *The visco-elastic properties of the arterial wall*. PhD thesis, University of London, London, 1960.
- D. Besdo and J. Ihlemann. A phenomenological constitutive model for rubberlike materials and its numerical applications. *International Journal of Plasticity*, 19:1019–1036, 2003.
- J. Betten. *Kontinuumsmechanik: Elastisches und inelastisches Verhalten isotroper und anisotroper Stoffe*. Springer, 2nd edition, 2001.
- M. Bhardwaj, D. Day, C. Farhat, M. Lesoinne, K. Pierson, and D. Rixen. Application of the FETI method to ASCII problems - scalability results on one thousand processors and discussion of highly heterogeneous problems. *International Journal for Numerical Methods in Engineering*, 47:513–535, 2000.
- W. Böcker, H. Denk, and P.U. Heitz, editors. *Pathologie*. Urban & Fischer - Elsevier, München, 4th edition, 2008. ISBN 978-3-437-42382-6.

- J.P. Boehler. On irreducible representations for isotropic scalar functions. *Zeitschrift für angewandte Mathematik und Mechanik*, 57:323–327, 1977.
- J.P. Boehler. A simple derivation of representations for non-polynomial constitutive equations in some cases of anisotropy. *Zeitschrift für angewandte Mathematik und Mechanik*, 59:157–167, 1979.
- J.P. Boehler. Introduction to the invariant formulation of anisotropic constitutive equations. In J. P. Boehler, editor, *Applications of Tensor Functions in Solid Mechanics*, volume 292 of *CISM Courses and Lectures*, pages 13–30. Springer, 1987a.
- J.P. Boehler. Representations for isotropic and anisotropic non-polynomial tensor functions. In J.P. Boehler, editor, *Applications of Tensor Functions in Solid Mechanics, Courses and Lectures of CISM*, number 292. Springer, 1987b.
- D. Böse, C. von Birgelen, and R. Erbel. Intravascular ultrasound for the evaluation of therapies targeting coronary atherosclerosis. *Journal of the American College of Cardiology*, 49(9):925–932, 2007.
- D. Braess. *Finite Elements: Theory, Fast Solvers and Applications in Solid Mechanics*. Cambridge University Press, Cambridge, 2nd edition, 2001.
- D. Brands, J. Schröder, A. Klawonn, O. Rheinbach, D. Böse, and R. Erbel. Numerical simulations of arterial walls based on IVUS-data. *Proceedings in Applied Mathematics and Mechanics*, 9(1):75–78, 2009.
- S. Brinkhues, A. Klawonn, O. Rheinbach, and J. Schröder. Augmented lagrange methods for quasi-incompressible materials – Applications to soft biological tissue. *International Journal for Numerical Methods in Biomedical Engineering*, 2012. accepted 6/2012.
- M.S. Brown and J.L. Goldstein. Lipoprotein metabolism in the macrophage: implications for cholesterol deposition in atherosclerosis. *Annual Reviews of Biochemistry*, 52(1): 223–261, 1983.
- C. Bustamante and G.A. Holzapfel. Methods to compute 3D residual stress distributions in hyperelastic tubes with application to arterial walls. *International Journal of Engineering Science*, 48(11):1066–1082, 2010.
- B. Calvo, E. Peña, M.A. Martínez, and M.A. Doblaré. An uncoupled directional damage model for fibered biological soft tissues. *International Journal for Numerical Methods in Engineering*, 69:2036–2057, 2007.
- L. Cardamone, A. Valentin, J.F. Eberth, and J.D. Humphrey. Origin of axial prestretch and residual stress in arteries. *Biomechanics and Modeling in Mechanobiology*, 8:431–446, 2009.
- T.E. Carew, R.N. Vaishnav, and D.J. Patel. Compressibility of the arterial wall. *Circulation Research*, 23(1):61–68, 1968.
- W. Castaneda-Zuniga. Pathophysiology of transluminal angioplasty. In J. Meyer, R. Erberl, and H.J. Rupprecht, editors, *Improvement of myocardial perfusion*, pages 138–141. Martinus Nijhof, Boston, 1985.

- W.R. Castaneda-Zuniga, A. Formanek, M. Tadavarthy, Z. Vlodayer, J.E. Edwards, C. Zollikofer, and K. Amplatz. The mechanism of balloon angioplasty. *Radiology*, 135:565–571, 1980.
- P. Chadwick. *Continuum mechanics: concise theory and problems*. Dover Publications, 1999.
- H.R. Chaudhry, B. Bukiet, A. Davis, A.B. Ritter, and T. Findley. Residual stresses in oscillating thoracic arteries reduce circumferential stresses and stress gradients. *Journal of Biomechanics*, 30(1):57–62, 1997.
- Y.-C. Chen and J.F. Eberth. Constitutive function, residual stress, and state of uniform stress in arteries. *Journal of the Mechanics and Physics of Solids*, 60(6):1145–1157, 2012.
- A.V. Chobanian, G.L. Bakris, H.R. Black, W.C. Cushman, L.A. Green, J.L. Izzo Jr., D.W. Jones, B.J. Materson, S. Oparil, J.T. Wright Jr., E.J. Roccella, and the National High Blood Pressure Education Program Coordinating Committee. Seventh report of the joint national committee on prevention, detection, evaluation, and treatment of high blood pressure. *Hypertension*, 42:1206–1252, 2003.
- C.J. Chuong and Y.C. Fung. Three-dimensional stress distribution in arteries. *Journal of Biomechanical Engineering*, 105:268–274, 1983.
- C.J. Chuong and Y.C. Fung. Compressibility and constitutive equation of arterial wall in radial compression experiments. *Journal of Biomechanics*, 17(1):35 – 40, 1984.
- C.J. Chuong and Y.C. Fung. On residual stress in arteries. *Journal of Biomechanical Engineering*, 108:189–191, 1986.
- P.G. Ciarlet. *Mathematical Elasticity, Volume 1: Three Dimensional Elasticity*. Elsevier Science Publishers B.V., North Holland, 1988.
- R.H. Cox. Passive mechanics and connective tissue composition of canine arteries. *American Journal of Physiology – Heart and Circulatory Physiology*, 234:H533–H541, 1978.
- M.J. Davies. Stability and instability: two faces of coronary atherosclerosis. The Paul Dudley White lecture 1995. *Circulation*, 94:2013–2020, 1996.
- T.A. Davis. A column pre-ordering strategy for the unsymmetric-pattern multifrontal method. *ACM Transactions on Mathematical Software*, 30(2):165–195, June 2004.
- E.A. de Souza Neto, D. Perić, and D.R.J. Owen. A phenomenological three-dimensional rate-independent continuum damage model for highly filled polymers: formulation and computational aspects. *Journal of the Mechanics and Physics of Solids*, 42:1533–1550, 1994.
- E.A. de Souza Neto, D. Perić, and D.R.J. Owen. Continuum modelling and numerical simulation of material damage at finite strains. *Archive of Computational Methods in Engineering*, 5(4):311–384, 1998.

- J. Diani, M. Brieub, and J.M. Vacheran. A damage directional constitutive model for mullins effect with permanent set and induced anisotropy. *European Journal of Mechanics, A/Solids*, 25:483–496, 2006.
- A. Dorfmann and R.W. Ogden. A pseudo-elastic model for loading, partial unloading and reloading of particle-reinforced rubber. *International Journal of Solids and Structures*, 40:2699–2714, 2003.
- A. Dorfmann and R.W. Ogden. A constitutive model for the Mullins effect with permanent set in particle-reinforced rubber. *International Journal of Solids and Structures*, 41:1855–1878, 2004.
- C.T. Dotter. Transluminal angioplasty: a long view. *Radiology*, 135:561–564, 1980.
- C.T. Dotter and M. Judkins. Transluminal treatment of arteriosclerotic obstruction: description of a new technic and a preliminary report of its applications. *Circulation*, 30(5):654–70, 1964.
- A. Ehret and M. Itskov. A polyconvex hyperelastic model for fiber-reinforced materials in application to soft tissues. *Journal of the Mechanics and Physics of Solids*, 42:8853–9963, 2007.
- A. Ehret and M. Itskov. Modeling of anisotropic softening phenomena: application to soft biological tissues. *International Journal of Plasticity*, 25:901–919, 2009.
- E.B. Elliott. *An introduction to the algebra of quantics*. Oxford University Press, 2nd edition, 1913.
- A.C. Eringen. *Mechanics of continua*. Huntington, New York, Robert E. Krieger Publishing Co., 2nd edition, 1980.
- C. Farhat and F.-X. Roux. A method of Finite Element Tearing and Interconnecting and its parallel solution algorithm. *International Journal for Numerical Methods in Engineering*, 32:1205–1227, 1991.
- C. Farhat, M. Lesoinne, and K.H. Pierson. A scalable dual-primal domain decomposition method. *Numerical Linear Algebra With Applications*, 7:687–714, 2000a.
- C. Farhat, K.H. Pierson, and M. Lesoinne. The second generation of FETI methods and their application to the parallel solution of large-scale linear and geometrically nonlinear structural analysis problems. *Computer Methods in Applied Mechanics and Engineering*, 184:333–374, 2000b.
- C. Farhat, M. Lesoinne, P. LeTallec, K.H. Pierson, and D. Rixen. FETI-DP: A dual-primal unified FETI method - part I: A faster alternative to the two-level FETI method. *International Journal for Numerical Methods in Engineering*, 50:1523–1544, 2001.
- G.M. Fischer and J.G. Llaurodo. Collagen and elastin content in canine arteries selected from functionally different vascular beds. *Circulation Research*, 19:394–399, 1966.
- R. Fletcher. *Practical Methods of Optimization*. John Wiley and Sons, 1987.

- P.J. Flory. Thermodynamic relations for high elastic materials. *Transaction of the Faraday Society*, 57:1691–1702, 1961.
- M. Fortin and A. Fortin. A generalization of Uzawa’s algorithm for the solution of the Navier-Stokes equations. *Communications in Applied Numerical Methods*, 1(5):205–208, 1985.
- P. Fratzl. Collagen: structure and mechanics, an introduction. In P. Fratzl, editor, *Collagen : structure and mechanics*, pages 1–13. Springer, 2008.
- C. Freischläger. *Konzepte zur Formulierung versteifungsfreier Volumenelemente*. PhD thesis, University of Karlsruhe, 2000.
- Y.C. Fung. What are the residual stresses doing in our blood vessels? *Annals of Biomedical Engineering*, 19(3):237–249, 1991.
- Y.C. Fung. *Biomechanics – Mechanical properties of living tissues*. Springer, New York, Berlin, Heidelberg, 1993.
- Y.C. Fung and S.Q. Liu. Strain distribution in small blood vessels with zero-stress state taken into consideration. *American Journal of Physiology – Heart and Circulatory Physiology*, 262:H544–H552, 1992.
- Y.C. Fung, K. Fronek, and P. Patitucci. Pseudoelasticity of arteries and the choice of its mathematical expression. *American Journal of Physics*, 237:H620–H631, 1979.
- Y.C. Gao. Large deformation field near a crack tip in rubber-like material. *Theoretical and Applied Fracture Mechanics*, 26(3):155 – 162, 1997.
- H.M. Garcia-Garcia, M.A. Costa, and P.W. Serruys. Imaging of coronary atherosclerosis: intravascular ultrasound. *European Heart Journal*, 3:2456–2469, 2010.
- T.C. Gasser and G.A. Holzapfel. Finite element modeling of balloon angioplasty by considering overstretch of remnant non-diseased tissues in lesions. *Computational Mechanics*, 40:47–60, 2007.
- T.C. Gasser, R.W. Ogden, and G.A. Holzapfel. Hyperelastic modelling of arterial layers with distributed collagen fibre orientations. *Journal of the Royal Society Interface*, 3: 15–35, 2006.
- A.N. Gent. A new constitutive relation for rubber. *Rubber Chemistry and Technology*, 69:59–61, 1996.
- P.E. Gill, W. Murray, and M.H. Wright. *Practical optimization*. Academic Press, London, 1981.
- R. Glowinski and P. Le Tallec. Finite element analysis in nonlinear incompressible elasticity. In J.T. Oden and G.F. Carey, editors, *Finite elements, Vol V: Special Problems in Solid Mechanics*. Prentice-Hall, Englewood Cliffs, NH, 1984.
- R. Glowinski and P. Le Tallec. *Augmented Lagrangian methods for the solution of variational problems*. Springer, Berlin, 1988.

- R. Glowinski and P. Le Tallec. *Augmented Lagrangian and operator-splitting methods in nonlinear mechanics*, volume 9 of *SIAM Studies in Applied Mathematics*. Society for Industrial and Applied Mathematics (SIAM), Philadelphia, PA, 1989. ISBN 0-89871-230-0.
- S. Göktepe and C. Miehe. A micro-macro approach to rubber-like materials. Part III: The micro-sphere model of anisotropic Mullins-type damage. *Journal of the Mechanics and Physics of Solids*, 53(10):2259–2283, 2005.
- S. Govindjee and J.C. Simo. A micro-mechanically based continuum damage model for carbon black-filled rubbers incorporating Mullins' effect. *Journal of the Mechanics and Physics of Solids*, 39:87–112, 1991.
- J.H. Grace and A. Young. *The algebra of invariants*. Cambridge University Press, Cambridge, 1903.
- J.F. Granada, D. Wallace-Bradley, H.K. Win, C.L. Alviar, A. Builes, E.I. Lev, R. Barrios, D.G. Schulz, A.E. Raizner, and G.L. Kaluza. In vivo plaque characterization using intravascular ultrasound-virtual histology in a porcine model of complex coronary lesions. *Arteriosclerosis, Thrombosis, and Vascular Biology*, 27:387–393, 2007.
- S.E. Greenwald, J.E. Moore, A. Rachev, T.P.C. Kane, and J.-J. Meister. Experimental investigation of the distribution of residual strains in the artery wall. *Journal of Biomechanical Engineering*, 119:438–444, 1997.
- A. Grüntzig. *Die perkutane transluminale Rekanalisation chronischer Arterienverschlüsse mit einer neuen Dilatationstechnik*. G. Witzstock, 1977. ISBN 9783879210671.
- A. Grüntzig, W. Vetter, B. Meier, U. Kuhlmann, U. Lütolf, and W. Siegenthaler. Treatment of renovascular hypertension with percutaneous transluminal dilatation of a renal artery stenosis. *The Lancet*, 311(8068):801 – 802, 1978.
- N. Gundiah, M.B. Ratcliffe, and L.A. Pruitt. Determination of strain energy function for arterial elastin: experiments using histology and mechanical tests. *Journal of Biomechanics*, 40:586–594, 2007.
- Z. Guo and L.J. Sluys. Computational modelling of the stress-softening phenomenon of rubber-like materials under cyclic loading. *European Journal of Mechanics, A/Solids*, 25:877–896, 2006.
- H.S. Gupta. Nanoscale deformation mechanisms in collagen. In P. Fratzl, editor, *Collagen: Structure and Mechanics*, pages 155–173. Springer, 2008.
- G.B. Gurevich. *Foundations of the theory of algebraic invariants*. Nordhoff, 1964.
- H.C. Han and Y.C. Fung. Residual strains in porcine and canine trachea. *Journal of Biomechanics*, 24:307–315, 1991.
- S. Hartmann and P. Neff. Existence theory for a modified polyconvex hyperelastic relation of generalized polynomial-type in the case of nearly-incompressibility. *International Journal of Solids and Structures*, 40:2767–2791, 2003.

- P. Haupt. *Continuum Mechanics and Theory of Materials*. Springer, Berlin, Heidelberg, New York, 2000.
- M.R. Hestenes. Multiplier and gradient methods. *Journal of Optimization Theory and Applications*, 4:303–320, 1969.
- J. Hokanson and S. Yazdani. A constitutive model of the artery with damage. *Mechanics Research Communications*, 24(2):151–159, 1997.
- G.A. Holzapfel. *Nonlinear solid mechanics: a continuum approach for engineering*. John Wiley & Sons, 2000.
- G.A. Holzapfel and T.C. Gasser. Computational stress-deformation analysis of arterial walls including high-pressure response. *International Journal of Cardiology*, 116:78–85, 2007.
- G.A. Holzapfel and R.W. Ogden, editors. *Mechanics of biological tissue*. Springer-Verlag, Heidelberg, 2006.
- G.A. Holzapfel and R.W. Ogden. Modelling the layer-specific 3d residual stresses in arteries, with an application to the human aorta. *Journal of the Royal Society Interface*, 7:787–799, 2010.
- G.A. Holzapfel, T.C. Gasser, and R.W. Ogden. A new constitutive framework for arterial wall mechanics and a comparative study of material models. *Journal of Elasticity*, 61: 1–48, 2000a.
- G.A. Holzapfel, C.A.J. Schulze-Bauer, and M. Stadler. Mechanics of angioplasty: wall, balloon and stent. In J. Casey and G. Bao, editors, *Mechanics in biology*, pages 141–156. New York, 2000b.
- G.A. Holzapfel, T.C. Gasser, and R.W. Ogden. Comparison of a multi-layer structural model for arterial walls with a fung-type model, and issues of material stability. *Journal of Biomechanical Engineering*, 126:264–275, 2004a.
- G.A. Holzapfel, G. Sommer, and P. Regitnig. Anisotropic mechanical properties of tissue components in human atherosclerotic plaques. *Journal of Biomechanical Engineering*, 126:657–665, 2004b.
- G.A. Holzapfel, G. Sommer, T.C. Gasser, and P. Regitnig. Determination of the layer-specific mechanical properties of human coronary arteries with non-atherosclerotic intimal thickening, and related constitutive modelling. *American Journal of Physiology – Heart and Circulatory Physiology*, 289:H2048–H2058., 2005.
- G.A. Holzapfel, G. Sommer, M. Auer, P. Regitnig, and R.W. Ogden. Layer-specific 3d residual deformations of human aortas with non-atherosclerotic intimal thickening. *Annals of Biomedical Engineering*, 35(4):530–545, 2007.
- C.O. Horgan, R.W. Ogden, and G. Saccomandi. A theory of stress softening of elastomers based on finite chain extensibility. *Proceedings of the Royal Society London A*, 460: 1737–1754, 2004.

- L. Horný, E. Gultova, H. Chlup, R. Sedláček, J. Kronek, J. Veselý, and R. Žitný. Mullins effect in an aorta and limiting extensibility evolution. *Bulletin of Applied Mechanics*, 6(21):1–5, 2010.
- H. Huang, R. Virmani, H. Younis, A.P. Burke, R.D. Kamm, and R.T. Lee. The impact of calcification on the biomechanical stability of atherosclerotic plaques. *Circulation*, 103:1051–1056, 2001.
- T.J.R. Hughes. *The finite element method*. Dover Publications, 2000.
- J.D. Humphrey. Mechanics of the arterial wall: review and directions. *Critical Reviews in Biomedical Engineering*, 23:1–162, 1995.
- J.D. Humphrey. *Cardiovascular solid mechanics. Cells, tissues, and organs*. Springer-Verlag, New York, 2002.
- J.D. Humphrey. Review paper: Continuum biomechanics of soft biological tissues. *Proceedings of the Royal Society London A*, 459(2029):3–46, 2003.
- M. Itskov and A. Aksel. A class of orthotropic and transversely isotropic hyperelastic constitutive models based on a polyconvex strain energy function. *International Journal of Solids and Structures*, 41:3833–3848, 2004.
- L.C.U. Junqueira and J. Carneiro. *Histologie*. Springer Medizin Verlag Heidelberg, 6th edition, 2005. ISBN 3-540-21965-X.
- L.M. Kachanov. Time of the rupture process under creep conditions. *Izvestija Akademii nauk Sojuza Sovetskich Socialisticeskich Respubliki (SSSR) Otdelenie Techniceskich Nauk (Moskra)*, 8:26–31, 1958.
- G. Karypis, K. Schloegel, and V. Kumar. ParMETIS - Parallel graph partitioning and sparse matrix ordering. Version 3.1. Technical report, University of Minnesota, Department of Computer Science and Engineering, August 2003.
- A. Klarbring, T. Olsson, and J. Ståhlhand. Theory of residual stresses with application to an arterial geometry. *Archives of Mechanics*, 59(4-5):341–364, 2007.
- A. Klawonn. FETI domain decomposition methods for second order elliptic partial differential equations. *GAMM-Mitteilungen*, 29(2):319–341, 2006.
- A. Klawonn and O. Rheinbach. Inexact FETI-DP methods. *International Journal for Numerical Methods in Engineering*, 69:284–307, 2007a.
- A. Klawonn and O. Rheinbach. Robust FETI-DP methods for heterogeneous three dimensional linear elasticity problems. *Computer Methods in Applied Mechanics and Engineering*, 196:1400–1414, 2007b.
- A. Klawonn and O. Rheinbach. Highly scalable parallel domain decomposition methods with an application to biomechanics. *Zeitschrift für angewandte Mathematik und Mechanik*, 90(1):5–32, 2010.

- A. Klawonn and O. Bra Rheinbach. A parallel implementation of dual-primal FETI methods for three dimensional linear elasticity using a transformation of basis. *SIAM Journal on Scientific Computing*, 28(5):1886–1906, 2006.
- A. Klawonn and O.B. Widlund. Dual and dual-primal FETI methods for elliptic problems with discontinuous coefficients in three dimensions. In *Domain decomposition methods in sciences and engineering (Chiba, 1999)*, pages 29–39 (electronic). DDM.org, Augsburg, 2001.
- A. Klawonn and O.B. Widlund. FETI-DP methods for elliptic problems with discontinuous coefficients in three dimensions. In *Domain decomposition methods in science and engineering (Lyon, 2000)*, Theory Eng. Appl. Comput. Methods, pages 405–411. Internat. Center Numer. Methods Eng. (CIMNE), Barcelona, 2002.
- A. Klawonn and O.B. Widlund. Selecting constraints in dual-primal FETI methods for elasticity in three dimensions. In *Domain decomposition methods in science and engineering*, volume 40 of *Lect. Notes Comput. Sci. Eng.*, pages 67–81. Springer, Berlin, 2005.
- A. Klawonn and O.B. Widlund. Dual-primal FETI methods for linear elasticity. *Communications on Pure and Applied Mathematics*, 59:1523–1572, 2006.
- A. Klawonn, O.B. Widlund, and M. Dryja. Dual-primal FETI methods for three-dimensional elliptic problems with heterogeneous coefficients. *SIAM J. Numer. Anal.*, 40(1):159–179 (electronic), 2002. ISSN 0036-1429. doi: 10.1137/S0036142901388081.
- A. Klawonn, P. Neff, O. Rheinbach, and S. Vanis. FETI-DP domain decomposition methods for elasticity with structural changes: P -elasticity. *ESAIM Math. Model. Numer. Anal.*, 45(3):563–602, 2011. ISSN 0764-583X.
- A. König and V. Klauss. Virtual histology. *Heart*, 93:977–982, 2007.
- J. Korsgaard. On the representation of two-dimensional isotropic functions. *International Journal of Engineering Science*, 28(7):653–662, 1990a.
- J. Korsgaard. On the representation of symmetric tensor-valued isotropic functions. *International Journal of Engineering Science*, 28(12):1331–1346, 1990b.
- D. Krajcinovic. *Damage mechanics*. Elsevier Science B.V., North-Holland, 1996.
- C. Landau, R.A. Lange, and L.D. Hillis. Percutaneous transluminal coronary angioplasty. *New England Journal of Medicine*, 330(14):981–993, 1994.
- R.T. Lee, A.J. Grodzinsky, E.H. Frank, R.D. Kamm, and F.J. Schoen. Structure-dependent dynamic mechanical behavior of fibrous caps from human atherosclerotic plaques. *Circulation*, 83:1764–1770, 1991.
- R.T. Lee, S.G. Richardson, H.M. Loree, A.J. Grodzinsky, S.A. Gharib, F.J. Schoen, and N. Pandian. Prediction of mechanical properties of human atherosclerotic tissue by high-frequency intravascular ultrasound imaging. an in vitro study. *Arteriosclerosis, Thrombosis, and Vascular Biology*, 12:1–5, 1992.

- J. Lemaitre. Evaluation of dissipation and damage in metals submitted to dynamic loading. *Proceedings of the First International Conference on Mechanical Behavior of Materials. The Society of Material Science, Kyoto, Japan, 1971.*
- J. Lemaitre. *A course on damage mechanics.* Springer, Berlin, Heidelberg, New York, 2nd edition, 1996.
- J. Lemaitre and J.-L. Chaboche. *Mechanics of solid materials.* Cambridge University Press, 1990.
- J. Lemaitre and R. Desmorat. *Engineering damage mechanics - Ductile creep, fatigue and brittle failures.* Springer, Berlin, Heidelberg, 2005.
- C.L. Lendon, M.J. Davies, G.V.R. Born, and P.D. Richardson. Atherosclerotic plaque caps are locally weakened when macrophages density is increased. *Atherosclerosis*, 87(1):87–90, 1991.
- C.L. Lendon, M.J. Davies, P.D. Richardson, and G.V.R. Born. Testing of small connective tissue specimens for the determination of the mechanical behaviour of atherosclerotic plaques. *Journal of Biomechanical Engineering*, 15(1):27–33, 1993.
- T. Lenz. *Hypertonie in Klinik und Praxis.* Schattauer GmbH, Verlag für Medizin und Naturwissenschaften, 1st edition, 2007. ISBN 3-7945-2458-6.
- P. Libby and P.M. Ridker. Inflammation and atherothrombosis: From population biology and bench research to clinical practice. *Journal of the American College of Cardiology*, 48:33–46, 2006.
- S.Q. Liu. Biomechanical basis of vascular tissue engineering. *Critical Reviews in Biomedical Engineering*, 27:75–148, 1999.
- S.Q. Liu and Y.C. Fung. Zero-stress states of arteries. *Journal of Biomechanical Engineering*, 110:82–84, 1988.
- S.Q. Liu and Y.C. Fung. Relationship between hypertension, hypertrophy, and opening angle of zero-stress state of arteries following aortic constriction. *Journal of Biomechanical Engineering*, 111:325–335, 1989.
- H.M. Loree, A.J. Grodzinsky, S.Y. Park, L.J. Gibson, and R.T. Lee. Static circumferential tangential modulus of human atherosclerotic tissue. *Journal of Biomechanics*, 27(2): 195 – 204, 1994.
- R. Lüllmann-Rauch. *Histologie.* Georg Thieme Verlag, Stuttgart, 3rd edition, 2009. ISBN 978-3-13-129243-8.
- G. Marckmann, E. Verron, L. Gornet, G. Chagnon, P. Charrier, and P. Fort. A theory of network alteration for the Mullins effect. *Journal of the Mechanics and Physics of Solids*, 50:2011–2028, 2002.
- J.E. Marsden and T.J.R. Hughes. *Mathematical Foundations of Elasticity.* Prentice-Hall, 1983.

- T. Matsumoto, T. Goto, T. Furukawa, and M. Sato. Residual stress and strain in the lamellar unit of the porcine aorta: experiment and analysis. *Journal of Biomechanics*, 37(6):807–815, 2004.
- A. Menzel and P. Steinmann. A theoretical and computational framework for anisotropic continuum damage mechanics at large strains. *International Journal of Solids and Structures*, 38:9505–9523, 2001.
- J. Merodio and P. Neff. A note on tensile instabilities and loss of ellipticity for a fiber-reinforced nonlinearly elastic solid. *Archive of Applied Mechanics*, 58:293–303, 2006.
- C. Miehe. Discontinuous and continuous damage evolution in Ogden-type large-strain elastic materials. *European Journal of Mechanics, A/Solids*, 14:697–720, 1995.
- C. Miehe and J. Keck. Superimposed finite elastic-viscoelastic-plastoelastic stress response with damage in filled rubbery polymers. Experiments, modelling and algorithmic implementation. *Journal of the Mechanics and Physics of Solids*, 48:323–365, 2000.
- A. Mielke. Necessary and sufficient conditions for polyconvexity of isotropic functions. *Journal of Convex Analysis*, 12:291–314, 2005.
- G.S. Montes. Structural biology of the fibres of the collagenous and elastic systems. *Cell Biology International*, 20:15–27, 1996.
- L. Mullins. Effect of stretching on the properties of rubber. *Rubber Chemistry and Technology*, 21(2):281–300, 1948.
- J.C. Nagtegaal, D.M. Parks, and J.R. Rice. On numerically accurate finite element solutions in the fully plastic range. *Computer Methods in Applied Mechanics and Engineering*, 4(2):153–177, 1974.
- A. Nair, B.D. Kuban, E.M. Tuzcu, P. Schoenhagen, S.E. Nissen, and D.G. Vince. Coronary plaque classification with intravascular ultrasound radiofrequency data analysis. *Circulation*, 106:2200–2206, 2002.
- K. Nasu, E. Tsuchikane, O. Katoh, H. Fujita, J.F. Surmely, M. Ehara, Y. Kinoshita, N. Tanaka, T. Matsubara, Y. Asakura, K. Asakura, M. Terashima, and T. Suzuki. Plaque characterisation by virtual histology intravascular ultrasound analysis in patients with type 2 diabetes. *Heart*, 94(4):429–433, 2008.
- A.N. Natali, P.G. Pavan, E.L. Carniel, and C. Dorow. A transversally isotropic elasto-damage constitutive model for the periodontal ligament. *Computer Methods in Biomechanics and Biomedical Engineering*, 6:329–336, 2003.
- A.N. Natali, P.G. Pavan, E.L. Carniel, M.E. Lucisano, and G. Tagliavero. Anisotropic elasto-damage constitutive model for the biomechanical analysis of tendons. *Medical Engineering & Physics*, 27(3):209–214, 2005.
- W.W. Nichols and M.F. O'Rourke, editors. *McDonalds's blood flow in arteries*. Hodder Arnold, London, 4th edition, 1998.
- W. Noll. *The foundations of mechanics and thermodynamics*. Springer, 1974.

- M.U. Nollert, N.J. Panaro, and L.V. McIntire. Regulation of genetic expression in shear stress-stimulated endothelial cells. *Annals of the New York Academy of Sciences*, 665 (1):94–104, 1992.
- R.W. Ogden and D.G. Roxburgh. An energy-based model of the Mullins effect. In A. Dorfmann and A. Muhr, editors, *Proceedings of the First European Conference on Constitutive Models*, pages 23–28. A. A. Balkema, Rotterdam, Brookfield, 1999a.
- R.W. Ogden and D.G. Roxburgh. A pseudo-elastic model for the Mullins effect in filled rubber. *Proceedings of the Royal Society London A*, 455:2861–2877, 1999b.
- H.S. Oktay, T. Kang, J.D. Humphrey, and G.G. Bishop. Changes in the mechanical behavior of arteries following balloon angioplasty. In R.L. Spilker and M.H. Friedman, editors, *ASME 1991 Biomechanics Symposium, AMD-Vol. 120*. The American Society of Mechanical Engineers, 1991.
- T. Olsson and A. Klarbring. Residual stresses in soft tissue as a consequence of growth and remodeling: application to an arterial geometry. *European Journal of Mechanics, A/Solids*, 27:959–974, 2008.
- T. Olsson, J. Ståhlhand, and A. Klarbring. Modeling initial strain distribution in soft tissues with application to arteries. *Biomechanics and Modeling in Mechanobiology*, 5: 28–38, 2006.
- J.H. Omens and Y.C. Fung. Residual strain in rat left ventricle. *Circulation Research*, 66 (1):37–45, 1990.
- D.J. Patel and D.L. Fry. The elastic symmetry of arterial segments in dogs. *Circulation Research*, 24:1–8, 1969.
- E. Peña. A rate dependent directional damage model for fibred materials: application to soft biological tissues. *Computational Mechanics*, 48:407–420, 2011.
- E. Peña, M.A. Martínez, B. Calvo, and M. Doblaré. On the numerical treatment of initial strains in biological soft tissues. *International Journal for Numerical Methods in Engineering*, 68:836–860, 2006.
- E. Peña, J.A. Peña, and M. Doblaré. On the Mullins effect and hysteresis of fibered biological materials: a comparison between continuous and discontinuous damage models. *International Journal of Solids and Structures*, 46:1727–1735, 2009.
- A.C. Pipkin and A.S. Wineman. Material symmetry restrictions on non-polynomial constitutive equations. *Archive for Rational Mechanics and Analysis*, 12:420–426, 1963.
- M.J.D. Powell. A method for nonlinear constraints in minimization problems. In R. Fletcher, editor, *Optimization*, pages 283–298. Academic Press, New York, 1969.
- M.J.D. Powell. Variable metric methods for constrained optimization. In A. Bachem, M. Grotchel, and B. Korte, editors, *Mathematical programming: the state of the art*, pages 288–311. Springer Verlag, 1983.
- A. Quarteroni and A. Valli. *Domain decomposition methods for partial differential equations*. Oxford Science Publications, 1999.

- Y.N. Rabotnov. Creep rupture. In *Proceedings of the XII international congress on applied mechanics, Stanford, California*, pages 342–349, 1968.
- A. Rachev. Theoretical study of the effect of stress-dependent remodeling on arterial geometry under hypertensive conditions. *Journal of Biomechanics*, 30:819–827, 1997.
- A. Rachev and S.E. Greenwald. Residual strains in conduit arteries. *Journal of Biomechanics*, 36:661–670, 2003.
- O. Rheinbach. *Parallel scalable iterative substructuring: robust exact and inexact FETI-DP methods with applications to elasticity*. PhD thesis, Department of Mathematics, University of Duisburg-Essen, Essen, Germany, 2006.
- J.A.G. Rhodin. *Handbook of physiology, section 2: the cardiovascular system, volume II: vascular smooth muscle*, chapter Architecture of the Vessel Wall, pages 1–31. American Physiological Society, 1980. ISBN 9780470650714.
- P.D. Richardson, M.J. Davies, and G.V.R. Born. Influence of plaque configuration and stress distribution on fissuring of coronary atherosclerotic plaques. *The Lancet*, 334 (8669):941 – 944, 1989.
- R.S. Rivlin and J.L. Ericksen. Stress-deformation relations for isotropic materials. *Journal of Rational Mechanics and Analysis*, 4:323–425, 1955.
- M.R. Roach and A.C. Burton. The reason for the shape of the distensibility curves of arteries. *Canadian Journal of Biochemistry and Physiology*, 35:681–690, 1957.
- J.F. Rodríguez, F. Cacho, J.A. Bea, and M. Doblaré. A stochastic-structurally based three dimensional finite-strain damage model for fibrous soft tissue. *Journal of the Mechanics and Physics of Solids*, 54:864–886, 2006.
- J.F. Rodríguez, V. Alastrué, and M. Doblaré. Finite element implementation of a stochastic three dimensional finite-strain damage model for fibrous soft tissue. *Computer Methods in Applied Mechanics and Engineering*, 197(9-12):946–958, 2008.
- G.A. Rodriguez-Granillo, P.W. Serruys, H.M. Garcia-Garcia, J. Aoki, M. Valgimigli, C.A.G. van Mieghem, E. McFadden, P.P.T. de Jaegere, and P. de Feyter. Coronary artery remodelling is related to plaque composition. *Heart*, 92:388–391, 2006.
- T.G. Rogers. Yield criteria, flow rules, and hardening in anisotropic plasticity. In J.P. Boehler, editor, *Yielding, damage and failure of anisotropic solids*, pages 53–79, 1987.
- M.H. Ross and W. Pawlina. *Histology: a text and atlas: with correlated cell and molecular biology*. Lippincott Williams & Wilkins, 2006.
- R. Ross. The gordon wilson lecture: Atherosclerosis – a response to injury gone awry. *Transactions of the American Clinical and Climatological Association*, 93:78–86, 1982.
- R. Ross and J.A. Glomset. Atherosclerosis and the arterial smooth muscle cell. *Stahlbau*, 180(4093):1332–1339, 1973.
- R. Ross and J.A. Glomset. The pathogenesis of atherosclerosis. *New England Journal of Medicine*, 295(7):369–377, 1976.

- A. Saini, C. Berry, and S. Greenwald. Effect of age and sex on residual stress in the aorta. *Journal of Vascular Research*, 32:398–405, 1995.
- N.V. Salunke, L.D.T. Topoleski, J.D. Humphrey, and W.J. Mergner. Compressive stress-relaxation of human atherosclerotic plaque. *Journal of Biomedical Material Research*, 55(2):236–241, 2001.
- J. Schröder. *Theoretische und algorithmische Konzepte zur phänomenologischen Beschreibung anisotropen Materialverhaltens*. Phd-thesis, Universität Hannover, Institut für Mechanik (Bauwesen), Lehrstuhl I, Bericht Nr.: I-1, 1996.
- J. Schröder and S. Brinkhues. A novel numerical scheme for the computation of residual stresses in arterial walls. 2012. In preparation.
- J. Schröder and P. Neff. Invariant formulation of hyperelastic transverse isotropy based on polyconvex free energy functions. *International Journal of Solids and Structures*, 40:401–445, 2003.
- J. Schröder, D. Balzani, and D. Gross. Aspects of modeling and computer simulation of soft tissues: applications to arterial walls. *Material- und Werkstofftechnik*, 36:795–801, 2005a.
- J. Schröder, P. Neff, and D. Balzani. A variational approach for materially stable anisotropic hyperelasticity. *International Journal of Solids and Structures*, 42(15):4352–4371, 2005b.
- J. Schröder, P. Wriggers, and D. Balzani. A new mixed finite element based on different approximations of the minors of deformation tensors. *Computer Methods in Applied Mechanics and Engineering*, 200:3583–3600, 2011.
- C.A.J. Schulze-Bauer, M. Auer, and G.A. Holzapfel. Layer-specific residual deformations of aged human aortas. In *13th Conference of the European Society of Biomechanics*, 2002a.
- C.A.J. Schulze-Bauer, P. Regitnig, and G.A. Holzapfel. Mechanics of the human femoral adventitia including the high-pressure response. *American Journal of Physiology – Heart and Circulatory Physiology*, 282:H2427–H2440, 2002b.
- I. Schur. *Vorlesungen über Invariantentheorie*. Springer, 1968.
- F.H. Silver, D.L. Christiansen, and C.M. Buntin. Mechanical properties of the aorta: a review. *Critical Reviews in Biomedical Engineering*, 17(4):323–58, 1989.
- F.C. Simo and R.L. Taylor. Quasi-incompressible finite elasticity in principal stretches. continuum basis and numerical algorithms. *Computer Methods in Applied Mechanics and Engineering*, 85(3):273–310, 1991.
- J.C. Simo. On a fully three-dimensional finite-strain viscoelastic damage model: formulation and computational aspects. *Computer Methods in Applied Mechanics and Engineering*, 60:153–173, 1987.
- J.C. Simo. Numerical analysis and simulation of plasticity. In P.G. Ciarlet and J.L. Lions, editors, *Handbook of numerical analysis*, number 6. Elsevier Science, 1998.

- J.C. Simo and J.W. Ju. Strain- and stress-based continuum damage models, I. formulation, II. computational aspects. *International Journal of Solids and Structures*, 23: 821–869, 1987.
- J.C. Simo and R.L. Taylor. Penalty function formulations for incompressible nonlinear elastostatics. *Computer Methods in Applied Mechanics and Engineering*, 35:107–118, 1982.
- J.C. Simo, R.L. Taylor, and K.S. Pister. Variational and projection methods for the volume constraint in finite deformation elasto-plasticity. *Computer Methods in Applied Mechanics and Engineering*, 51:177–208, 1985.
- J.J. Skrzypek and A. Ganczarski. *Modeling of material damage and failure of structures, theory and applications*. Springer, 1999.
- B.F. Smith, P.E. Bjørstad, and W. Gropp. *Domain decomposition: parallel multilevel methods for elliptic partial differential equations*. Cambridge University Press, 1996.
- G.F. Smith. On a fundamental error in two papers of C.-C. Wang “On representations for isotropic functions, Parts I and II”. *Archive for Rational Mechanics and Analysis*, 36:161–165, 1970.
- G.F. Smith. On isotropic functions of symmetric tensors, skew-symmetric tensors and vectors. *International Journal of Engineering Science*, 9:899–916, 1971.
- G. Sommer, P. Regitnig, L. Költringer, and G. A. Holzapfel. Biaxial mechanical properties of intact and layer-dissected human carotid arteries at physiological and supra-physiological loadings. *American Journal of Physiology – Heart and Circulatory Physiology*, 298:H898–912, 2010.
- A.J.M. Spencer. Theory of invariants. In A.C. Eringen, editor, *Continuum Physics*, volume I – Mathematics, pages 239–353. Academic Press, New York, 1971.
- A.J.M. Spencer. *Deformations of fibre-reinforced materials*. Oxford University Press, 1972.
- D.J. Steigmann. Frame-invariant polyconvex strain-energy functions for some anisotropic solids. *Mathematics and Mechanics of Solids*, 8:497–506, 2003.
- E. Stein and F.-J. Barthold. Elastizitätstheorie. In G. Mehlhorn, editor, *Der Ingenieurbau: Grundwissen*, number 4. Ernst und Sohn, 1996.
- P. Steinmann and I. Carol. A framework for geometrically nonlinear continuum damage mechanics. *International Journal of Engineering Science*, 36:1793–1814, 1998.
- J. Ståhlhand, A. Klarbring, and M. Karlsson. Towards in vivo aorta material identification and stress estimation. *Biomechanics and Modeling in Mechanobiology*, 2:169–186, 2004.
- K. Takamizawa and K. Hayashi. Strain energy density function and uniform strain hypothesis for arterial mechanics. *Journal of Biomechanics*, 20:7–17, 1987.

- A.-K. Tielke. Sensitivity analysis of plaque components within arterial wall simulations based on patient specific data. Master's thesis, Institut für Mechanik, Universität Duisburg-Essen, 2009.
- L.D.T. Topoleski and N.V. Salunke. Mechanical behavior of calcified plaques: a summary of compression and stress-relaxation experiments. *Zeitschrift für Kardiologie*, 89:S085–S091, 2000.
- A. Toselli and O.B. Widlund. *Domain decomposition methods – algorithms and theory*, volume 34 of *Series in Computational Mathematics*. Springer-Verlag, Berlin, Heidelberg, New York, 2005.
- C. Truesdell. *Rational Thermodynamics*. McGraw-Hill, New York, 1969.
- C. Truesdell and W. Noll. *The Non-Linear Field Theories of Mechanics*. Springer, 3rd edition, 2004.
- C. Truesdell and R. Toupin. The classical field theories. In S. Flügge, editor, *Encyclopedia of Physics*, volume 3, pages 226–793. Springer, 1960.
- H.W. Turnbull. *The theory of determinants, matrices and invariants*. Dover, New York, 3rd edition, 1960.
- R.N. Vaishnav and J. Vossoughi. Estimation of residual strains in aortic segments. In C.W. Hall, editor, *Biomedical Engineering II: Recent Developments*. Pergamon Press, New York, 1983.
- R.N. Vaishnav, J.T. Young, and D.J. Patel. Distribution of stresses and of strain-energy density through the wall thickness in a canine aortic segment. *Circulation Research*, 32:577–583, 1973.
- A. Valentin and J.D. Humphrey. Evaluation of fundamental hypotheses underlying constrained mixture models of arterial growth and remodelling. *Philosophical Transactions of the Royal Society A: Mathematical, Physical and Engineering Sciences*, 367(1902): 3585–3606, 2009.
- W.-W. von Maltzahn, R.G. Warriyar, and W. Keitzer. Experimental measurements of elastic properties of media and adventitia of bovine carotid arteries. *Journal of Biomechanics*, 17:839–847, 1984.
- J. Vossoughi, Z. Hedjazi, and F.S. Borris. Intimal residual stress and strain in large arteries. In N.A. Langrana, M.H. Friedman, and E.S. Grood, editors, *Proceedings of the Summer Bioengineering Conference, New York*, pages 434–437. American Society of Mechanical Engineers, 1993.
- G.Z. Voyiadjis and P.I. Kattan, editors. *Advances in damage mechanics: metals and material matrix composites with an introduction to fabric tensors*. Amsterdam, Elsevier, 2006.
- C.-C. Wang. On a general representation theorem for constitutive relations. *Archive for Rational Mechanics and Analysis*, 33:1–25, 1969a.

- C.-C. Wang. On representations for isotropic functions: part I. Isotropic functions of symmetric tensors and vectors. *Archive of Rational Mechanics and Analysis*, 33:249–267, 1969b.
- C.-C. Wang. On representations for isotropic functions: part II. Isotropic functions of skew-symmetric tensors, symmetric tensors and vectors. *Archive of Rational Mechanics and Analysis*, 33:268–287, 1969c.
- C.-C. Wang. A new representation theorem for isotropic functions: an answer to Professor G.F. Smith’s Criticism of my papers on representations for isotropic functions. Part 1. Scalar-valued isotropic functions. *Archive for Rational Mechanics and Analysis*, 36:166–197, 1970a.
- C.-C. Wang. A new representation theorem for isotropic functions: an answer to Professor G. F. Smith’s Criticism of my papers on representations for isotropic functions. Part 2. Vector-valued isotropic functions, symmetric tensor-valued isotropic functions, and skew-symmetric tensor-valued isotropic functions. *Archive for Rational Mechanics and Analysis*, 36:198–223, 1970b.
- C.-C. Wang. Corrigendum to my recent papers on ”Representations for isotropic functions”. *Archive for Rational Mechanics and Analysis*, 43:392–395, 1971.
- P.N. Watton, Y. Ventikos, and G.A. Holzapfel. Modelling the mechanical response of elastin for arterial tissue. *Journal of Biomechanics*, 42:1320–1325, 2009.
- H. Weisbecker, D.M. Pierce, P. Regitnig, and G.A. Holzapfel. Layer-specific damage experiments and modeling of human thoracic and abdominal aortas with non-atherosclerotic intimal thickening. *Journal of the Mechanical Behavior of Biomedical Materials*, 12:93–106, 2012.
- J.A. Weiss, B.N. Maker, and S. Govindjee. Finite element implementation of incompressible, transversely isotropic hyperelasticity. *Computer Methods in Applied Mechanics and Engineering*, 135:107–128, 1996.
- U. Welsch. *Lehrbuch Histologie: Zytologie, Histologie, Mikroskopische Anatomie*. Urban & Fischer - Elsevier, München, 2nd edition, 2006. ISBN 978-3-437-44430-2.
- H. Weyl. *The classical groups: their invariants and representation*. Princeton University Press, Princeton, New Jersey, 1946.
- A.S. Wineman and A.C. Pipkin. Material symmetry restrictions on constitutive equations. *Archive for Rational Mechanics and Analysis*, 17:184–214, 1964.
- P. Wriggers. *Nonlinear finite element methods*. Springer, 2008.
- J. Xie, J. Zhou, and Y.C. Fung. Bending of blood vessel wall: stress-strain laws of the intima-media and adventitia layers. *Journal of Biomechanical Engineering*, 117:136–145, 1995.
- Q. Yu, J. Zhou, and Y. C. Fung. Neutral axis location in bending and young’s modulus of different layers of arterial wall. *American Journal of Physiology – Heart and Circulatory Physiology*, 265:H52–H60, 1993.

- Q.-S. Zheng and A.J.M. Spencer. Tensors which characterize anisotropies. *International Journal of Engineering Science*, 31(5):679–693, 1993.
- Y.Y. Zhu and S. Cescetto. A fully coupled elasto-visco-plastic damage theory for anisotropic materials. *International Journal of Solids and Structures*, 32:1607–1641, 1995.
- O.C. Zienkiewicz and R.L. Taylor. *The finite element method, volume 1: basic formulations and linear problems*. McGraw Hill, 4th edition, 1989.
- O.C. Zienkiewicz and R.L. Taylor. *The finite element method for solid and structural mechanics*. Elsevier, 6th edition, 2005.
- O.C. Zienkiewicz, R.L. Taylor, and J.Z. Zhu. *The finite element method: its basis and fundamentals*. Elsevier, 2005.
- C.L. Zollikofer, E. Salomonowitz, R. Sibley, J. Chain, W.F. Bruehlmann, W.R. Castaneda-Zuniga, and K. Amplatz. Transluminal angioplasty evaluated by electron microscopy. *Radiology*, 153:369–374, 1984.

Curriculum Vitae

Der Lebenslauf ist in der Online-Version aus Gründen des Datenschutzes nicht enthalten.

In dieser Schriftenreihe bisher erschienene Berichte:

- Nr. 1 (2004) *Ein Modell zur Beschreibung finiter anisotroper elasto-plastischer Deformationen unter Berücksichtigung diskreter Rissausbreitung*, J. Löblein, Dissertation, 2004.
- Nr. 2 (2006) *Polyconvex Anisotropic Energies and Modeling of Damage applied to Arterial Walls*, D. Balzani, Dissertation, 2006.
- Nr. 3 (2006) *Kontinuumsmechanische Modellierung ferroelektrischer Materialien im Rahmen der Invariantentheorie*, H. Romanowski, Dissertation, 2006.
- Nr. 4 (2007) *Mehrskalen-Modellierung polykristalliner Ferroelektrika basierend auf diskreten Orientierungsverteilungsfunktionen*, I. Kurzhöfer, Dissertation, 2007.
- Nr. 5 (2007) *Proceedings of the First Seminar on the Mechanics of Multifunctional Materials*, J. Schröder, D. Lupascu, D. Balzani (Ed.), Tagungsband, 2007.
- Nr. 6 (2008) *Zur Modellierung und Simulation diskreter Rissausbreitungsvorgänge*, O. Hilgert, Dissertation, 2008.
- Nr. 7 (2009) *Least-Squares Mixed Finite Elements for Solid Mechanics*, A. Schwarz, Dissertation, 2009.
- Nr. 8 (2010) *Design of Polyconvex Energy Functions for All Anisotropy Classes*, V. Ebbing, Dissertation, 2010.
- Nr. 9 (2011) *Modeling of Electro-Mechanically Coupled Materials on Multiple Scales*, M.-A. Keip, Dissertation, 2011.
- Nr. 10 (2012) *Geometrical Modeling and Numerical Simulation of Heterogeneous Materials*, D. Brands, Dissertation, 2012.